



National Library
of Canada

Acquisitions and
Bibliographic Services Branch

395 Wellington Street
Ottawa, Ontario
K1A 0N4

Bibliothèque nationale
du Canada

Direction des acquisitions et
des services bibliographiques

395, rue Wellington
Ottawa (Ontario)
K1A 0N4

Your file Votre référence

Our file Notre référence

NOTICE

The quality of this microform is heavily dependent upon the quality of the original thesis submitted for microfilming. Every effort has been made to ensure the highest quality of reproduction possible.

If pages are missing, contact the university which granted the degree.

Some pages may have indistinct print especially if the original pages were typed with a poor typewriter ribbon or if the university sent us an inferior photocopy.

Reproduction in full or in part of this microform is governed by the Canadian Copyright Act, R.S.C. 1970, c. C-30, and subsequent amendments.

AVIS

La qualité de cette microforme dépend grandement de la qualité de la thèse soumise au microfilmage. Nous avons tout fait pour assurer une qualité supérieure de reproduction.

S'il manque des pages, veuillez communiquer avec l'université qui a conféré le grade.

La qualité d'impression de certaines pages peut laisser à désirer, surtout si les pages originales ont été dactylographiées à l'aide d'un ruban usé ou si l'université nous a fait parvenir une photocopie de qualité inférieure.

La reproduction, même partielle, de cette microforme est soumise à la Loi canadienne sur le droit d'auteur, SRC 1970, c. C-30, et ses amendements subséquents.

UNIVERSITY OF ALBERTA

**HYDROGEN RELATED DISBONDING
OF WELD OVERLAY OF CORROSION RESISTANT ALLOYS**

by



YUNJIAN WU

A THESIS

SUBMITTED TO THE FACULTY OF GRADUATE STUDIES AND RESEARCH
IN PARTIAL FULFILLMENT OF THE REQUIREMENTS FOR THE DEGREE OF

DOCTOR OF PHILOSOPHY

IN

METALLURGICAL ENGINEERING

DEPARTMENT OF MINING, METALLURGICAL AND PETROLEUM
ENGINEERING

EDMONTON, ALBERTA

SPRING, 1993



National Library
of Canada

Acquisitions and
Bibliographic Services Branch

395 Wellington Street
Ottawa, Ontario
K1A 0N4

Bibliothèque nationale
du Canada

Direction des acquisitions et
des services bibliographiques

395, rue Wellington
Ottawa (Ontario)
K1A 0N4

Your file Votre référence

Our file Notre référence

The author has granted an irrevocable non-exclusive licence allowing the National Library of Canada to reproduce, loan, distribute or sell copies of his/her thesis by any means and in any form or format, making this thesis available to interested persons.

L'auteur a accordé une licence irrévocable et non exclusive permettant à la Bibliothèque nationale du Canada de reproduire, prêter, distribuer ou vendre des copies de sa thèse de quelque manière et sous quelque forme que ce soit pour mettre des exemplaires de cette thèse à la disposition des personnes intéressées.

The author retains ownership of the copyright in his/her thesis. Neither the thesis nor substantial extracts from it may be printed or otherwise reproduced without his/her permission.

L'auteur conserve la propriété du droit d'auteur qui protège sa thèse. Ni la thèse ni des extraits substantiels de celle-ci ne doivent être imprimés ou autrement reproduits sans son autorisation.

ISBN 0-315-82247-3

Canada

RECEIVED Elsevier Science Publishers B.V. FEB. 1993

606 Chem/Min. Engr. Bldg.
University Campus
92 ave - 116 street
Edmonton, Alberta
Canada T6G 2G6
Phone (403) 426 - 0395
(403) 492 - 2863
Fax (403) 492 - 3409

North - Holland
Elsevier Science Publishers B.V.
P.O. Box 211
100 AE Amsterdam
The Netherlands

Re: Copyright

To whom it may concern:


I am writing you to apply for the permission to use photocopies of figures in the book published by your company for my Ph.D. degree thesis.

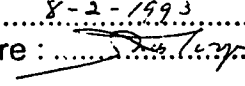
I am now a Ph.D. student in welding metallurgy at the Department of Mining, Metallurgical and Petroleum Engineering in The University of Alberta. I would like to copy three figures in the book titled as *Welding Theory and Practice*, edited by David L. Olson, Ray Dixon and Alan L. Liby. p.cm - (Materials processing, theory and practice, V.8) ISBN 0-444-87427-5. The three figures I am going to copy are: Fig.3 on Page 42, Fig.12 on Page 57 and Fig.20 on Page 68. I use the three figures in my literature survey part of my thesis.

I would appreciate it very much if my application receives your consideration. If you have any other limitation on this matter, please let me know.

I am looking forward to your earliest reply.

Sincerely yours,


Yun Jian Wu

Permission granted subject to
permission from the author(s)
and to full acknowledgement of
the source, provided that no
credit is made to another source
of publication.
ELSEVIER SCIENCE PUBLISHERS BV
Academic Publishing Division
Date : 8-2-1993
Signature : 

UNIVERSITY OF ALBERTA

RELEASE FORM

Name of Author : **Yunjian Wu**


Title of Thesis: **Hydrogen Related Disbonding of Weld Overlay of Corrosion Resistant Alloys**

Degree : **Doctor of Philosophy**

Year This Degree Granted: **Spring 1993**

Permission is hereby granted to the University of Alberta Library to reproduce single copies of this thesis and to lend or sell such copies for private, scholarly or scientific research purpose only.

The author reserves all other publication and other rights in association with the copyright in the thesis, and except as hereinbefore provided neither the thesis nor any substantial portion thereof may be printed or otherwise reproduced in any material form whatever without the author's prior written permission.



Yunjian WU

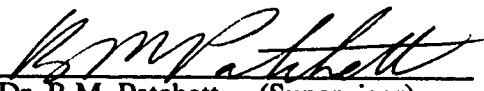
606 Chemical/Mineral Engineering Building
116 street - 92 avenue
Edmonton, Alberta T6G 2G6

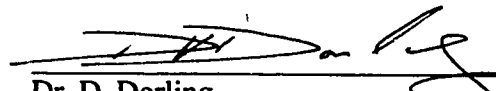
Date: April 23, 1993

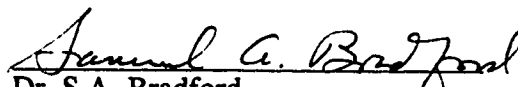
University of Alberta


Faculty of Graduate Studies and Research

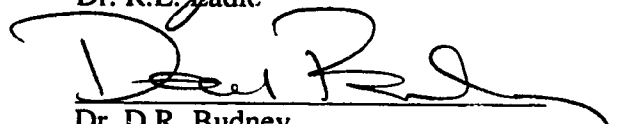
The undersigned certify that they have read and recommend to the faculty of Graduate Studies and Research for acceptance, a thesis entitled **Hydrogen Related Disbonding of Weld Overlay of Corrosion Resistant Alloys** submitted by **Yunjian WU** in partial fulfillment of the requirements for the degree of **Doctor of Philosophy in Metallurgical Engineering**.



Dr. B.M. Patchett (Supervisor)


Dr. D. Dorling


Dr. S.A. Bradford


Dr. R.L. Badie


Dr. D.R. Budney


Dr. K. Barron

Date: April 16/93

In Blessed Memory of My Father

Baohua Wu

Whose untimely pass away intensified my confidence to success.

ABSTRACT

For the manufacture of hydrogenation pressure vessels of heavy wall sections, cladding with a layer or multilayer of corrosion resistant alloy on the inside wall of the vessel by Submerged Arc Welding with a strip electrode has become a common practice. However, the occurrence of disbonding of the overlay from the base steel, usually Cr - Mo low alloy steel, has remained a problem, especially during cooling down of the vessel in an emergency. There are three major factors attributing to the disbonding. One is the hydrogen accumulation at the interface between the overlay and the base steel as a result of the difference in solubility and diffusivity of hydrogen between the overlay of austenitic structure and the base steel of ferritic structure. The second factor is the residual tensile stresses developed in the overlay during cooling down of the vessel from operation due to the difference in thermal expansion between the dissimilar materials. Finally, the susceptible microstructure along the interface to the disbonding plays another principal role. Nevertheless, the influence of the microstructure, and the actual mechanism of disbonding, remain obscure.

A simulation of hydrogen accumulation in the Type II grain boundary is established based on a Finite Differential Method. A level of more than 120 ppm of hydrogen can be reached at the Type II boundary. This well exceeds the solubility of hydrogen in ferrite (~6 ppm in weight) or in austenite (~60 ppm) under normal conditions.

A dissimilar material bond was employed to evaluate the level of residual tensile stresses in the overlay. Tensile stresses exist perpendicular and parallel to the interface in the overlay near the interface.

A systematic investigation on the formation of a crack-susceptible structure was carried out, and the mechanisms for the formation of such a structure are proposed. A so-called Type II grain boundary adjacent and parallel to the interface in the overlay side has been confirmed as detrimental. A phase change during solidification and/or the presence of inclusions from the base steel due to dilution effect segregating at the front of planar grains in the initial stage of solidification are responsible for the formation of Type II grain boundaries.

A proper selection of overlay materials and the welding procedure can eliminate or reduce the chance for the formation of Type II grain boundaries. Hence the hydrogen related disbonding can be minimized.

ACKNOWLEDGEMENT

I would like to express my gratitude to Dr. Barry Patchett, my supervisor, for his guidance throughout the course of this project.

My special appreciation is also given to Mr. Clark Bicknell for his skillful assistance during the experiment. Ms. Tina Barker's help in the analysis on SEM is gratefully appreciated.

Thanks are also extended to Dr. R. Ergeton at Physics Department, Dr. M. Chen at Surgical Medicine Research Institute and Dr. D. Ivey for their permissions to work on their equipment to complete the experiments.

The valuable suggestions and proof reading by the Supervisory Committee members: Dr. B. Patchett, Dr. S. Bradford, Dr. R. Eadie and Dr. D. Budney, especially the external reader, Dr. D.V. Dorling, are heartily acknowledged.

The encouragement from my wife, Rensha Luo, was invaluable for me to complete this project.

Table of Contents

Chapter	Page
1. INTRODUCTION	1
2. LITERATURE REVIEW	4
2.1 Hydrogen Distribution	4
2.1.1 General Consideration about Hydrogen Distribution	4
2.1.2 Variables Influencing Hydrogen Accumulation	6
2.1.2.1 Operation Conditions	6
2.1.2.2 Cooling Rates during Shut-down	8
2.1.2.3 Thickness of the Weld Overlay and the Base Steel Wall	8
2.1.2.4 Composition and Microstructure	9
2.1.2.5 Stresses and Strains	9
2.1.2.6 Welding Procedure	10
2.2 Effects of Residual Stresses	11
2.3 Effect of Composition and Microstructure.....	12
2.3.1 Weld Overlay	12
2.3.2 Base Steel	15
2.4 Effects of Welding Processes and Procedures	16
2.4.1 Welding Processes	16
2.4.2 Welding Speed	17
2.4.3 Post Weld Heat Treatment	18
2.4.4 Other Welding Conditions	20
3. STATEMENTS OF PROBLEMS AND OBJECTIVES	23
4. THEORY	25
4.1 Diffusion and Trapping of Hydrogen	25
4.1.1 General Equation for the Diffusion of Mass	25
4.1.2 Activity Coefficient of Diffusion Mass	26
4.1.3 Formulation of Boundary Conditions for Hydrogen Diffusion and Trapping	28
4.1.4 Finite Difference Method for the Diffusion Analysis	29
4.2 Hydrogen Induced Cracking (HIC)	30
4.3 Stress Field of the Bonded Dissimilar Materials	31
4.4 Morphology of Weld Overlay	34
4.4.1 The Geometry of Weld Overlay	34
4.4.2 The Structure of Weld Overlay	36

4.4.2.1 Overlay Microstructure	36
4.4.2.2 Microsegregation of Solutes	41
4.5 Effect of Flux on the Structure of Welds	43
5. EXPERIMENTAL EQUIPMENT, MATERIALS AND PROCEDURES	45
5.1 Equipment	45
5.2 Materials	46
5.2.1 Strips of Corrosion Resistant Alloys	46
5.2.2 Plate of the Base Steel	47
5.2.3 Welding Flux	47
5.3 Experimental Procedure	47
5.3.1 Welding Procedure	47
5.3.2 Ultrasonic Examination	48
5.3.3 Post Weld Heat Treatment (PWHT)	48
5.3.4 Autoclave Test	48
5.3.5 Microhardness	49
5.3.6 Dilatometric Examination	49
5.3.7 Optical Metallographic Observation	50
5.3.8 Measurement of Dilution	50
5.3.9 Observation on Scanning Electron Microscope	51
5.3.10 Observation on Transmission Electron Microscope	51
6. EXPERIMENTAL RESULTS	52
6.1 Effect of Welding Procedures on Dilution	52
6.2 Thermal Expansion Coefficients	52
6.3 Microhardness across the Interface	53
6.4 Ultrasonic Examination of Disbonding	55
6.5 Optical Metallographic Observation	55
6.5.1 Optical Microstructures in As-welded Condition	55
6.5.2 Optical Microstructures in PWHT Condition	59
6.5.3 Disbonding Phenomena	61
6.6 Observation on SEM and TEM	62
7. DISCUSSION	66
7.1 Introduction	66
7.2 Hydrogen Accumulation in Type II Grain Boundaries	66
7.3 Residual Stresses in Overlay	69
7.4 Microstructures in the Overlays	71
7.4.1 General Consideration of the Formation of the Interface	

Microstructure	71
7.4.2 Formation of Type II Grain Boundaries	72
7.4.2.1 Effect of Overlay Chemistry	73
7.4.2.2 Effect of Welding Procedure	83
7.5 Disbonding of Overlay	89
8. SUMMARY AND CONCLUSIONS	92
8.1 Summary	92
8.2 Conclusions	93
9. SUGGESTIONS FOR FURTHER WORK	96
TABLES	97
FIGURES	100
REFERENCES	183
APPENDICES	
Appendix A Coefficients of Compliance for the Plate Components	195
Appendix B Analysis of Stress Field of Bonded Dissimilar Materials	197
Appendix C Computer Program to Simulate the Hydrogen Accumulation in the Type II	
Grain Boundary	200
Appendix D Paper Read at the 31st Metallurgists Conference of CIM	206

List of Tables

Table	Page
1. Chemical compositions of alloys used as cladding materials	97
2. Chemical composition of base steel	97
3. Chemical composition of weld flux	97
4. Cladding conditions in Submerged Arc Welding	98
5. Dilution of welding procedures	98
6. Thermal expansion coefficients of alloys and possible residual stresses at interface	98
7. Disbonding analysis by ultrasonic C - scan	99
8. Equivalents of chromium and nickel of overlays	99

List of Figures

Figure	Page
1. Hydrogen Distribution in the Operation Condition	100
2. Hydrogen Distribution after Shut-Down	101
3. Effects of Shut-Down Condition on Hydrogen Accumulation	102
4. Effects of Cooling rate, Thickness of Base Steel and Overlay on Hydrogen Accumulation	103
5. Variation in Surface Strain due to Slicing	104
6. Distribution of the Residual Stresses in Through-Thickness Direction across the Overlay Welds	105
7. A Typical Microstructure of Austenitic Stainless Steel Overlay	106
8. Crack Running along Type II Grain Boundary after Autoclave Test	107
9. Illustration of Four Types of Disbonding Location.....	108
10. Disbonding Phenomena Related to Welding Current, Travel Speed and Microstructure	109
11. Cross-section through a Strip Clad Specimen Showing the Relative Contribution of Electrode (F) and Base Steel (Fo) to the Deposit Chemistry	110
12. Schematic Representation of Microstructure for Various Growth Modes	
(a) Planar Growth Mode	111
(b) Cellular Growth Mode	112
(c) Cellular Dendrite Growth Mode	113
13. Effect of PWHT Condition on Hydrogen Induced Disbonding	114
14. Element Profile Close to the Interface between Weld Overlay and 2.25Cr- 1 Mo Base Steel after PWHT	115

15. Disbonding crack in 309/347 Overlay and Crack ends at Intrusion	116
16. One dimensional element system for diffusion analysis by finite difference method	117
17. Plate of weld overlay and base steel	118
18. Variations in solidification patterns as a function of percent solute and $G/R^{1/2}$	119
19. (a) Schematic of an Fe-Cr-Ni pseudo-binary	120
(b) Schematics of stainless steel weld structures for primary austenite and primary ferrite solidification	120
20. Solute banding resulting from changes in solidification velocity	121
21. Schematic of set-up of the operation for the cladding	122
22. Schematic of set-up of the operation for ultrasonic examination	123
23. Schematic of set-up of operation for the autoclave test	124
24. Schematic of set-up of operation for dilatometric test	125
25. Thermal expansion curve of base steel	126
26. Thermal expansion curve of overlay 2205	127
27. Thermal expansion curve of overlay 309L	128
28. Thermal expansion curve of overlay 254SMO	129
29. Thermal expansion curve of overlay 904L	130
30. Thermal expansion curve of overlay C22	131
31. Thermal expansion curve of standard sample Ni	132
32. Microhardness across the interface of overlay 2205 As-welded	133
33. Microhardness across the interface of overlay 309L As-welded	134
34. Microhardness across the interface of overlay 254SMO As-welded	135

35. Microhardness across the interface of overlay 904L As-welded	136
36. Microhardness across the interface of overlay C22 As-welded	137
37. Microhardness across the interface of overlay 2205 after PWHT	138
38. Microhardness across the interface of overlay 309L after PWHT	139
39. Microhardness across the interface of overlay 254SMO after PWHT	140
40. Microhardness across the interface of overlay 904L after PWHT	141
41. Microhardness across the interface of overlay C22 after PWHT	142
42. C-Scan plot revealing disbonding in Overlay 309L	143
43. C-Scan plot revealing disbonding in Overlay 254SMO	143
44. As-welded optical microstructure of Specimen 2205 by Procedure I	144
45. As-welded optical microstructure of Specimen 2205 by Procedure II	144
46. As-welded optical microstructure of Specimen 309L by Procedure I	145
47. As-welded optical microstructure of Specimen 309L by Procedure II	145
48. As-welded optical microstructure of Specimen 309LMo by Procedure I	146
49. As-welded optical microstructure of Specimen 309LMo by procedure II	146
50. As-welded optical microstructure of Specimen 309LNb by Procedure I	147
51. As-welded optical microstructure of Specimen 309LNb by Procedure II	147
52. As-welded optical microstructure of Specimen 254SMO by Procedure I	148
53. As-welded optical microstructure of Specimen 254SMO by Procedure II	148
54. As-welded optical microstructure of Specimen 904L by Procedure I	149
55. As-welded optical microstructure of Specimen 904L by Procedure II	149
56. As-welded optical microstructure of Specimen C22 by Procedure I	150

57. As-welded optical microstructure of Specimen C22 by Procedure II	150
58. As-welded optical microstructure of Specimen 5923 by Procedure I	151
59. As-welded optical microstructure of Specimen 5923 by Procedure II	151
60. PWHT optical microstructure of Specimen 2205 by Procedure I	152
61. PWHT optical microstructure of Specimen 2205 by Procedure II	152
62. PWHT optical microstructure of Specimen 309L by Procedure I	153
63. PWHT optical microstructure of Specimen 309L by Procedure II	153
64. PWHT optical microstructure of Specimen 309LMo by Procedure I	154
65. PWHT optical microstructure of Specimen 309LMo by Procedure II	154
66. PWHT optical microstructure of Specimen 309LNb by Procedure I	155
67. PWHT optical microstructure of Specimen 309LNb by Procedure II	155
68. PWHT optical microstructure of Specimen 254SMO by Procedure I	156
69. PWHT optical microstructure of Specimen 254SMO by Procedure II	156
70. PWHT optical microstructure of Specimen 904L by Procedure I	157
71. PWHT optical microstructure of Specimen 904L by Procedure II	157
72. PWHT optical microstructure of Specimen C22 by Procedure I	158
73. PWHT optical microstructure of Specimen C22 by Procedure II.....	158
74. PWHT optical microstructure of Specimen 5923 by Procedure I	159
75. PWHT optical microstructure of Specimen 5923 by Procedure II	159
76. Disbonding in overlay 309LMo	160
77. Disbonding along Type II grain boundary in overlay 254SMO	160
78. Disbonding running parallel to the interface in overlay 254SMO	161

79. Disbonding extended from Type II boundary to the bainite region	161
80. Disbonding wandering along Type II boundary and through bainite region in overlay 254SMO	162
81. Disbonding along Type II boundary in overlay 904L	162
82. Cracking stopped at the turning point of planar grain boundary	163
83. Microstructure along fusion line in overlay 2205	163
84. Skeletal ferritic network and enveloped martensite in overlay 2205	164
85. Precipitation in martensite and skeletal ferrite	165
86. Microstructure along fusion line between base steel and overlay 254SMO	166
87. Type II grain boundary in 254SMO observed on SEM	166
88. Fine martensite right on the interface in overlay 254SMO	167
89. (a) Coarse bainitic structure in the transition zone from the base steel to Overlay 254SMO	168
(b) Coarse Bainitic Structure intruding into austenite in overlay 254SMO	168
90. EDX analysis and microstructure around Type II grain boundary	169
91. Lathes of martensite at the root of interface in specimen 309LMo	169
92. A narrow planar grain boundary in specimen C-22 As-welded	170
93. A close look at the planar grain boundary in specimen C-22	170
94. EDX examination shows a higher content of Fe in the planar grain boundary	171
95. A narrow band of martensite serving as the transition of crystal structures aside the interface in specimen C-22	172
96. Precipitates on the planar grain boundary in specimen C-22	173
97. Carbides precipitating in the interfacial region in specimen C-22	

(a) Coarse Carbides precipitate in the base steel under the interface	174
(b) M_2C Type Carbide Precipitating in the Transition Zone	175
(c) Precipitation of Carbides on the Planar grain Boundary in Overlay C-22	176
98. Less Precipitation occurs in Overlay C-22 by Low Current Welding	177
99. A simulation of hydrogen accumulation in Type II grain boundary	178
100. Schematic of Fe - Cr - Ni ternary phase diagram and compositions of overlay materials	179
101. Schematic of Schaeffler diagram showing possible structures in overlays	180
102. A part of the vertical profile of Fe - Cr - Ni ternary phase diagram	181
103. Schematic illustration of the formation of Type II grain boundary	182

1. INTRODUCTION

Reactor vessels used for crude oil refining usually operate at high temperatures and high pressures in hydrogen-containing and corrosive environments. Due to their excellent mechanical properties with good corrosion resistance and heat resistance, corrosion resistant alloys such as austenitic stainless steels and nickel based alloys are very suitable for the lining of such pressure vessels in the petrochemical industries. However, the construction of large objects such as pressure vessels, with large capacity and heavy wall section in huge petrochemical plants, requires minimal use of corrosion resistant alloys to minimize cost. Thus composite construction with low alloy steel as the pressure containing component was developed. Consequently, corrosion resistant alloy clad composite materials are being used ^{1,2,3} to achieve the optimum balance of mechanical strength, chemical properties, surface properties, and economy. Because this kind of structure usually involves a large clad area or the use of plates with thickness exceeding 100 mm, the only practicable method of cladding, especially on shaped areas, is weld overlay, despite the fact that some other technologies are apparently competitive with weld overlay ^{4,5}. Among weld cladding techniques, such as Submerged Arc Welding (SAW), Electroslag Welding (ESW), Shielded Metal Arc Welding (SMAW), etc., SAW with strip electrode cladding receives the most attention due to its ability to combine excellent deposit properties and controllable penetration with high deposition rates. The most typical application of this weld cladding technique is for the making of pressure vessels used in the hydrotreatment of heavy oils and oilsands (bitumen) and operated at temperatures from 350 to 500 °C and at pressures as high as 10 to 20 MPa in hydrogen-contained corrosive environments. This kind of pressure vessel is usually composed of a thick outside wall, made of Cr-Mo low alloy steel to withstand the high temperature and pressure due to its reputation of high creep strength, and an inner surface of corrosion resistant alloy clad by welding.

Cladding of corrosion resistant alloy by welding has been successfully applied to the manufacture of pressure vessels, and the weld overlay behaves well at the operating conditions of the pressure vessels. However, the occurrence of disbonding of the overlay from the base metal during shut-down of the

pressure vessels for maintenance or in an emergency remains a major problem confronted by the application of this technique. The hazard has been investigated by several groups ^{6,7,8,9,10}, and some knowledge has been gained. It is believed there are three major factors contributing to the disbonding. The first is the accumulation of hydrogen at the interface between the overlay and the base steel. After the steady-state condition has been attained in the hydrogenation process during the hydrotreatment of the crude oil in a pressure vessel, there is an equilibrium distribution of hydrogen and pressure across the vessel wall. Once the steady-state condition is disturbed, the hydrogen will accumulate at the interface between the overlay and the base steel owing to the difference in diffusivity and solubility of hydrogen in the overlay and the base steel as temperature decreases during vessel shut down. The second factor is that the stress and strain will be intensified at the interface region due to the difference in thermal expansion coefficient and in structure between the overlay and the base steel during the cooling down of the vessel from the operation temperature and pressure. Finally, the microstructure of the interface may be susceptible to fracture. The structure of the interface is determined by the composition of the overlay and the base steel and by the welding procedure as well. Once an overlay material is chosen from the view of corrosion resistance capability, the structure of the interface is the only controllable factor in the consideration to prevent the overlay from disbonding.

However, there are still arguments about the causes of the disbonding. Some research groups suggested a high dilution of the base metal to the weld metal would be beneficial to the resistance to hydrogen-induced disbonding.¹¹ Other researchers believed that a low dilution ratio would minimize adverse fusion line microstructure¹². It was also found^{13,14} that disbonding in most cases initiated and propagated along a so-called Type II grain boundary parallel and adjacent to the fusion line in the overlay side. But it is unclear how the Type II boundary forms and if the Type II boundary is the site for the accumulation of hydrogen. In addition, what level of thermal residual tensile stress and strain can exist in the interface region also requires more detailed evaluation.

Thus, to obtain a clear understanding of what causes the disbonding of the overlay from the base

steel, one needs to investigate the formation of the microstructures along the interface region, the distribution of hydrogen and the residual tensile stress and strain across the interface. Then one can, possibly, establish a model or a theory to describe the phenomenon of the disbonding. Hence, the overall objective of this study is to examine the formation of the microstructure along the interface region, its relation to the cladding composition and welding procedure, and find out the relation between the microstructure and the distribution of hydrogen and residual stresses. Finally, an attempt will be made for the improvement of the weld cladding technique to reduce or eliminate the occurrence of hydrogen-related disbonding.

2. LITERATURE REVIEW

2.1 Hydrogen Distribution

2.1.1 General Consideration about Hydrogen Distribution

It has been found that disbonding does not happen when the vessel is placed in operation at high temperatures and high pressures, rather it takes place during a certain period after the shut-down of the pressure vessel for maintenance or in an emergency^{15,16,17}. The phenomenon of disbonding showed characteristics of hydrogen-related fracture in consideration of the four prerequisites for hydrogen-assisted cracking (HAC): 1) A low temperature, usually ambient temperature or less than 200°C; 2) Tensile stresses exist, either applied or residual; 3) Sufficient hydrogen, 5 ppm or more in the ferritic structure, or 60 ppm or more in the austenitic structure; and 4) Crack-susceptible microstructures such as martensite, bainite, and ferrite. It is, therefore, believed that the disbonding must be connected to the redistribution of hydrogen during the shut-down, in which hydrogen diffuses out from the vessel interior, and pressure and temperature reach the ambient condition.

Before the determination of the redistribution of hydrogen across the vessel wall after shut-down, the equilibrium distribution of hydrogen in the steady-state condition in the hydrogenation process has to be considered. When the pressure vessel is operated in hot and high pressure hydrogen atmospheres, the typical equilibrium hydrogen distribution can be deduced by considering the solubility and diffusivity of hydrogen in the weld overlay, commonly austenitic stainless steel, and the base steel, usually Cr - Mo low alloy steel. The solubility of hydrogen in the austenitic stainless steel overlay is much higher and the diffusivity is much lower than those in the ferritic base Cr - Mo steel. When the steady-state condition is achieved, the hydrogen concentration at locations of interest in the operation condition is then given by ¹⁸

$$c_1 = k_1 \sqrt{p_{H_2}} \quad (2-1)$$

$$c_2 = \frac{k_1}{k_2} \cdot c_3 = \alpha \cdot c_3 \quad (2-2)$$

$$c_3 = \frac{D_s \cdot x_b \cdot c_1}{D_b \cdot x_s + \alpha \cdot D_s \cdot x_b} \quad (2-3)$$

where, c_1 : hydrogen concentration at the surface of weld overlay (ml/100 g Fe),

c_2 : hydrogen concentration in the overlay at the interface (ml/100 g Fe),

c_3 : hydrogen concentration in the base steel at the interface (ml/100 g Fe),

x_s, x_b : thickness of the overlay and base steel, respectively, cm,

k_1, k_2 : solubility constants for weld overlay and Cr-Mo steel, respectively,

$\alpha = k_1/k_2$, partition ratio.

p_{H_2} : hydrogen partial pressure at the surface of weld overlay, kg/cm²,

D_s, D_b : diffusion coefficients of hydrogen in weld overlay and base steel respectively, cm²/sec.

The magnitude of hydrogen concentration c_1 , c_2 , and c_3 depends primarily on the operation pressure (10 - 20 MPa) and temperature (400 - 450 °C). The schematic of hydrogen distribution in the operation condition is shown in Figure 1. From Figure 1 it is seen that there is a steep gradient of hydrogen concentration in the interface region between the weld overlay and the base steel due to dissimilar solubility and diffusivity of hydrogen in these two different crystal structures. During shut-down, the steady-state condition of high temperature and high pressure is disturbed. The relative difference in solubility and diffusivity of hydrogen in ferrite and austenite phases increases with the drop of temperature. Calculations^{15,17} have shown that a large amount of hydrogen is still present in the overlay after shut-down, even when the pressure of hydrogen in the vessel is reduced to and kept at zero. More importantly, the hydrogen in the wall accumulates to a considerable level in the austenitic overlay near the

interface between these two materials at lower temperatures. The peak concentration of hydrogen in this region can be higher than 100 ppm in the weld overlay adjacent to the fusion line as seen in Figure 2. Such high concentration of hydrogen, apparently exceeding the equilibrium concentration at the ambient temperature, is most likely to cause hydrogen-related cracking or disbonding. Disbonding test results for a 7 mm thick cladding layer have shown that disbonding took place when hydrogen concentration at the interface exceeded 100 ppm ¹⁰. The extent to which hydrogen accumulates depends upon the original steady-state hydrogen concentration and the cooling rates, and it is also affected by the local stress and strain, and the microstructures in the overlay and the base steel. In a one dimensional diffusion model ¹⁷, a value of 220 ppm of hydrogen was representative of a layer at the interface approximately 10 micrometers wide after cooling down from 450 °C at the hydrogen pressure of about 16 MPa. Clearly, if a susceptible structure to cracking is present, in addition to the high concentration of hydrogen as high as above 150 ppm at a point 50 micrometers away from the interface where the through-thickness thermal tensile stress was built up as a result of dissimilar thermal and mechanical properties in the overlay and the base steel, disbonding of the overlay from the base steel will unavoidably take place since all requirements responsible for the hydrogen embrittlement are present.

2.1.2 Variables Influencing Hydrogen Accumulation

2.1.2.1 Operation Conditions

The solubility of hydrogen in the overlay and the base steel which determine the original distribution of hydrogen during steady-state operations of the pressure vessel is affected by the temperature and pressure at which the vessel works. Due to the difference in crystal structure, the solubility of hydrogen in face-centered cubic (FCC) structure is about an order of magnitude greater than that in body-centered cubic (BCC) structure of Cr-Mo base steel. The basic relationships of the solubility and diffusivity of hydrogen in low alloy steel of BCC structure and in austenitic stainless steel of FCC structure with temperature are given by Tadamichi et al.¹⁹

$$k_1 = 7.6 \exp(-630/T), \quad (2-4)$$

$$k_2 = 23.4 \exp(-3257/T) \\ = 1.8 \exp(-1789/T), \quad \text{for } T \leq 573 \text{ K} \quad (2-5)$$

$$D_b = 2.4 \times 10^{-3} \exp(-2132/T) \\ = 4.3 \times 10^{-4} \exp(-3358/T) \quad \text{for } T \leq 423 \text{ K} \quad (2-6)$$

$$D_s = 7.11 \times 10^{-4} \exp(-4555/T) \\ = 6.0 \times 10^{-3} \exp(-5781/T) \quad \text{for } T \leq 573 \text{ K} \quad (2-7)$$

where k_1 and k_2 are the solubility constants and D_b and D_s are the diffusion coefficients in the base steel and overlay materials respectively. Then the concentration of hydrogen at the entry surface of the weld overlay can be decided by the equation

$$C_0 = k_1 \sqrt{p_{H_2}} \quad (2-1)$$

where p_{H_2} = hydrogen pressure in kg/cm².

The hydrogen concentration at the interface between the base steel and the overlay is calculated by the ratio of hydrogen concentrations for each material exposed directly to the hydrogen atmosphere:

$$C_w = \alpha C_0 \quad (2-2)$$

where $\alpha = k_1/k_2$.

From the exponential relationship of the solubility and diffusivity with the temperature, higher temperatures have a larger influence on the solubility and diffusivity than the pressure does. Nevertheless, solubility increases with both temperature and pressure. But, an increase in the operation temperature will result in a decrease in the retained hydrogen after shut-down in the overlay. This is attributed to the longer time of hydrogen diffusion from a higher temperature to ambient temperature if cooling rate

remains constant. For typical petrochemical operation conditions, pressure vessels work at temperatures between 400 and 450°C with pressures at 10 to 20 MPa. If a pressure vessel with a thickness of overlay of 5 mm and a thickness of base steel wall of 65 mm works at the temperature of 450 °C and at the hydrogen pressure of 130 kg/cm², the saturated hydrogen content can be reached at about 40 ppm near the interface in the overlay in the steady-state condition¹⁷. The large amount of hydrogen introduced during operation needs to redistribute through diffusion during shut-down of the pressure vessel. Then accumulation of hydrogen at the interface takes place.

2.1.2.2 Cooling Rates during Shut-down

The cooling rates during shut-down have a remarkable influence on the hydrogen diffusion. A slow cooling rate allows a longer time for hydrogen to redistribute in the overlay, base metal and interface between them. With a higher cooling rate, less time is available for hydrogen to redistribute itself or escape the vessel wall, and a higher concentration will be found at the interface region. The effects of shut-down conditions on hydrogen accumulation are shown in Figure 3. Disbonding may be avoided if the hydrogen is allowed enough time to diffuse away from the interface before room temperature is attained²⁰. This requires holding the temperature above 100 °C long enough to reduce the peak level of hydrogen below the critical value at the interface. However, it is not always possible to heat or keep the vessel at a higher temperature and ensure hydrogen removal. Thus other contributing factors must be considered.

2.1.2.3 Thickness of the Weld overlay and the Base Steel Wall

The hydrogen concentration at the interface increases as the thickness of the base steel increases, while the hydrogen concentration decreases as the overlay thickness increases. This is attributed to the lower concentration of hydrogen at the interface for the thicker overlay in the same operation condition, resulting in a lower hydrogen spike upon cooling if the hydrogen flux is held constant in the prolonged pressure vessel operation. The effects of cooling rate, thickness of base steel and overlay on hydrogen accumulation are presented in Figure 4.

2.1.2.4 Composition and Microstructure

Composition and microstructure exhibit their influences on through-thickness stresses and on hydrogen diffusivity and accumulation. As for the diffusivity, the change in the microstructure across the interface, accompanied by strains and stresses, is the most influential factor for the hydrogen accumulation which is likely to depend on the proportion of different crystallographic phases present rather than on the composition of any given phase. However, the composition will determine which phases are present. Grain size is another microstructural feature that influences hydrogen diffusion¹⁹. The solubility of hydrogen depends on grain size as well as the disorientation across the grain boundaries. The effect of grain size on the hydrogen diffusivity is complex²¹, and no model is available now to consider the grain size effect on the hydrogen diffusion. The trapping effect of carbides or other precipitates drew the interests of researchers¹⁷. The addition of strong carbide-forming elements such as Ti, Nb, V etc. in the overlay and base steel is believed to reduce the peak concentration of hydrogen at the interface. The trapping effect of carbides impedes the accumulation of hydrogen at the interface.

A model of numerical analysis of the diffusion and trapping of hydrogen in steel weldments has been proposed by Kohira et al.²² In this model, the effects of two different phases, one of which serves as trapping sites, on the diffusion and trapping of hydrogen is discussed. It demonstrated that the diffusion of hydrogen would be significantly retarded by the trapping sites such as plastic strain area, and second phase particles.

2.1.2.5 Stresses and Strains

Stresses are generated due to the different coefficient of thermal expansion between the overlay and the base steel during cooling. Plastic strains result if the stress level is over the yield strength of the materials, especially with a high cooling rate. It is suspected⁷ that the presence of a stress field would enhance stress-assisted hydrogen diffusion from the region under compression to the region under tension, whereas plastic strains would retard hydrogen movement by increasing trapping density. Post-weld heat

treatment (PWHT) can reduce the residual stresses to a large extent provided that the thermal expansion properties of the overlay and the base steel are similar to each other. However, for situations where weld metal and base metal have different compositions and different thermal expansion coefficients as in the case of the corrosion resistant alloy overlay on the Cr-Mo low alloy steel, the effect of PWHT may not be very effective to reduce the residual stresses. What is more, residual stresses are created from the cooling during shut-down of the pressure vessel, not only from welding.

The stresses of interest are those parallel (shear stress) and perpendicular (through-thickness stress) to the interface. The shear stresses are likely to be confined near the interface region, and their effect on hydrogen diffusion may not be important, but the resulting strains may increase the solubility. Perpendicular stresses are more important to affect the diffusion of hydrogen to the interface region, and to be responsible for the disbonding at the interface.

The magnitude of the residual stresses depends on the cooling rate and the difference in the thermal expansion properties of the overlay and the base steel. For an overlay of 309 stainless steel on 2.25% Cr-1% Mo low alloy steel with a microstructure of austenite plus 6% ferrite at the interface after PWHT at 690°C for 24 hours, Fuji ⁷ et al found the residual tensile stress level higher than 400 MPa. This level of stress exceeds the yield strength of the most used overlay materials, hence a plastic strain zone is expected near the interface. Consequently, a higher concentration of hydrogen would be present in this zone.

An attempt ²³ has been made to set up the relationship between the hydrogen distribution and the state of stress and strain field in the heat affected zone (HAZ) of welds. It is suggested that this model could be used to treat the situation of corrosion resistant alloy overlay on low alloy steel.

2.1.2.6 Welding Procedure

The effect of welding procedure on the diffusion and accumulation of hydrogen lies in that the welding procedure can adjust the chemistry of the weld metal, influence the macrostructure of the welds and develop a certain level of residual stresses since the welding procedure has strong effects on the

composition near the interface region. The microstructure along the fusion lines is also affected by the procedure, especially by the dilution effects. Chakravarti ¹⁷ et al suggested that the Schaeffler or DeLong diagram may be used to predict the microstructure of the overlay. But the phase transformation in welds during welding is usually a nonequilibrium process ²⁴. The Schaeffler diagram may be used to estimate what kind of structure exists in the weld metal, but it cannot predict where this kind of structure locates in the weld metal, at the root or in the middle of the weld metal. This is especially true when there is a large difference in chemical composition between the weld metal and the base steel. Therefore, the Schaeffler diagram cannot be simply applied to predict the microstructure of the overlay, especially the microstructure near the fusion line where there is a sharp change in composition. The composition at the interface is affected by dilution and lack of mixing during welding, and so is the microstructure. The preheat and PWHT also have influences on the hydrogen accumulation at the interface by affecting the formation of different microstructures at the interface. The number and the shape of precipitates, for example, which serve as the trapping sites of hydrogen, is strongly dependent on PWHT.

2.2 Effect of Residual Stresses

If the chemical composition and the microstructure of the overlay were similar to the base steel, the residual stresses could be released by post weld heat treatment (PWHT) after cladding. However, the composition and structure of overlay materials are usually different from the base steel due to the consideration of corrosion resistance. The corrosion-resistant alloys usually possess larger thermal expansion coefficients than the base steel. Therefore, even if the cladding is stress-relieved at PWHT, stresses may reappear on cooling from the operation condition to the room temperature. Kume²⁵ et al measured the strains in the overlay of austenitic stainless steel and in the base steel. The results are presented in Figure 5. It showed that there were high biaxial tensile strains in the overlay adjacent to the fusion line, and high compression strains in the base steel at the overlay interface. It was believed that the Poisson effect associated with the tensile strain in the interfacial region of the overlay produced a tensile stress across the fusion boundary which contributed to the disbonding phenomenon. These stresses are

significantly reduced during PWHT after welding. But they showed up again during cooling down in the shut-down period, especially in an emergency, due to the difference in thermal expansion coefficients of the two materials. Measurements²⁶ of the residual stresses parallel to the interface with a hole drilling method showed that the residual stresses were in the order of 140 MPa. The 0.2% strain was reached by only a 525 K change in temperature for 309 stainless steel on a 1020 steel plate.

Several Japanese researchers^{7,11} had found that the developed residual stresses in the overlay could be reduced to some extent if a mixed structure of austenite and martensite was present along the fusion line. They attributed this to the transformation of martensite in the overlay, which reduced the residual strain and hence the residual stress. Some of their results are shown in Figure 6.

Up to now no attempt has been made to evaluate the residual stresses or strains in the overlay system by a numerical method.

2.3 Effects of Composition and Microstructure

2.3.1 Weld Overlay

Since the main application of pressure vessels is in the petrochemical and chemical industries, the specifications of the clad layers are usually of stainless steels of ASTM 300 or 300L series to possess adequate corrosion resistance to the working media. For most corrosion resistant alloy overlay specifications, three major objectives have to be considered³:

- a) Chemical composition within the range of the relevant corrosion resistant alloy composition over the whole overlay;
- b) A minimum thickness of cladding within the corrosion resistant alloy specification;
- c) Suitable deposit microstructure and mechanical properties.

Because the cladding of corrosion resistant alloy, in most cases, is carried out on thick plates of carbon or low alloy steels, the dilution of weld overlay by the base steel plate becomes a problem in

meeting the overlay specification. Consequently, the corrosion resistant alloys used for this purpose are usually composed of Cr and Ni more than 18% and 8%, respectively, and of carbon no more than 0.04% with carbide stabilizers such as niobium, titanium, etc.. Molybdenum is also a frequent addition for imparting increased resistance to certain corrosive environments such as the presence of Cl^- . Sometimes Cr and Ni powders are added to welding flux to compensate for the loss of these elements during welding. Two layers of cladding of corrosion resistant alloy on the base steel are often employed to achieve the specification on chemical composition in the top layer. The most common combination is 309L in the first layer and 347 in the top layer.

From existing results ^{4,10,18} on common procedures, it is found that the weld overlay serves well in the steady-state operation of the pressure vessel, and it is not susceptible to disbonding. But the disbonding may happen after PWHT and hydrogenation, especially during the shut-down of the pressure vessel for maintenance or in an emergency. The disbonding takes place almost always near (not at) the interface in the overlay side. Therefore as far as the disbonding is concerned, the interfacial zone between the base steel and the overlay is the most interesting. Initially it was believed that the martensitic structure was the culprit in disbonding, as for hydrogen embrittlement in high strength steels, and that austenite or austenite plus partial ferrite was the most suitable structure in the overlay. However, several experiments have shown that a mixture of austenite and martensite had a higher resistance to disbonding, even though the reason was not clear^{7,27,28}. Experimental results¹² also showed that lowering the carbon content of the overlay materials used for the overlay helped to increase the resistance to disbonding. In effect, the chemical composition variation of the deposited overlay to a large extent depends upon the welding procedure, particularly in the interfacial zone.

A typical microstructure of austenitic stainless steel overlay, the most used overlay material, showed dendritic austenitic grains with a certain amount of ferrite within interdendritic spaces, and the dendritic grains extended from the interface region as shown in Figure 7. Usually there was a narrow transition zone where no ferrite was observed, and austenite grains grew epitaxially from the Cr-Mo base steel plate

during welding. The austenite grain boundaries at the interface showed that the overlay initially solidified as a planar interface, a so-called Type II grain boundary, which is susceptible to disbonding. Subsequent solidification then progressed into a dendritic mode. Zhang⁸ et al thought that the epitaxial growth of austenite from the base steel in planar mode was halted by austenite grains formed at the front of solidification which developed into dendritic growth, so the planar grain boundary formed as an indication of the two different growth modes. Within the transition zone there was a "shining band" which could not be affected by etching either for the stainless steel or for the base steel in as-welded condition, and this band turned dark after PWHT and etching. This band of tempered martensite and bainite extended across the austenite zone along the interface boundary. After PWHT and hydrogen-charging, cracking took place in the interface region, mostly along Type II grain boundaries as shown in Figure 8. In a simulation test⁶ of hydrogen induced disbonding, four types of disbonding location were identified as seen in Figure 9. Type A cracking took place along grain boundaries which tilted an angle to the fusion line and was linked to the interdendritic boundary. These grain boundaries in effect were the extension of the planar grain boundary. Type II grain boundary, along which Type B cracking happened. Type C cracking occurred in a brown-colored martensite zone and Type D cracking in the black-colored martensite zone. The two different-colored martensite zones were believed due to precipitation in the black-colored zone. The structure in the brown-colored zone might be bainite, which showed a different response to the etchant from that of martensite in the black-colored zone. Although there might be several types of disbonding, it was postulated by almost all researchers that the initiation of disbonding took place as Type B cracking, i.e., along Type II grain boundaries. The presence of martensite at the interface was the topic of arguments concerning the resistance to disbonding. Ohnishi¹¹ et al concluded that a duplex structure of austenite and martensite with a lower amount of ferrite at the interface possessed more resistance to disbonding. The improvement came from a lowering in the residual stresses across the interface for the duplex structure as a direct consequence of martensite transformation. For this reason, the overlays which had relatively lower nickel and chromium equivalencies and less ferrite than conventional austenite stainless steel overlay showed the lowest disbonding tendency as presented in Figure 10.

2.3.2 Base Steel

Because pressure vessels usually work at high temperatures and high pressures, a suitable combination of strength and ductility is necessary. Low alloy Cr - Mo steels are commonly employed for the manufacture of pressure vessels in consideration of their properties to resist creep and oxidation in addition to the suitable combination of strength and ductility. Typically 2 1/4 % Cr - 1% Mo steel is chosen as the main material of the pressure vessel. To overcome temper embrittlement, the contents of P, S, Sn, Sb, and As should be as low as possible, and the contents of Si and Mn are also reduced. Carbon content of the base steel is lower than that of conventionally used Cr -Mo low alloy steels in order to minimize the dilution effect confronted in weld cladding. Nakanishi²⁹ et al proposed Al and B treatment to suppress the temper embrittlement and to keep suitable strength. Masumoto³⁰ found that the main cause for the embrittlement of base steel was the coarsening of carbides during a long period of service at high temperatures. Therefore, a certain amount of strong carbide-forming elements such as titanium, niobium, vanadium, etc. is added to stabilize carbides. These special carbides precipitate at an early stage at higher temperatures to control the grain growth and to prevent carbon migration to Type II grain boundaries during PWHT. Hence, the level of hydrogen accumulation at Type II grain boundaries is reduced. The grain size of base steel is also an important parameter affecting the nucleation in the weld overlay, since the dendritic grains in the overlay grow epitaxially from the grains in the base steel. It is proposed¹² that the addition of titanium and boron promote rapid transition toward dendritic growth during solidification, hence reducing the extent of Type II grain boundaries.

The typical microstructure of base steel in the region of the interface is usually the heat affected zone (HAZ) with coarse grains of martensitic and bainitic structures as shown in Figure 7. Carbides precipitate preferentially on prior austenitic grain boundaries in the HAZ. It is seen that Type II grain boundaries and the columnar dendrites in the overlay are strongly dependent upon the grain size of the base steel. A test¹⁴ on a low alloy Cr-Mo steel with extra low carbon content showed that the grain growth in the base steel was suppressed during welding, resulting in finer microstructures both in the base steel and the overlay,

and a reduction of precipitation of carbides in the interfacial region. Consequently, disbonding was minimized.

2.4 Effects of Welding Processes and Procedures

2.4.1 Welding Processes

There are several welding processes available for the cladding. In practice, ASME qualifies only four welding processes for the overlaying process in the manufacture of pressure vessels: Shielded Metal Arc Welding (SMAW), Submerged Arc Welding (SAW), Electroslag Welding (ESW) and Gas Metal Arc Welding (GMAW). In consideration of the high deposition rate and high efficiency required in the manufacture of pressure vessels with heavy sections, only SAW and ESW processes have been widely employed for cladding. The electroslag welding process has the advantage of reduced dilution as compared with submerged arc welding. Thus it may be possible to obtain an acceptable cladding composition with one layer only. However, the electroslag welding process generates a coarser grained heat affected zone (HAZ) than the SAW process, so that the sensitivity to underclad cracking and hydrogen-induced disbonding is increased³¹. The submerged arc welding process with a strip electrode produces satisfactory cladding with high deposition rates, and it is relatively easy to control the process, and thus the quality of overlay. Therefore, SAW is the most widely used cladding technique for the overlaying of corrosion resistant alloys on the base steel in the manufacture of hydrogenation pressure vessels.

To meet the overlay specifications, the dilution effect of overlay from the base steel has to be considered. Generally, the effect of dilution can be solved either by depositing more than one layer or by using a dual strip procedure. Nevertheless, a number of experiments¹ showed that it was possible with suitable combination of strip and flux compositions to clad some corrosion resistant alloys in a single pass only. Due to its obvious economical advantage in using one single-pass technique, attention has been paid to study the effects of welding parameters and welding consumables necessary to predict and control the

deposition composition, dimensions, and microstructures of weld overlay in a single pass.

2.4.2 Welding Speed

The chemical composition and microstructure in the transition region of the interface between the overlay and the base steel depend heavily on the welding procedures, especially the welding speed, in addition to the chemical compositions of the overlay materials and the base steel themselves. Once a level of heat input is chosen to achieve a suitable fusion pool for the control of the dimension and shape of weld overlay, the main parameter reflecting the influence of welding speed is the dilution extent, i.e. the volume fraction of base steel involved in the weld overlay bead as a whole, as shown in Figure 11. Obviously, the magnitude of dilution affects the chemical composition and microstructures in the overlay, and thus the resistance to the disbonding. Therefore, a close control of composition, and the consistent and predictable value of dilution of overlay by welding procedure is definitely required. It has been found that an increase in welding speed with a constant level of heat input (current increases proportionally to welding speed) will produce an increase in overall dilution^{12,32,33}. The effects of voltage and polarity of electrode are still in controversy although their effects are relatively smaller compared to the current and speed.

In the initial stage of the application of this cladding technique, it was expected³ that the dilution should be as low as possible to eliminate the formation of martensite at the interface region. However, experiments¹¹ later showed that a mixture of martensite and austenite at the interface possessed better resistance to the disbonding. Afterwards, a high current and high welding speed procedure was employed to promote the formation of this microstructure. The formation of martensite was assumed to be reducing the residual tensile stresses in the through-thickness direction of the overlay⁷. Consequently the severity of disbonding was reduced. Godden¹⁰ et al found that disbonding would more likely occur with an overlay produced by a welding procedure of lower current and lower speed with the same nominal heat input as that in the procedure mentioned above. It was supposed that Type II grain boundaries formed owing to the planar grain growth of austenite from the base steel. Savage³⁴ proposed a model to show how the

solidification structures were affected by the local constitutional supercooling, as is shown in Figure 12. The structure was related to temperature gradient, growth rate, and solute distribution. A high speed welding procedure would produce an overlay with faster cooling rates in the fusion region, resulting in a finer grain structure and the inhibition of the formation of planar grain boundaries. Also, the finer grain structure would reduce the concentration of impurities on grain boundaries. On the other hand, the grain growth in the base steel side would be retarded too, due to the faster thermal cycle of high speed heating and cooling. Nevertheless, Matsuda⁶ et al argued that increasing current and speed did not produce a satisfactory metallurgical solution to the overlay bonding. In their experiment, some reduction in disbonding with high speed welding was found for 309 and 308 stainless steel overlays, but the amount of disbonding increased for 310 stainless steel overlay. It is obvious that the welding speed factor is related to the compositions of the overlay materials.

It appears that the factors determining the capability to resist the disbonding make a complex pattern as far as the microstructure factor is concerned. For a constant level of heat input, welding speed would influence the microstructures along the interface by changing heating and cooling rates, adjusting dilution level, and affecting the growth modes of the weld metal.

2.4.3 Post Weld Heat Treatment

In the as-welded condition, precipitation of carbides or other secondary phase particles does not take place to any significant extent and austenite grain boundaries are difficult to see at the interface region by a normal metallographic etching method. After PWHT, a precipitation layer of carbides became apparent. Several researchers^{35,36,37,38} investigated the structure changes during PWHT along the interface region. It was found that carbon migrated from the base steel toward the overlay, and carbides precipitated within the weld metal along the interface, forming a contrast with a decarburized zone in the adjacent band of base steel³⁸. The width of the band depended upon the temperature, the time and the nature of the cladding materials and it can be predicted by using the results of Christoffel and Curran³⁹. Carbides turned coarser and segregated to the grain boundaries⁴⁰. The hardness of weld metal in the

interfacial region remained as high as that in the as-welded condition, and for some alloys the hardness was even higher than that in the as-welded condition. The precipitation region extended about 100 μm from the fusion line. The increase in hardness was ascribed to the high carbide volume fraction precipitated during PWHT or in service⁴¹. Due to the sharp change in microstructure and hardness it was reported³⁸ that the fracture toughness in the heat affected zone immediately adjacent to the fusion line in the base steel was reduced significantly, although disbonding in most cases took place along so-called Type II grain boundaries. Also, precipitation of carbides along the planar grain boundaries in the weld metal adjacent to the fusion line was observed¹¹. These precipitates along the planar grain boundaries might serve as the trapping site for the accumulation of hydrogen. Consequently, the binding strength of the boundary was reduced due to the existence of hydrogen, and disbonding took place with the assistance of the residual tensile stresses developed during cooling down.

Kinoshita⁴² et al constructed a relationship between the hydrogen concentration and the PWHT. The influence of PWHT on the peak hydrogen concentration along the interface was shown in Figure 13. The disbonding tendency was also increased as the Larson - Miller parameter increased, which reflected the extent of PWHT. From this result, it was seen that the critical hydrogen concentration to induce disbonding dropped linearly as the P value increased. These researchers argued that the incidence of disbonding was attributed to the extent of carbide precipitation in the overlay and particularly to the precipitation of carbides on Type II grain boundaries. With high current and high speed welding procedure, the precipitated M_{23}C_3 carbides in overlay adjacent to the fusion line were found to be much finer than those in low current and low speed welding procedure as the same PWHT procedure was employed. Hattori⁴³ et al applied interlayers of ferrous alloys with extra-low carbon, or low carbon plus strong carbide-forming elements such as niobium, vanadium, etc. on the base steel before cladding of corrosion resistant alloys with high chromium and high nickel content and subsequent autoclave test. The results showed that the chance for the formation of the planar grain boundaries was greatly reduced, the grain structure turned finer, and few precipitates segregated on the grain boundaries. As a result, disbonding was minimized. The results confirmed that low carbon content and strong carbide-forming

elements would diminish the occurrence of disbonding. The improved properties were ascribed to a fine dispersion of carbides in the whole region across the interface, which functioned as trap sites for hydrogen to reduce the peak concentration of hydrogen right on the interface. Also the strong carbide-forming elements such as niobium, titanium and vanadium reduced the precipitation of carbides on Type II grain boundaries, and retarded the formation of Cr - rich carbides.

In the cladding interface region, higher temperatures and longer time in PWHT would result in higher hardness in the weld metal immediately adjacent to the fusion line as a consequence of the diffusion of carbon from the base steel and the formation of carbides. The coarsening of the carbides in the interfacial region, especially along Type II grain boundaries, would greatly degrade the binding strength of the overlay to the base steel. That is, the resistance to disbonding declined. For the coarse carbides, disbonding might occur along the carbide/metal bond too. A typical chemical composition profile across the interface after PWHT was presented in Figure 14. The concentrations of chromium and nickel exhibit a sharp change across the interface, while a carbon peak shows up at the weld metal side immediately adjacent to the fusion line, turning out together with a decarburized layer in the base metal side. It was found that strong carbide stabilizers were beneficial to keep the peak carbon level low.

If PWHT was carried out at temperatures higher than 700 °C, sigma phase might develop and carbides would coarsen quickly³¹. The material would then be more brittle. Hence the resistance to disbonding would decrease further.

2.4.4 General Submerged Arc Welding Process Conditions

The effect of polarity in submerged arc welding with strip electrode was examined by Horsfield⁴⁴ et al. It was found that the greater heat input by employing positive polarity yielded greater carbon diffusion from the base steel. A precipitation band of carbides appeared in the interfacial region as the consequence of the carbon migration to the bond zone. For negative polarity, the depth of decarburization in the base metal side is smaller and the precipitation band of carbides narrowed.

The heat input of submerged arc welding with strip electrodes affects the profile of the weld bead³. A higher heat input produced a convex weld bead, while a low heat input gave a concave shape. With a strip electrode 100 mm wide and 0.5 mm thick, heat inputs in the range from 8.8 to 11.5 kJ per mm yielded a flat bead, best suitable for cladding. Patchett^{45,46} et al found that penetration and bead reinforcement increased with current and decreased as the size of the electrode wire increased at a constant heat input. The increase in voltage reduced the electrode melting rate, while increasing the consumption of flux. The welding efficiency was reduced due to the decline in the I^2R resistance preheating of the electrode stickout and the increase of the arc cavity size.

The welding flux used in submerged arc welding plays an important role. The flux serves as the degassing agent of the weld metal, protects the melts from the atmosphere, stabilizes the arc and makes the weld bead in desired shape, etc. The chemical compositions of fluxes does not significantly affect the heat transfer in the submerged arc welding with wire electrodes, except the high carbonate flux which causes heat losses^{45,46}. Several researchers^{3,44,47} had found that appreciable losses of chromium might occur during overlaying and that addition of extra chromium metal to the flux was necessary to ensure that the composition of the overlay met the specifications. The composition of a flux for welding is not widely known in this industry. Regrettably, few details of flux composition can be obtained for the special case. The only common concept used to distinguish among fluxes is that of basicity, developed from the historical concept in the steel industry of "acid" and "basic" refractory furnace linings. There are several formulas used to calculate basicity, all of which tend to give similar rankings. But the formulas cannot predict any physical changes in process behavior due to flux composition, and they are at best a crude representation of the chemical behavior of fluxes. It is usually applied to assessing weld metal quality, particularly fracture toughness. More basicity means better toughness as a general proposition. However, no systematic investigation of the effects of the flux composition on the properties of dissimilar metal welds has been done in the open literature.

Preheat of the cladding is usually carried out at 150 °C to minimize the tendency of cracking and

retention of hydrogen during welding. And hydrogen-induced cold cracking after welding in the interface region or heat affected zone is avoided by preheating the flux to reduce the moisture content.

3. STATEMENT OF PROBLEMS AND OBJECTIVES

From the previous discussion, it is seen that further work is required to reveal the mechanism of the disbonding of weld overlay of corrosion resistant alloys. First, the hydrogen distribution should be evaluated during operation and shut-down of the pressure vessel under different structural conditions in consideration of the trapping effect. Next, the effect of residual stresses on the disbonding needs to be investigated in consideration of the welds with and without flaws. Thirdly, very importantly, it is necessary to investigate the relationship between the disbonding phenomenon and the microstructure in and near the interfacial region to clarify which structure is the most susceptible one to the hydrogen related cracking and how it is produced in the cladding. Finally, the role of welding procedures in the formation of crack-susceptible structure needs to be investigated too. The composition of welding flux may also be influential, but not as important as the microstructure, tensile stress and the hydrogen level. Since the flux interaction with the weld metal has not been thoroughly assessed, only one flux should be used, preferably a basic one with minimum potential to alter the deposit chemistry.

As for the hydrogen distribution, several models have been established to evaluate the concentration of hydrogen at the interface between the overlay of austenitic structure and the base steel of ferritic structure without consideration of the trapping effect. It is therefore necessary to set up a model to take the Type II grain boundary into consideration, since the most cracking-susceptible microstructure is the Type II grain boundary, which serves as a trapping site. This is located in the weld metal instead of the interface between the overlay and base steel. An increase of the overlay thickness would decrease the accumulation of hydrogen at the interface region. But, clearly, from the viewpoint of pressure vessel design, the economics of a thicker overlay must be weighed against the risk of disbonding. As mentioned in the previous section, the most susceptible structure to disbonding is the so-called Type II grain boundary. The mechanism responsible for the formation of this kind of microstructure needs to be sought out, and then measures can be taken to prevent the formation of this kind structure.

A model of stress distribution in the weld between dissimilar materials is needed to estimate the

severity of stresses on the hydrogen-related disbonding caused by the difference in microstructure and thermal response.

For assessing the microstructure it is necessary to choose a series of corrosion resistant alloys with widely different compositions welded by a few welding procedures with one flux for a systematic study, since the structure on the interface between the overlay and base steel is under the influence of both composition and welding procedure. It needs to be clear if the existence of martensite in the transition zone between the overlay and the base steel is a benefit to the resistance to disbonding. Both the welding procedure and the electrode chemistry will be involved in achieving the required microstructure. A wide range of electrode chemistry will allow the investigation of alloys which solidify as primary ferrite, primary austenite, or a mixture of the two. Some encroachment or islands of base steel intruding into the overlay formed during welding were observed by some researchers¹⁰ and these structures would interfere with the potential cracking path, effectively acting to stop the propagation of a crack as seen in Figure 15. The mechanism of the formation of such structures, however, is not clear, and it might be related to the dynamics of the welding arc and the pool. Arc mobility on stainless electrodes is somewhat unstable, which may lead to localized dilution variations. Overall, the integration of differing electrode compositions and welding procedure variation should offer a reasonable way to assess microstructural effects.

The objective of this project is therefore to model the hydrogen and stress distribution near the interface, then integrate this knowledge with a microstructural assessment of the incidence of Type II grain boundaries. A variety of corrosion resistant alloys will be used to provide a wide range of microstructures to determine the source of Type II grain boundaries.

4. THEORY

4.1 Diffusion and Trapping of Hydrogen

The theory on the hydrogen diffusion and trapping is mainly based on Yurioka Model¹⁶. Based on this theory the hydrogen distribution before and after autoclave testing was calculated numerically.

4.1.1 General Equation for the Diffusion of Mass

In accordance to the principle of mass conservation, if no mass is formed or taken out from a system by a chemical reaction the mass balance in the system can be shown as follows:

$$\iiint_v \frac{\partial c}{\partial t} dv + \iint_s \vec{J} \cdot \vec{n} ds = 0 \quad (4-1)$$

The first term in the equation represents the mass accumulating rate in the system of a volume, v , and the second term the mass flow rate through the surface of the system, s . \vec{J} in the equation is the mass flux vector. From the divergence theorem, Eq.(4-1) can be rewritten as:

$$\iiint_v \left(\frac{\partial c}{\partial t} + \nabla \cdot \vec{J} \right) dv = 0 \quad (4-2)$$

Therefore, the mass diffusion equation is generally expressed as:

$$\frac{\partial c}{\partial t} = -\nabla \cdot \vec{J} \quad (4-3)$$

where c is the concentration of diffusion mass. The flux of the diffusion mass is defined in terms of a chemical potential (μ) as:

$$\vec{J} = -\frac{Dc}{RT} \nabla \mu \quad (4-4)$$

where D , R and T are diffusion coefficient, gas constant and absolute temperature respectively. The chemical potential itself is defined as

$$\mu = \mu_o + RT \ln a \quad (4-5)$$

where a is the activity of the diffusion mass, which is defined as $a = \gamma c$. γ is the activity coefficient. μ_o is the standard potential.

From equations (4-3), (4-4) and (4-5), the general equation of mass diffusion becomes

$$\frac{\partial c}{\partial t} = \nabla \cdot \left(\frac{D}{\gamma} \nabla(\gamma c) + \frac{Dc}{T} (\ln \gamma c) \nabla T \right) \quad (4-6)$$

Under the condition that the temperature gradient is negligible, i.e., $\nabla T \equiv 0$, Eq.(4-6) simplifies to

$$\frac{\partial c}{\partial t} = \nabla \cdot \left(\frac{D}{\gamma} \nabla(\gamma c) \right) \quad (4-7)$$

$$\text{or} \quad \frac{\partial c}{\partial t} = \nabla \cdot (D \nabla c) + \nabla \cdot \left(\frac{Dc}{\gamma} \nabla \gamma \right) \quad (4-8)$$

Eq.(4-7) can be rewritten in terms of the activity of diffusion mass ($a = \gamma c$) as

$$\frac{\partial a}{\partial t} = \frac{a}{\gamma} \frac{\partial \gamma}{\partial t} + \gamma \nabla \cdot \left(\frac{D}{\gamma} \nabla a \right) \quad (4-9)$$

If the activity coefficient is independent of time ($\partial \gamma / \partial t = 0$), Eq.(4-9) is reduced to

$$\frac{\partial a}{\partial t} = \gamma \nabla \cdot \left(\frac{D}{\gamma} \nabla a \right) \quad (4-10)$$

If the activity coefficient is a constant, Eq.(4-10) virtually becomes Fick's second law of diffusion. However, the activity coefficient may change in a heterogeneous system. This situation will be discussed in the following section.

4.1.2 Activity Coefficient of Diffusion Mass

As mentioned in the second section, the apparent diffusion coefficient and occlusible amount of hydrogen in steel showed anomalies and the extent of the anomaly depends upon the amount of plastic

deformation and microstructures. Usually steels contain local strain fields around cohesive inclusions, martensite, grain boundaries, etc. Therefore, steels cannot be homogeneous media for hydrogen diffusion. It follows that hydrogen diffusion in steel is not governed by Fick's second law but by the general mass transfer law of Equation (4-8) or (4-10).

If the pressure, P , and the chemical potential vary locally, the diffusion flux of the mass can be expressed as:

$$J = -\frac{Dc}{RT} \nabla(PV^* + \mu') \quad (4-11)$$

where V^* is the partial molar volume of the diffusion mass, and the hydrostatic pressure, P , is considered as the mean of the negative stresses in the triaxial directions in solids. μ' is defined as the chemical potential which is normally considered in thermodynamics. By comparing Eq.(4-11) with Eq.(4-4), the following relation is obtained:

$$\mu = PV^* + \mu' \quad (4-12)$$

Therefore, μ is considered as the generalized potential of diffusing mass. The chemical potential used in thermodynamics is expressed by rewriting Eq.(4-5) as follows:

$$\mu' = \mu_o + RT \ln(\gamma_o c) \quad (4-13)$$

where γ_o is the activity coefficient influenced by the amount of plastic strain and the microstructure.

If the pressure effect can be written as:

$$\gamma_p = \exp(PV^*/RT) \quad (4-14)$$

the generalized potential turns into:

$$\mu = \mu_o + RT \ln(\gamma_p \gamma_o c) \quad (4-15)$$

By comparing Eq.(4-15) with Eq.(4-5), the generalized activity coefficient is given as the product of γ_p and γ_o :

$$\gamma = \gamma_p \cdot \gamma_o \quad (4-16)$$

Therefore, γ_o and γ_p can be looked as the interactivity coefficients due to strain and microstructure, and stress, respectively.

For the convenience of mathematical analysis, phases a and b are taken as the matrix and trapping site respectively, and, consequently, the activity coefficient, γ , does not change continuously in the whole system but abruptly at the phase boundary.

4.1.3 Formulation of Boundary Conditions for Hydrogen Diffusion and Trapping

As a prerequisite the diffusible hydrogen is assumed to diffuse without change of its atomic status in the trapping phases and chemical reactions when the lattice diffusing hydrogen moves into a trapping site. Under this assumption, two conditions have to be satisfied at the boundary between the normal lattice site and the trapping site. The first condition is that the chemical potential of hydrogen must change smoothly at the boundary. Since the chemical potential of hydrogen in the matrix and in the trapping phase is defined as

$$\begin{aligned} \mu_\alpha &= \mu_o + RT \ln(\gamma_\alpha c_\alpha), \\ \mu_\beta &= \mu_o + RT \ln(\gamma_\beta c_\beta), \end{aligned} \quad (4-17)$$

the continuity condition gives

$$\gamma_\alpha c_\alpha = \gamma_\beta c_\beta \quad \text{at a boundary} \quad (4-18)$$

and the smooth continuity provides

$$\nabla \mu_\alpha = \nabla \mu_\beta \quad \text{at a boundary} \quad (4-19).$$

The second condition requires that the mass of hydrogen is conserved at the boundary. From this condition, $J_\alpha = J_\beta$, Eq.(4-4) gives

$$\frac{D_{\alpha}c_{\alpha}}{RT} \nabla \mu_{\alpha} = \frac{D_{\beta}c_{\beta}}{RT} \nabla \mu_{\beta}. \quad (4-20)$$

From Equations (4-19) and (4-20), the following equation is obtained

$$D_{\alpha}c_{\alpha} = D_{\beta}c_{\beta} \quad \text{at a phase boundary.} \quad (4-21)$$

Substituting c with γ , the relationship of diffusion and activity coefficients in the different phases is obtained

$$D_{\alpha} / \gamma_{\alpha} = D_{\beta} / \gamma_{\beta} \quad (4-22)$$

From the deduction it is seen that the diffusion coefficient of hydrogen in the trapping phase depends on the ratio of the local equilibrium concentration at each site or the inverse ratio of the activity coefficient at each site.

4.1.4 Finite Difference Method for the Diffusion Analysis

For a one dimensional diffusion problem a one dimensional element system can be set up along the direction of the diffusion as shown in Figure 16. At the internal nodal point i in the system where the i th element with volume V_i locates between elements of $(i-1)$ and $(i+1)$, the principle of mass conservation confers the following finite difference equation

$$V_i [c_i(t + \Delta t) - c_i(t)] = \Delta t \left(\frac{\overline{D}_{i-1,i}}{\overline{\gamma}_{i-1,i}} \frac{a_{i-1}(t) - a_i(t)}{d_{i-1,i}} + \frac{\overline{D}_{i,i+1}}{\overline{\gamma}_{i,i+1}} \frac{a_i(t) - a_{i+1}(t)}{d_{i,i+1}} \right) A \quad (4-23)$$

where \overline{D} , $\overline{\gamma}$, d and A are the mean diffusion coefficient, the mean activity coefficient, the distance between elements, and the interfacial area, respectively. If the activity coefficient varies from site to site and does not depend on time, the activity in the i th element at time $t + \Delta t$ is obtained as

$$a_i(t + \Delta t) = a_i(t) + \frac{\Delta t \gamma_i}{V_i} \left(\frac{\overline{D}_{i-1,i}}{\overline{\gamma}_{i-1,i}} \frac{a_{i-1}(t) - a_i(t)}{d_{i-1,i}} + \frac{\overline{D}_{i,i+1}}{\overline{\gamma}_{i,i+1}} \frac{a_i(t) - a_{i+1}(t)}{d_{i,i+1}} \right) A. \quad (4-24)$$

From this equation the finite differential program can be established.

4.2 Hydrogen Induced Cracking (HIC)

If the microstructure of a material susceptible to cracking experiences a tensile stress field, hydrogen induced cracking (HIC) may take place at the presence of a certain amount of hydrogen in the material. The cracks from hydrogen induced cracking may be transgranular or intergranular and usually have sharp tips with minor branching and cleavage-like morphology of crack surfaces. Various mechanisms have been proposed for HIC, including hydrogen pressure, surface absorption, decohesion, and enhanced plastic flow. The hydrogen pressure theory was proposed in 1940s⁴⁸. In this theory hydrogen pressure has been thought to build up internally to weaken structure at crystalline and metallurgical defects, such as dislocations and secondary-phase interfaces, etc.. When sufficient hydrogen builds up at crystalline or metallurgical inhomogeneities, atomic or nascent hydrogen will combine to form molecular H_2 . Accumulated molecules nucleate the gas phase, which develops very high pressures sufficient to rupture interatomic bonds, forming microscopic voids and macroscopic blisters. The blisters will embrittle the lattice and generally degrade mechanical properties. This kind of hydrogen induced cracking is especially prevalent in the petroleum industry because of the ubiquity of sulfides and H_2S in the associated environments. Surface absorption of hydrogen has been reported to occur on free surface in the volume ahead of the crack tip, reducing the energy necessary to form a brittle crack surface⁴⁹. The decohesion model proposed that dissolved hydrogen would weaken the interatomic bonding force⁵⁰. Direct evidence of bond weakening by dissolved hydrogen has not been forthcoming, but the decohesion theory has not been ruled out entirely.

Most recently, considerable evidence has accumulated to support localized enhanced plastic flow to account for HIC^{51,52,53}. Since Beachem first suggested this model in the 1970s⁵⁴, the mechanism of enhanced plasticity has not been fully defined. According to this theory, the highly non-uniform distribution of hydrogen under stresses would reduce the flow stress locally, resulting in localized deformation which leads to highly localized failure by ductile processes, while the total macroscopic deformation remains small. The softened structure, which would normally deform plastically, can do so to

only a limited extent in the microscopic volume ahead of cracks, when constrained by the surrounding material of full strength and hardness. Microstrain within the softened, yet constrained, crack tip volume produces a triaxial stress state (plane strain condition), which suppresses plastic slip. Continued strain can only propagate a brittle crack. The condition at the crack tip of this model was described as like that of soft solder joining the ends of two steel bars⁵⁵.

Another important hydrogen induced cracking model is the stress induced hydride formation and cleavage crack mechanism. Hydride embrittlement occurs only in certain metals and in a certain range of temperature and strain rate^{56,57,58}. Under that condition new hydrides grow at the tips of cracks which are formed by the fracture of the hydrides. It is this stress stabilized (or say, induced) hydride which is responsible for the propagation of brittle cracks. Hydride formation is not considered to be significant in the alloys involved in the disbonding.

4.3 Stress Field of Bonded Dissimilar Materials

Usually an analytical simulation of the residual stress field of a weldment is quite complex, and often impractical⁵⁹ due to the difficulties involved in the determination of inconsistent strains of a weldment. In consideration of the cladding of corrosion resistant alloy on the base metal of low alloy steel, a simplified approach is adopted. Since no disbonding was found just after welding, it was conceptualized that the residual stresses were significantly reduced by preheating and post weld heat treatment right before and after welding. Also, the residual stresses of weldments would be eliminated while the pressure vessel operated at high temperatures. Disbonding happened during and after the shut down of pressure vessels at a high cooling rate from service at high temperature and high pressure of hydrogen. From this phenomenon it is seen that the disbonding was promoted by the existence of tensile stresses and the accumulation of hydrogen along the interface between the overlay and the base metal. Therefore only the residual stress field formed during shut down of the pressure vessel is dealt with in this section.

The structure of the overlay is macroscopically a bond of two different materials. The shape of the

specimen normally used in the experiment of disbonding is like a thermostat as shown in Figure 17. So the analysis can be based on the Timoshenko theory of bi-metal thermostats⁶⁰. Under this assumption, let a bi-metal plate of size of $2L \times B$, whose component strips are welded together, be uniformly cooled by the temperature of ΔT . The thermal expansion coefficients of the overlay and the base metal are α_1 and α_2 , respectively. Along the longitudinal direction the displacements $u_1(x)$ and $u_2(x)$ of the lowest layer of the overlay and of the upper layer of the base metal can be expressed as

$$u_1(x) = \alpha_1 \Delta T x + \frac{1 - \nu_1^2}{E_1 h_1 B} \int_0^x Q(\zeta) d\zeta - \kappa_1 q(x) - \frac{h_1}{2} \int_0^x \frac{d\zeta}{\rho(\zeta)} \quad (4-25)$$

$$u_2(x) = \alpha_2 \Delta T x - \frac{1 - \nu_2^2}{E_2 h_2 B} \int_0^x Q(\zeta) d\zeta + \kappa_2 q(x) + \frac{h_2}{2} \int_0^x \frac{d\zeta}{\rho(\zeta)} \quad (4-26)$$

where E_1 , ν_1 and E_2 , ν_2 are the elastic constants for the strip materials of the overlay and the base metal, h_1 and h_2 are the thickness of the two strips, B is the width of the plate,

$$\kappa_1 = \frac{2(1 + \nu_1)}{3E_1} \frac{h_1}{B} \quad (4-27)$$

$$\kappa_2 = \frac{2(1 + \nu_2)}{3E_2} \frac{h_2}{B} \quad (4-28)$$

are the coefficients of interfacial compliance (see Appendix A), $\rho(x)$ is the radius of curvature, $q(x)$ is the shearing force per unit plate length,

$$Q(x) = \int_{-L}^x q(\zeta) d\zeta \quad (4-29)$$

is the force at the x cross section, and L is half of the plate length. The origin of the rectangular coordinates x , y is in the middle of the plate on the interface.

Based on this thermostat model a detailed calculation was carried out in Appendix B. The stress field

in the bonded bi-metal plate can be found as:

$$\tau(x) = \frac{q(x)}{B} = \frac{\Delta\alpha\Delta T}{k\kappa \cosh kL} \sinh kx \quad (4-30)$$

is the shear stress, the maximum of which happens at the edge of the plate

$$\tau_{\max} = \tau(L) = \frac{\Delta\alpha\Delta T}{k\kappa} \tanh kL = \frac{\Delta\alpha\Delta T}{\sqrt{\lambda\kappa}} \tanh kL; \quad (4-31)$$

$$\sigma_o(x) = \frac{\Delta\alpha\Delta T}{\lambda h_1} \left[1 + \frac{3hD_1}{h_1D} \right] \chi(x) \quad (4-32)$$

and

$$\sigma_b(x) = -\frac{\Delta\alpha\Delta T}{\lambda h_2} \left[1 + \frac{3hD_2}{h_2D} \right] \chi(x) \quad (4-33)$$

are the normal stresses parallel to the interface of the bond, and subscripts, o and b, denote the overlay and the base metal, respectively. The meaning of other symbols can be found in Appendix B. And the "peeling" stresses, or the transverse normal stresses acting on the interface, are found to be

$$p(x) = \frac{\omega}{\kappa} \Delta\alpha\Delta T \frac{\cosh kx}{\cosh kL} \quad (4-34)$$

the maximum of which occurs at the end cross sections of the plate as follows

$$p_{\max} = p(L) = \frac{\omega}{\kappa} \Delta\alpha\Delta T = \omega k \tau_{\max} \coth kL. \quad (4-35)$$

From the analysis above it is seen that the highest shearing stresses and the "peeling" stresses would develop near a point where the interface met the free edge.

The cooling rate should have effects on the development of residual stresses and strains. However, it needs more detailed modelling and theoretical research.

4.4 Morphology of Weld Overlay

The microstructure of the interface between the overlay of corrosion resistant alloys and the low alloy steel mainly depends on the solidification of the weld metal. The weld metal solidification can be very complex when the wide range of welding processes, solidification patterns, and cooling rates of complex engineering alloys are put into consideration. Therefore only the submerged arc welding process is examined here due to its advantages in the cladding for the manufacture of pressure vessels of heavy sections as mentioned in the literature survey.

Since welding performance can often be directly related to weld structure, the critical welding conditions leading to the development of the weld structure, the size scale of the structure, the weld macrostructure incorporating grain orientations and morphology, the microsegregation and partitioning on the size scale of the dendrite spacing of alloying elements and impurities are analyzed below.

4.4.1 The Geometry of Weld Overlay

Submerged arc welding is performed under a blanket of granular flux, the arc operating within a cavity formed in the flux. The effects of most operating parameters of submerged arc welding on submerged arc weld bead morphology involve a substantial amount of empiricism in various combinations of such factors as machine parameters, arc stability, flux property, physical dimensions of the weld electrode, plate thickness and weld joint dimensions. Usually, a regression analysis is used to evaluate coefficients of each of the variables in a particular experiment.

Of the several submerged arc welding parameters, current is the most important welding variable which influences deposition rate, penetration, and overall weld size. It is the single most important variable in controlling submerged arc weld penetration. An increase in current increases the penetration almost proportionally, while bead width increases only slightly. Based on the work of Gunnert^{61,62}, the effects of current, voltage and speed on weld penetration using round wire electrodes can be expressed as follows

$$d = K \left(\frac{I^4}{vV} \right)^{1/3}, \quad (4-36)$$

where d is the depth of penetration, I is the current, V is the voltage, and v is the welding speed. The value of K depends on other parameters such as flux and metal composition. It is seen that the current has a strong effect on the penetration of the weld bead. As for the width of the bead, there is some disagreement on the contribution of current on the width of the bead. Apps et al.⁶³ observed a steady increase in the bead width with the increasing current level. Renwick and Patchett⁴⁶ noted that the bead width passed through a maximum as current levels increased, either decreasing or remaining constant at higher currents. Renwick and Patchett attributed the maximum in weld width as being associated with a transition to a mode in which plasma jets assumed a more significant role as a penetration mechanism. At higher current levels the more powerful jets may be able to create a depression in the weld pool surface, enhancing penetration at the expense of bead width.

As indicated in Eq.(4-36), an increase in welding voltage results in a decrease in the penetration. Although voltage has a modest effect on penetration, it changes the fusion zone shape by exerting a direct influence on bead width. Higher voltages correspond to longer, and therefore broader, arcs. The distributed heat source conduction solution predicts a wider pool for a broader arc energy distribution. But the effect of voltage on the size of reinforcement of the weld bead is still a topic of argument^{46,62}.

Variations in welding speed affect both penetration and bead width in the same direction. Higher speeds produce a more narrow and more shallow bead with less filler deposition per unit length, and hence a smaller overbead. As far as penetration alone is concerned, welding speed is second only to current in effect.

At a given current the electrode size influences bead shape by changing both penetration and size of the overbead. A smaller electrode will give a higher deposition rate, with less energy expended in melting the base metal, resulting in a larger overbead. Renwick and Patchett⁴⁶ found that the use of a smaller electrode resulted in increased penetration and thought that it was the consequence of a more restricted

arc. On the other hand, larger electrodes can carry higher currents so the deeper penetration is achievable with larger electrode diameters. However, a strip electrode usually results in some uneven penetration in the cross-section of the weld bead as a result of the erratic movement of arc at the end of the strip. The random shifting of the arc along the end of the strip is also under the effect of the traveling speed and current of the welding procedure. With very wide strips, 100 mm or wider, an alternating magnetic field is used to drive the arc across the strip. This is considered unnecessary in 60 mm strip, as used for this project.

4.4.2 The Structure of Weld Overlay

In general, the overall overlay structure depends on the welding procedure and the chemistry of the overlay materials. In other words, the weld pool solidification structure is characterized by a microstructure which depends on chemical composition and cooling rate conditions, and by a macrostructure which depends on the crystallographic orientation of grains with respect to the thermal gradients in the weld pool.

4.4.2.1 Overlay Microstructure

The development of overlay microstructure is highly dependent on the solidification conditions, which are a function of welding parameters and the original compositions of the overlay materials and the base steel.

Generally the nucleation of the weld metal initiates at the solid-liquid interface by epitaxial growth from the base metal. Each grain forms as a continuation of one of the grains that lie along that part of the fusion boundary. As the fusion line moves with the proceeding of the welding, grains grow in cellular or columnar fashion. The growth mode greatly depends on the solidification rate and the thermal gradient across the solid/liquid boundary.

In fusion welding with wire electrodes, the increase in weld speed will change the shape of weld pool

from roughly oval to elliptical, and will cause an increase in the solidification speed of the weld metal as well. In an assumption of two-dimensional heat flow⁶⁴, the solidification rate of the weld metal at different region along the weld pool is estimated as

$$R = v \sin \theta, \quad (4-37)$$

where v is the welding speed and θ is the angle between the welding direction and the tangent to the solid/liquid interface. From Eq.(4-37) the maximum solidification rate is along the centerline of the weld and the possible maximum speed of solidification is approaching the weld speed.

In contrast, the thermal gradient in the liquid turns out to be a maximum along the solid/liquid interface and becomes a minimum at the weld centerline. The temperature gradient $\partial T / \partial x$ is

$$\frac{\partial T}{\partial x} = \frac{\partial T}{\partial t} \frac{\partial t}{\partial x} = \frac{\partial T}{\partial t} / v = \frac{1}{v} \frac{\partial T}{\partial t} \quad (4-38)$$

while the theoretical value of the thermal history $\partial T / \partial t$ can be estimated from the thermal analysis. Consequently, the temperature gradient will vary as a function of the thermal properties of the materials, the size of the specimen and the temperature range over which the weld metal solidifies. For three dimensional heat flow, the thermal gradient at the rear of the weld pool on the solid/liquid boundary is

$$G_l = \frac{1}{v} \frac{\partial T}{\partial t} = \frac{T_m}{d_l} \quad (4-39)$$

where T_m is the solidification temperature and d_l is the distance from the heat source to the rear of the weld pool. For an alloy system, the composition of the solidifying phase will differ from the composition of the liquid at the front of the solid/liquid interface as long as the solidification process is not fast enough to fully restrain the diffusion of atoms. As solidification proceeds, solutes will diffuse from the solid/liquid interface and form a solute boundary layer in the liquid ahead of the interface. When the boundary layer is fully established and reaches steady state, the composition of the solidifying phase will be C_0 , the nominal composition, and the liquid composition at the interface will be C_0/k , where k is the equilibrium partition coefficient, defined as C_s^*/C_l^* at temperature T^* . For an alloy system whose partition coefficient is less

than one, the equilibrium liquidus temperature increases with distance from the interface because the lower the solute content, the higher the liquidus temperature. There is then the possibility that the real temperature of the liquid immediately ahead of the interface is below its liquidus temperature. It is, therefore, supercooled. This kind of supercooling owing to the change of the composition, not the temperature, at the solidifying front is called constitutional supercooling. On the basis of the ternary alloy solidification model set by Flemings⁶⁵, for a single phase alloy, the constitutional supercooling criterion can be written as

$$\frac{G_l}{R} \leq -\frac{p(C_{lm}^* - C_{on})}{D_{mn}} - \frac{s(C_{ln}^* - C_{om})}{D_{nn}}, \quad (4-40)$$

where p is the slope of the liquidus surface at the concentration of element n , C_{ln}^* , in the liquid, s is the slope of liquidus surface at the concentration of element m , C_{lm}^* , in the liquid, C_{om} and C_{on} are the nominal concentrations of solutes m and n , respectively, and D_{mn} and D_{nn} are the on-diagonal coefficients of the two solutes in the liquid.

As long as the actual G_l/R ratio at the interface is equal to or greater than the right-hand side of Eq.(4-40), a planar front will be maintained. However, if the ratio is less than the right side of Eq.(4-40), the liquid ahead of the interface will be supercooled. This supercooling can lead to interface instabilities and, thereby, to the development of cellular and dendritic grains.

During the initial stage of the weld solidification, where new grains just start to grow epitaxially from grains along the interface in the base metal, which temperature is relatively lower than the weld pool, and the solute boundary is being established, the amount of solute rejection at the interface is negligible, and thus the ratio G_l/R in the liquid right ahead of the interface is a maximum and the constitutional supercooling condition cannot be met. Under these conditions, the solid/liquid interface is stable and planar growth occurs. To achieve constitutional supercooling and disturb the planar solidifying front, the left side of Eq.(40) must be less than the right side. That is, the thermal gradient should be reduced and/or the solidification rate should be increased.

As analyzed above, the solidification velocity and temperature gradients are continually changing from region to region around the weld pool solid/liquid interface. The solidification structure will then vary according to the constitutional supercooling conditions. From Eq.(4-40), it is seen that for a given G/R , established by the welding conditions, the amount of constitutional supercooling will depend upon the alloy system and will increase with the increase of solute content, C_0 , and the decrease of the partition ratio, k . On the other hand, for a given alloy system, welding parameters which increase R and decrease G will enhance the degree of the constitutional supercooling.

A simplified model to describe the relationship between the constitutional supercooling condition and the solidification structure was proposed by Savage et al^{65,66,67}. In this model, the solidification patterns of welds were related to the magnitude of the square root of G/R as shown in Figure 18⁶⁸. Since the thermal gradient and the solidification velocity in the weld pool both vary as a function of distance, a number of different solidification patterns can occur within a single weld, as the solid/liquid interface moves forward following the arc.

In most fusion welds, a planar solidification structure present during the initial stages of solidification becomes difficult to maintain as the boundary layer becomes further established and G decreases and R increases as distance changes.

As solidification proceeds, the degree of constitutional supercooling increases and the actual temperature of the liquid starts to fall below the effective liquidus temperature. The extent to which the actual liquid temperature falls below the effective liquidus temperature determines the degree of constitutional supercooling. For small amounts of supercooling, instabilities in the interface will promote the formation of cellular grains. As the amount of supercooling increases and the interface turns more unstable, secondary arms may arise from the primary arms, indicating a transition between cellular and cellular-dendritic structures, the predominant structure in most welds. If constitutional supercooling extends, approximately, over the magnitude of a grain diameter, columnar dendrites can form.

Theoretically, the effect of constitutional supercooling on the transition from a planar solidification front to cellular and dendritic growth can be predicted using linear perturbation theory. Based on this theory, Trivedi⁶⁹ estimated that a critical solidification rate at which the cellular growth to dendritic transition occurs is given by $R/k \sim 0.78 \text{ mm/s}$ for middle range solidification velocity. Due to the difficulties in examining the actual thermal gradient and grain growth rate in fusion welds, however, less attempt has been made to apply this theory to actual weld structures.

Macroscopically, the size of grains when grown from the base metal depends upon the size of the base metal grains at the solid/liquid interface. As solidification proceeds, growth of the grains in the weld pool occurs roughly perpendicular to the fusion zone. The rate of growth depends strongly upon the steepness of the thermal gradients and the orientation of the crystals. Those crystals aligned with the preferred crystallographic growth directions most nearly parallel to the steepest thermal gradients will tend to grow most efficiently. As the direction of the steepest thermal gradient changes, some grains continue to grow as others terminate their growth. The transition between epitaxial growth and competitive column growth depends largely on the welding parameters, in particular welding speed. At low welding speeds (less than 2.5 mm/sec.) in carbon steels, it becomes possible for favorably oriented grains at the trailing edge of the weld pool to grow parallel to the weld direction, forming an axial grain structure. The increase either in welding speed or in constitutional supercooling will break down and even eliminate the growth of the axial grains. As the speed continues to increase, the weld pool elongates and the competitive columnar grains oriented in the preferred crystallographic direction appear to bend along the direction of the steepest thermal gradients. As the solidification rate reaches a maximum limit for a given weld pool geometry, a distinct centerline arises again. At this point, the columnar grains grow almost perpendicularly from the fusion zone boundary to the weld centerline. Changes in welding speed can also cause a disruption of the epitaxial growth mechanism^{70,71,72}. High welding speed, small grains in the base metal, and narrow weld bead all tend to favor non-epitaxial growth. Unlike the epitaxial growth, where the grains in the weld metal are an extension of the partially melted base metal grains, in non-epitaxial growth a metallurgical (high angle) grain boundary separates the partially melted heat affected zone

grains from the fusion zone grains. Metallographically, the fusion zone consists of single crystals of the same orientation separated by numerous low angle subgrain boundaries, rather than columnar grain boundaries. Since the single crystals tend to orient themselves perpendicular to the weld direction, growth occurs only from favorably oriented base metal grains, in comparison to epitaxial growth, where growth occurs initially from almost every base metal grain.

With a planar strip as the electrode, conditions are somewhat different and not well researched up to now. There is a planar front ahead of the solidifying pool, and growth tends to be from the plate surface of the base steel towards the free interface with the molten slag, rather than towards the weld centerline as that in a weld pool of a wire electrode. Also the erratic arc at the end of the strip electrode makes the fusion line jagged between the base steel and the weld metal. The temperature distribution becomes more complicated than that in a weld pool obtained by a wire electrode. The magnitude of dilution of the weld pool with the base steel varies along the fusion line microscopically. This will significantly affect the nucleation and growth of the weld metal.

4.4.2.2 Microsegregation of Solutes

Another important phenomenon accompanying the solidification of the weld metal is microsegregation. It occurs over distances of the order of the dendritic spacing and can lead to large variations in alloy or impurity composition between the solidification cell core and the cell boundary. As a result, phase equilibrium and microstructures of the weld materials can be considerably different from those of base material of the same composition. There are three models proposed to describe the microsegregation in solidification of alloys. These models assume that composition equilibrium is maintained at the solid/liquid interface during solidification and that no solid state diffusion take place. The difference in the three models lies in the degree of mixing of solute that happens in the liquid. The first model⁷³ assumes that the complete mixing occurs in the liquid. That the mixing in the liquid takes place only by diffusion in the liquid⁷⁴ is the assumption in the second model. For the plane-front solidification, the third model⁷⁵ assumes that the mixing occurs by convection as well as by diffusion in

the liquid. Recently, a new treatment for microsegregation was proposed by Brooks and co-workers^{76,77} who combined the first model with solid-state diffusion and applied these to weld solidification. The following discussion is mainly based on this new model.

The solidification and solid-state transformations of the austenitic stainless steels are quite complex, especially when austenitic stainless steels are welded with low alloy steels, and a variety of ferritic morphologies can exist in a two-phase ferritic/austenitic structure. Thus, it is very difficult to verify a solidification model using this complicated alloy system, and there still are a number of unknowns about the whole transformation process from the liquid to the final solid state. The skeletal ferritic morphology, which was used to verify an initial transient model, contains a ferrite core surrounded by austenite. This structure forms as a result of peritectic solidification, schematically shown in Figure 19⁷¹. As the schematic shows, during solidification and cooling, a large fraction of ferrite transforms to austenite by a diffusion controlled solid-state transformation. In this case initial transient regions were assigned to the ferrite-containing core of cells that solidified by a peritectic reaction of ferrite followed by austenite. The large difference in Cr and Ni contents of δ and γ solidification products, and further modification of the core region by the diffusion-controlled solid-state transformation proved the model of the complete mixing plus diffusion in the solid.

Another important segregation of solutes in welds is solute banding that is associated with the growth fluctuation of the solid/liquid interface of the weld pool. The fluctuation is caused by a number of factors, including:

- 1) periodical heat flow associated with the extraction of the latent heat of fusion, which retards growth until heat is dissipated and the growth front again advances;
- 2) periodical heat input due to power source ripples; or
- 3) natural oscillations of the weld pool, controlled by the surface tension or the temperature dependence on the surface tension as the weld pool surface fluctuates with the temperature.

At the initial solidification stage a planar interface is assumed at the solid/liquid boundary. There will

be a layer of solute ahead of the boundary, and the thickness of this layer depends on the diffusivity of the solutes and the solidification rate. A rapid increase of the solidification rate will result in a solute dump in the solidifying solid, while a decrease in the velocity will decrease the solute content in the solidifying front until a steady-state condition is again established at the interface. The effects of changing solidification velocity on the solute content of the solidifying solid is shown schematically in Figure 20.⁷² This mechanism is more pronounced for interfaces that exhibit more planar features.

In practice, the solidification structure is, therefore, usually rather complex. The solidification structure of a particular alloy system can depend greatly upon welding process and welding parameters, which can both affect the shape of the solidifying weld pool and morphology of the solidifying structure. The development and interactions of the thermal stresses within the solidifying structure are also related in a complex manner to the conditions of welding. So a detailed model, incorporating coupled thermal/solidification and microsegregation codes that could accurately predict the solidification and the defects behavior, would be extremely complex. The only cladding materials, which solidify in a relatively simple way, are those which are strongly ferritic or strongly austenitic. Most industrial applications for cladding are the intermediate type, such as 309 + 347, which may involve both ferritic and austenitic solidifications. This project therefore selected a variety of cladding alloys to cover this spectrum as completely as possible in order to observe the overall pattern.

4.5 Effect of Flux on the Structure of Welds

The most complex factor relating to the macrostructure and microstructure of submerged arc welding is the effect of flux composition. Although the flux is an important factor in controlling welding bead morphology and arc stability, a clear understanding capable of correlating data generated for a wide variety of flux compositions and welding conditions has not yet been developed. As it is seen, small or even minute amounts of certain elements can have dramatic effects on any arc welding process, acting via changes in surface tension properties or changes in the total arc energy or the distribution of that energy⁴⁵. Furthermore, it is obvious that there may be more than one mechanism by which fluxes may

interact with the welding system and this makes it difficult to unambiguously establish relationships between physical properties of the various fluxes and their welding characteristics. To date there are three general mechanisms proposed to explain the link between weld bead and physical properties of the fluxes. They may be classified as arc effects, surface tension effects, and flux viscosity effects.

The stability of arc is the necessary condition to achieve an evenly penetrating weld bead. Some flux components produce an erratic arc which does not efficiently transmit energy to the weld pool. Fluxes which produce the most stable arc operation and deepest penetration were considered to be the fluxes which provide the most easily ionized atoms to the arc. Also, slag compositions with higher oxygen activity contribute greater amounts of oxygen and produce more stable and more deeply penetrating arcs⁷⁸. Surface tension forces between the flux and the atmosphere and between the flux and the weld pool may be one of the factors controlling the bead shape by controlling the spreading of the weld pool. Another factor controlling spreading may be the viscosity of the molten pool. Since the molten weld metal overbead must push the flux aside as it spreads, a flux which can resist this force for the brief duration of the molten state may be able to contribute to confining the weld overbead and, thereby, limit the distribution of energy to a smaller region^{79,80}.

The chemistry of weld metal is also under the influence of flux composition⁸¹. The influence of fluxes on the weld metal structure does not rest only with the bulk chemistry of the weld metal but also with the nucleation of new solid grains through the presence of inclusions. This could be the result of incomplete separation of the slags or of the inclusions formed in the welding process, from the molten weld pool. These inclusions relate not only to the major flux composition but also to the minor elements in the flux. Proper selection and control of flux composition is mostly in the control of consumable manufacturers, who recommend certain fluxes for particular applications. In consideration of the complexity of the flux composition, it was decided to use only one flux in this experiment to eliminate variability due to flux type.

5. EXPERIMENTAL EQUIPMENT, MATERIALS AND PROCEDURES

5.1 Equipment

To clad corrosion resistant alloys on the plate of Cr - Mo low alloy steel, the submerged arc welding machine used in this experiment is the A6 system made by ESAB R & D Department of Sweden. The maximum allowable current is 1500 amp. The set-up of this machine for cladding is schematically shown in Figure 21.

To release the residual stresses of the weld specimen developed during welding, post weld heat treatment was performed in a furnace with heating and cooling control. A specified heat treatment schedule agreed to represent typical fabrication practice was used.

To examine the occurrence and the extent of disbonding of the overlay, ultrasonic tests in C-scan mode were carried out on a set of Sonatest and TSI Ultrasonic Immersion Programmable Scanner. The set-up of this equipment for the ultrasonic test on the specimen is shown in Figure 22.

To promote the disbonding of the overlay from the plate of the base steel, autoclave tests in conditions of high pressure of hydrogen and high temperatures were carried out in a stainless steel vessel, with the heating and piping system as shown in Figure 23.

To observe the microstructure of the interface between the overlay and the base steel and analyze the chemistry profile across the interface, metallographic observations were carried out on an optical microscope made by Zeiss, on electron transmission microscopes EM300, Hitachi 700 and JEOL 2000 with accelerating voltages of 100 kV, 125 kV and 200 kV, respectively, and on a scanning electron microscope, Hitachi Model 2001.

To examine the hardness of the microstructures across the interface, a microhardness tester made by Shimadzu was employed. The Knoop scale was used to check the microhardness across the interface of the specimens. The diamond pyramid indenter was loaded with a weight of 25 grams.

To evaluate the thermal expansion coefficients of overlay materials and the base steel for the purpose of estimating residual stresses, a NETZSCH dilatometer made by Geratebau GmbH was utilized to measure the variation of the specimens in length with temperature. The set-up of this dilatometer for the experiment is shown in Figure 24.

Due to the variations in chemical composition across the interface, special chemical etching and thinning techniques must be performed to reveal the structure along the interface. Therefore, an electrolytic polishing apparatus was used to prepare the specimen for metallographic observation and an ion mill with a cold stage made by Gatan was employed to thin the specimens for TEM.

5.2 Materials

5.2.1 Welding Flux

The granular flux used in this experiment was supplied by Sandvik with the designation 34SF. The nominal chemical composition of this flux was provided by the company as presented in Table 3. The property of the flux can be estimated from its basicity which is derived from the concept of the slag in steel making. According to the formula of International Institute of Welding (IIW) in the determination of the Basicity of flux below,

$$\text{B.I.} = (\Sigma \text{ basic oxides} + 1/2\Sigma(\text{FeO} + \text{MnO}) + \text{CaF}_2) / (\Sigma \text{ acid oxides} + 1/2\Sigma(\text{Zr,Al,Ti oxides})), \quad (5-1)$$

the basicity of the flux used in this test can be calculated as:

$$\text{B.I.} = \frac{\text{Na}_2\text{O} + \text{CaO} + \text{MgO} + \text{CaF}_2 + \text{K}_2\text{O} + \frac{1}{2}(\text{MnO} + \text{FeO})}{\text{SiO}_2 + \frac{1}{2}(\text{Al}_2\text{O}_3 + \text{Cr}_2\text{O}_3)} \quad (5-2)$$

in this particular case. Based on this formula, it is determined that the basicity index of the flux used in this experiment was 0.81. Since B.I. is less than 1, the flux is considered as acidic.

5.2.2 Steel Plate

1.25%Cr - 0.5% Mo low alloy steel was used as the base steel which was made into a plate 600 × 110 × 65 mm. The amount of chemical components of the base steel is listed in Table 1. This type of Cr - Mo low alloy steel is typical of steels used for the clad vessels.

5.2.3 Strips of Corrosion Resistant Alloys

Eight commercial alloys possessing corrosion resistance to most corrosive environments were used as the overlay materials in this experiment, and they were made into a strip 60 × 0.5 mm, which was the electrode in the submerged arc welding. The chemical compositions of the eight alloys are presented in Table 2. The alloys were selected to span the range from totally ferritic to strongly austenitic, and to contain a variety of carbide stabilizing elements. For the alloy of 309L series, two more alloys with carbide-stabilizer molybdenum (309LMo) and niobium (309LNb) were chosen to investigate the influence of carbide precipitation on disbonding. Some of these materials were made for this project (C-22), others were fabricated from sheet materials as no strip was commercially available (2205, 254SMO).

5.3 Experimental Procedure

5.3.1 Welding Procedure

The eight strips of corrosion resistant alloys mentioned above were clad on plates of Cr - Mo low alloy steel by the Submerged Arc Welding process. The main parameters of the welding procedure employed in the strip cladding are listed in Table 4. If the linear heat input, q_s , is taken as

$$q_s = \frac{60\eta IV}{v} \text{ J/mm} \quad (5-3)$$

where η is the arc efficiency coefficient, 0.95 for submerged arc welding⁸², I is the welding current in amp, V is the welding potential in volts, and v is the welding speed in mm/min., the nominal heat input for the two procedures will be the same level as 8.55 kJ/mm. The current is doubled and speed is also

doubled for the second procedure. This technique has been shown to be effective in minimizing disbonding⁷. However, the fundamental reasons remained obscure.

The flux used in the cladding was first baked at 260 °C for 2 hours, and then the flux was placed in a holding oven at 45 °C before immediate welding. The flux was not recycled.

After the welded specimens cooled down, the ultrasonic test was carried out to check if there were any cracks in the welds.

5.3.2 Ultrasonic Examination

Specimens were examined by ultrasonic test in C-scan mode in conditions of as-welded, post-weld heat treatment and after-autoclave to examine disbonding in every experimental step. The specimens were immersed in water, and the ultrasonic probe was set about 40 mm above the back surface of the specimen to be tested. The scanning step was set at 2.5 mm. The frequency used for the ultrasonic test was in the range of 2.5 to 5.0 MHz.

5.3.3 Post Weld Heat Treatment (PWHT)

The welded specimens were put into a furnace for post weld heat treatment. The purpose of PWHT was to stabilize the structure of the welds and to release the residual stresses developed during welding. Therefore, the welded specimens were heated and cooled uniformly at a rate of 50 °C per hour to minimize the risk of developing transient thermal stresses in the specimen. Specimens were heated up to 690°C and kept at that temperature for 24 hours, and then slowly cooled down to room temperature.

After PWHT specimens were put through ultrasonic test again to examine if cracking happened during PWHT by the transient stresses induced by heating and cooling.

5.3.4 Autoclave Test

The purpose of the autoclave test was to increase the hydrogen concentration in the welds and then to

examine the susceptibility of these overlays to disbonding.

After the specimens were post-weld heat treated, they were put into a pressure chamber to carry out the autoclave test. First, nitrogen gas of high pressure was used to inspect for any leakage in the system. Then hydrogen gas was introduced into the chamber to replace the nitrogen gas until the pressure of hydrogen reached 10 MPa. Afterwards, the specimens were heated at a rate of 100 °C per hour up to 450 °C. The pressure of hydrogen in the chamber was increased by heating but was maintained at 15 MPa by a release valve connected to the chamber. After being held at the temperature of 450 °C and at the hydrogen pressure of 15 MPa for 48 hours, the specimens were cooled down to room temperature (~ 22 °C) at a cooling rate of 222 °C per hour by controlled nitrogen blow down. The high cooling rate was supposed to promote the hydrogen-induced disbonding since the faster cooling would result in more severe disbonding⁸³. The faster cooling rate also simulated the practical emergency situation in which a faster cooling down is a necessity. After the temperature of the specimens reached room temperature and held at that temperature for about 8 to 10 hours, the specimens were examined by ultrasonic test again to find out if disbonding happened.

5.3.5 Microhardness

The coupons for microhardness testing were cut from specimens in the as-welded and the PWHT conditions. Microhardness was assessed with a load of 25 grams for 15 seconds in the scale of Knoop. Measurements were made across the interface.

5.3.6 Dilatometric Examination

The coupons for the dilatometric test were cut directly from the welded overlay where the dilution had happened to some extent. It was expected that the results would more accurately reflect the difference in thermal expansion between the overlay material and the base steel. The coupons were made into specimens 5mm in diameter and 50 mm in length. Two coupons of each alloy were cut, one from the specimen by Procedure I and another from the specimen by Procedure II. The measurements were

calibrated to a standard sample of nickel. The heating rate was set at 180 °C per hour and cooling rate at 300 °C per hour owing to the limitation of this apparatus. The thermal expansion test was carried out in the temperature range between 180 to 500 °C. During the test, the coupons were protected from oxidation by helium gas.

5.3.7 Optical Metallographic Observation

The specimens for the optical metallographic observation were cut from welds in conditions of as-welded, PWHT and autoclave tested, respectively. The profiles of observation were made available both for the direction along the weld direction and for the direction transverse to the weld direction.

After the surfaces of specimens were abraded and polished, the specimens were put into a solution of 0.1% chromic acid for electrolytic etching. The voltage was set at about 8 to 12 volts, and the current was set in the range between 20 to 200 mA according to the size and the composition of the specimen to be prepared. After etching for 5 to 10 seconds in the chromic acid solution, the specimens were put into another solution of 1% nital for another 3 to 5 seconds before cleansing and drying. The first electrolytic etching was for the corrosion resistant alloy overlay and the second etching by nital solution was for the base steel.

The interface area, the weld metal and the heat affected zone in the base steel were then viewed under the optical microscope. The macrostructure and microstructure of the weld overlays were measured or observed.

5.3.8 Measurement of Dilution

The area of the whole weld metal in the cross-section vertical to the welding direction, F , and the area of weld metal in the base steel side only, F_2 , were measured on an image analysis system of Bioscan. The ratio of F_2 to F was then taken as a measurement of the dilution effect.

Also the effects of welding procedures on the geometry of weld bead in the cladding were examined

by measuring the width of the weld bead, the penetration of the weld metal and the height of weld bead crown, i.e., the part of the weld metal above the surface level of the base steel.

5.3.9 Observations with Scanning Electron Microscope

The specimens prepared for the observation on the SEM were made in the same manner as those for optical metallographic observation, but these specimens were etched in the etching solutions for a relatively longer time to achieve a better contrast.

The chemistry profile across the interface of specimens was also scrutinized by EDX on SEM.

5.3.10 Observations with Transmission Electron Microscope

The specimens for the TEM were chosen from the specimens prepared for optical metallographic observation. The specimens were cut into chips on a diamond saw with the section vertical to the interface between the overlay and the base steel and then ground to a thickness of about 50 μm . A perforating punch was used to cut the specimens into discs 3 mm in diameter with the interface across the center. Initially, thinning was attempted with an electrolytic process, but the differing corrosion resistance across the interface between the Cr-Mo low alloy steel and the cladding alloy made it impossible to thin the cladding evenly. An ion mill was then tried. The uneven thinning persisted, although the situation was improved. A cold sample stage was added in order to improve the thinning behavior. Finally, a low angle ion beam was used, which increased thinning time considerably, but produced acceptable results.

6. EXPERIMENTAL RESULTS

6.1 Effect of Welding Procedures on Dilution

The result of the measurements on the dilution effect is presented in Table 5. From the result, it is seen that the main parameters of the welding procedure have a significant influence on the dilution of weld metal. In general, the high current welding procedure produced higher dilution, deeper penetration and a thicker deposit, although the nominal heat input was the same for both procedures. The higher the dilution, the more the base steel was dissolved into the weld metal. The composition of the weld metal would be affected, and the microstructure. The cross-section of overlaid specimens also showed that the dilution varied along the interface as penetration varied. This is due to the erratic motion of arc across the strip electrode during welding which produces variable time of residence for the arc in different places. However, this effect is unpredictable in the absence of a driving magnetic field to control arc movement. The dilution variation is also typical of deposits made in real fabrications.

6.2 Thermal Expansion Coefficients

The result of the measurements on the thermal expansion test is shown in Table 6. The thermal expansion coefficients shown here are the average value of two coupons cut from specimens by Procedure I and Procedure II, respectively, for each alloy. There is no obvious difference between the specimens by the two procedures. Since the coupons used in this test were directly cut from the overlay which had been affected by the dilution from the base steel, the result should show some differences from the data provided by the alloy producers. The thermal expansion coefficients were calculated based on the cooling curves in the range from 500 °C to 180 °C at a cooling rate of 5 °C per minute. A part of the experimental curves in the thermal expansion test were shown in Figures 25 to 31.

A large difference in thermal expansion coefficient between the base steel and the overlay materials would develop a high level of tensile residual stresses in the overlay during cooling down from high temperatures if the overlay material possesses a higher thermal expansion coefficient. The overlay would

tend to contract more than the base steel during cooling down and the materials would tend to be stronger as the temperature dropped, so the stresses could not be released as occurs during heating up. Since the largest difference in thermal expansion occurs between the base steel and the overlay of 254SMO, it is expected that the high level of tensile residual stresses in this cladding would make the disbonding more severe. The magnitude of the residual stresses can be estimated based on the theory mentioned in Section 4.3. If the following data are selected for the calculation: $E_o = 220$ GPa, $E_b = 200$ GPa, $\nu_o = 0.32$, $\nu_b = 0.3$, $\alpha_o = 20 \times 10^{-6}$, $\alpha_b = 14 \times 10^{-6}$, $\Delta T = 300^\circ\text{C}$, $h_o = 10$ mm, $h_b = 60$ mm and the width of plate $b = 60$ mm, the maximum shearing stress is found to be 142 MPa, the maximum tensile stress along the interface 305 MPa, and the maximum "peeling force", or the stress vertical to the interface, 37 MPa. These estimated maximum "peeling stresses" are shown for each cladding alloy in Table 6. The estimated tensile stress is lowest for the 2205 alloy, rises through the 309 series to peak at the the 254SMO alloys, then decreases through the 904L alloy to the high Ni alloys C22 and 5923 alloys. It is seen that the residual tensile stress along the interface is close to the yield strength of the overlay 254SMO, 300 MPa. In this case, plastic deformation is expected near the interface. Furthermore, the accumulation of hydrogen will be elevated in the strained region under the tensile stresses. This makes the disbonding even worse.

6.3 Microhardness across the Interface

The results of the Knoop microhardness measurements for specimens in as-welded condition are shown in Figures from 32 to 36, and those for specimens after PWHT are shown in Figures from 37 to 41. In all of the figures the base metal side was designated as the negative distance from the interface.

From the measurements of specimens in the as-welded condition, there exists a considerable spike of hardness just across the interface in the weld metal side in specimens of 2205, 309L and 254SMO. Specimens of 904L and C-22 showed just a small rise in hardness at the interface and the level was below HK 600. These phenomena indicated that there was martensite or bainite formed along the interface in specimens of 2205, 309L and 254SMO but not in specimens of 904L and C-22. The hard band was

remarkably wider in the specimen 2205 than that in other specimens. In most cases the greatest hardness was produced by the high current welding procedure, where dilution was higher.

After PWHT the spike of hardness in the specimen of 2205 disappeared although the hardness was still higher than HK 600, as is seen in Figure 37. And it was noted that there was a valley of hardness at the weld metal side about 300 μm away from the interface. The high hardness may be maintained by the precipitation of carbides along the interface. There was a band of austenite ahead of the precipitation zone, as seen in the next section on the optical structure, which was softer than the ferrite. The hardness spike remained visible (Figures 38 and 39) in specimens of 309L and 254SMO, showing the occurrence of carbide precipitation. The most interesting thing was that an increase in hardness along the interface in specimens of 904L and C-22 was observed after PWHT as shown in Figures 40 and 41. This indicated the precipitation of carbides at the interface. After PWHT, the hardness of the weld metal and the base steel tended, in general, to be the same level in specimens of 309L, 254SMO and 904L. While the hardness of weld metal of 2205 and C-22 remained almost the same before and after PWHT despite the fact that the hardness of the base steel decreased after heat treatment. This showed that the structures of the weld metal in specimens of 2205 and C-22 were relatively stable after solidification.

Right under the interface in the base steel side there was a plunge in hardness. This might be the result of depletion of carbon that moved into the overlay to form carbides due to the existence of strong carbide forming elements such as chromium and molybdenum in the overlay, and the coarsening of grains in the HAZ of the base steel. The sharp change in hardness in a narrow distance from one side to the other side of the interface may reduce the mechanical properties, especially fracture toughness, along the interface region. The hardness of the heat-affected zone in the base steel was remarkably reduced by PWHT from above HK 400 in the as-welded condition to HK 300 after PWHT, showing the incidence of recrystallization of ferrite and the coarsening of carbides and grains.

6.4 Ultrasonic Examination of Disbonding

No disbonding along the interface was revealed in any specimens in the as-welded and after PWHT conditions by the ultrasonic C-scan test.

The results of the ultrasonic examination on the disbonding of specimens after autoclave testing are given in Table 7. The extent of disbonding is expressed as the ratio in percentage of disbonding area to the whole clad area on the surface of the base steel plate. A part of the records in the ultrasonic C-scan are presented in Figures 42 and 43. It is seen that the disbonding is more severe in specimens 309L and 254SMO prepared by Procedure I than those prepared by Procedure II. The disbonding areas locate near the center of the whole clad area.

From Table 7 it is seen that there was no disbonding found in specimens of 2205 by either welding procedure. A few disbonding areas showed up in specimens of C-22. The disbonding phenomena in the 309L series were obviously affected by the welding procedures. More disbonding took place along the interface by the low current welding procedure. The tendency was also shown in specimens of 254SMO in which disbonding appeared more severe. The result for 904L showed quite large scatter. In some specimens more disbonding showed up while in others there was less disbonding. For the nickel based alloy 5923, disbonding became worse if high dilution occurred.

6.5 Optical Metallographic Observation

6.5.1 Optical Microstructures in As-welded Condition

The optical microstructures of specimens cut transverse to the welding direction from the weld overlay in the as-welded condition are presented in Figures from 44 to 59. There was a shining band adjacent to the fusion line at the overlay side in specimens in as-welded condition, indicating that the transition zone was not easily affected either by the etchant for the overlay or by the etchant for the base steel. In this transition zone the base steel and the overlay materials were partially blended together due to

the quasi-static layer near the fusion line, since the Lorentz force (the electrical magnetic forces produced by the electric arc during welding) was not strong enough to homogenize the layer adjacent to the solid heat affected zone as uniformly as those in the rest of the weld metal zone. Also the width of the "shining band" varied among specimens indicating the difference in dilution and the composition effect. By adjusting the composition of etchants and the current for the electrolytic etching, some details could be revealed along the fusion line in some specimens. The results in both conditions are shown together to see the difference.

In general there were three microstructural zones across the interface from the base steel to the overlay. Below the interface is the heat affected zone in the base steel, above the interface is the dendritic structure of weld metal, and between these zones is the most interesting transition zone that includes the interface.

In the heat affected zone, the microstructures showed normal patterns occurring in most steel welds. As-welded, some subzones with different microstructures could be recognized in the HAZ. Adjacent to the fusion line there is usually a coarse grain zone with martensite or bainite structures. The coarse grains were produced by the heating of the area to just under T_m during the welding. Next to the coarse grain zone, a fine grain zone appeared as a result of fast solid transformation during heating and cooling in the welding. Downwards was the intercritical zone where the grains showed a little bit of growth by the heating in the welding. Further down was the unaffected zone where grains remained in the normal structure before welding.

Cellular dendritic grains stretching from the interface toward the surface of the weld overlay exhibited the typical weld metal structure in all specimens. But a difference in morphology existed among these specimens. In the specimen of 2205, the cellular dendrites of weld metal showed a vermicular structure in Figures 44 and 45, reflecting the result of the $\delta - \gamma$ solid transformation during which the vermicular delta ferrite was formed between the longish austenitic grains formed along the interdendrites of original cellular delta ferrite. In the specimens of 309L series, the fine residual ferrite is only barely

visible as a bright skeleton-like region or isolated spots in the interdendritic zones in the austenite. With the increase of nickel content the cellular dendrites appeared relatively coarser in the specimens of 254SMO, 904L, 5923 and C-22. There was less chance for the precipitation of ferrite in the weld metal. The size of cellular dendrites turned finer as the welding speed increased.

Along the fusion line at the side of overlay, there was the transition zone. In most fusion welds, the initial solidification takes place epitaxially from the base steel and assumes the planar grain growth mode due to the highest thermal gradient and the low growth rate at the initial stage of solidification. The transition zone consisted of the planar grains along the fusion line between the base steel and the overlay. The state of the stagnant layer makes the convection in the weld pool not uniform so the composition is non-uniform. There is a sharp composition change across the transition zone. In the transition zone martensite, or bainite, or acicular ferrite formed during the cooling down of the welds, depending on the local composition and cooling rate. In general, the width of the transition zone increased with the welding current as a result of higher dilution effects. The appearance of an interface between the base steel and overlays of C-22 and 5923 was the sharpest among these specimens, showing the strong effect of nickel on the transition in a dissimilar material weld. At the end of the transition zone, the planar grain boundary became difficult to maintain as the thermal gradient decreased and the growth rate increased along the preferred growth direction. The planar grain growth mode turned to cellular grain growth.

Nevertheless, the change in growth mode showed differently among these specimens.

In specimens of 2205 the cellular grains could directly grow from the planar grains without the formation of grain boundaries between the planar grains and the cellular grains, since the whole solidification process was dominated by δ - ferrite during cladding, as seen obviously in Figures 44 and 45. The two welding procedures could not make a significant difference for the appearance at the end of the transition zone. Only a thicker transition zone showed up in the high current welding.

In specimens of 309L series, the transition from the planar grain growth to cellular grain growth was

affected by the welding current. In the low current welding, the planar grains could only grow to a short distance from the fusion line, and the cellular grains grew from the grain boundaries of the planar grains in some regions, showing a grain boundary parallel and adjacent to the fusion line, the so-called Type II grain boundary. In the high current welding, the transition zone became wider. More martensite, bainite and acicular ferrite formed in this zone, with some strands of ferrite stretching upwards at the root of cellular grains. Type II grain boundaries still turned out in some places along the interface, the evidence of the inhomogeneity in a fusion welding with a strip electrode. The chance of finding a Type II grain boundary was reduced in the high current welding.

In specimens of 254SMO, more Type II grain boundaries showed up in both welding procedures. From Figure 53 it was seen that the staggered shape of Type II grain boundaries at the end of the transition zone gave evidence that there was a competition between the growth of ferrite and the growth of austenite. Due to the higher content of nickel in the alloy the transition from the initial δ - ferrite growth from the base steel to the γ - austenite growth of the weld metal took place shortly after the immediate epitaxial solidification from the stagnant layer right on the base steel.

In specimens of 904L, more nickel in the alloy made the initial solidification be γ - austenite. But the growth of γ - austenite would reject impurities dissolved in by mixing from the base steel during welding. When the amount of impurities rejected at the solidification front reached a certain level, the continuity of the γ - austenite growth would be disturbed by the segregation of these impurities. Then a layer of such segregation appeared between the initial grains and the cellular grains formed later. This gave the emergence of Type II grain boundaries in the overlay of 904L alloy as shown in Figures 54 and 55.

In the specimens of C-22 and 5923, the sharp appearance of the fusion line indicated that the growth of ferrite was totally stopped due to the very high nickel content in these alloys. There was still a planar grain growth stage at the initial solidification. The cellular grains of γ - austenite grew from the planar grains of γ - austenite without new nucleation and then without the Type II grain boundary. However, the mixing with the base steel also produced changes in the weld metal, especially where there was a high

dilution effect. As seen from Figures 57 and 59, segregates showed up along the grain boundaries in the specimens prepared by the high current welding.

6.5.2 Optical Microstructures in PWHT Condition

The precipitation of carbides along the interface between the base steel and the overlay and the recrystallization of ferrite in the base steel occurred in this region. The optical microstructures of specimens after PWHT were presented in Figures from 60 to 75.

At the base steel side, the lath-like structure of ferrite disappeared and the ferritic grains became equiaxed and larger after recrystallization and growth during PWHT. There was a non-precipitation region right under the interface at the base steel side, showing a distinct difference from the dark layer right on the interface.

The transition zone between the base steel and the overlay became more obvious after PWHT, since the precipitation of carbides and the decomposition of martensite or bainite made the microstructure more easily etched. The enrichment in carbon content along the fusion line gave an appearance of a dark layer at the interface and the acicular structures showed a gray band above the dark layer. Type II grain boundaries, if they existed in the as-welded condition, became more pronounced as the cellular dendrites readjusted their orientation with the planar grains during PWHT.

In PWHT condition the difference in width of the transition zone became noticeable. Usually the "band" was narrower in low current welding than that obtained by high current welding. Although the nominal linear heat input was the same for both welding procedures, the stronger arc force in the high current welding would stir up more base steel into the weld pool than the low current welding, resulting in deeper penetration and a thicker transition zone.

The compositions of overlays gave their contribution to the morphology of the interface. In the specimens of 2205, the planar grain boundaries were not found after PWHT. The thickness of the

transition zone could only be estimated by the extent of the dark and gray bands. In the dark layer it was the tempered martensite with dense precipitated carbides. The colonies of lath ferrite growing from the martensite layer appeared gray because of less carbide precipitation. In low current welding, the thickness of the dark and gray band was in the range of about 20 μm , while the band increased to 200 μm in the high current welding procedure. The lath of ferrite extended much longer from the fusion line toward the weld metal in the high current welding than that in the low current welding. After PWHT there was virtually no change in the microstructural features in the weld metal.

The appearances of specimens of the 309L series after PWHT were quite similar to each other. On the interface, there was a dark layer of tempered martensite with precipitated carbides like that in specimens of 2205. Clusters of acicular ferrite grew directly from the dark layer, showing the vestige of the original strand of austenite. The cellular dendritic grains turned gradually into equiaxed grains in the weld overlay, though the traces of dendrites were still faintly visible. Nevertheless, in some of the specimens Type II grain boundaries emerged as the border between the dendritic grains and the planar grains, especially in the specimens made by the low current welding. Type II grain boundaries in some cases were some distance away from the tips of the clusters of ferrite, and sometimes cut through the tips of the ferritic clusters. The addition of carbide-stabilizers, molybdenum and niobium, made no obvious difference in microstructure among these overlays of the 309L series.

In the specimens of 254SMO, Type II grain boundaries became more obvious. The cellular grains retained their original solidification pattern because of their high content of alloying elements. The precipitation layer of carbides on the fusion line appeared not as dark as that in the overlays mentioned above. It may be the influence⁸⁴ of nickel and molybdenum which promoted the formation of bainite and hence retarded the formation of martensite. In these specimens Type II grain boundaries in most locations were at a distance away from the tips of the clusters of acicular structure, and in some locations they extended into the acicular structure.

The microstructures in the specimens of 904L were similar to those in specimens of 254SMO. The

cellular structure in overlays of 904L was retained after PWHT. The precipitation layer showed almost the same appearance as those in specimens of 254SMO. Only the layer was narrower, reflecting the effect of nickel on the dilution.

The strong retardation effect⁸⁵ of nickel on the dilution and on the diffusion of carbon made the transition zone in the specimens of C-22 much narrower than those in other specimens. The dark layer on the fusion line only appeared like a string on which fine acicular structures extended merely a short distance from the fusion line. From the appearance of the faintly visible grain boundaries, cellular grains also tended to become granular after PWHT. These grain boundaries might reveal the traces of the planar grain boundaries formed during solidification. No obvious Type II grain boundary was found in specimens of C-22.

The higher dilution in the overlay of 5923 as compared to C-22 produced a thicker transition zone. The precipitation took place along the fusion line in a relatively larger scale. More inclusions from the base steel because of the high dilution increased the chance of segregation of impurities on grain boundaries. As a result, the grain boundaries were much more visible in the overlay 5923 as compared to specimens of C-22. In some locations this kind of grain boundary appeared like Type II grain boundaries.

6.5.3 Disbonding Phenomena

After the autoclave test disbonding of the overlay from the base steel happened in some of the specimens as mentioned in the results of ultrasonic examination. Observation with the optical microscope revealed the cracking paths details.

The disbonding in the specimen of 309LMo is shown in Figure 76. The crack traveled along Type II grain boundary. More cracks were found in specimens of 254SMO as seen in Figures from 77 to 80. All the cracks extended along Type II grain boundaries and sometimes wandered through the acicular structure. Seldom did the crack go through the dark layer of tempered martensitic structure, right on the fusion line. Disbonding in the specimens of 904L also took place along Type II grain boundaries as shown

in Figures 81 and 82. The extension of cracks might be retarded by the grain boundaries with tortuous shapes in that the crack was stopped at the turning point of the grain boundary. The cracks extended more easily along paths parallel or near parallel to the interface than along paths tilted at an angle, especially high angles, to the interface.

No disbonding was observed extending in the heat affected zone in the base steel although it was reported^{85,86} that the heat affected zone possessed the lowest fracture toughness.

No disbonding was observed in overlays of 2205 in which no Type II grain boundaries formed. Since the disbonding was related to Type II grain boundary, more Type II grain boundaries were found in the specimens of 309L series by the low current welding thus more disbonding happened after autoclave test. The specimens of 254SMO showed a similar tendency. Type II grain boundaries in overlays of 904L developed almost to the same extent in both welding procedures and seemed not to be significantly affected by the welding procedures. Thus disbonding was displayed to the same extent by both procedures. For high nickel alloys of C-22 and 5923, the higher dilution by the high current welding procedure caused more Type II grain boundaries with the segregation of inclusions on the planar grain boundaries, hence, the tendency toward disbonding increased. This phenomenon was just opposite to that occurring in specimens of 309L series, indicating a different mechanism for the formation of Type II grain boundary. The observations in the microscope were fully consistent with the results of ultrasonic examination on disbonding.

From the characteristics of disbonding along the Type II grain boundaries, the mechanism of the hydrogen induced cracking in this case is mostly possible under the control of hydrogen pressure theory. The relatively loose crystal structure in the grain boundaries may make it easy for hydrogen atoms to gather and turn to hydrogen molecules.

6.6 Observation on SEM and TEM

Some of the specimens were observed on the scanning electron microscope and transmission electron

microscope in order to reveal the detail microstructure formed during the whole experimental process. The most interesting portions of overlays were the microstructures right on the interface and Type II grain boundary.

The microstructure on the interface in the specimen of 2205 prepared by low current welding as observed on the SEM showed (Figure 83) that the cellular dendrites grew from the transition zone where lath martensitic structures of random orientation served as the structural pattern transition from the equiaxed grains in the base steel to the cellular grains in the weld metal. Further detailed observation on the TEM revealed a skeletal ferritic network structure in the transition zone as seen in Figure 84. Lathes of martensite were enveloped in the network of δ - ferrite adjacent to the fusion line. While the δ - ferritic network extended towards the upper part of the weld metal, the enveloped turned out to be retained γ - austenite. The orientation relationship between the δ - ferrite and the γ - austenite was Kurdjumov - Sachs relation: $(111)_{\gamma} // (110)_{\alpha}$ and $[011]_{\gamma} // [001]_{\alpha}$. After PWHT, the microstructures in the overlay appeared more complex. Carbides precipitated in the ex-martensite region and Mo - rich particles, π - phase, turned up in the skeletal δ - ferritic network as seen in Figure 85. The precipitation process in this kind of high alloy duplex steel is believed to be rather complicated⁸⁷. Further work is required to reveal the detail of the precipitation process in the overlay.

At the root of the interface between the base steel and the overlay of 254SMO, there was no obvious distinct line between them, as seen on SEM (Figure 86). The appearance of Type II grain boundary in Figure 87 showed the traces of growth mode change from planar grain growth to cellular grain growth. No precipitation was found in the as-welded condition. The observation by TEM as seen in Figure 88 found that there was a layer of fine martensite right on the interface. Above this fine martensite layer, a relatively coarse bainite ferrite structure developed within an extension about 30 μm (Figure 89). The extended acicular ferrite directly intruded into the austenite and dense dislocations wrapped the cluster of needle-like ferrite. No defined relationship in orientation was found between the ferrite and the austenite. After PWHT, carbides precipitated between the lathes of tempered martensite adjacent to the fusion line.

Fewer carbides were observed in the base steel nearby due to the strong attraction of molybdenum and chromium to carbon atoms which migrated from the base steel into the overlay. In Figure 90, EDX analysis on the SEM on a specimen of 254SMO, which was electrolytically etched for about half an hour, manifested that there was a spike of nickel content right across Type II grain boundary, where the structure was less affected by the etching than the area right under Type II grain boundary.

Observation at the root of the interface in the specimen 309LMo revealed lathes of martensitic structure extending from the fusion line towards the top of the weld metal as seen in Figure 91. The chemical composition analysis along these lathes by EDX on the TEM is presented together with this picture. The calculation of the EDX results was based on the non-standard sample method⁸⁸. From this microstructure and the chemical composition analysis it was conceived that the first solidifying phase was very likely to be δ - ferrite epitaxially growing from the stagnant zone. It was seen from Figure 69 that after PWHT carbides precipitated mostly along the interlathes, especially in the upper part of the ferritic lathes.

Observing the interface of the base steel and the overlay C-22 in the as-welded condition under high magnifications on the SEM revealed that there was a narrow layer of planar grains right on the fusion line as seen in Figure 92. In the planar grain layer subgrains with small angles between each other also showed up. Looking closely at the planar grain boundary as seen in Figure 93, the planar grain boundary was not flat as seen under an optical microscope, and some of the cellular grains could directly grow from the planar grains but some could not. EDX analysis on the grain boundary showed that the content of iron was higher than normal in the planar grain as shown in Figure 94. Due to equipment limitations, the carbon content on the boundary could not be determined. Observations of the same area on the TEM revealed that there was a layer of very fine martensite spanning the lattice pattern transition from the BCC to the FCC just on the interface as seen in Figure 95. This layer of fine martensite was only about 3 or 4 μm wide. At one side of this layer there were relatively coarser lathes of ferritic grains. At the other side there were large austenitic grains. Dense dislocations tangled around the tips of these fine

martensitic zones. On the planar grain boundary a layer of carbide of $M_{23}C_6$ type with the combination of chromium, iron and molybdenum was found during the observation on the TEM (Figure 96).

After PWHT the precipitation took place along the interfacial region in the overlay C-22. The microstructures turned out to be more intricate in the presence of high contents of nickel, chromium, molybdenum and tungsten. Large amounts of carbides precipitated along the interface between the base steel and the overlay, as seen in Figure 97. However, the carbides were different in the base steel side from those in the overlay. Coarse but sparse carbides of M_3C type precipitated under the interface in the base steel. Dense needle-like carbides of Mo_2C type showed up in the ex-martensite region in the overlay. As seen in Figure 98, less precipitation was found in the specimen C-22 by the low current welding procedure since less base steel was melted into the weld pool. Due to the large difference in composition across the interface it was extremely difficult to thin this layer to obtain a good image of this area on the TEM.

7. DISCUSSION

7.1 Introduction

As seen from the experimental results, all the three factors: accumulation of hydrogen, residual tensile stresses and the cracking-susceptible microstructure, have played their roles in the hydrogen induced disbonding. Before the hydrogen-charged autoclave test, there were no signs of disbonding among these specimens. For specimens with less difference in thermal expansion between the base steel and the overlay, the tendency of disbonding was less than those specimens with a large difference in thermal expansion between the overlay and the base steel. From the observation on disbonding phenomena in these specimens, cracks, if there are any, almost always take place along Type II grain boundaries. In specimens that have no or few Type II grain boundaries, the chance of disbonding diminishes and may even disappear. Therefore it is necessary to examine the three factors individually and see how they are related to promote the disbonding of the overlay from the base steel.

In the following discussions, the theories mentioned in Chapter 4 and the experimental results obtained from Chapter 6 are to be combined together to explain the role of each factor in the hydrogen related disbonding and to discover how they can be controlled to reduce the disbonding.

7.2 Hydrogen Accumulation in Type II Grain Boundaries

As it is seen from the experimental results in this investigation and others mentioned in the chapter of literature review, the hydrogen related disbonding of the overlay from the base steel in most cases takes place along the so-called Type II grain boundary within the overlay. The weld metals in the overlays of corrosion resistant alloys can grow, mostly epitaxially, from the stagnant layer on the top of the base steel without a distinct border microscopically. Martensitic, bainitic or acicular ferritic structures formed afterwards in the overlay during cooling down of the weld pool along the interface produce the transition zone. There are coarse grains in the heat affected zone in the base steel adjacent to the interface, and these are often martensitic grains due to the experience of high temperature and cooling rate. Normally, it is

believed^{7,89,90} that these kinds of structures are susceptible to hydrogen-induced cracking as this occurs in most high strength steels with martensite or bainite. Hydrogen accumulates in or near these structures due to the residual stress field developed by the solid transformation of these structures. However, in this case, hydrogen induced cracking does not occur in these structures but along the Type II grain boundary inside the overlay. In the literature survey, hydrogen was supposed to accumulate at the interface between the base steel and the overlay. The role of Type II grain boundary in the accumulation of hydrogen is to be evaluated by a modification on the original model mentioned in the review which gave the result of highest concentration of hydrogen at the interface. This modified model is based on the theory set up in Section 4.1.

In the modified model to evaluate the distribution of hydrogen in the overlay system, the trapping effect of crystalline imperfections on the hydrogen diffusion is taken into account in addition to the difference in crystal structure between the base steel and the overlay. Here only the grain boundary, particularly Type II grain boundary, which is parallel to the interface, is considered.

According to the trapping theory in Section 4.1, the diffusible hydrogen treated here is assumed without change of its atomic form and without chemical reactions during the diffusion and trapping process. By satisfying the continuities of chemical potential and mass flux at the boundary between the trapping phase and the matrix, the relation of the diffusion coefficients between the trapping phase and the matrix can be expressed as

$$D_{\text{trap}}/\gamma_{\text{trap}} = D_m/\gamma_m \quad (4-22)$$

where γ_{trap} and γ_m are the activity coefficients of hydrogen in the trapping site and in the matrix, respectively. If the trapping sites are taken as phases containing a certain amount of pores, the following relation^{91,92} can be established:

$$\gamma_m/\gamma_{\text{trap}} = 1 + 1.228 \times 10^{-3} V_{\text{pore}} \exp(6733/RT) \quad (7-1)$$

where V_{pore} is the volume percentage of pores in the trapping site, R is the gas constant (Cal./mole-K) and

T is the temperature in Kelvin.

By assuming the volume of pores in Type II grain boundary to be 0.5%⁹¹ and γ_m unity in the matrix, a computer program of finite difference method was written to solve the hydrogen distribution in the after-shut-down condition across the interface between the base steel and the overlay with austenitic structure. The computer program is attached in Appendix C. The initial and boundary conditions were determined from the steady-state operation of pressure vessels at the temperature of 450 °C and the hydrogen pressure of 15 MPa.

The result of this simulation is presented in Figure 57. It is seen that the highest concentration of hydrogen is now shifted to the position of the Type II grain boundary at a level of about 120 ppm after 30 hours of shut-down of the pressure vessel. Although this concentration is not as high as that obtained by the model without the consideration of the trapping effect, the hydrogen concentration at Type II grain boundary is much higher than that in normal welds, and is high enough to suggest disbonding of the overlay from the base steel with the combination of the residual tensile stresses. From the phenomenon of hydrogen induced disbonding, this modified model is better able to explain the accumulation of hydrogen in the overlay system.

For the overlay 2205, the accumulation of hydrogen may be not as severe as that in an overlay of almost fully austenitic structure since there is about 40% ferrite in the overlay by reference to the Schaeffler diagram⁹³. The similar diffusivity and solubility of hydrogen in the overlay 2205 to those in the base steel will reduce the accumulation of hydrogen. As there are no Type II grain boundaries in the overlay, the hydrogen will uniformly distribute across the whole section wall.

Along the interface of specimens of C-22 and 5923 there may be accumulation of hydrogen to some extent. However, less Type II grain boundaries, especially in the overlay C-22, serve as the trapping sites of hydrogen, hence the chance of disbonding is reduced. There might be some chance for the nickel to form hydrides in the existence of high concentration of hydrogen⁹⁴. But this kind of hydride is unstable

under normal conditions. Such hydrides can not be detected by the normal test techniques in this investigation. For the intermediate alloys such as 309L series, the chance of forming hydrides would be even smaller.

The evidence in this project shows that the disbonding phenomenon depends on the presence of Type II grain boundaries and that the actual bond rupture occurs intergranularly along these Type II boundaries, except for the rare occurrence of an extension of the crack into a local area of bainitic structure at the tip of the crack. Therefore the Hydrogen Pressure theory involving the formation of molecular hydrogen at a trapping site is consistent with the observed disbonding behaviour. The Beacham theory of localized plastic-flow induced rupture, which is more likely to apply to transgranular fracture, is less consistent with the observed features. The comments on the Beacham theory also apply to the decohesion theory. Therefore, the Hydrogen Pressure theory is the most probable cause of disbonding, although no direct proof is possible from this work.

7.3 Residual Stresses in Overlay

For the hydrogen induced disbonding, residual tensile stresses are required to promote the cracking along the interface, or along Type II grain boundary. The results of dilatometric test demonstrated (seen in Table 6) that there was a large difference in thermal expansion coefficients between the overlays and the base steel, especially overlays 254SMO and 904L. This is one of the reasons why there are many disbondings in these specimens.

During heating up, the thermal expansion of the overlay will be restrained by the base steel, since the overlay expands faster than the base steel due to its larger thermal expansion coefficient. So it is expected that there are compression stresses in the overlay, and that no disbonding will occur under such a compressive stress field. While the specimens are kept at high temperatures for a quite long time, the stresses in the overlays will be lowered by the diffusion process of atoms, for example, creep in the specimens. While cooling down the overlays shrink faster than the base steel. Tensile stresses will thus

develop in the overlay. These stresses cannot be released at low temperatures. Consequently, there are residual tensile stresses in the overlay and compressive stresses in the base steel.

The magnitude of the residual stresses is also affected by the cooling rates in addition to the difference in thermal expansion. Further work is required to analyze the detail of the cooling process to precisely determine the residual stresses.

Disbonding of the overlay does not take place in the heat affected zone in the base steel even though this zone contains a lot of coarse grains, and is predicted to possess the lowest fracture toughness across the whole section. It is the residual compressive stresses in this zone that makes this region withstand the hydrogen induced cracking.

Although lots of martensitic structures exist along the interface between the overlay 2205 and the base steel, the residual stresses in the overlay 2205 are expected to be small without any significant influence on the binding strength of the overlay to the base steel since there is only a small difference in thermal expansion coefficient between these two materials, and the thermal contraction of the overlay 2205 is even less than the base steel during cooling down. According to the bi-metal thermostat model, there are small compressive residual stresses, the maximum of which is approximately 40 to 50 MPa, in the overlay near the fusion line.

The low level of residual stresses in the overlays of C-22 reduces the chance of disbonding. Since the level of residual stress is proportional to the difference of the thermal expansion coefficient, the residual stresses in the overlay of C-22 are about one third of that in the overlay of 254SMO. The lesser amounts of martensite and Type II grain boundaries along the interfacial zone also lessen the severity of disbonding.

As for overlays of 309L series, 254SMO and 904L there are relatively high residual stresses along the interface, and these tensile stresses promote hydrogen diffusion into the interfacial region, especially in Type II grain boundaries where less dense structures could trap more hydrogen. The accumulation of hydrogen in Type II grain boundaries combined with the tensile stresses along the interface may greatly

reduce the binding strength of the overlay. As a result, large amounts of disbonding areas are produced in these specimens.

7.4 Microstructures in the Overlays

7.4.1 General Consideration of the Formation of the Interface Microstructure

For the welding of dissimilar materials, the solidification of the weld metal can be nucleated or grow epitaxially from the base metal since there is always a partially melted zone where the existing solid grains serve as the nuclei. Evidently, the observation on TEM shows that there is always a layer of martensite on the fusion line in all specimens. However, the continuous variation of the alloying elements in the transition zone from the fusion line towards the liquid weld metal will influence the growth of the weld metal, and, thereafter, the solid state transformation as well.

In normal fusion welding, the highest thermal gradient occurs at the edge of the fusion line and then the thermal gradient turns to decrease towards the centerline⁶⁶. Therefore, the critical constitutional supercooling condition cannot happen until the thermal gradient decreases to a certain level and the solute spike forms at the solidifying front. As a result, a planar grain growth takes place first during the initial transient build-up of solute. Until sufficient constitutional supercooling exists, the planar interface between the solid and the liquid will break down into the cellular growth mode. The microstructure along the interface of the specimens in this investigation is not excluded from the general model. Although the strip electrode and weld pool shape are different from the normal wire electrode, the fundamental process remains the same. It is seen from the observations on optical, electron scanning and electron transmission microscopes that there is always a planar grain zone just above the fusion line in all specimens. Nevertheless, the break-down of the planar interface into the cellular grain growth showed remarkable differences among these specimens. In some specimens, the cellular grains can grow directly from the planar grains in a preferred orientation without the formation of a border between the cellular grains and the planar grains, as seen in the specimens of 2205 by both welding procedures and C-22 by the low

current welding (Figures 42, 43, 49, 54 and 56). Yet, in some other specimens, the cellular grains could not grow directly from the planar grains, as seen in specimens of 309L, 254SMO and 904L (Figures 44, 46, 50 and 53), and a so-called Type II grain boundary turned up between the planar grains and the cellular grains. Afterwards, the cellular dendritic grains will grow along the preferred orientation to the end of the solidification since the decrease in the thermal gradient towards the centerline of the weld pool makes them easy to be maintained in the constitutional supercooled condition. These effects, since the weld pool configuration and heat flow conditions are virtually identical, are the results of solidification mode alternations caused by deposit compositional variations.

Due to the continuous change in the content of alloying elements, particularly the increase in the content of nickel, the strong austenite forming element, in the transition zone, and due to the continuous change in the cooling rate and the temperature gradient from the edge of the fusion line towards the molten area of the weld pool, a region of mixed microstructures will develop in the transition zone. At the root of the interface, a martensitic structure will form in the stagnant layer as a consequence of the fastest cooling rate and the mixing of the base steel with the overlay material. While the sharp increase in the nickel content and the successive decrease in the cooling rate at locations some distance away from the fusion line will progressively benefit the formation of other structures such as bainite, acicular ferrite and austenite according to the composition change and the cooling rate at that location. The extent of this mixed structure region is also dependent upon the welding procedure, as will be discussed below. Finally, in most of the specimens, the continuous increase in the alloying elements ahead of the solidifying front will stop the growth of non-austenitic structures and austenite turns out to be the prevailing phase towards the end of the solidification.

7.4.2 Formation of Type II Grain Boundaries

The observation on the disbonding phenomena in this investigation agrees well with the observations of other research groups^{6,11,14}: Disbonding in most cases takes places along Type II grain boundaries close to the fusion line at the overlay side. Therefore, it is vital to seek out the mechanisms

responsible for the formation of Type II grain boundaries in order to prevent the occurrence of disbonding. Since Type II grain boundaries locate in the overlay side adjacent to the fusion line, it is logical to assume that this structure must be connected to the solidification processes, i.e., the nucleation and growth of the weld metal, during welding.

Generally, the microstructures of the weld metal can be understood by consideration of the general theory of nucleation and growth behaviors of crystals in the Fe-Cr-Ni ternary system in a special welding process. There are two aspects affecting the formation of weld metals. One is the composition of the overlay and the base steel, and another is the welding procedure. In the case of welding dissimilar materials, welding procedure plays a more important part in the nucleation and growth during welding than that in similar materials welding.

7.4.2.1 Effect of Overlay Chemistry

The first step of the formation of the overlay of corrosion resistant alloys is the nucleation of the weld metal, and the nucleation of weld metal can be realized either by epitaxial growth from the base metal or by heterogeneous nucleation on the pre-existing surface of the base metal. It has been known that⁹⁵ the roughness of the pre-existing surface of the base metal, the chemical affinity between the base metal and the solidifying phase, and the crystal lattice discrepancy are three important factors affecting the nucleation efficiency during welding. In a fusion weld the surface roughness depends upon the grain size of the base metal and the welding procedures. In consideration of the chemical affinity, nickel and chromium, which are the main contents of the overlay materials, have good chemical affinity to iron, the main part of the base steel, since they can be combined together to form uniform solid solutions. Nevertheless, the body-centered cubic (BCC) structure of the base steel, which should be retained fully or partially at the high temperature as a hypoperitectic ferrite due to the presence of ferrite-stabilizing elements, chromium and molybdenum, and the low carbon level, may make it easy for the weld metals with a BCC structure as primary solidifying phase to nucleate or grow epitaxially from the base steel. As for the weld metals with different crystal structures from that of the base steel, it might not be so easy for them to grow epitaxially

from the surface of the base steel. There must be a transition to adjust the discrepancy between these two dissimilar crystal structures. So a distinctive interface between the base steel and the weld overlay appears, showing the change of lattice patterns across the fusion line.

By referring to the Fe-Cr-Ni ternary phase diagram⁹⁶ as shown in Figure 58, it is seen that the compositions of the materials chosen for the cladding locate around the 20% chromium line or an equivalent of about 24% Cr in this diagram. With the increase of nickel content the primary solid phase or phases in the specimens during solidification vary from δ , $\delta + \gamma$, to γ only. Other elements also have some influence on the primary solidifying mode. According to Lancaster³¹, the ratio of the equivalent amount of chromium to the equivalent amount of nickel will affect the solidification mode. If $Cr_{eq}/Ni_{eq} < 1.48$, the primary solidifying phase would be γ ; if the ratio is between 1.5 to 1.9, δ and γ would precipitate together from the liquid, basically by the peritectic reaction; and if the ratio is larger than 1.9, the primary solidifying phase must be δ , though it may transform fully or partially to γ during cooling down thereafter. Based on this assumption, the equivalent amounts of chromium and nickel of these specimens in this investigation are calculated, and the result is shown in Table 8. Accordingly, δ - ferrite was expected to be the primary solidification phase in the specimen 2205; $\delta + \gamma$ in specimens of 309L series, and γ - austenite in specimens of 254SMO, 904L, C-22 and 5923. This prediction is consistent with the alloys either of high nickel content, i.e., small Cr_{eq}/Ni_{eq} ratio, or of high chromium content, i.e., high Cr_{eq}/Ni_{eq} ratio. However, it may not be true for alloys with compositions close to the critical value, since this calculation is based on an equilibrium condition in the alloying system without the consideration of dilution effect in welding. Beside the existence of alloying elements in the weld metal, the dilution of the weld metal with the base steel will also influence the process during primary solidification. Therefore, these influences must also be considered in order to predict the primary solidification.

With the help of the Schaeffler diagram shown in Figure 59⁹⁷, it is possible to roughly predict the structure of a weld metal from the chemical compositions of the weld metal and the specific dilution effect in welding. Then, from the structure of the weld metal, the primary solidifying phase can be figured out.

By combining the effects of composition and dilution, the structures in each specimen can be estimated. In the weld metal of 2205 the microstructures locate in the region of A + M + F. The increase in dilution by the high current welding procedure will decrease the amount of austenite according to the diagram. The structures of weld metals in 309L series locate in the region including the boundary intersection of four structure zones: Austenite, A + F \rightleftharpoons M + F (δ) and A + M. The amount of martensite will increase with the dilution. In a low dilution, the weld metal structure in 254SMO is expected to be austenite only. The high dilution effect as a result of high current welding may give rise to the formation of martensite in the weld metal after cooling. There would be austenitic structure only in the weld metals of specimens 904L, C-22 and 5923 due to their high nickel content. But, as is known, the Schaeffler diagram is not an equilibrium diagram. Therefore, variations in cooling rate during welding are not taken into account for the microstructures. Particularly, the structures in the transition zone where a stagnant layer exists cannot be predicted by Schaeffler diagram. The Schaeffler diagram only gives the final possible structures but not the initial transient structure during welding. Also the morphology of the weld metal cannot be determined from the diagram although it is a valuable practical aid for the estimation of the weld metal structures. However, according to this diagram from which the final microstructures could be estimated, the initial primary solidifying phase or phases can be visualized.

Corresponding to the discussion above, the first solidifying phase or phases is δ - ferrite in overlays of 2205, δ + γ in overlays of 309L series and possibly in overlays of 254SMO, and γ - austenite only in overlays of 904L, C-22 and 5923. Consequently, the nucleation of weld metal of 2205 would be epitaxial without a distinct border between the base steel and the overlay. While the appearance of the border would be sharp between the overlay of C-22 and 5923, since the high nickel content in the overlay would stop quickly the possible growth of δ - ferrite from the stagnant layer and form new austenitic nuclei on the heterogeneous sites in the stagnant layer. The nucleation of weld metals of overlay 309L series and 254SMO may happen partially by growing epitaxially from the base steel and partially by forming new nuclei of austenite onto the surface of the half melted base steel. The content of nickel in the overlay 904L is not high enough to curb the growth of δ - ferrite as fast as those in the overlays of C-22 and 5923. So the

fusion line appeared a little bit wider than those in specimens of C-22 and 5923.

The lattice patterns of the primary solidifying phase are crucial for the formation of Type II grain boundaries with regard to the phase change of the solidifying phase at the solidifying front during solidification. For the overlay 2205, its content of chromium is so high that only δ - ferrite will form in the whole solidification process. γ - austenite can only be obtained in a following solid state transformation. The morphology of vermicular ferrite in the final structures is the evidence of such δ - γ transformation⁹⁵. The primary solidifying phase in C-22 and 5923 will be γ - austenite and it dominates the whole solidification process. The primary solidifying phases may be δ - ferrite in some locations and γ - austenite in other locations depending upon the extent of mixing of the overlay with the base steel and the local dilution level during welding. In the high current welding the diluted layer between the base steel and the liquid weld metal turns to be thicker due to the higher penetration of the stronger arc force. In this case the probability for the formation of δ - ferrite would increase since the higher dilution of weld metal with the base steel increases the chance for the crystals in the stagnant layer to assume the structure of the base steel. In consideration of the composition of 254SMO, which is close to the zone of $L + \gamma + \delta$ eutectic reaction in the ternary phase diagram, the dilution of weld metal with the base steel yields the chance for δ - ferrite to precipitate as the primary solidifying phase since the δ - ferrite may easily grow epitaxially from the stagnant layer on the base steel as compared to the γ - austenite which has to adjust its orientation to fit the transition of lattice pattern. The higher the dilution with the base steel, the higher the chance to form δ - ferrite at the initial transient stage of solidification. Although the initial solidifying phase will be γ - austenite in the specimen 904L, the content of nickel in the stagnant layer might not be high enough to fully halt the growth of δ - ferrite from the base steel. So the martensite layer right on the fusion line in this specimen was a little bit thicker than those in specimens of C-22 and 5923.

The growth mode of the solidifying phase directly determines the emergence of Type II grain boundaries. Two possibilities exist to explain the phenomenon of Type II grain boundary.

For alloys, as is known in the chapter of Theory, the growth mode of solidifying phase mainly

depends on the chemical composition of the weld metal, the cooling rate and the thermal gradient at the front of solidifying phase in the liquid metal. That is, the growth mode is governed by the constitutional supercooling condition. In dissimilar materials welding, the initial solids in the weld metal pool took the crystal pattern of the base steel and grew in the planar grain growth mode at the initial stage of solidification due to the dilution of weld metal with the base steel and the steepest thermal gradient at the edge of fusion line. The high thermal gradient also retards the growth of the initial crystals. So there is always a layer of planar grains extending some distance from the interface due to the high thermal gradient at the fusion line between the base steel and the liquid weld metal and the relatively slow growth rate. But the sharp variation in chemical composition from the base steel to the weld pool may compel the solidifying phase to change to another solidifying phase with a different lattice pattern for initial crystals. The solute rejection in the alloy solidification process also makes the solute pile-up at the front of the solidifying phase as discussed in Chapter 4. In specimens of 309L series and 254SMO, the slowly growing δ - ferrite at the initial stage of solidification rejected nickel to the planar solidifying front. The original high content of nickel in the alloys plus the rejected nickel from the solidifying δ - ferritic crystals makes the content of solute promptly reach the critical level for the change of solidifying phase. Once the level of nickel content reaches a certain magnitude, the solidifying phase would be thermodynamically forced to shift into another phase which was more thermodynamically stable. The original content of nickel will influence the extending distance of the δ - ferrite from the base steel. δ - ferrite will extend a shorter distance in the specimen of higher nickel content, showing a narrower transition zone. In this investigation, for alloys of 309L series and 254SMO, the first growing solid, δ - ferrite, is forced to change to the another solid, γ - austenite as the rejected nickel at the front of the initial δ - ferrite planar grains accumulates high enough to cause the phase change. As seen from the vertical profile of Fe-Cr-Ni ternary phase diagram⁹⁵ in Figure 60, the temperature gap between the liquidus and solidus of γ - austenite is larger than that of δ - ferrite. It means that the solidification of γ - austenite easily meets the constitutional supercooling condition as presented in Equation (4-40). Consequently, the solidifying phase change also increases the chance of the growth mode change from the planar grain growth to

cellular grain growth. The result of EDX examination on the specimen 254SMO as shown in Figure 68 gives the evidence of this phenomenon. This phenomenon was also reported by Lippold et al⁹⁸. It is the changes in the solidifying phase and the growth mode that give rise to the formation of Type II grain boundary. Hence, Type II grain boundaries emerge as the result of the mismatch of BCC and FCC structures during solidification. The following solid transformation turns the primary δ - ferrite into γ - austenite, and then the austenite transforms into martensite, bainite or is retained without change as the temperature drops. The formation of martensite and bainite depends on the local composition and cooling rate. The precipitation of carbides from the ex-martensite or ex-bainite might increase the strength difference between the overlay and the base steel, but it does not directly relate to the formation of Type II grain boundaries.

In the specimen 2205, δ - ferrite is the only solidifying phase without a phase change during solidification due to its high content of chromium. With the decrease of temperature, the δ - ferrite turns partially into austenite which may transform into martensite or is retained in the skeletal network of δ - ferrite as seen in the chapter of Results. Since there is no solidifying phase change in the overlay 2205, the cellular dendritic grains of the same crystal structure as the initial δ - ferritic crystals can grow directly from the planar grains along the preferred orientation without any signs of Type II grain boundary between the cellular grains and the planar grains.

Since the solidifying phase at the initial stage of solidification of specimens of 309L series may be either δ - ferrite or γ - austenite, the growth mode of the solids in the weld metal appeared differently at various positions along the fusion line. As there are δ - ferritic grains retained in the partially melted layer on the fusion line, δ - ferritic grains will be expected to grow / epitaxially from the existing δ - ferritic grains initially, and assume the planar grain growth mode due to the high thermal gradient. At locations where the composition is preferential for the growth of δ - ferrite in addition to the suitable thermal gradient, cellular grains can grow epitaxially from the planar grains without the appearance of Type II grain boundary. The cellular grains usually grow faster than the planar grains as they can proceed along

the preferred growth direction. As the temperature gradient gradually decreases towards the centerline of the weld pool, the cellular dendrites intrude into the liquid weld metal even faster until the enriched solute reaches the critical level. Consequently, the solidifying front breaks down from planar growth into staggered cellular growth. Thereafter, the γ - austenitic grains and the δ - ferritic grains grow alternatively as the rejected solutes gradually pile up at the front of the solidifying front until the end of solidification. The subsequent solid transformation of austenite at the interface will result in a mixed structure of martensite, bainite and acicular ferrite due to the continuous variation in chemical composition and cooling rate across the interface. The final structures show no distinctive boundary between the planar grains and the cellular dendrites at these locations. But, if the thermal gradient and the composition are not favorable for the cellular grain growth of δ - ferrite at the planar solidifying front, the low growing rate of the planar grains will increase the chance for the formation of Type II grain boundary. The slow growth rate of planar grains offers more time for the rejection of solutes at the solidifying front, and the pile-up of solutes at the planar solidifying front may stop the planar growth of the initial δ - ferritic grains once the solutes gather to the critical concentration for the formation of γ - austenite. The newly formed γ - austenite may retain the planar grain growth mode for a while, but the large temperature gap between the liquidus and the solidus for γ phase and the decrease of thermal gradient at a distance away from the fusion line give the γ - austenite more chance to grow in the cellular dendrite mode. Accordingly, Type II grain boundaries come into view as the borders between the planar δ - ferritic grains and the cellular dendritic γ - austenite. The initial δ - ferrite turns into austenite, and the austenite transforms into martensite, bainite or acicular ferrite as the temperature drops and time elapses. From the viewpoint of composition effect, this mechanism of forming Type II grain boundary is mainly responsible for overlays with chemical compositions in and close to the sector of peritectic and eutectic reaction in Fe - Cr - Ni ternary system.

The second possibility for the formation of Type II grain boundary is the pile-up of minor precipitates as a result of segregation to the solidifying front of the initial γ - austenite. The high content of nickel in specimens of C-22 and 5923 could stop the growth of δ - ferrite immediately on the fusion line, and there

was only a very narrow layer of transition zone which turned into martensite after cooling down to regulate the mismatch of the lattice patterns aside the interface as observed on the TEM. Like the other welds, the highest thermal gradient at the fusion line will give rise to planar grain growth at the initial stage of solidification in the cladding of high nickel alloys. But, the planar grains in this case are γ - austenite. Cellular dendritic grains of austenite can also grow epitaxially from the planar grains of γ - austenite without the transition of lattice patterns. In this case, there is no chance for the formation of Type II grain boundary. However, as is known^{99,100}, austenite has a much lower solubility for impurities such as oxygen, sulfur, phosphorus, and for ferrite-stabilizers such as silicon, molybdenum, tungsten than does the ferritic crystal structure. Some ferrite stabilizers are strong carbide formers (Mo, Cr, Cb, W) or inclusion formers (Si). These impurities and ferrite-stabilizers have a much stronger tendency towards segregation with austenitic solidification than they do with ferritic crystallization. The involvement of such elements in the weld metal can be caused by dilution with the base steel and the reaction with the flux. These elements may be rejected at the front of the solidifying phase, forming a film of some secondary phase as observed in Figure 54. These precipitates may be carbides, sulfides, oxides, etc., depending on specific dilution effect and local cooling rate. These nickel-bearing alloys have a remarkably low content of impurities due to their high quality and the diffusivity of such inclusion elements in the austenite is very low, so the segregation of the impurities may take place at a very low content^{101,102}. But this film of precipitates ahead of the solidifying front of the planar austenitic grains could possibly disturb the epitaxial growth of the cellular dendritic grains from the planar grains. Consequently, Type II grain boundaries may form as the precipitates disturb the transition from planar to cellular growth of austenite very close to the interface. Therefore, the appearance of Type II grain boundaries in the high nickel overlay is different from those formed by the first proposed mechanism. Type II grain boundaries formed by the first mechanism appear relatively flat and parallel to the interface, while Type II grain boundary in the high nickel overlay shows more curves since the cellular dendrites of austenite should be easy to grow from the planar grains of the same structure, and the tendency to form cellular dendrites is high for γ - austenite. According to this mechanism, the more the impurities in the weld metal the more the Type II

grain boundaries there would be. The experimental results showed that the high dilution of weld metal with the base steel gave rise to more Type II grain boundaries, thus more severe disbonding after the hydrogen autoclave test. After cladding, a segregation zone was introduced adjacent to the fusion line, and this segregation layer acts as the trapping sites for the accumulation of hydrogen in the autoclave test. In addition, the initially formed Type II grain boundaries also provide sites for the precipitation of carbides and other inclusions during PWHT. Thus hydrogen induced disbonding takes place along these segregated boundaries. The higher extent of dilution in the specimen 5923 by the high current welding gave more chances for the formation of an impurity film near the fusion line, appearing as a Type II grain boundary, as observed in Figure 53. Subsequently, more disbonding was revealed in this specimen.

In the overlay 254SMO, Type II grain boundaries may develop on the basis of the first mechanism. Its nickel content was not high enough to curb the δ - ferrite growth at the initial stage of the solidification in consideration of dilution with the base steel. The planar grains of δ - ferrite would form on the fusion line. A sharp increase in the content of nickel at the edge of the planar solidifying front increased the chance for the formation of Type II grain boundary as compared with specimens of 309L series. On the other hand, its chromium content is not high enough to promote cellular dendrites growing directly from the planar δ - ferritic grains. The content of molybdenum in the alloy 254SMO increases the chance to form bainite in the transition zone when the alloy was mixed with the base steel during welding. The coarse bainitic structure found by observation at the transition zone of the overlay 254SMO on the TEM showed the effect of the existence of molybdenum in the overlay. The observation on Type II grain boundary in the specimen 254SMO showed no significant segregation on Type II grain boundary as seen in Figures 85, 86, 87 and 88. However, the microstructure apart from the Type II grain boundaries has some differences. In the planar grain side, the grains appeared coarser than those in the cellular grain side.

As for the 904L alloy, the formation of Type II grain boundary may be attributed to both mechanisms. Its nickel content is not as high as C-22 and 5923 and 904L thus cannot stop the growth of δ - ferrite right on the fusion line. But, its nickel content is high enough to reduce significantly the chance for extensive

growth of δ - ferrite as cellular grains in the liquid weld metal directly from the planar δ - ferritic grains at the interface. Therefore, the transition zone in this overlay was wider than those in specimens C-22 and 5923, but narrower than those in specimens 309L series and 254SMO. From the phenomena of the formation of Type II grain boundary in these specimens, it is seen that high current welding will reduce the chance for the formation of Type II grain boundary under the first mechanism but increase the chance for the formation of Type II grain boundary under the second mechanism as comparing the specimens 309L series with the specimens C-22 and 5923. That the disbonding appears to be almost the same by both welding procedures for the specimen 904L is the result of the first mechanism playing a major role in the low current welding and the second mechanism having more influences in high current welding.

In addition to the functions of chromium and nickel, the major compositions of the overlays, other alloying elements also played some role in the formation of Type II grain boundary. Among them the amount of carbon takes a major role. Less carbon in the base steel makes it possible for the base steel to retain BCC structure at high temperatures for a longer time as the temperature drops at the initial stage of solidification. Less involvement of carbon in the weld pool may reduce the formation of Type II grain boundary by increasing the chance to form cellular δ - ferritic grains from the planar grains and by reducing the precipitation of carbides on the planar grain boundary. Molybdenum is a ferrite-forming element in ferrous alloys. The existence of molybdenum in the overlays increases the chance for the precipitation of δ - ferrite from the liquid weld metal. This may be used to explain why there is a larger transition zone in the overlay 5923 than that in the overlay C-22. Molybdenum can form some complex metallic compounds too such as χ and π phases in the Fe - Cr - Ni ternary system. But their effects on the formation of Type II grain boundary and disbonding may not be as pronounced as the effects of chromium and nickel. As seen from the observation of the specimen of 2205, π -phase locates in the ferritic network. The relatively high contents of phosphorus and sulfur in alloys 254SMO and 904L also increase the possibility for the formation of Type II grain boundary and disbonding as well. Manganese is a weaker austenite former as compared to nickel and it can increase the hot cracking resistance by forming sulfide with sulfur. When Mn is combined with the low alloy steel, the hardenability may be increased, i.e., more

martensite forms in the transition zone. The addition of strong carbide-forming elements such as molybdenum or niobium in 309L stainless steel does not significantly influence the formation of Type II grain boundaries. From the observation on the disbonding, the precipitation of carbides on the Type II boundary was not a major cause for cracking. In other words, the addition of carbide-forming elements does not measurably alter the incidence of the disbonding in 309L alloys.

In addition to the influence of overlay chemistry on the formation of Type II grain boundary, the occurrence of Type II grain boundary is strongly dependent upon the supercooling conditions in the overlays. The difference in disbonding phenomena among the specimens by different welding procedures is the evidence of this effect. The extent of constitutional supercooling condition is also determined by the welding condition.

7.4.2.2 Effect of Welding Procedure

Welding procedures influence the solidification process of the weld metal by adjusting the magnitude of dilution, hence the chemical composition in the weld pool, by controlling the dynamic thermal field in welds and by regulating the cooling rates of the weld metal. Therefore the nucleation and growth of the crystals in the weld metal will also depend to a large extent upon the welding procedures.

In the case of high current and high speed welding, more base steel in volume is mixed into the weld pool with the overlay materials due to the deeper penetration effect under the more fierce arc force. The thickness of the diluted layer would also be increased as seen in the microhardness test and under the metallographic observation. The chance for the formation of δ - ferrite as the initial solidifying phase increases as a result of the chemical composition in the stagnant layer being close to that of the base steel and new δ - ferritic grains are easy to grow from the stagnant zone with the similar composition and the same crystal structure. This effect is particularly obvious in specimens with compositions in and close to the $l + \delta + \gamma$ sector in the Fe - Cr - Ni ternary phase diagram, because the solidifying phases, δ and γ , in these alloys will compete with each other during growth. In a high dilution of the weld metal with the

base steel, the growth of γ - austenite may be delayed as a consequence of the favorable condition for the growth of δ - ferrite at the initial stage of solidification. Moreover, the high current and high speed welding will result in high rates of heating-up and cooling-down. The nucleation rate or the epitaxial growth rate of crystals in the weld metal increases as a result of the two high rates. Thus the configuration of grain structures in the specimens obtained by the high current and high speed welding appears finer than that in the specimens obtained by the low current and low speed welding despite of the same linear heat input in the overlays.

As mentioned above, the growth behavior of crystals in the weld metal during solidification is vital for the formation of Type II grain boundary. As is known⁹³, the possible growing modes of crystals in weld metal can be classified as planar growth, cellular growth, columnar dendritic growth and equiaxial dendritic growth. In an alloy system the growth mode of crystals in the weld metal is mainly determined by the extent of constitutional supercooling condition as expressed in Equation (4 - 40). By assuming that the slope of the liquidus curve at the concentration points of specimens is linear in the Fe - Cr - Ni ternary system, this expression can be simplified as¹⁰³

$$\frac{G_i}{R} \leq \frac{\Delta T_o}{\bar{D}_i} \quad (7-2)$$

where ΔT_o is the temperature interval between the liquidus and the solidus at the nominal concentration of the overlay material, and \bar{D}_i is the average diffusion coefficient of solutes in the liquid weld metal since $-p\Delta C = \Delta T$. According to the thermal analysis¹⁰⁴, the steepest temperature gradient occurs at the surface of the base steel while the liquid metal from the electrode just drops on it. Consequently, the crystals nucleating on the surface of the base steel can only grow along the surface of the base steel in the planar mode as schematically shown in Figure 61. Due to the high temperature gradient ahead of the solidifying front the growing rate of the crystals is slow near the interface region. So the initially formed crystals almost always grow, more or less, in the planar growth mode.

The welding procedures may influence the time for planar grain growth. The temperature and the

temperature gradient at the edge of the interface between the base steel and the weld metal in the weld pool in the high current and high speed welding would decline in a shorter time than those in the low speed welding, since the heating source moves at a higher speed and the cooling rate is high. The decline of the temperature gradient makes it possible for the liquid metal ahead of the solidifying front to meet the constitutional supercooling condition, and thus leads to the break down of planar growth. If the planar grain growth breaks down a short time after the beginning of the solidification, the pile-up of solutes at the solidifying front may be not high enough to turn the initial crystals into another kind of crystal due to the chemical composition. On the other hand, the low current and low speed welding will allow the planar growth to develop for a longer time because the slow moving heating source makes the temperature gradient take longer time to decline. Then the austenite stabilizing solutes will not be trapped into the solidifying crystals and can accumulate at the solidifying front due to the slow growing rate of the planar grains. This phenomenon has been discussed in the chapter of Theory on the formation of solute "band" in welds as shown in Figure 20. Therefore the tendency of the formation of Type II grain boundary increases with the decrease of welding speed if the heat input is kept at the same level. This phenomenon is particularly apparent in specimens 309L series and 254SMO since their initial crystals growing from the half melted and half solid zone in the solidification process is possibly δ - ferrite and this δ - ferrite growth is going to be replaced by the γ - austenite growth after the accumulation of solutes, especially nickel, reaches the critical level for this change. As discussed above, the shifting of the solidifying phase from the δ - ferrite to the γ - austenite at the planar grain boundary will give rise to the emergence of Type II grain boundaries.

While the crystals grow towards the top of the overlay and the centerline of the weld pool, the temperature gradient in the liquid ahead of the solidifying front will decrease because of the moving away of the heating source and the release of the latent heat as a result of the formation of solid phases. The growth rate will increase as a consequence of the drop in thermal gradient and the readjustment of preferred growth orientation. The growth direction of crystals is opposite to the heat flow direction. Thus the upper part of the weld metal shows the structures of cellular dendrites and columnar dendrites which

bend towards the welding direction.

For the overlay 2205, the primary solidifying phase will be δ - ferrite only through the whole solidification process and the transformation of $l \rightarrow \delta$ cannot be affected by the welding procedure since the ratio of chromium to nickel is so high in this alloy that no austenite will directly precipitate from the liquid metal. Furthermore, the narrow temperature interval between the liquidus and solidus of $l + \delta$ zone in Fe - Cr - Ni ternary system as seen in Figure 60 shortens the solidification time so that nickel content cannot accumulate high enough at the solidifying front in a short time to shift the solidifying crystals to the austenitic structure. From the observation on microscopes, the border between the base steel and the overlay is not as sharp as that in other specimens. The same crystal structure of the overlay and the base steel during the solidification makes the transition smooth. The skeletal δ - ferritic network enveloping martensite and austenite in it in the interfacial region at the room temperature shows the evidence of transformation during cooling. High penetration in high current welding results in a thicker transition zone in the overlay. As a consequence, there is a thicker layer of martensite lying on the interface. This transition zone also shows the trace of planar growth at the initial stage of solidification without exception. However, the cellular grains growing epitaxially from the planar grains leave no signs of border between the planar grains and the cellular grains. The welding speed increases the cooling rate of the weld metal so that finer grain structures are expected. The subsequent solid transformation, $\delta \rightarrow \gamma$, in the weld metal gives the appearance of vermicular ferrite.

The microstructures in the 309L series are obviously affected by the welding procedures. In the high current welding, the high dilution of the weld metal with the base steel increases the chance for the δ - ferrite to grow as the first solidifying crystals, since the composition in the partially melted zone is close to that of the base steel as a result of more base steel dilution. The fast cooling rate and the fast decline of the temperature gradient at the edge of the solidifying front in high speed welding yields more chances for the liquid weld metal in the weld pool to meet the constitutional supercooling criterion. The accumulation of solutes at the solidifying front is also reduced by the high cooling rate. Therefore, the planar growth mode

will break down more easily in the high current and high speed welding procedure without the formation of Type II grain boundaries as compared to low current and low speed welding. On the other hand, the dilution of weld metal with the base steel will be low and the cooling rate of the weld metal will be low as well if the overlay is clad by the low current and low speed welding procedure. The low dilution means that the chemical composition in the weld pool is close to the original alloy, whose high nickel content will favor γ - austenite as the first solidifying crystals. The low cooling rate causes less trapping of the austenite stabilizing elements in the growing ferrite, thus allowing the solutes to diffuse to and accumulate at the solidification front. Accordingly, the accumulation of nickel at the front of the slowly growing planar δ - ferritic grains would stop the growth of the δ - ferrite and cause the change of the solidifying phase. Thus, Type II grain boundaries come into view as the evidence of such change in the solidifying phase. The newly formed austenite may retain the planar growth for a while and then turns into cellular growth mode as the temperature gradient decreases at the edge of the solidifying front. The initial δ - ferrite adjacent to the fusion line changes into austenite and the austenite transforms to martensite, bainite or is retained without change as the temperature drops to ambient. Due to the continuous variation in chemical composition across the interface, the microstructures show different configurations with the distance away from the fusion line. Right on the fusion line there is a layer of fine martensitic structure which turns a dark color after PWHT and etching. Adjacent to the fine martensite is the coarse bainitic structure with an appearance of bunches of acicular ferrite. Since the content of nickel becomes higher and higher towards the top of the overlay, at some locations a retained austenitic layer lies between the tips of acicular ferritic bunches and Type II grain boundary. The acicular ferrite can even show up across Type II grain boundary at some locations where the cooling rate may be high. However, Type II grain boundaries, once formed, stay between the planar grains and the cellular grains. Type II grain boundaries subsequently serve as the trapping sites for the accumulation of hydrogen, and become the most susceptible structure to disbonding. The high current and high speed welding can improve the resistance of the overlays of 309L series to the hydrogen induced disbonding but it cannot get rid of this disbonding, since there are still some Type II grain boundaries in the overlays produced by high current and high

speed welding. The appearance of such Type II grain boundaries may be the result of the temperature distribution being non-uniform and the temperature gradient in the center being not as high as it is at the edge of the weld pool as discussed in the chapter on Theory.

For the overlay 254SMO, the higher content of nickel in this alloy than that in alloys 309L series makes it more difficult for the δ - ferrite to grow cellularly from the initial planar δ - ferritic grains. On the other hand, the content of nickel in this alloy is not high enough to stop the growth of δ - ferrite at the initial stage. The high current and high speed welding may reduce the chance for the formation of Type II grain boundary by stirring up more base steel into the weld pool. But the result will not be as obvious as that in the 309L series due to its high nickel content.

The even higher content of nickel in alloys C-22 and 5923 makes the epitaxial growth of δ - ferrite grains from the initial planar δ - ferritic grains totally impossible. The high content of nickel in these alloys can cause γ - austenite to grow directly from the base steel. But the dilution of the weld metal with the base steel makes this growth occur unevenly along the interface. Since the austenitic grains grow from the partially melted zone on the fusion line, elements from the base steel may be rejected by the solidifying austenitic crystals. These segregates produced in the weld pool owing to dilution may appear at the solidifying front due to the low solubility of some elements in austenite. These rejected elements at the solidifying front may disturb the continuity of the austenitic growth and a boundary comes out to show the discontinuity of the austenitic growth. The observation and EDX analysis on the boundary showed $M_{23}C_6$ type carbide of the combination of chromium, molybdenum and iron. The initial growth of austenitic grains has to be kept in the planar growth mode due to the high temperature gradient at the edge of the fusion line. As a result the boundaries formed by the disturbing of impurities usually become visible near the fusion line. In high current welding more impurities from the base steel are expected to be involved into the weld pool, so more boundaries would appear near the interface. This kind of boundary may behave like the Type II grain boundary mentioned above. That is, they can trap hydrogen during service in an environment of high pressure of hydrogen. Therefore, the formation of Type II grain boundaries in

high nickel alloys is caused by the disturbing effect of segregates on the growth continuity of austenite.

The formation of Type II grain boundaries in the specimen 904L may happen by both mechanisms. Its high nickel content can fully curb the growth of δ - ferrite from the planar grain but not high enough to initiate γ - austenitic epitaxial growth directly from the half melted and half solid zone in the whole range of weld pool. Which mechanism plays the major role responsible for the formation of Type II grain boundary needs more work. The first mechanism may have more influence in the low current welding while the high current welding may cause more Type II grain boundaries under the control of the second mechanism. The chemical composition of this alloy may just locate in the critical range, so the experimental results on the disbonding seem quite scattered. Varying dilution due to change in arc residence time across the width of the overlay makes this scatter even more pronounced.

7.5 Disbonding of Overlay

From the discussion above, it is seen that the concentration of hydrogen can reach as high as 120 ppm at Type II grain boundaries if the overlay is assumed to be an austenitic structure. This concentration is much higher than the critical concentration in a normal welding environment which is usually less than 10 ppm¹⁰⁵. Under a tensile stress field this concentration may be even higher. In this situation it is very likely for hydrogen to accumulate in the less dense zone such as Type II grain boundary to form hydrogen gas with high pressures. Consequently, cracking takes place by the "blister" effect of hydrogen.

Hydrogen induced cracking takes place only in a tensile stress condition. Without the tensile stresses, the coarse grain zone in HAZ under the interface shows no sign of cracking although it is reported to have the lowest fracture toughness.³⁶ In the overlay system, the residual tensile stresses may be reduced by a very slow cooling rate from the working temperature. But it usually cannot be realized in practice. Sometimes a high cooling rate is necessary, such as in an emergency. This will result in higher residual tensile stresses in the overlay. Another possible solution for this problem is to choose a clad material with a thermal expansion coefficient similar to the base steel. However, this kind of material may not be able to

meet the criterion for the corrosion resistance.

The microstructures along the interface are another controllable factor to prevent the hydrogen related disbonding. As seen from the disbonding phenomena, cracking in most cases takes place along the Type II grain boundary, and sometimes extends into the bainitic structure region. Seldom do the cracks penetrate the dense martensite layer in the base steel. After PWHT, there is usually a dense precipitation of carbides in the original martensite region of the transition zone. During PWHT carbon atoms move from the base steel towards the overlay since most of the overlay alloys contain chromium and molybdenum, stronger carbide-forming elements than iron, and austenite possesses a higher solubility for carbon than ferrite does. This results in a spike of hardness in the precipitation region in the transition zone located below Type II grain boundary and a valley of hardness in the heat affected zone adjacent to the fusion line. The sharp change in the mechanical properties across the interfacial region from the base steel to the weld metal may also have some influence on the formation and propagation of the disbonding. These precipitates in the transition zone may serve as trapping sites for the hydrogen too. Since they distribute uniformly in this zone, the possible highest concentration of hydrogen in a certain site is reduced. The coarse grains and carbides in the heat affected zone in the base steel adjacent to the fusion line also have low fracture toughness. Cracks may happen in this region if they are under tension as reported by Gittos³⁸. However, cracking does not take place in this region in this test owing to the compressive stresses in this region. Therefore, the most susceptible microstructure to the hydrogen induced disbonding is the Type II grain boundary. The bainitic structure near Type II grain boundary possesses low resistance to the disbonding as it is seen that cracks sometimes wander into this structure. Ferrite has relatively high resistance to disbonding since the crack stops at the intrusion of base steel at the interface. This may reflect the effect of surface roughness of the base steel on the disbonding.

The occurrence of disbonding, if any, in most coupons takes place near the middle of the clad surface not at the edge as predicated by the thermostat model. There are a few possibilities here. There are probably more Type II grain boundaries in the central region of the coupons (also the central area during

cladding) due to a slower cooling rate than exists at the edges. In addition, if hydrogen molecules accumulate on the Type II boundaries, the gas pressure would increase tensile stresses in the central region. Few Type II boundaries and less accumulation of hydrogen near the edges of the specimens due to a faster cooling rate and due to the release of hydrogen to the atmosphere make the bonding strength higher at the edges than that in the middle of the clad area.

Eliminating the emergence of Type II grain boundary is the most effective method to minimize the hydrogen induced disbonding. This can be achieved in two ways. One is to select suitable materials such as the duplex steel 2205. It was reported¹⁴ that applying a butter cladding of extra-low carbon steel before the overlaying of stainless steel on the base steel would reduce the chance for the formation of Type II grain boundary. The explanation to this phenomenon should be that the low carbon steel will solidify as δ -ferrite first, the same crystal structure as the base steel. The chance for the formation of δ -ferrite as the primary crystal will be increased for the second stainless steel layer of 309L. Another way is to choose a well tuned welding procedure. The welding parameters should be chosen on the basis of the chemistry of the overlay materials and the base metal. Since there are large variations in the chemistry of corrosion resistant alloys, it is obvious that more research is needed on the effect of welding for a specific problem.

The higher sensitivity of the 5923 alloy in comparison to the C-22 alloy and the fact that even the C-22 alloy is not immune to some disbonding induced by dilution give a sufficient notice that welding procedural variations are critical. Only the 2205 alloy appears immune, at least, for the parameters used in this study.

8. SUMMARY AND CONCLUSIONS

8.1 Summary

From the experimental results and the discussion above, it is clear that there are three major factors contributing to the hydrogen induced disbonding of the overlay of corrosion resistant alloys from the base Cr - Mo low alloy steel. Firstly, due to the differences in solubility and diffusivity of hydrogen between the austenitic structure of the overlay and the ferritic structure of the base steel and the trapping effect of imperfections in weldment, the hydrogen accumulation in Type II grain boundaries parallel and close to the fusion line between the base steel and the overlay is a necessary condition for the occurrence of disbonding. Next, disbonding propagation needs a tensile stress field. The highest residual tensile stresses develop in the overlay during cooling down from high temperatures to ambient temperature due to the difference in thermal expansion coefficient between the base steel and the overlay. Compressive stresses develop in the HAZ of the base steel, protecting otherwise susceptible, low toughness microstructures from disbonding. Finally, the most susceptible microstructure to hydrogen induced disbonding, Type II grain boundary in this specific environment, may appear as a result of either a phase change during solidification of the weld metal due to the solute "banding" effect in an alloy system or the disturbing effect of precipitates on the growth continuity of solidifying phase due to the dilution of weld metal with the base steel. This grain boundary is also parallel to the interface and is in the tensile stress field.

The controllable determinant for the prevention of disbonding is the microstructure in the interfacial region between the base steel and the overlay. The microstructures developed in this region are determined by the composition of overlays and the welding procedures. If the primary solidifying crystal of the overlay is δ - ferrite, the same as that of the primary solidifying crystals in the base steel, the chance of forming a Type II grain boundary is almost totally eliminated. This occurs in the specimens of 2205. If the content of nickel in the overlay is high enough to curb the growth of δ - ferrite at the initial stage of solidification, the low current welding procedure may reduce the chance for the emergence of Type II grain boundary. This happens in the specimens of C-22 and 5923. For alloys in which the primary

solidifying crystals are δ and γ together, or δ followed by γ . the welding procedure of high current and high speed will increase the chance for the δ - ferritic grains to grow cellularly from the planar ferritic grains. Hence the chance for the formation of Type II grain boundary is minimized and so is the disbonding. But the tendency to form Type II grain boundary is still there due to the chemical composition of these alloys. The local variation in dilution due to arc wander also influences the formation of the Type II grain boundary.

Disbonding in most cases takes place along Type II grain boundaries. Sometimes cracking wanders into the bainitic structure which locates above the martensitic structure, seldom stretches farther into tempered martensitic structure adjacent to the fusion line and stops at a ferritic structure. Without Type II grain boundaries in the overlay, no disbonding is found.

8.2 Conclusions

Based on the experimental results and the discussions above, several conclusions can be drawn:

1. Disbonding of the overlay of corrosion resistant alloys from the base Cr - Mo low alloy steel takes place only in the co-existence of three factors: hydrogen accumulation to a certain level in the overlay, residual tensile stresses and a crack-susceptible microstructure.
2. Analysis of the effect of Type II grain boundaries on hydrogen diffusion demonstrates that hydrogen will concentrate to the highest level in the Type II boundaries, not at the cladding-base metal interface, as proposed by other investigators.
3. The most probable mechanism of disbonding at the Type II grain boundaries is hydrogen pressure developed by the conversion of atomic hydrogen to molecular hydrogen in the boundary. Theories involving decohesion, hydride formation and localized plastic flow are less consistent with the observed intergranular nature of the disbonding phenomenon, with any transgranular cracking restricted to occasional extension of intergranular Type II boundary disbonding into bainitic regions adjacent to the

primary disbonding areas.

4. Tensile residual stresses will develop in the overlays which have a larger thermal expansion coefficient than the base steel during cooling down from high temperatures to ambient temperature, while compressive stresses occur in the base steel adjacent to the interface. These residual tensile stresses in both directions parallel to and perpendicular to the interface promote hydrogen diffusion to the interfacial region of the overlay and accumulation in the Type II grain boundary. As a result, the bonding strength of the overlay to the base steel, is severely reduced. Analysis of the state of stress in the clad joint based on experimental thermal measurements of actual interface material has shown that there is substantial tensile stress near and perpendicular to the interface. The magnitude varies with the chemistry of the cladding alloy and correlates very well with the amount of disbonding observed.

5. The standard industrial cladding of type 309 stainless steel has been shown to be very prone to disbonding, due to the mixed α - γ solidification mode, which is inclined to form Type II boundaries. Modification of the chemistry by the addition of molybdenum or niobium has no discernable effects.

6. Alloys 254SMO and 904L are even more prone to disbonding, due to the large amount of Type II grain boundaries produced by their higher nickel chemistry and to the larger difference in thermal expansion coefficient from the base steel.

7. High nickel alloys, C-22 and 5923, minimize Type II boundary formation due to an early forced change to a fully γ solidification mode. Minor amounts of Type II boundary are formed in the presence of segregates, notably carbides.

8. Duplex stainless steel cladding of 2205 eliminates Type II grain boundaries and disbonding due to a fully ferritic epitaxial solidification mode.

9. The so-called Type II grain boundary, parallel to and close to the fusion line between the base steel and the overlay, is confirmed as the microstructural feature most susceptible to hydrogen induced

disbonding. In addition, the coarse acicular bainitic structure between Type II grain boundary and the fine tempered martensitic structure on the fusion line has low resistance to the propagation of cracking. The fine tempered martensitic structure on the fusion line is relatively less sensitive to hydrogen induced disbonding. Carbide precipitation is not directly related to the formation of Type II grain boundaries and does not obviously influence the bonding strength, at least for low carbon levels. Low toughness structures in the base steel, even the coarse-grained heat affected zone, are free from cracking due to the compressive stress state in this region. The unstable austenitic structure near the interface due to the dilution with the base steel forms bainitic structures which can extend cracks initiated in Type II grain boundaries, but this microstructure is unlikely to initiate disbonding.

10. There are two mechanisms responsible for the formation of Type II grain boundary. One is the solidifying crystal change from δ - ferrite to γ - austenite during the solidification as a result of solute accumulation at the solidifying front. Another is the disturbing effect of segregates on the growth continuity of the solidifying crystals, which appear in the weld pool due to dilution with the base steel and by rejection from primary austenite .

11. The welding procedure of high current and high speed will reduce the chance to form Type II grain boundary in overlays with primary solidifying crystals as $\delta + \gamma$, but will increase the chance to form Type II grain boundary in overlays with higher nickel contents. No Type II grain boundary forms in the overlay 2205 by either welding procedure due to its primary solidifying crystals being the same as those of the base steel. Less Type II grain boundaries means less disbonding in the overlay.

9. SUGGESTIONS FOR FURTHER WORK

It is clear that the bonding strength of the weld overlay with the base steel is strongly affected by the microstructure along the interfacial region. As seen above, there are two ways to improve this property. One is to apply a nickel based alloy such as C-22 with a suitable welding procedure. The welding procedure needs to be fine tuned to achieve an optimum result. Corrosion tests and hydrogen induced cracking assessment are needed to investigate whether a single pass cladding is possible to replace the double-pass cladding of 309L+347 alloys, the mostly employed cladding process. There is an economic balance between the high nickel alloy of high price and a single cladding pass and a relatively cheaper stainless steel but two passes. The real cost may be reduced by applying a single pass of high nickel alloy.

Another way is to apply duplex stainless steel such as 2205 as the cladding material. The producer of this alloy (Sandvik) claims¹⁰⁶ that this alloy has a high corrosion resistance to hydrogen sulphide and chloride-bearing corrosive media. However, further work is required to investigate if the duplex stainless steel can stand the vicious environments encountered in the petrochemical industries.

Due to their high content of alloying elements, these alloys may result in the possibility for the formation of some special metallic compounds after service at high temperatures for a long time. This kind of effect on the bonding strength of overlay needs to be clarified.

Table 1 Chemical composition of base steel, wt. %

C	Si	Mn	P	S	Cr	Ni	Mo	Cu	V	Ti	Fe
0.125	0.547	0.51	0.005	0.014	1.279	0.206	0.49	0.171	0.005	0.001	bal.

Table 2 Chemical compositions of alloys used as cladding materials, wt. %

element	2205	309L	309LMO	309LNb	254SMO	904L	C22	5923
C	0.015	0.009	0.012	0.017	0.014	0.016	0.006	0.007
Si	0.35	0.51	0.20	0.34	0.39	0.48	<0.02	0.04
Mn	1.61	1.79	1.69	1.93	0.48	1.75	0.31	0.15
P	0.029	0.015	0.013	0.012	0.026	0.018	0.01	0.002
S	0.003	0.003	0.001	0.001	0.001	0.003	<0.003	0.003
Cr	21.77	23.75	20.33	23.74	20.1	19.92	21.22	22.50
Ni	5.70	12.88	13.52	12.37	17.9	24.95	56.97	60.90
Mo	2.99	0.06	2.86	0.03	6.13	4.43	13.43	15.50
Co		0.035	0.038	0.02			0.84	0.02
Cu		0.037	0.07	0.02	0.74	1.46		
Al								0.31
N	0.16	0.045	0.029	0.031	0.192			
Nb				0.70				
W							3.29	
V							0.14	
Ti							0.03	
Fe	balance	balance	balance	balance	balance	balance	3.70	0.54

Table 3 Chemical composition of weld flux, wt. %

Na ₂ O	MgO	Al ₂ O ₃	SiO ₂	K ₂ O	CaO	MnO	FeO	ZrO ₂	CaF ₂	Cr ₂ O ₃
0.29	0.26	25.06	30.89	3.06	20.57	1.42	1.87	0.0	11.36	5.42

Table 4 Cladding conditions in Submerged Arc Welding

Procedure	Current, amp	Voltage, volts	Travel speed, mm/min
I	750	28	140
II	1500	28	280
Electrical stick-out	35 mm		
Polarity	Direct current, electrode positive		
Preheat	150 °C		
Electrode angle	90° to the plate of welding		
Overlap thickness	~ 6mm		

Table 5 Dilution of welding procedures

	F ₂ , mm ²	F, mm ²	D, %	W, mm	P, mm	C, mm
Procedure I						
2205	53.6	236.3	22.7	57.7	2.04	3.27
309L	53.9	242.6	22.2	59.0	1.65	3.50
309LMo	99.8	319.3	31.3	65.1	2.66	4.39
309LNb	86.1	289.3	29.8	63.7	1.92	3.32
254SMO	81.2	289.7	28.0	60.9	2.30	3.75
904L	63.7	274.6	23.2	59.0	1.65	3.50
C22	52.9	249.9	21.1	61.5	1.60	3.62
5923	142.1	419.0	33.9	65.6	3.10	5.20
Procedure II						
2205	86.3	267.9	32.0	61.0	1.90	4.6
309L	147.6	340.9	43.3	60.3	3.20	3.7
309LMo	145.3	376.2	38.6	64.6	3.62	4.2
309LNb	131.5	358.8	36.6	65.7	3.34	4.3
254SMO	119.2	337.8	35.0	64.9	3.45	4.1
904L	84.5	274.2	31.0	58.9	3.04	3.5
C22	93.4	320.2	29.0	60.0	2.26	4.2
5923	165.7	423.8	39.1	73.3	2.48	5.2

where F: the area of the whole weld metal in a cross section vertical to the welding direction,

F₂: the area of the weld metal in the base metal side only,

D: the dilution effect which is defined as the ratio of F₂ to F and expressed in percentage.

W: the width of the weld bead,

P: the penetration of the weld metal into the base steel, and

C: the height of the weld metal above the surface level of the base steel.

Table 6 Thermal expansion coefficients of alloys, and possible residual stresses at interface, $\times 10^{-6} \text{ } ^\circ\text{C}^{-1}$ MPa

alloy	base steel	2205	309L	254SMO	904L	C22
α	14.14	13.46	19.61	20.18	19.15	15.96
difference		- 5 %	39 %	43 %	35 %	13.0 %
σ , MPa		- 40	270	305	250	120
τ , MPa		- 18	125	140	110	55
"peeling"		- 4	33	37	30	15

Table 7 Disbonding analysis by ultrasonic C - scan, %

specimen	1	2	3	1	2	3
Procedure I			Procedure II			
2205	0.0	0.0	0.0	0.0	0.0	0.0
309L	7.5	7.6	3.9	0.0	0.7	3.5
309LMo	3.1	2.4	4.2	2.0	1.8	1.1
309LNb	10.3	8.2	3.2	7.3	1.3	2.1
254SMO	28.5	17.8	14.2	11.4	17.8	10.7
904L	0.1	23.1	2.8	19.6	2.1	8.2
C22	0.0	0.1	0.0	0.1	0.0	0.1
5923	4.2	3.8	1.3	6.1	9.5	4.8

Table 8 Equivalents of Chromium and Nickel of overlays, wt. %

	Schaeffler		Schneider		Hammar		Thieleman		Schoefer	
	Ni _{eq}	Cr _{eq}	Ni _{eq}	Cr _{eq}	Ni _{eq}	Cr _{eq}	Ni _{eq}	Cr _{eq}	Ni _{eq}	Cr _{eq}
2205	6.95	25.29	10.96	26.96	9.61	26.39		15.23	13.37	21.49
309L	14.05	24.58	15.22	24.86	15.20	24.62		-15.96	17.47	19.61
309LMo	14.73	23.49	15.51	25.02	16.64	24.55		-11.11	17.73	19.64
309LNb	13.85	24.98	14.65	25.69	14.77	25.69		-12.89	16.90	20.00
254SMO	18.56	26.82	23.57	30.08	22.06	29.22		- 8.09	25.80	24.28
904L	26.31	25.07	26.74	27.53	28.18	26.71		-39.43	29.08	21.85
C-22	57.31	34.65	58.14	43.95	57.35	39.71		-85.48	60.08	35.03
5923	61.19	38.06	61.30	47.54	61.18	43.80		-91.75	63.96	39.27

* Formulas used for the calculation of equivalents of nickel and chromium are based on:

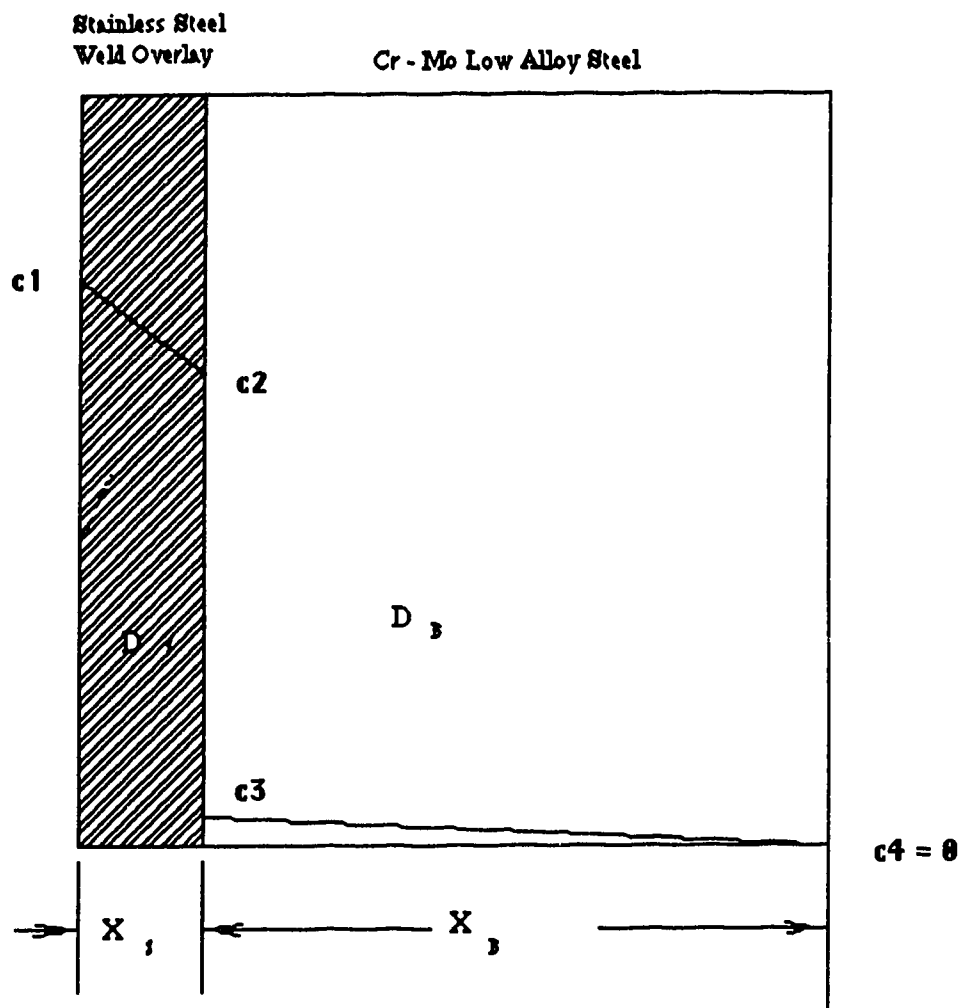
- Schaeffler¹: $Ni_{eq} = \%Ni + 30\%C + 0.5\%Mn$
 $Cr_{eq} = \%Cr + \%Mo + 1.5\%Si + 0.5\%Nb$
- Schneider and Delong^{2,3}:
 $Ni_{eq} = \%Ni + \%Co + 0.3\%Cu + 0.5\%Mn + 25\%N + 3\%C$
 $Cr_{eq} = \%Cr + 2\%Si + 1.5\%Mo + 5\%V + 5.5\%Al + 1.75\%Cb + 1.5\%Ti + 0.75\%W$
- Hammar and Svenson⁴:
 $Ni_{eq} = \%Ni + 22\%C + 14.2\%N + 0.81\%Mn + \%Cu$
 $Cr_{eq} = \%Cr + 1.37\%Mo + 1.5\%Si + 2\%Cb + 3\%Ti$
- Thieleman formula is a complex Cr equivalent combined with the effects of Cr and Ni:
 $Cr_{eq} = \%Cr + 5.2\%Si + 4.2\%Mo + 11\%V + 12\%Al + 4.5\%Cb + 7.2\%Ti +$
 $+ 2.1\%W + 2.8\%Ta - 40\%C - 3\%Ni - 2\%Mn - 1\%Cu$
- Schoefer formula used in the foundry industry:
 $Ni_{eq} = \%Ni + 30\%C + 26(\%N - 0.02) + 0.5\%Mn + 2.77$
 $Cr_{eq} = \%Cr + 1.4\%Mo + 1.5\%Si + \%Cb - 4.99$

¹ A. Schaeffler, "Constitutional Diagram for Stainless Steel Weld Metal", *Metal Progress*, 56 (5), 1949, p680

² H. Schneider, *Foundry Trade Journal*, 108, 1960, p562

³ W.T. Delong, "Ferrite in Austenitic Stainless Steel Weld Metal", *Welding Journal*, 53 (7), 1974, 273s

⁴ J.F. Lancaster, *Metallurgy of Welding*, 4th Edition, Allen & Unwin, London, 1987



C1: hydrogen concentration at the surface of stainless steel overlay,
 C2: hydrogen concentration in stainless steel overlay at the interface,
 C3: hydrogen concentration in the base steel at the interface, and
 C4: hydrogen concentration at the surface of base steel.

unit in $\text{cm}^3 \text{ H/cm}^3 \text{ Fe}$

X_b and X_o : thickness of base steel and overlay, respectively, in cm.

Fig. 1 Schematic of steady - state hydrogen concentration profile across the wall of pressure vessel (Ref. 6).

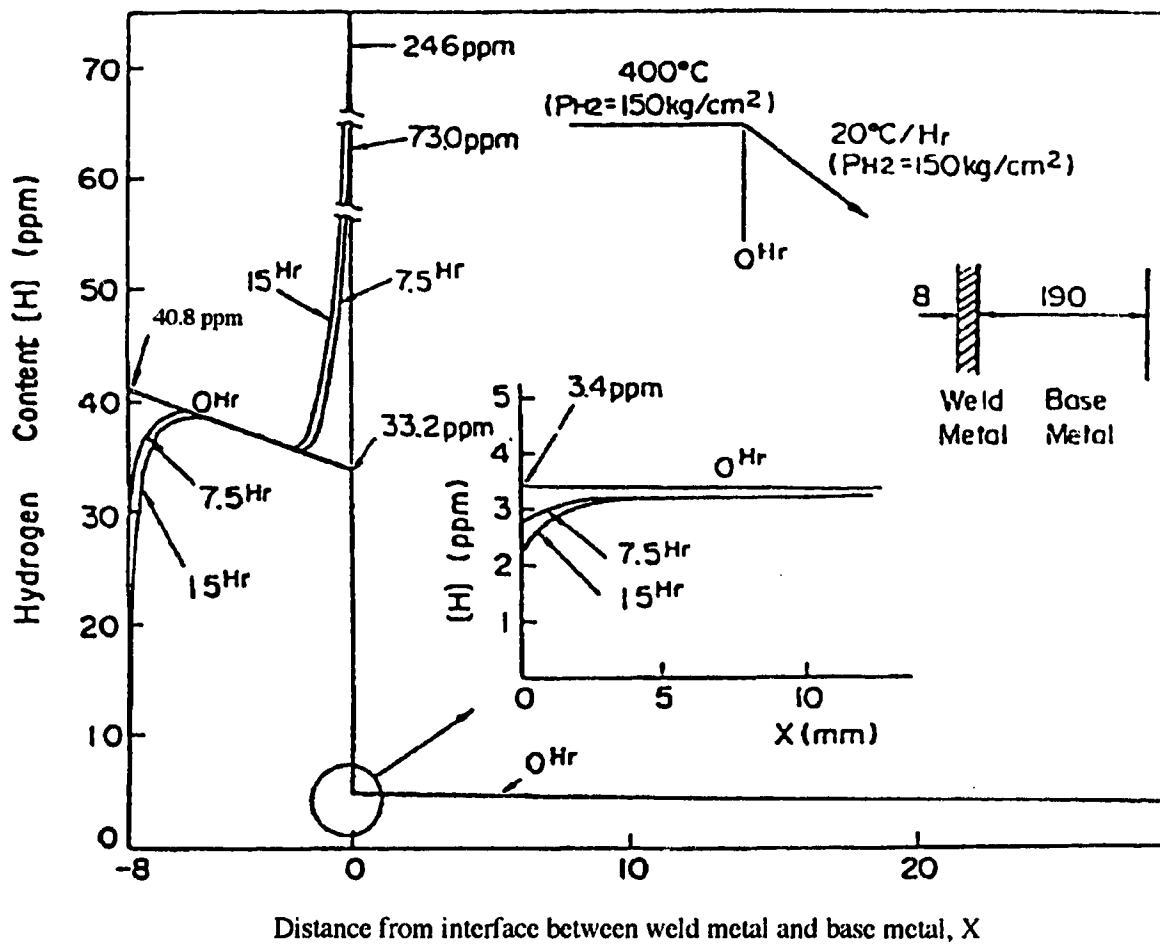


Fig. 2 Through - wall profile of hydrogen concentration for steady - state operation and shut - down coolin process (Ref. 6).

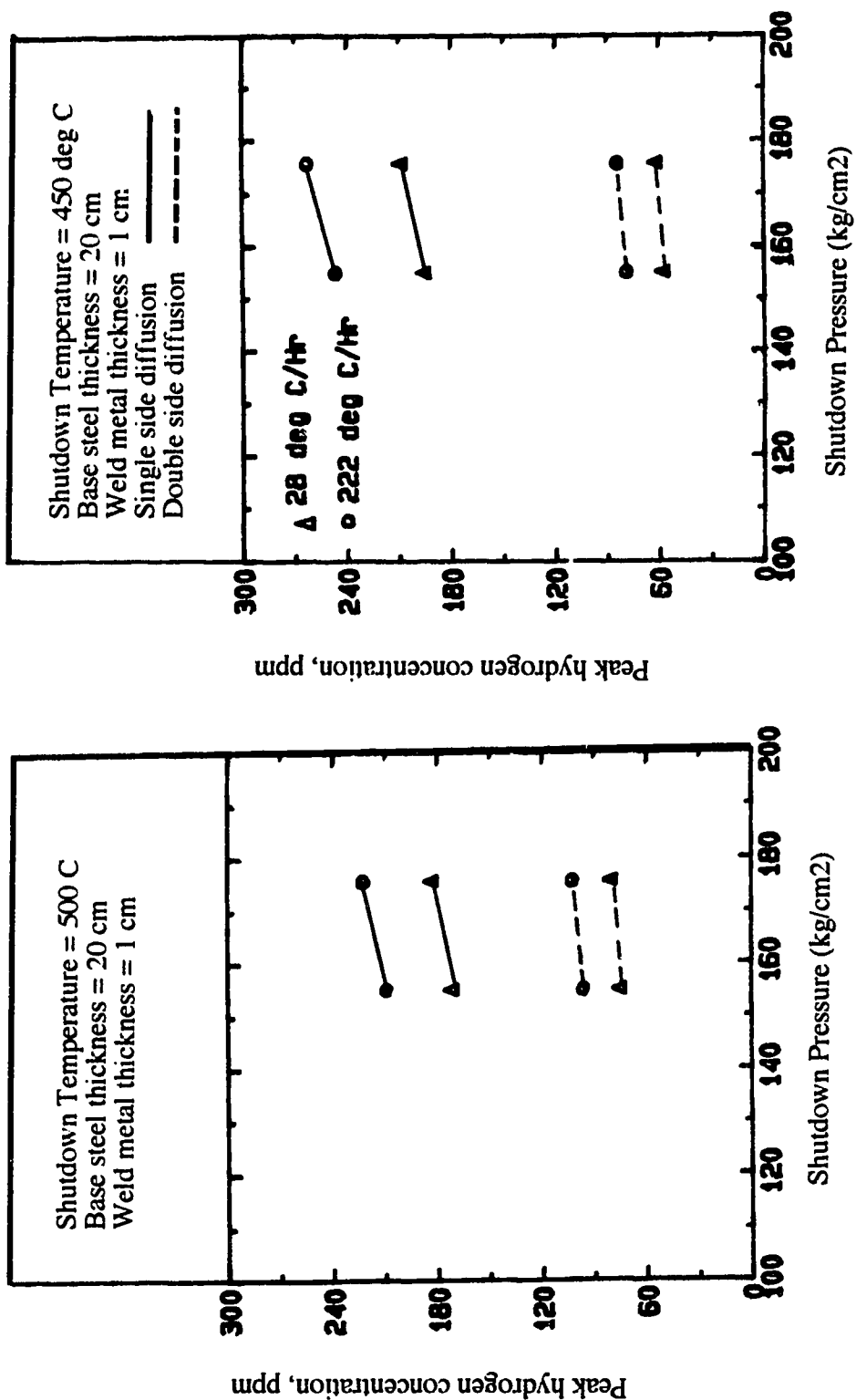


Fig. 3 Effects of Shut-down Condition on Hydrogen Accumulation (Ref. 17).

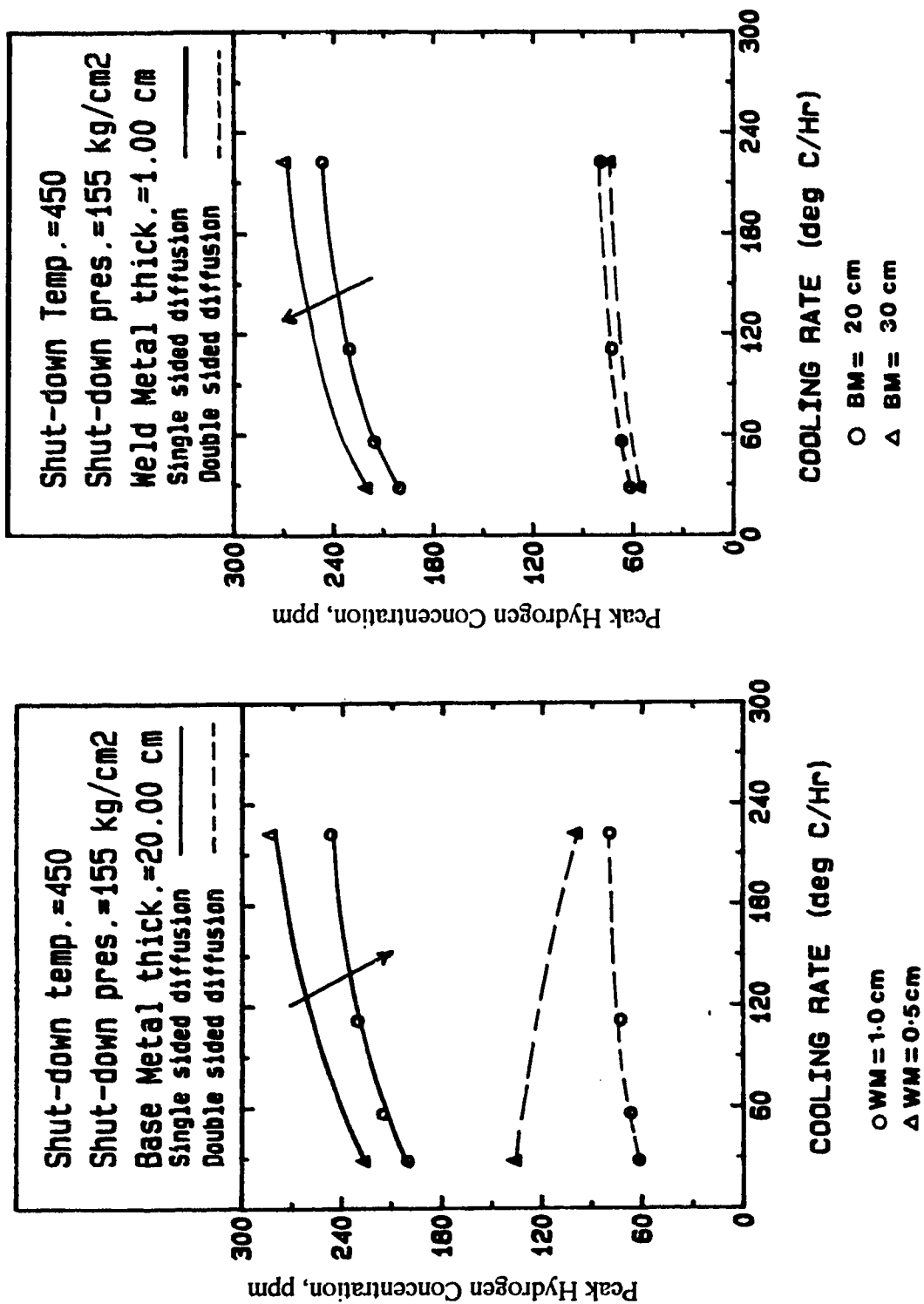


Fig. 4 Effects of Cooling Rate, Thickness of Base Steel and Overlay on Hydrogen Accumulation (Ref. 17).

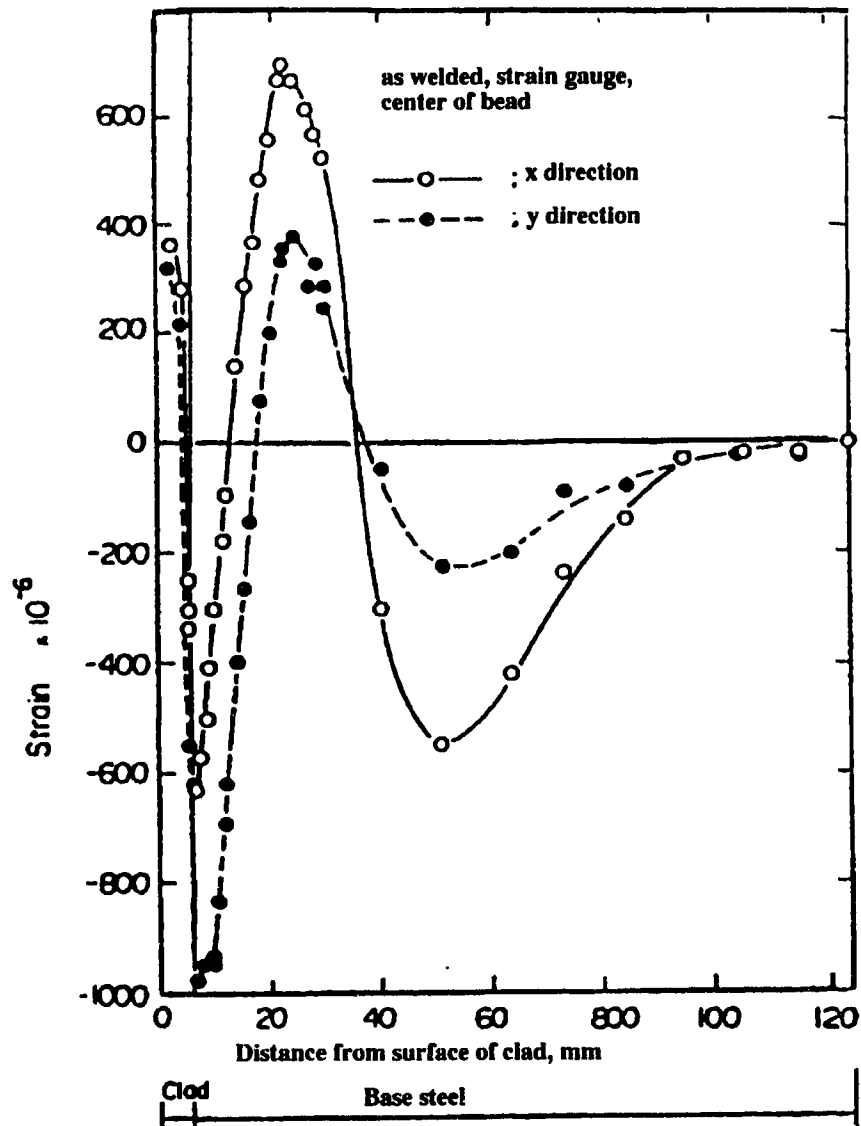


Fig. 5 Variation in surface strain due to slicing. Location of strain gauge: center of bead, as-welded (Ref. 22).

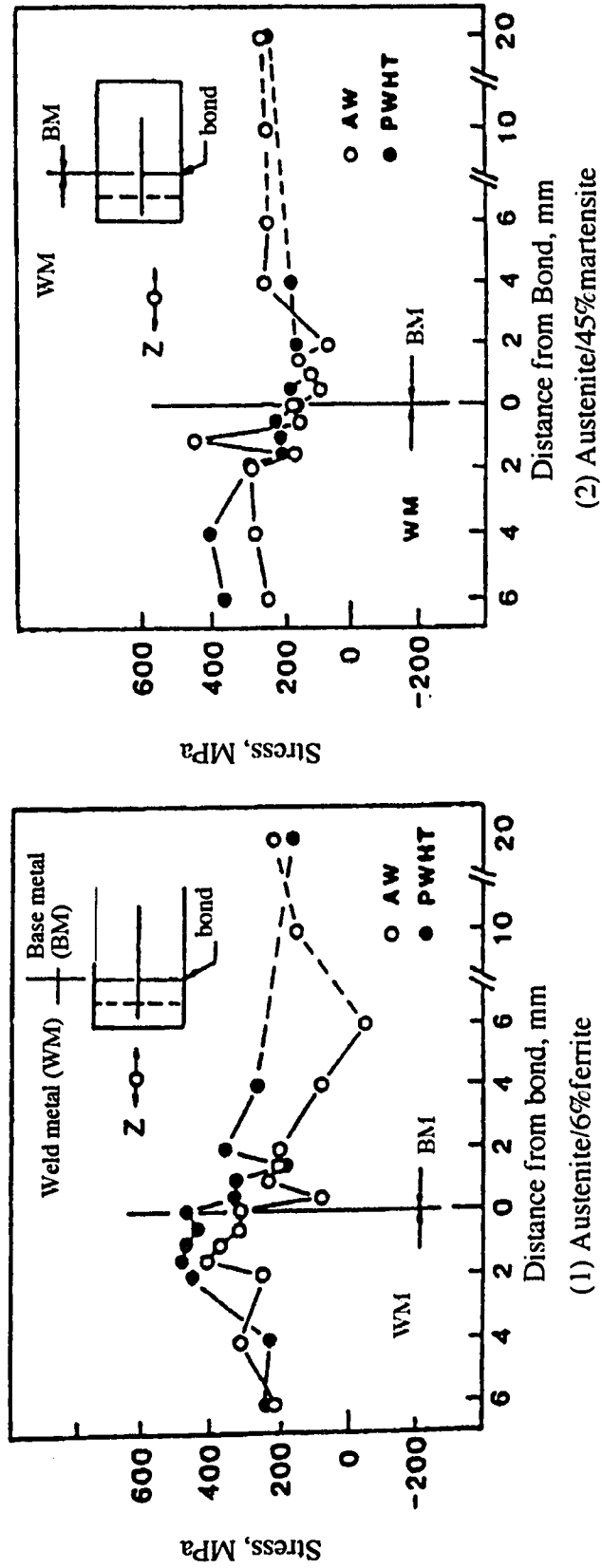


Fig. 6 Distribution of Residual Stresses in through - thickness Direction across the Overlay Welds (Ref. 22)



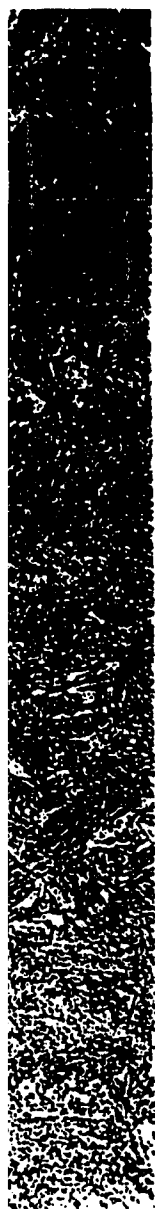


Fig. 7 As - welded 309/347 overlay, etched electrolytically at 5 V in 2% chromic acid for 45 s and then etched in 2% nital for 30 s (Ref. 10).

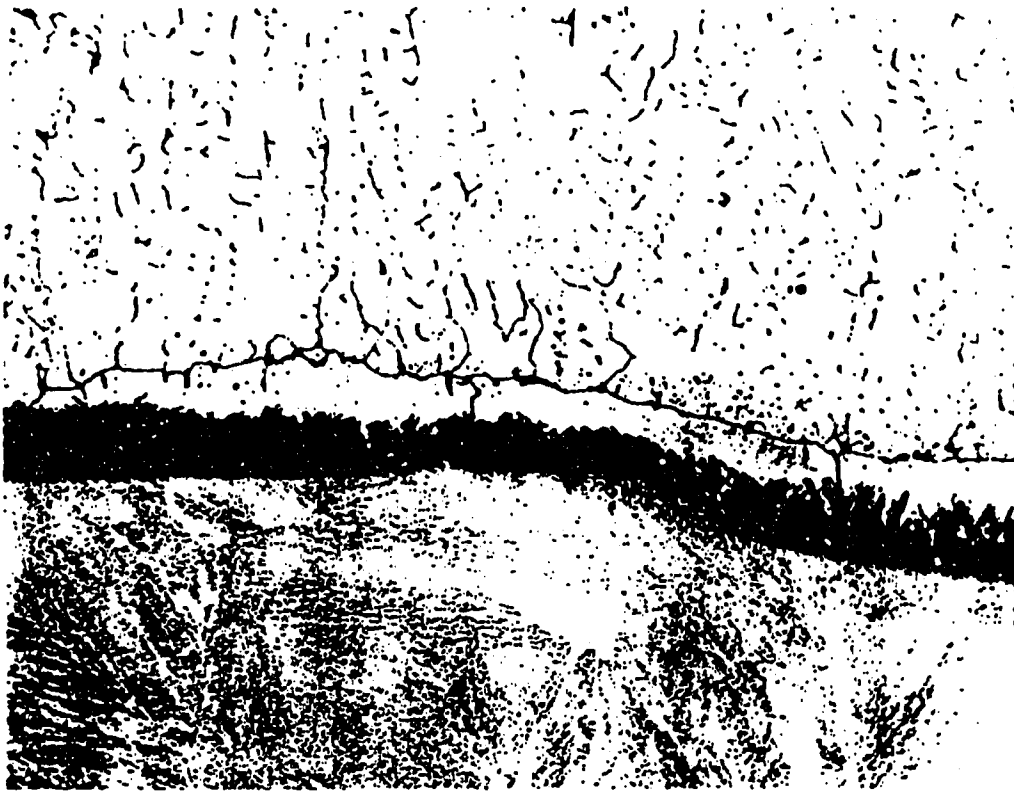


Fig. 8 Cracks running along the Type II grain boundaries of specimen E309L by welding of low travel speed after autoclave testing, X200 Mag. (Ref. 12)

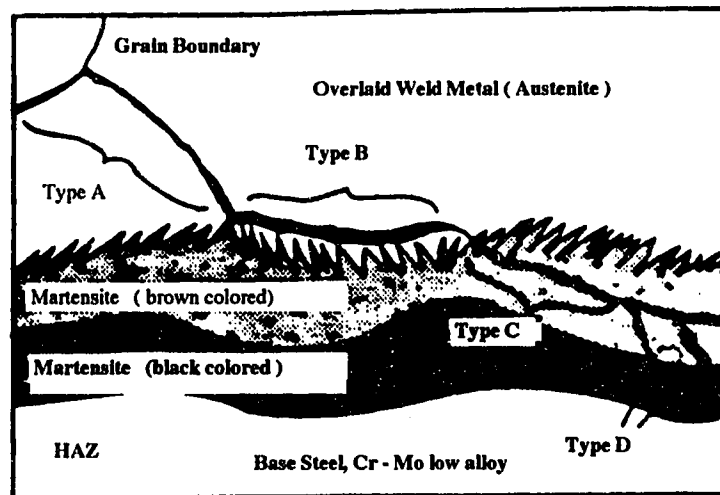
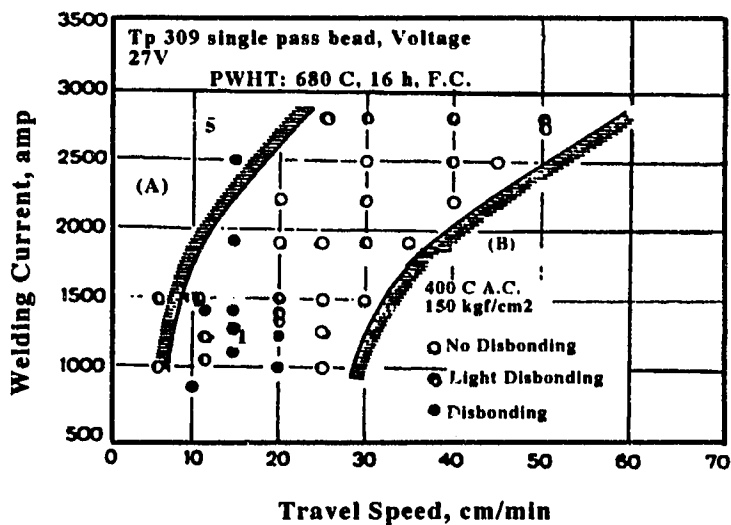
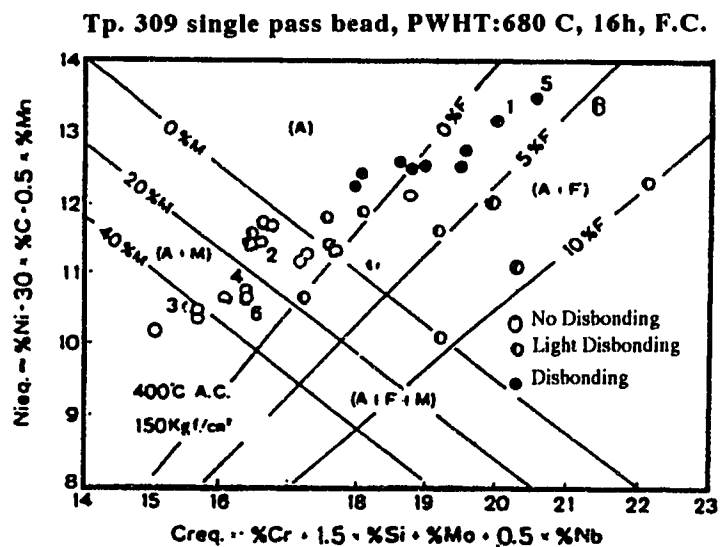


Fig. 9 Illustration of four types of disbonding (Ref. 6).



(a) Effects of Welding Current and Travel Speed On Disbonding (Ref.20);



(b) Effect of Microstructure on Disbonding (Ref.20).

Fig. 10 Disbonding related to welding current, travel speed and microstructure.

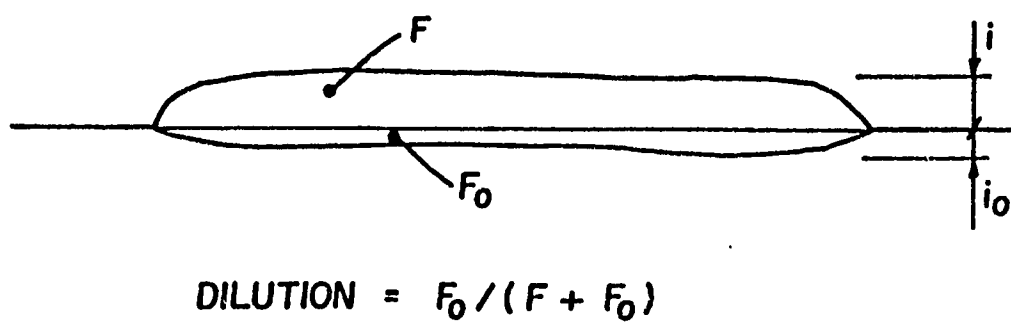
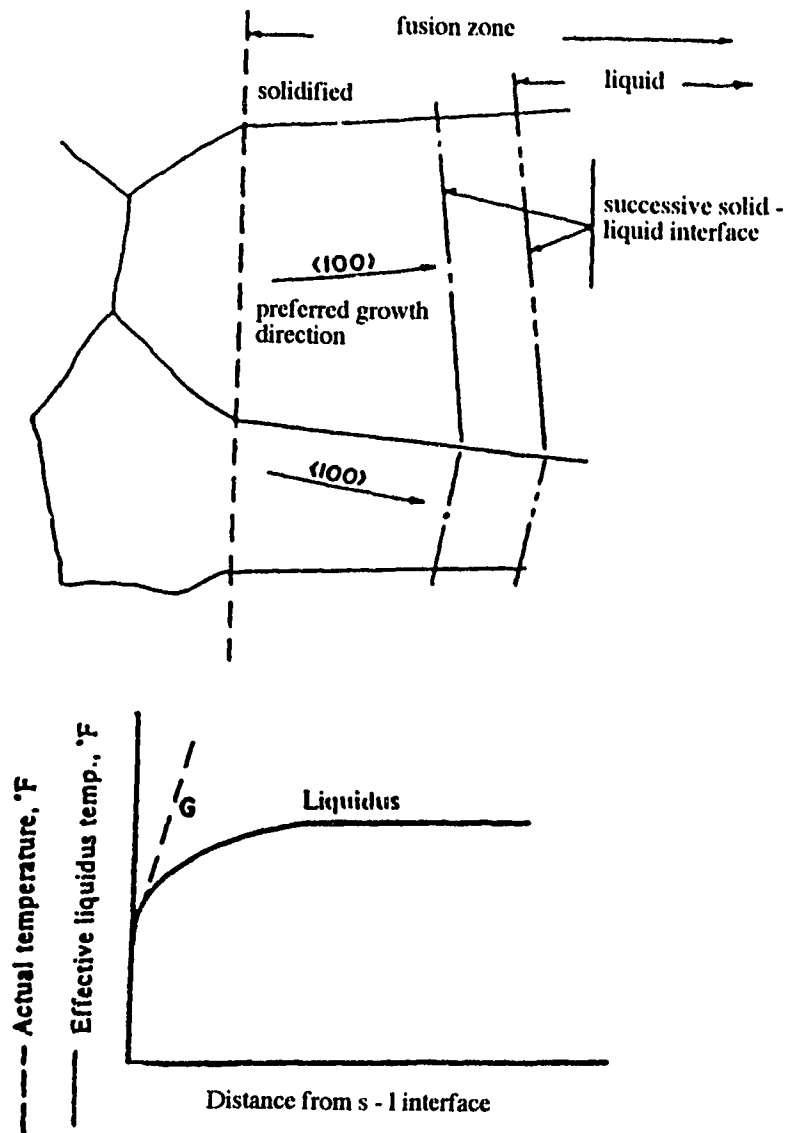
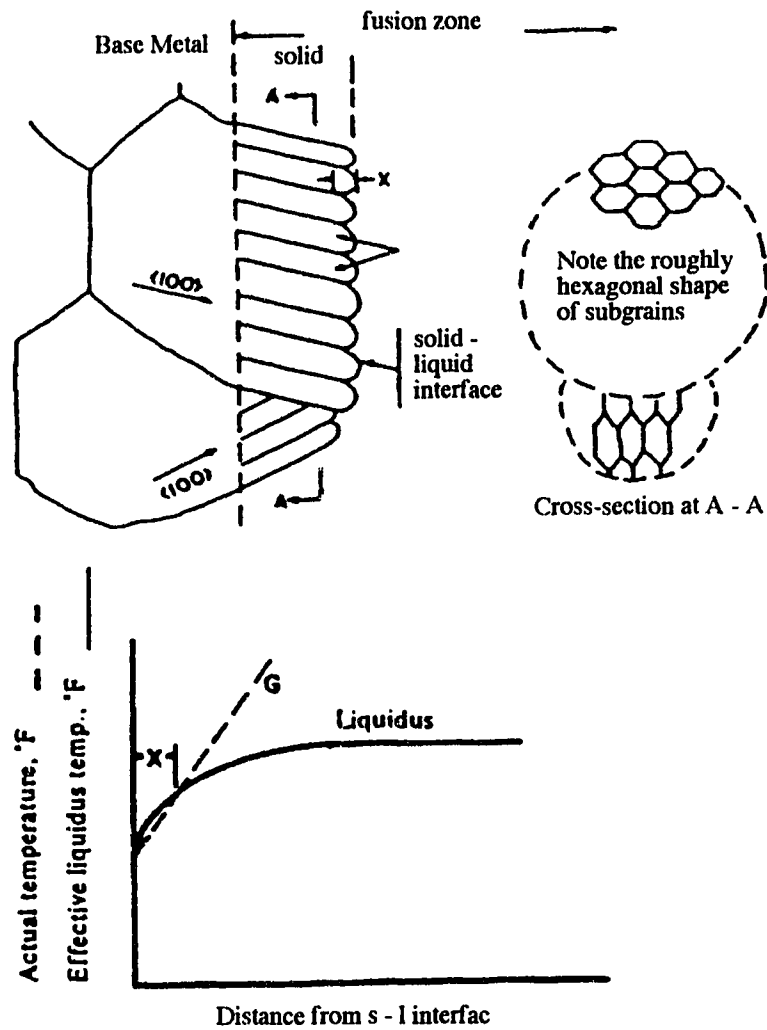


Fig. 11 Cross - section through a strip clad specimen showing the relative contribution of electrode (F) and base metal (F_0) to the deposit chemistry (Ref. 25).



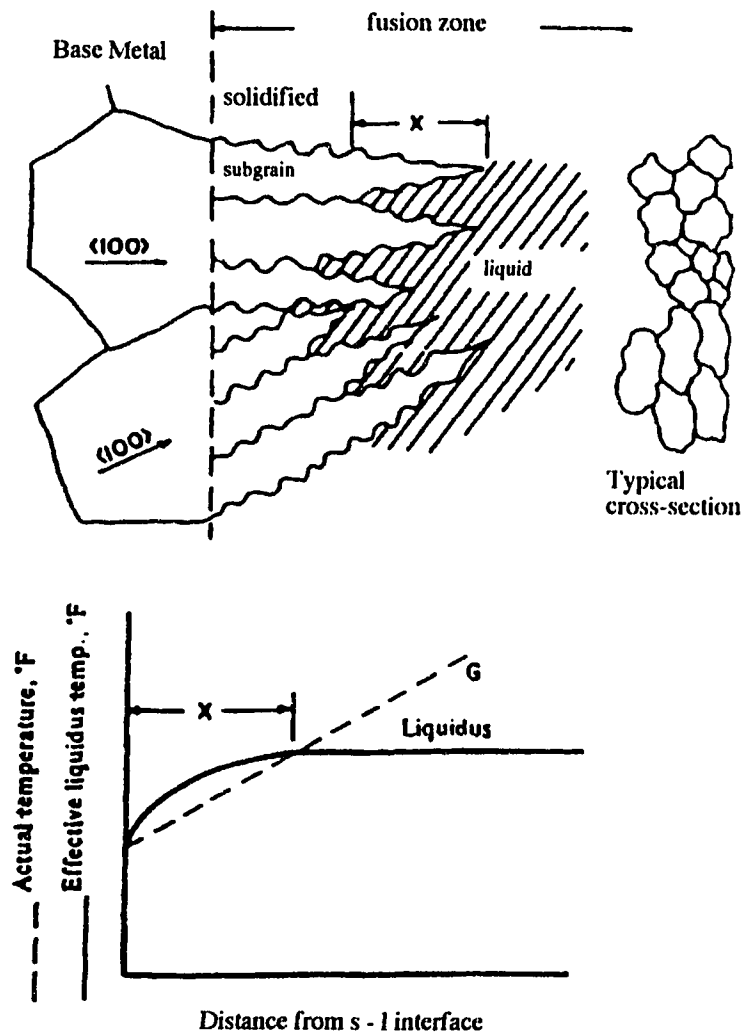
(a) Schematic showing the appearance of solid - liquid interface during planar growth mode of solidification.

Fig. 12 Schematic representation of microstructure for various growth modes (Ref. 26).
(Continuing to the next page)



(b) Schematic showing the appearance of solid - liquid interface during cellular growth mode of solidification.

Fig. 12 (Continued) Schematic representation of microstructure for various growth mode (Ref.26). (Continuing to the next page.)



(c) Schematic showing the appearance of solid - liquid interface during cellular - dendritic growth mode.

Fig. 12 (Continued) Schematic presentation of microstructure for various growth modes.

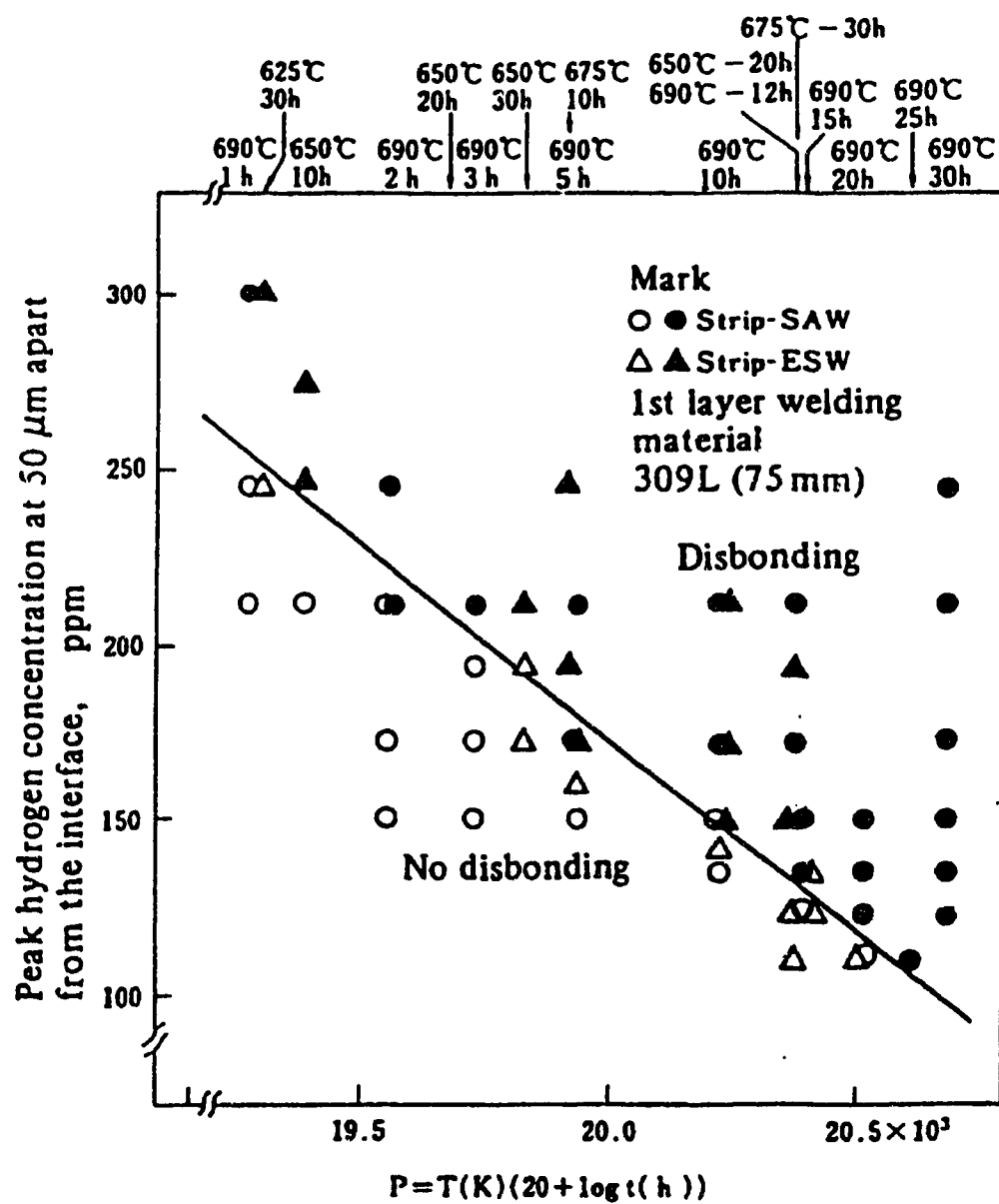


Fig. 13 Effect of PWHT conditions on hydrogen induced disbonding (Ref. 30).

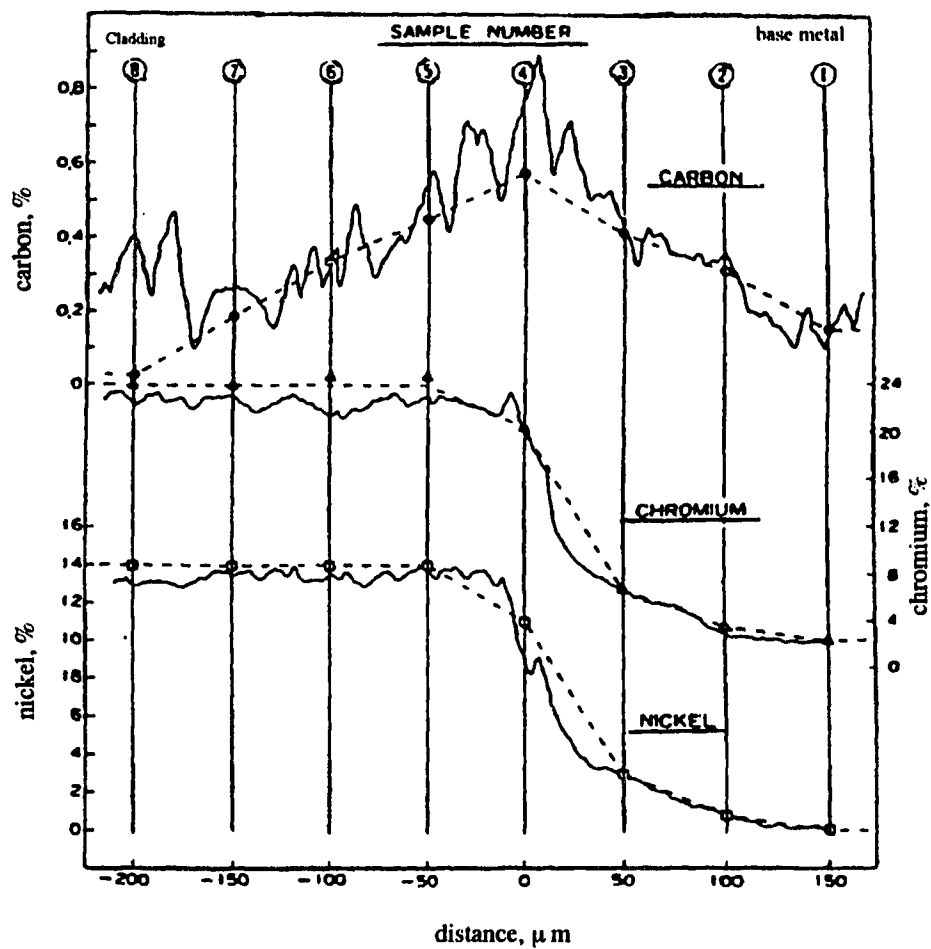


Fig. 14 Element profile close to the interface between weld overlay and 2.25Cr-1 Mo base steel after PWHT (Ref. 30).



Fig. 15 Disbonding crack in 309/347 overlay. Note crack ends at intrusion (Ref. 10).

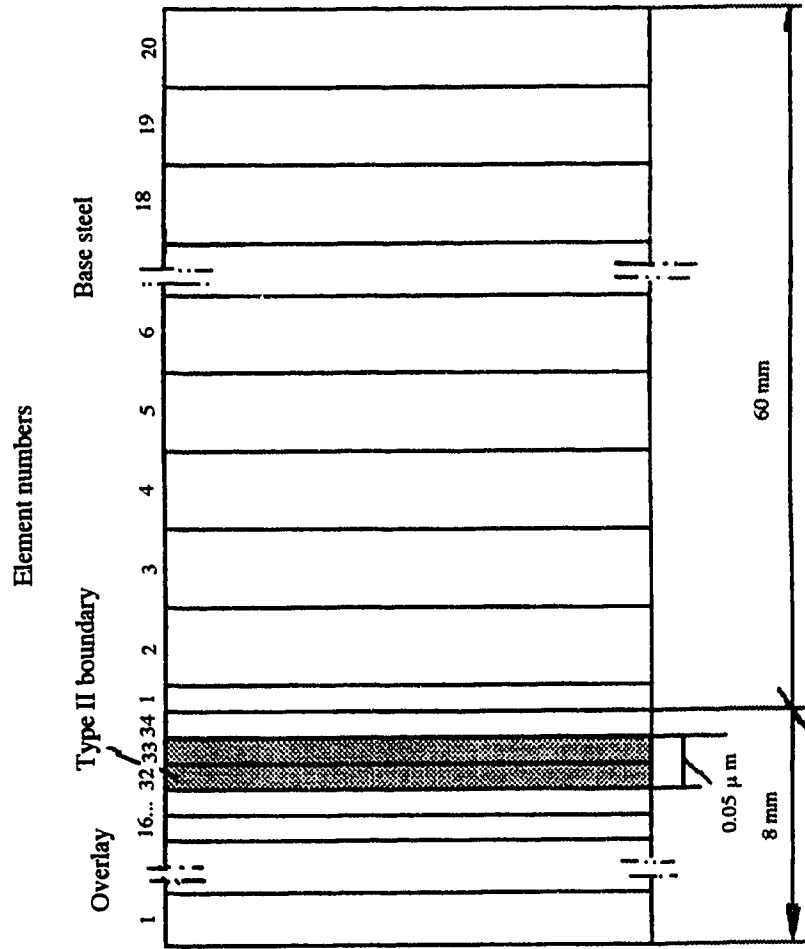
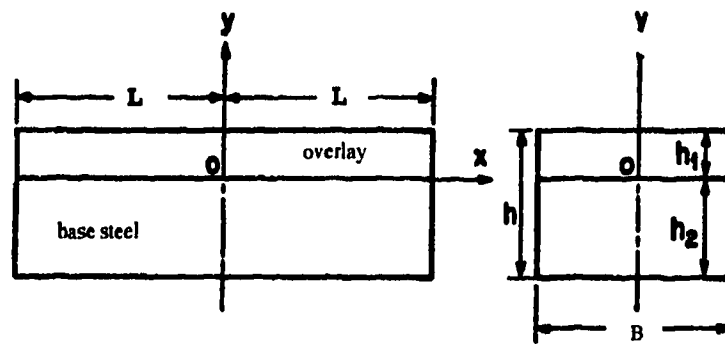
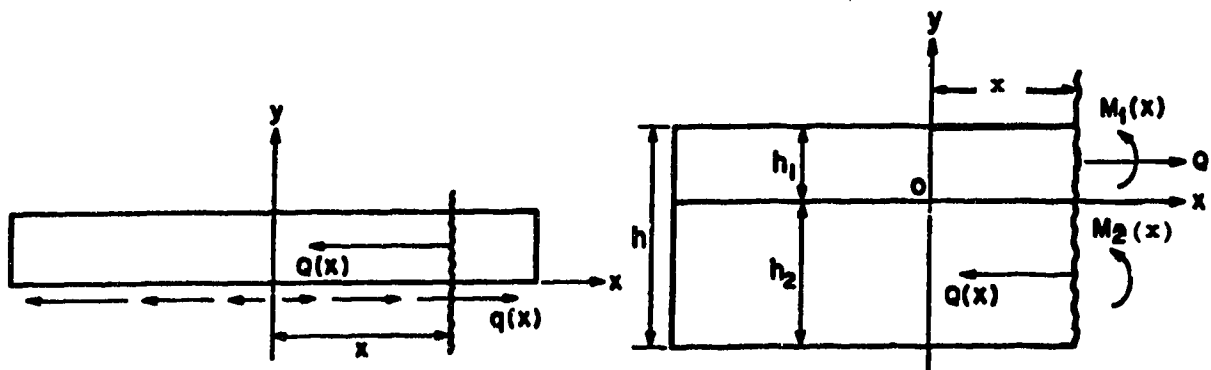
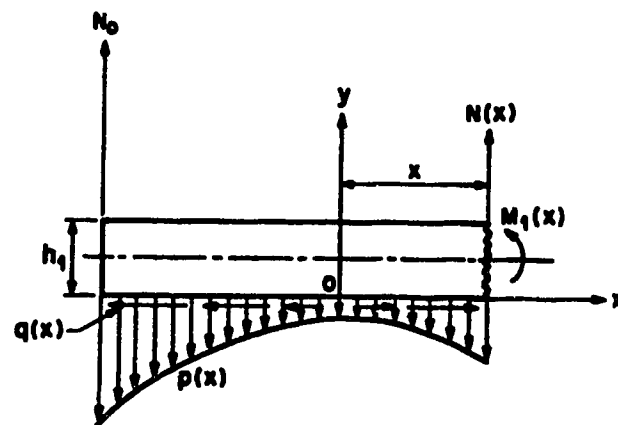


Fig. 16 Element system for diffusion analysis by finite difference method.



(a) Structure of overlay system

(b) Forces and moments at the x - cross section.

(c) Forces and moments acting on a portion of the overlay.

Fig. 17 Plate of the overlay system and the possible forces in it.

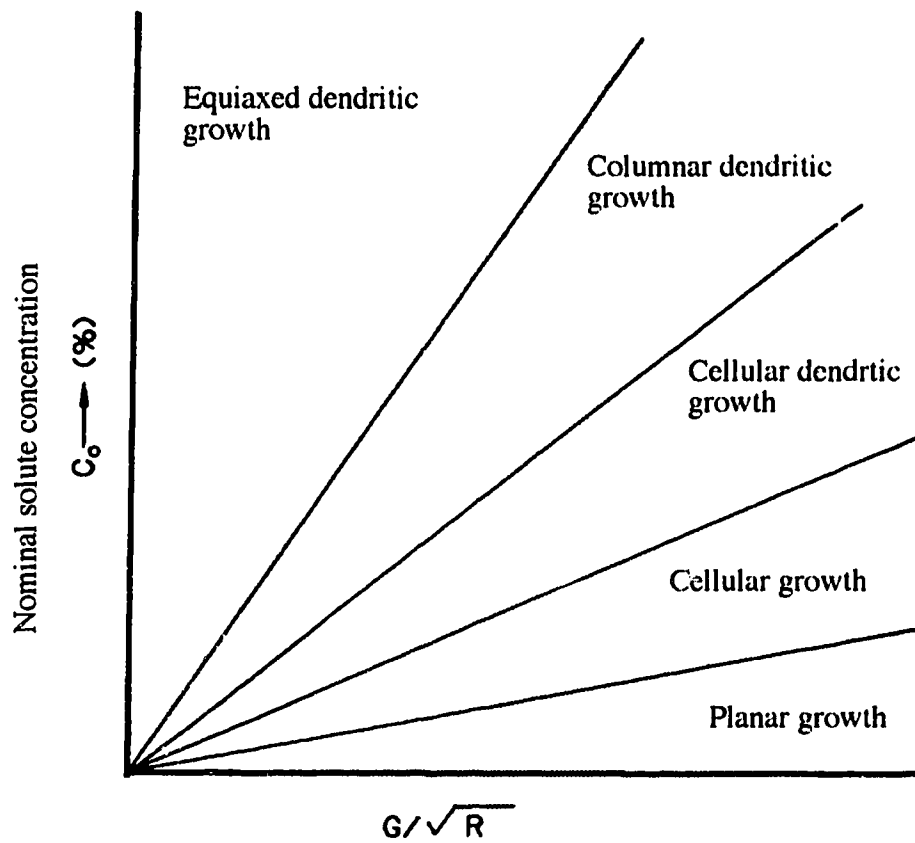


Fig. 18 Schematic plot describing solidification structure as a function of percent solute and G/\sqrt{R} (Ref. 26).

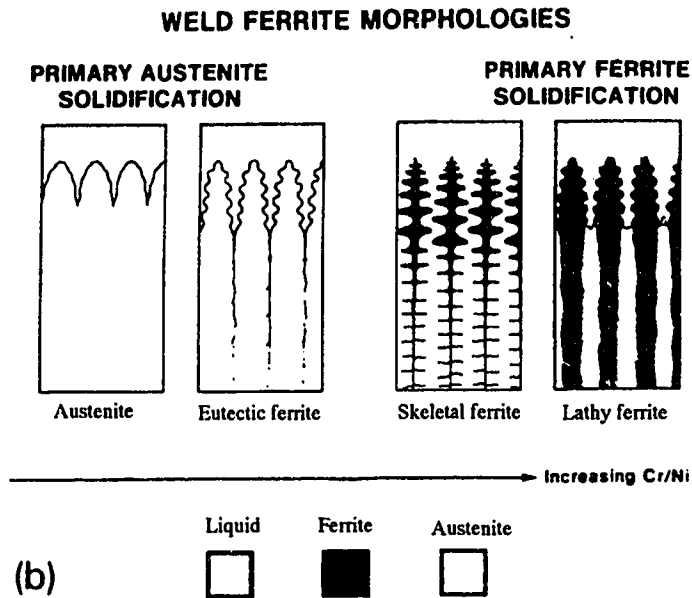
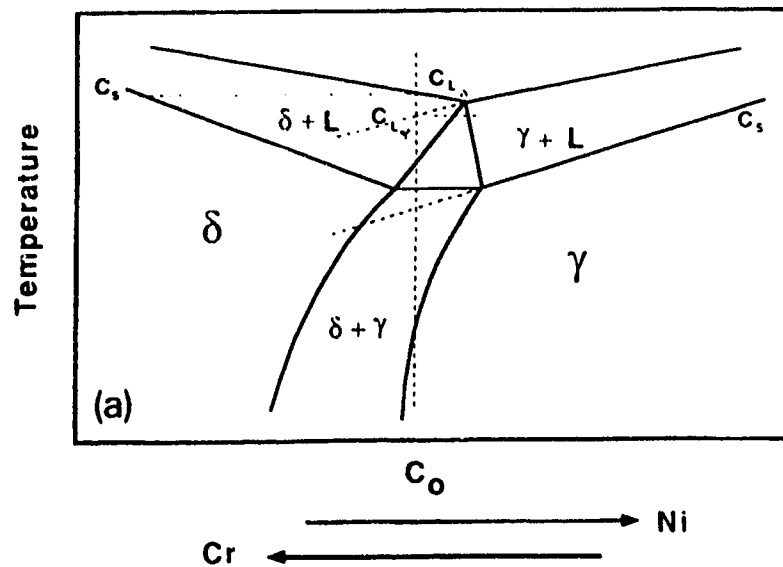


Fig. 19 (a) Schematic of an Fe - Cr - Ni pseudo-binary.
 (b) Schematic of stainless steel weld structures for primary austenite and primary ferrite solidification.

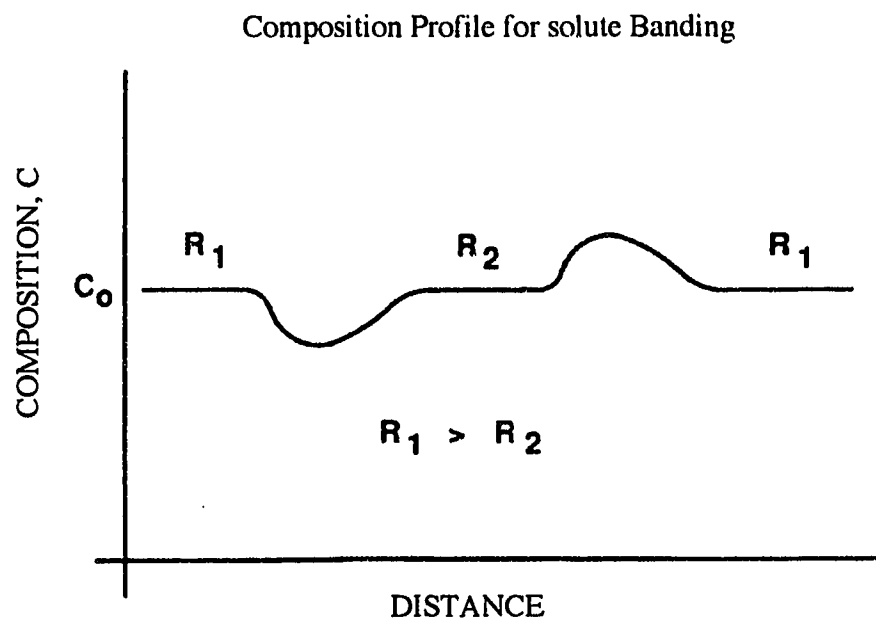


Fig. 20 Solute banding resulting from the change of solidification velocity, R (Ref.34)

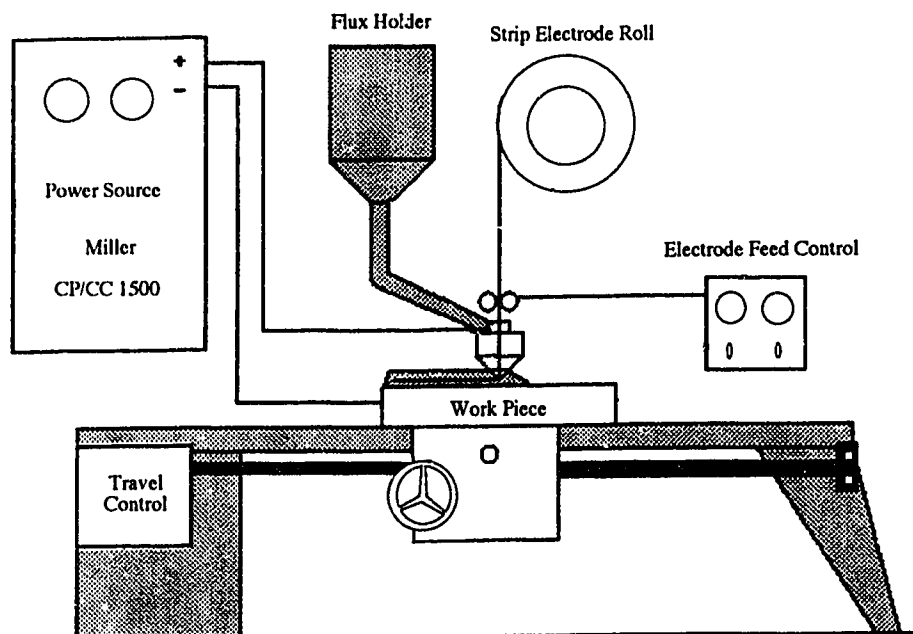


Fig. 21 Schematic of set-up of operation for the cladding.

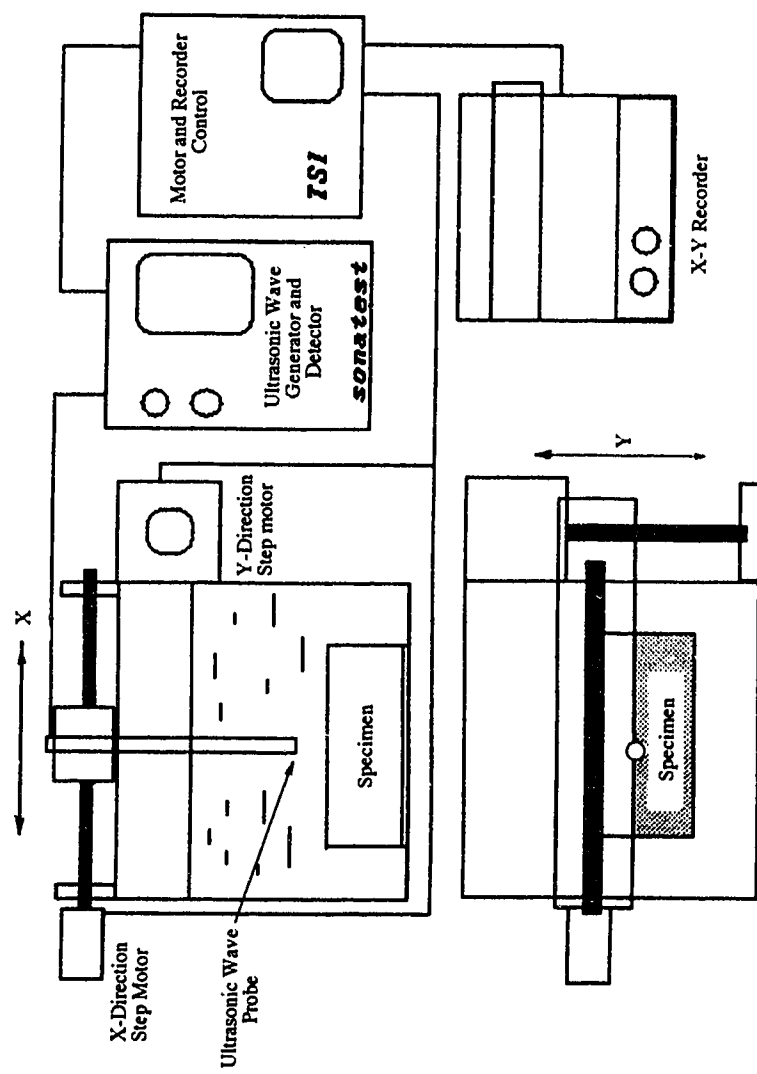


Fig. 22 Schematic of set-up of operation for ultrasonic examination.

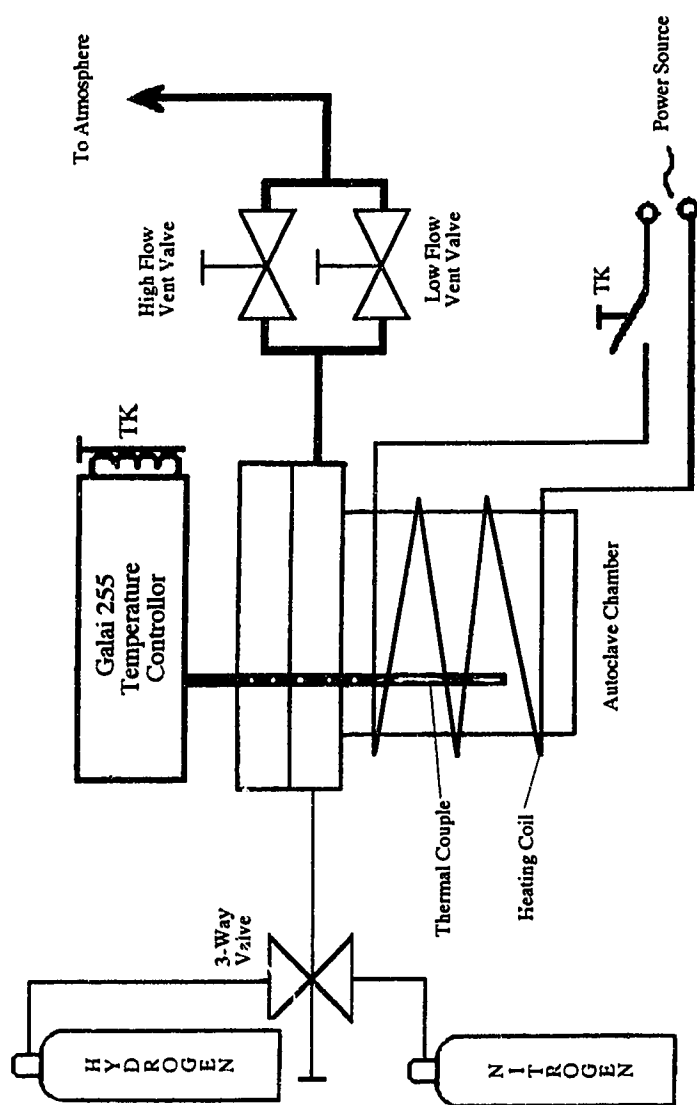


Fig. 23 Schematic of set-up of operation for autoclave test.

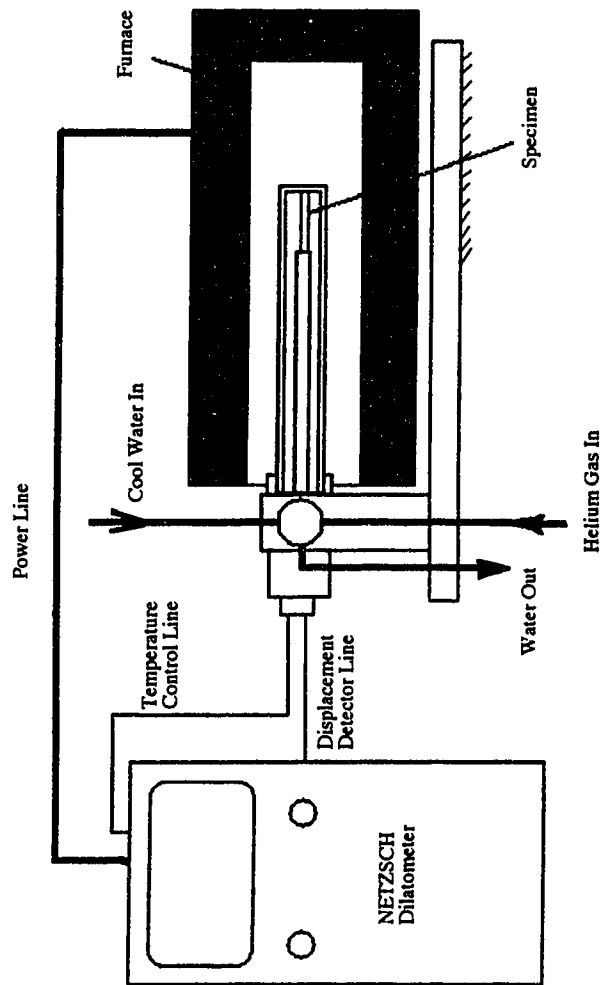


Fig. 24 Schematic of set-up of operation for dilatometric test.

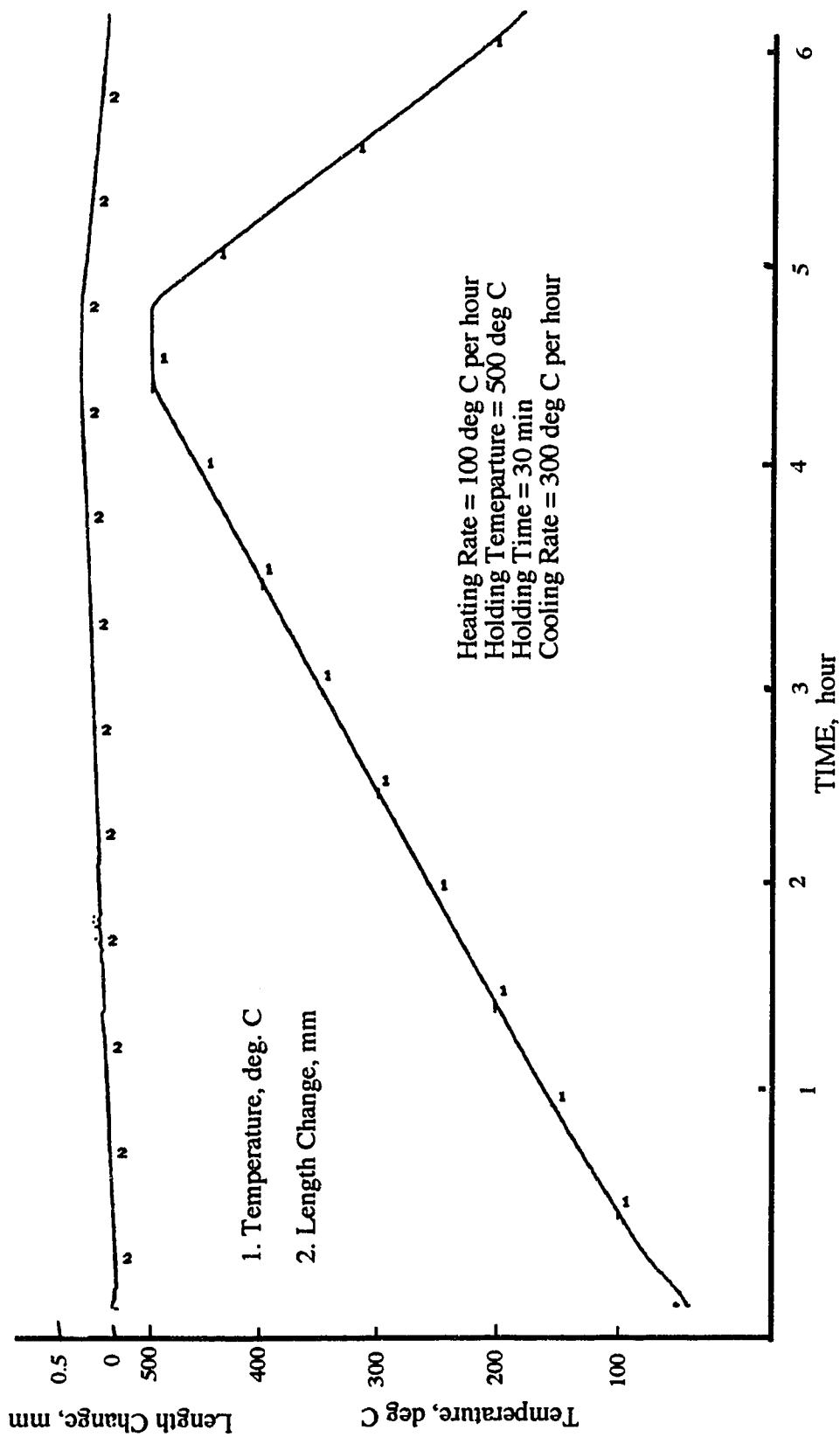


Fig. 25 Thermal Expansion Curve of the Base Steel.

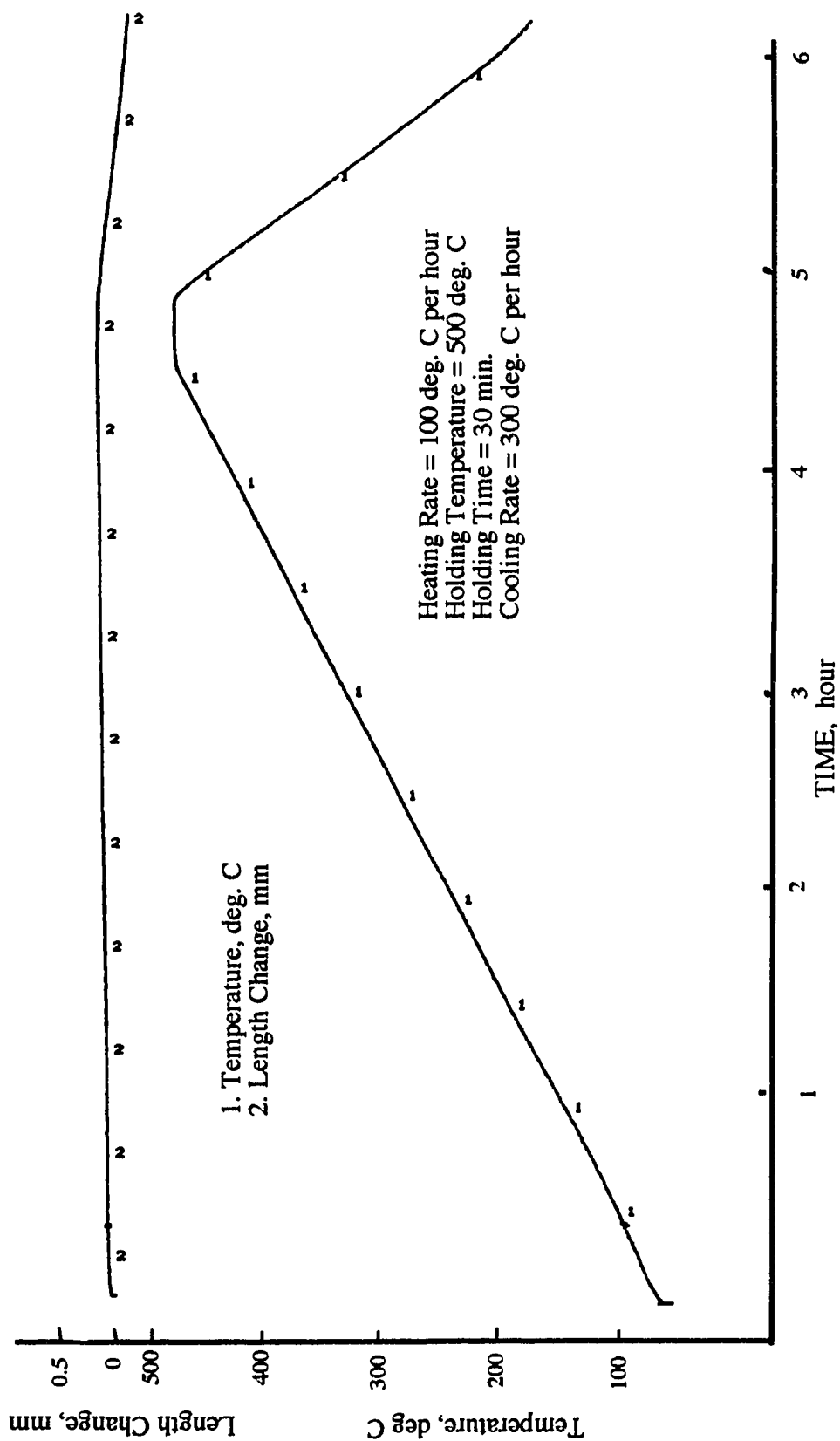


Fig. 26 Thermal Expansion Curve of Overlay 2205.

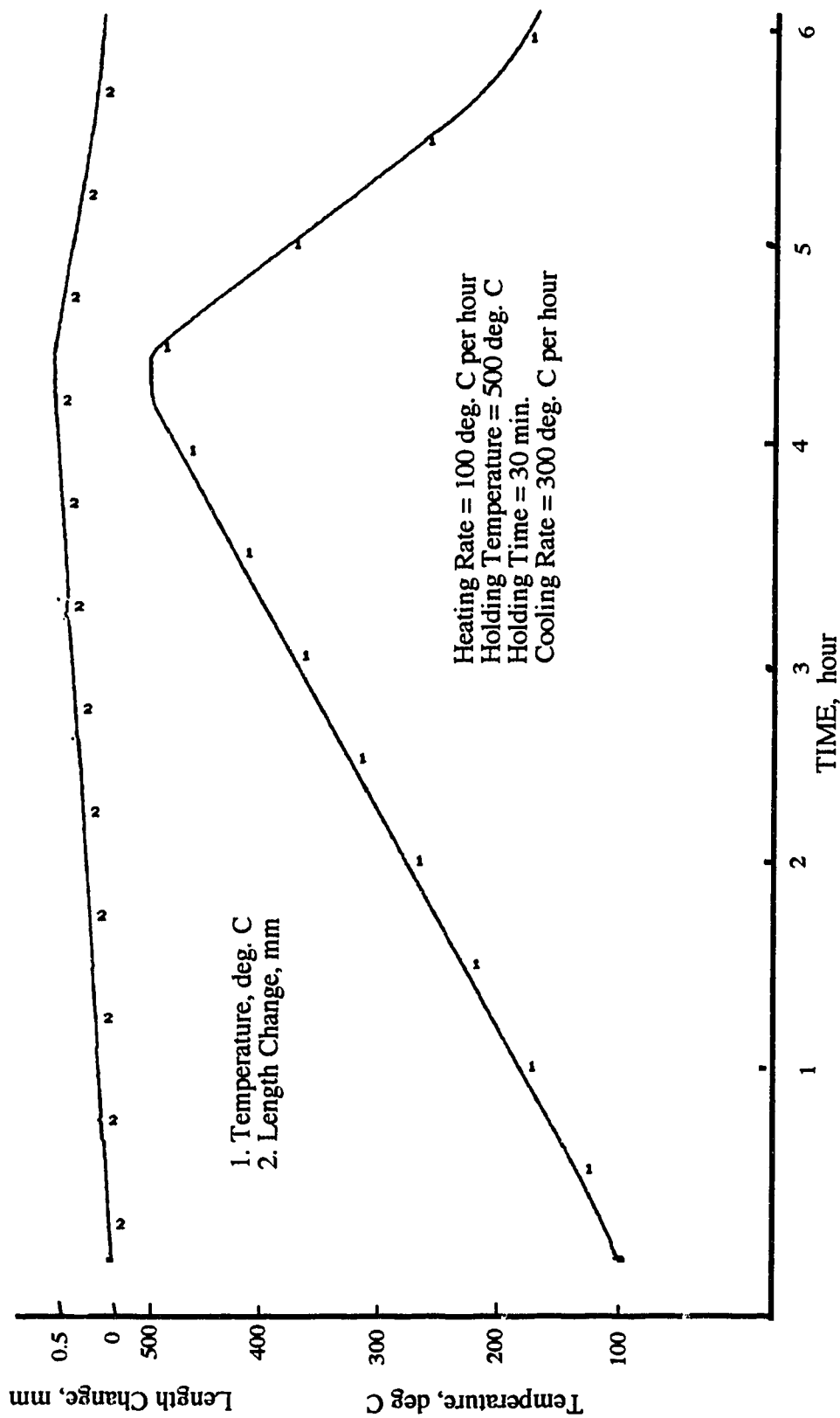


Fig. 27 Thermal Expansion Curve of Overlay 309L.

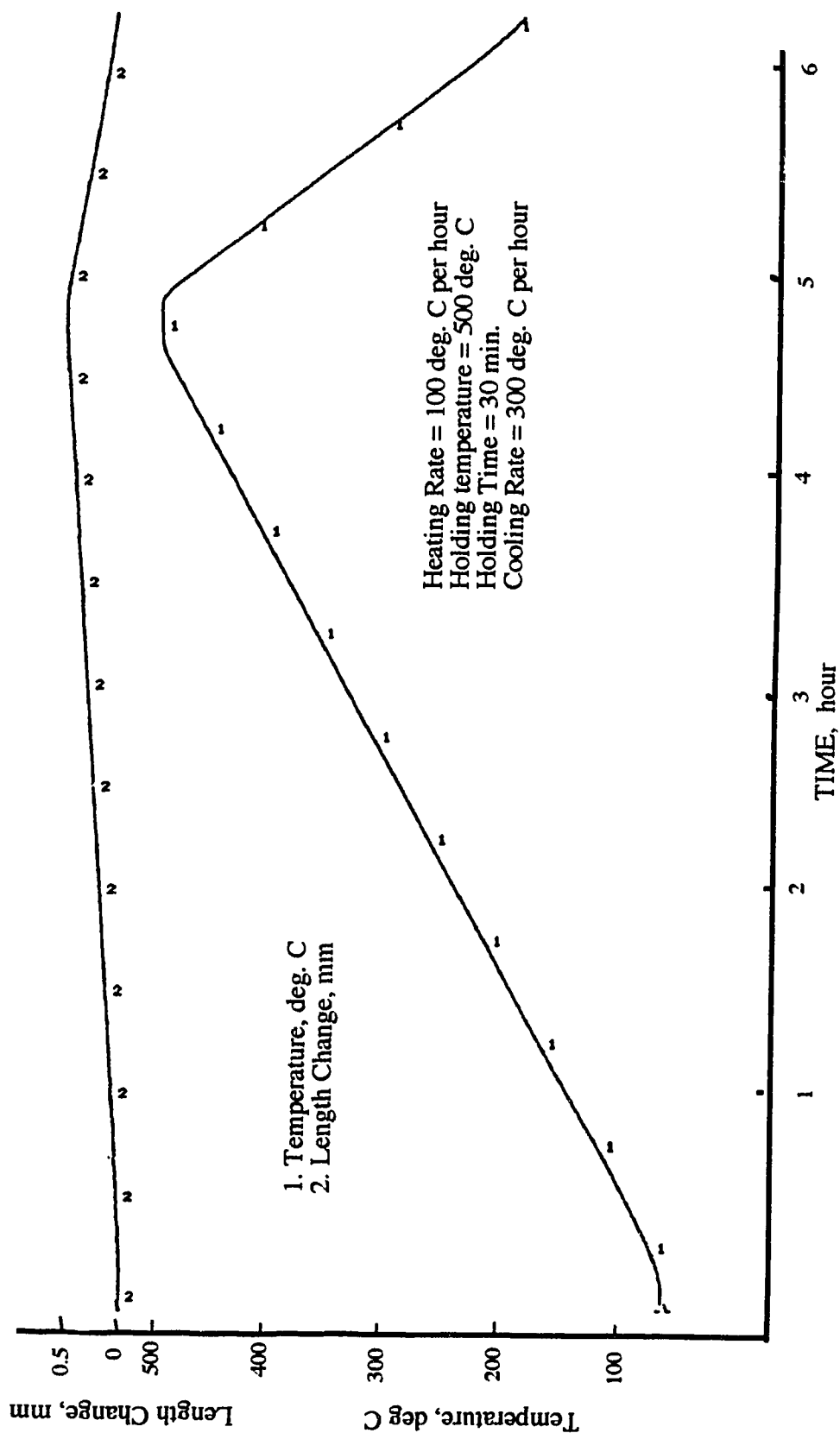


Fig. 28 Thermal Expansion Curve of Overlay 254SMO.

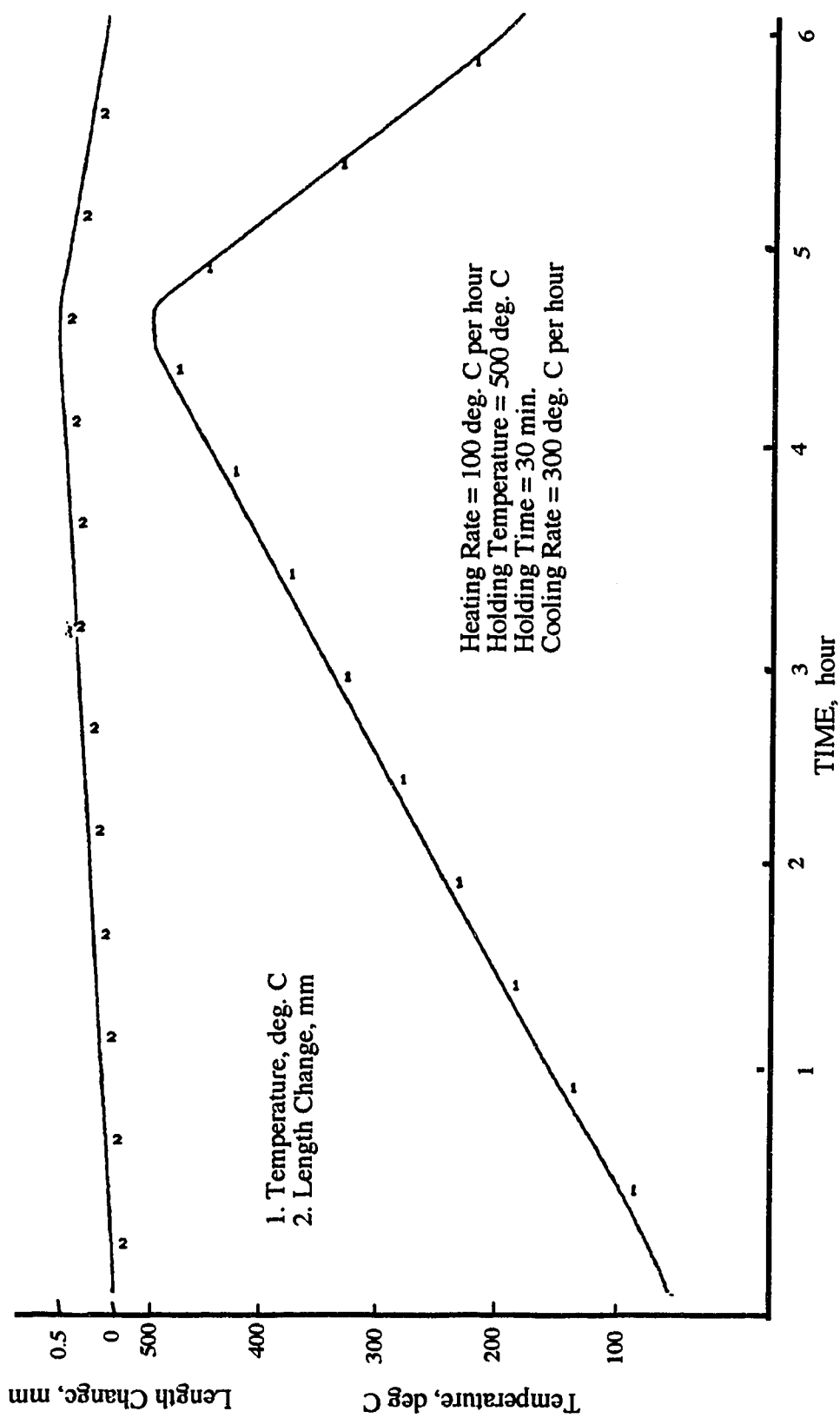


Fig. 29 Thermal Expansion Curve of Overlay 904L.

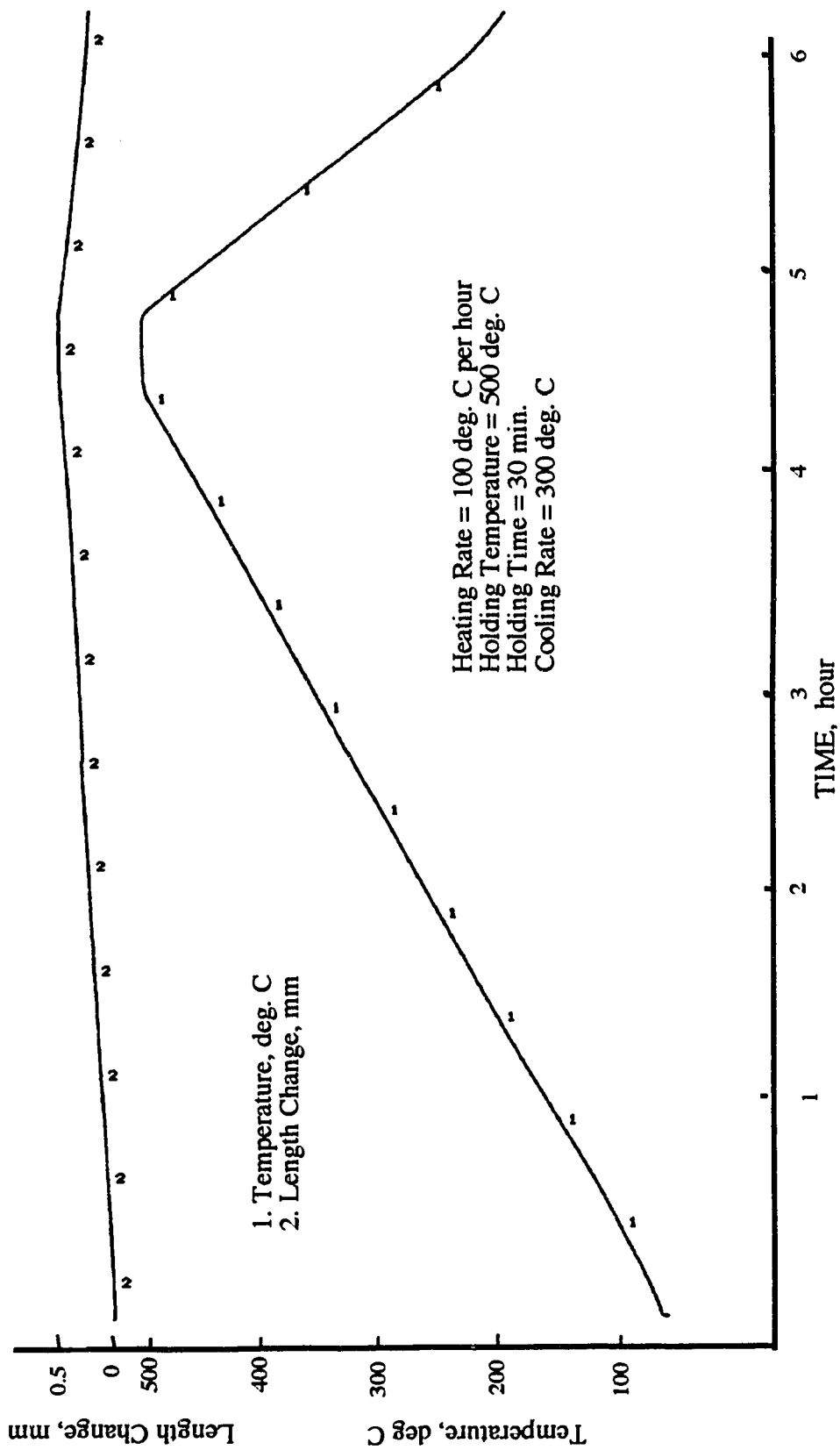


Fig. 30 Thermal Expansion Curve of Overlay C-22.

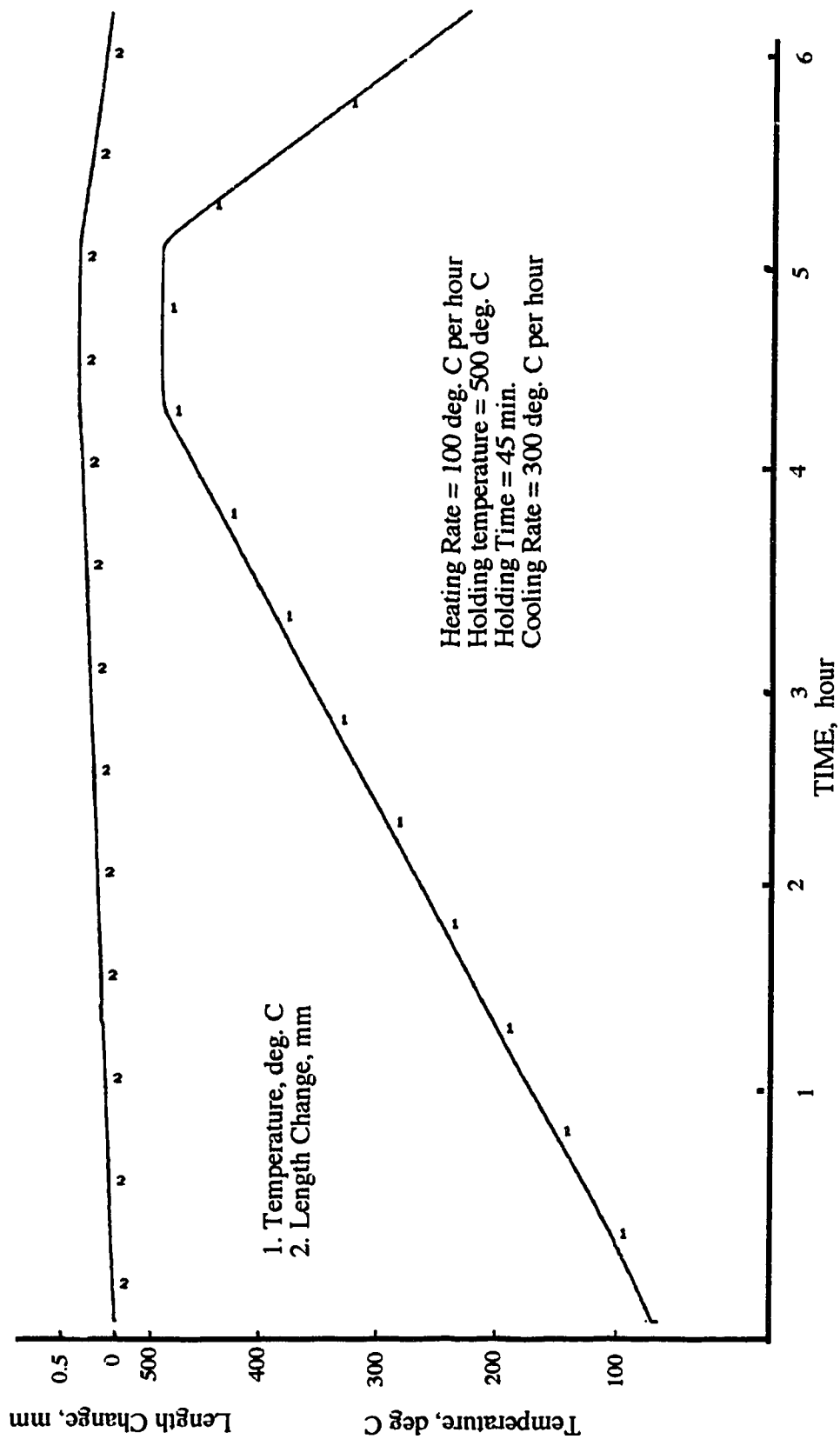


Fig. 31 Thermal Expansion Curve of Standard Sample, Ni.

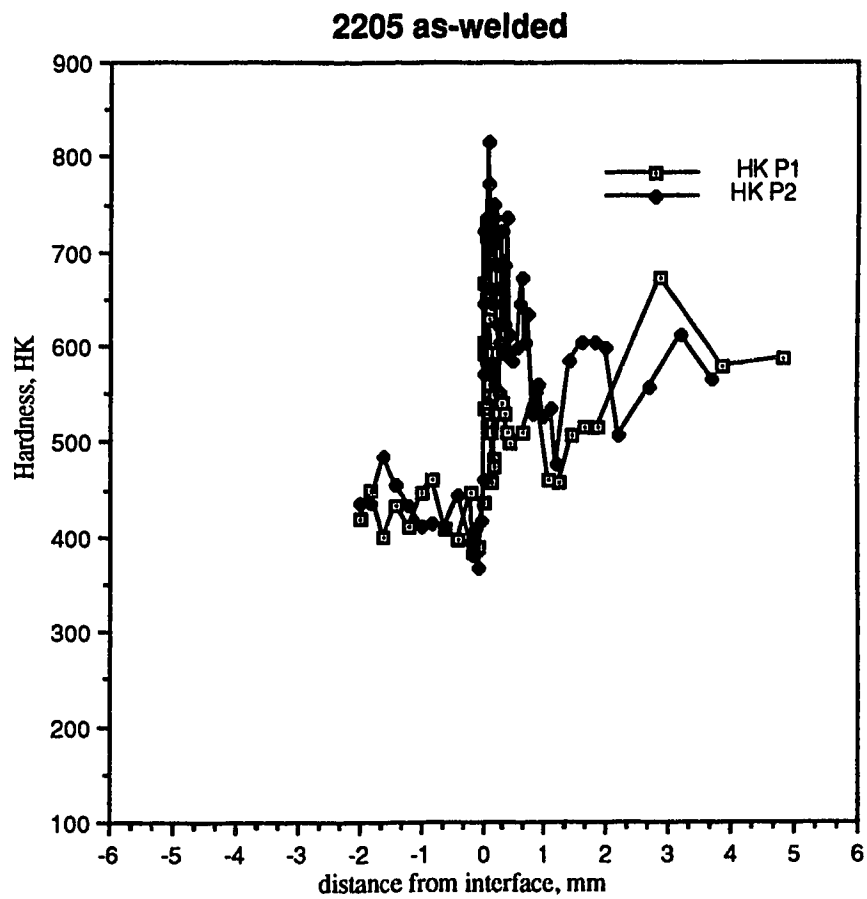


Figure 32 Microhardness of 2205 across interface, as-welded.

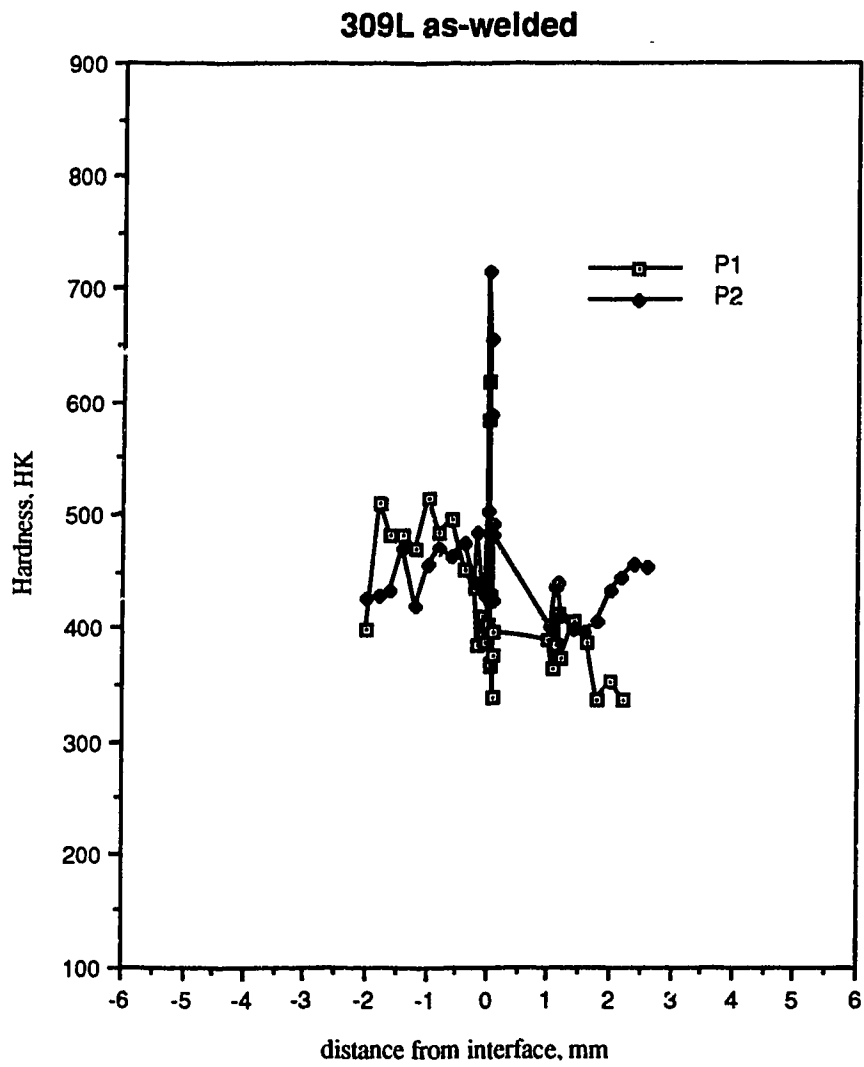


Figure 33 Microhardness of 309L across interface, as-welded.

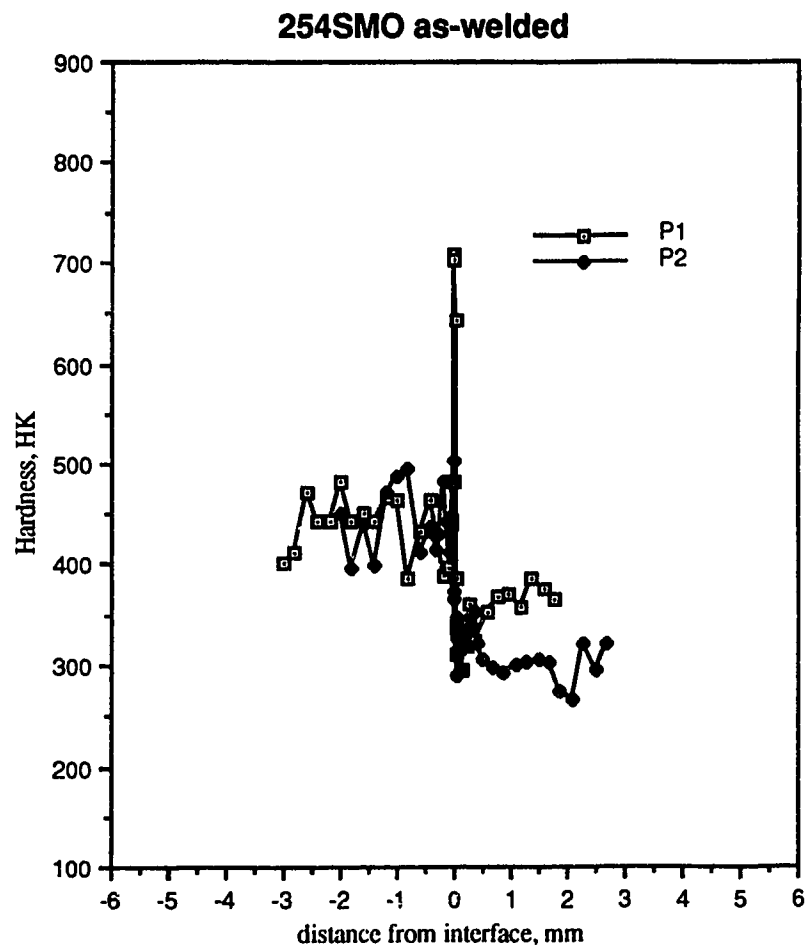


Figure 34 Microhardness of 254SMO across interface, as-welded.

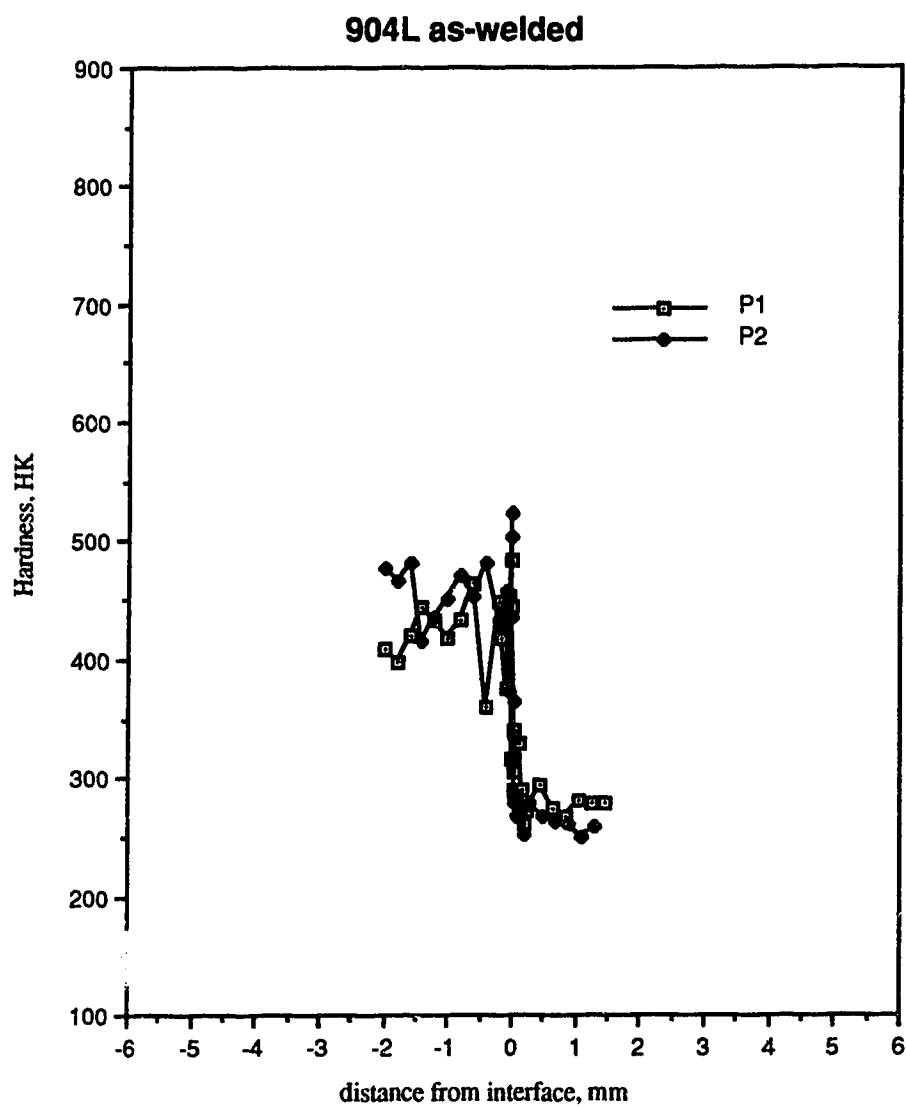


Figure 35 Microhardness of 904L across interface, as-welded

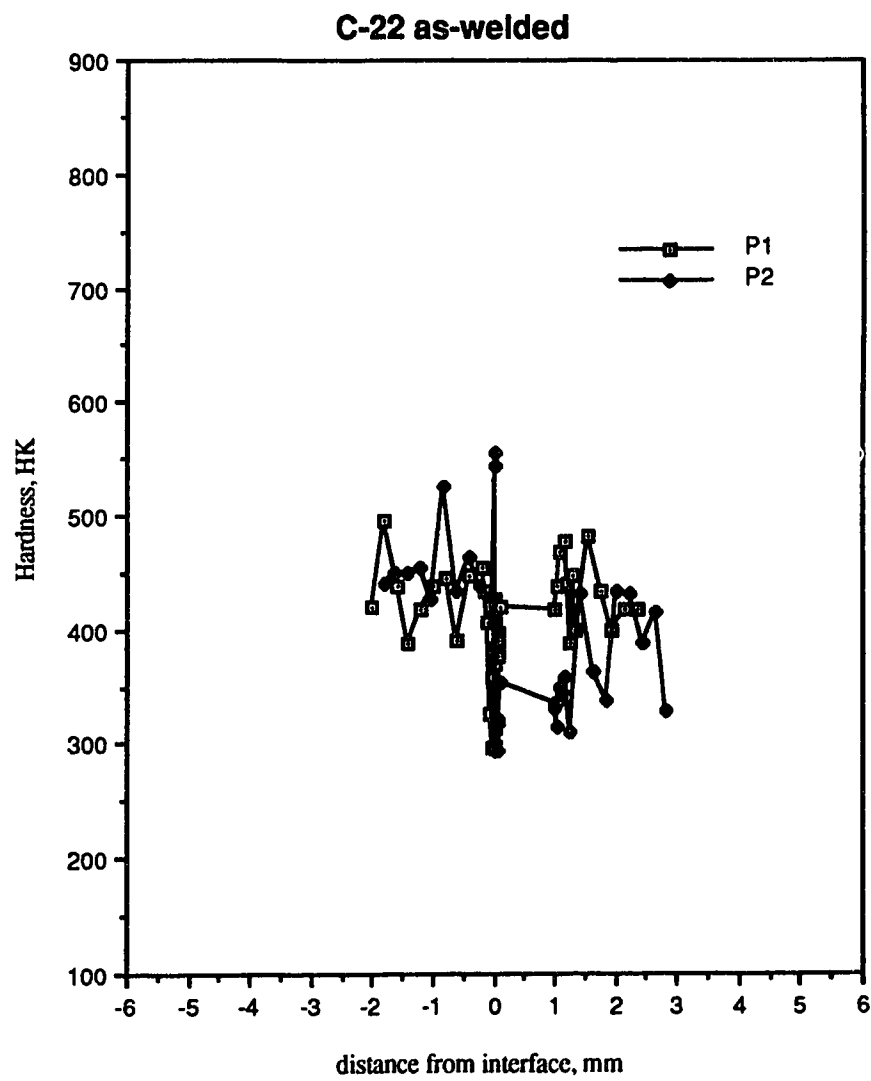


Figure 36 Microhardness of C-22 across interface, as-welded

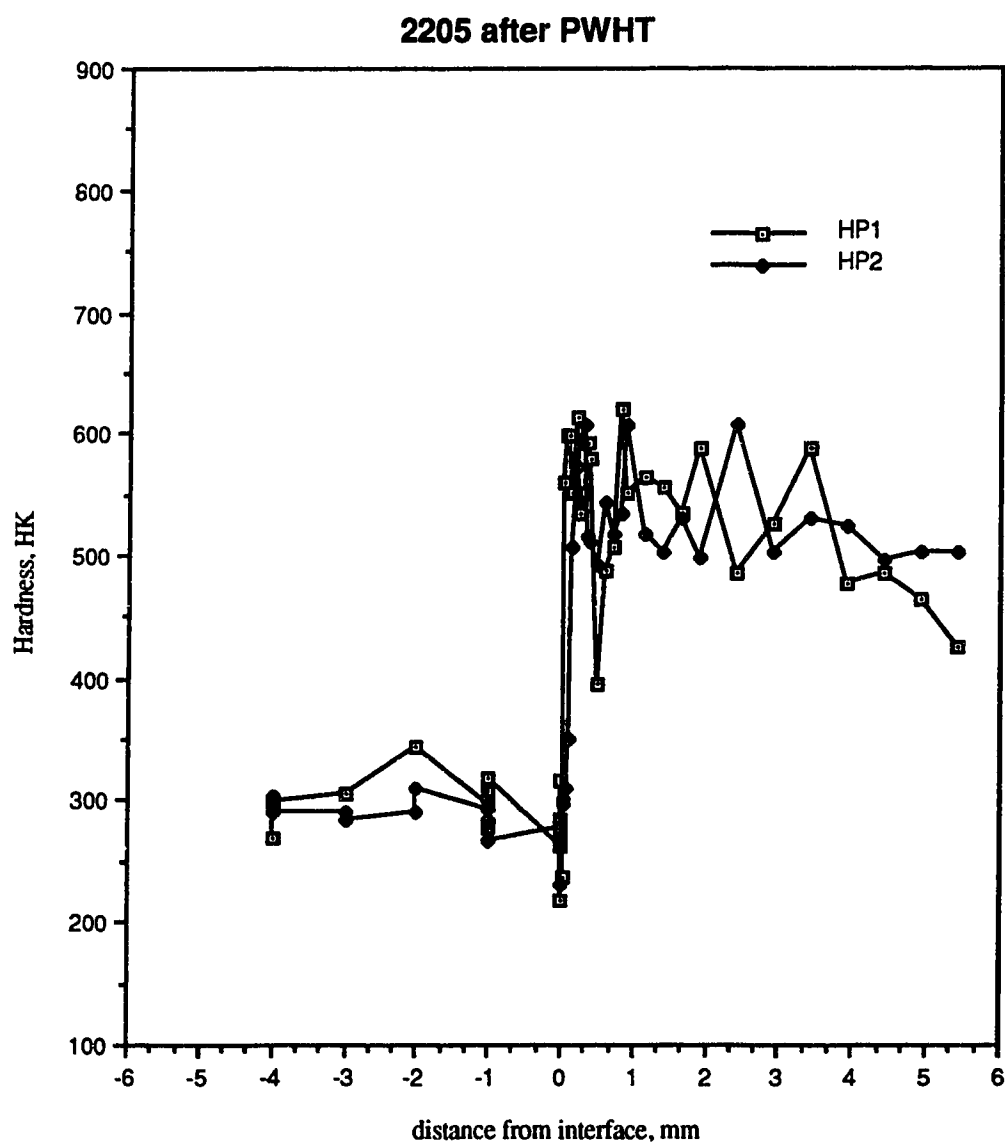


Figure 37 Microhardness of 2205 across interface, after PWHT.

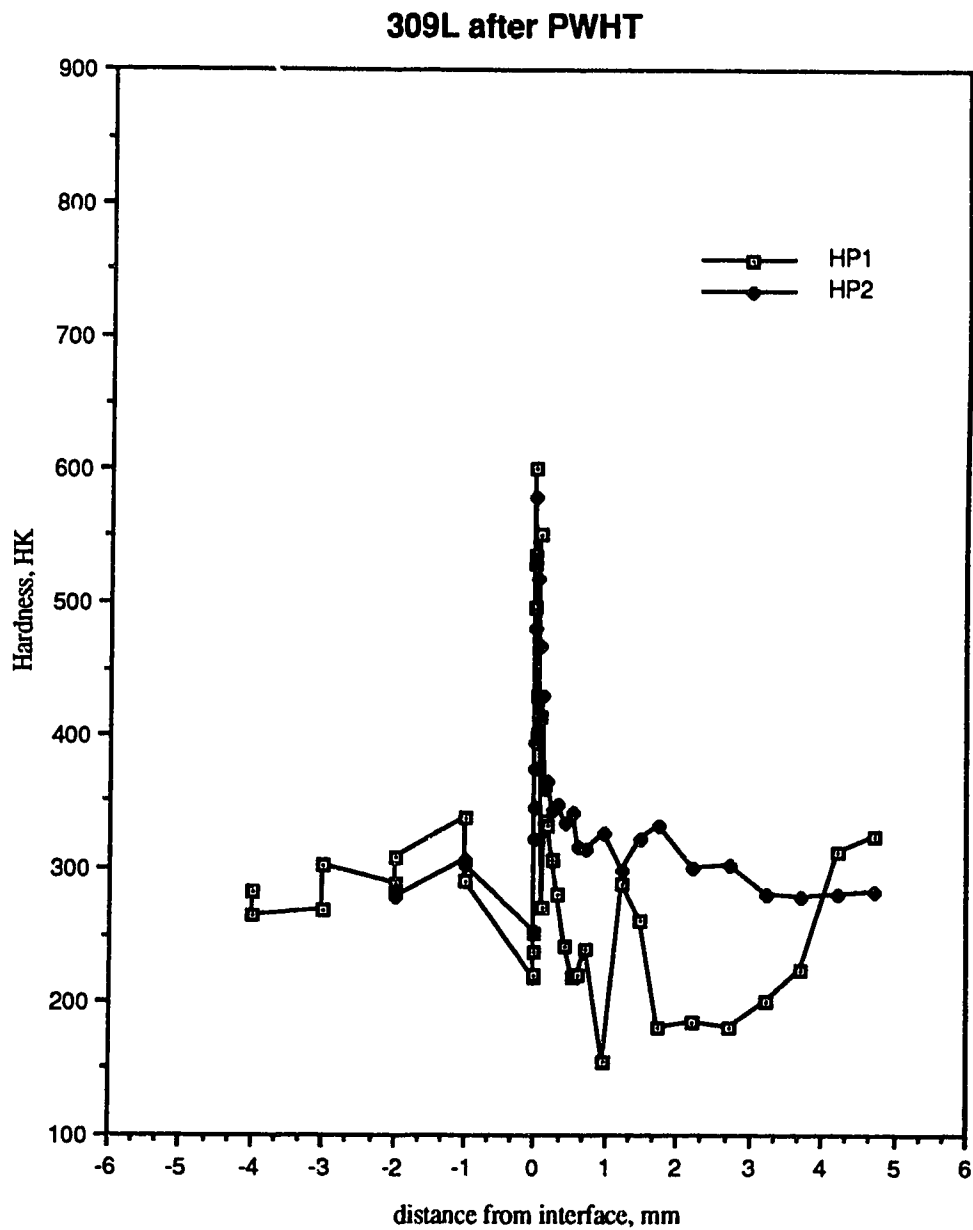


Figure 38 Microhardness of 309L across interface, after PWHT.

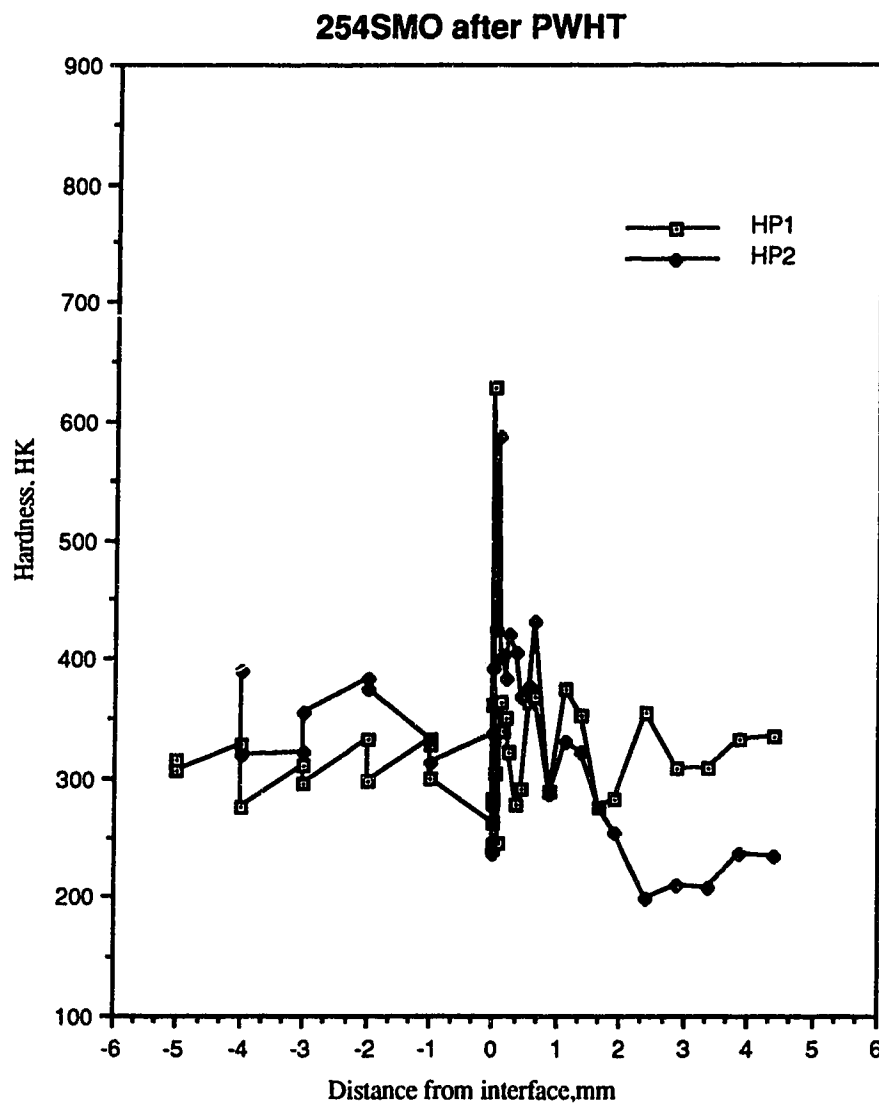


Figure 39 Microhardness of 254SMO across interface, after PWHT

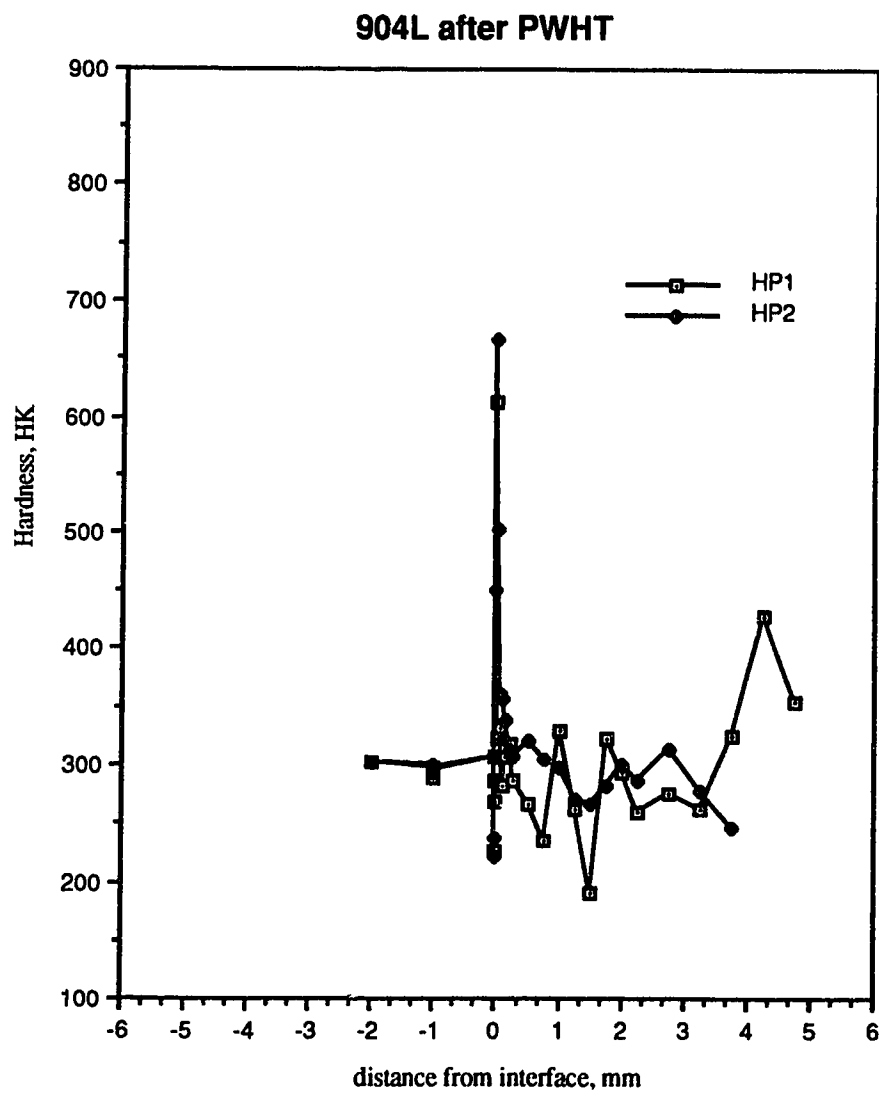


Figure 40 Microhardness of 904L across interface, after PWHT.

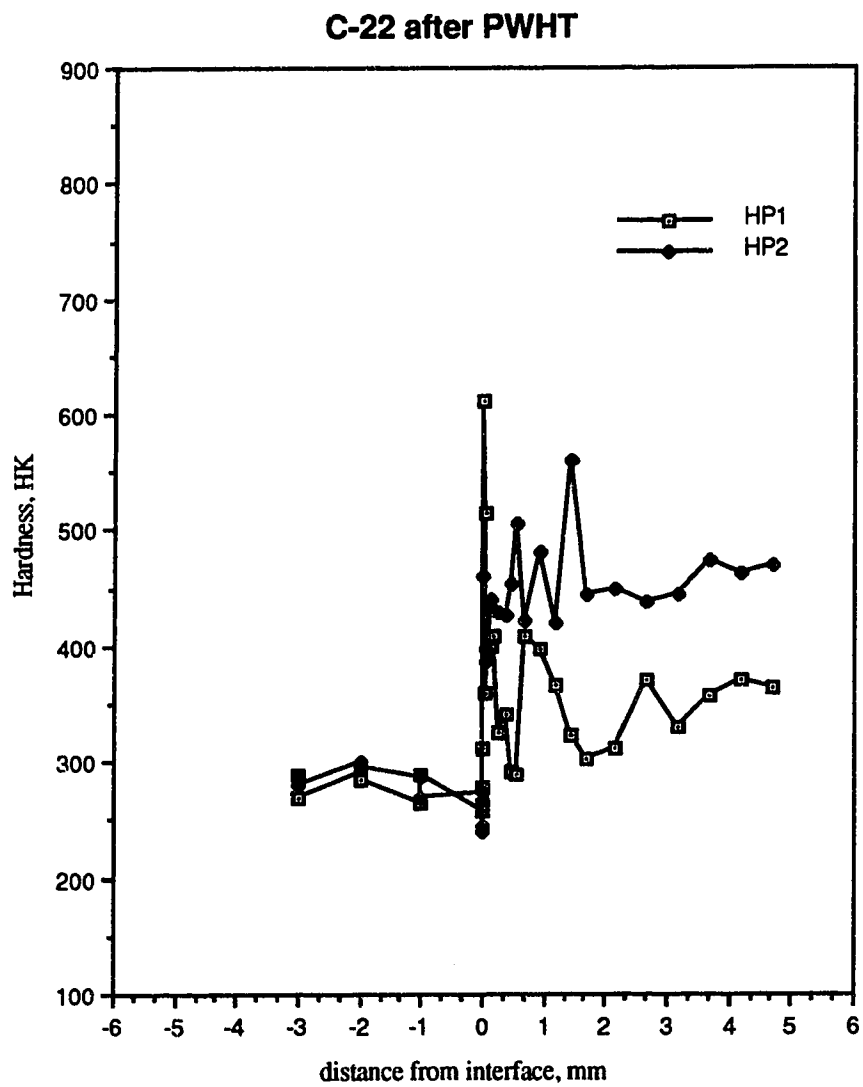


Figure 41 Microhardness of C-22 across interface, after PWHT.

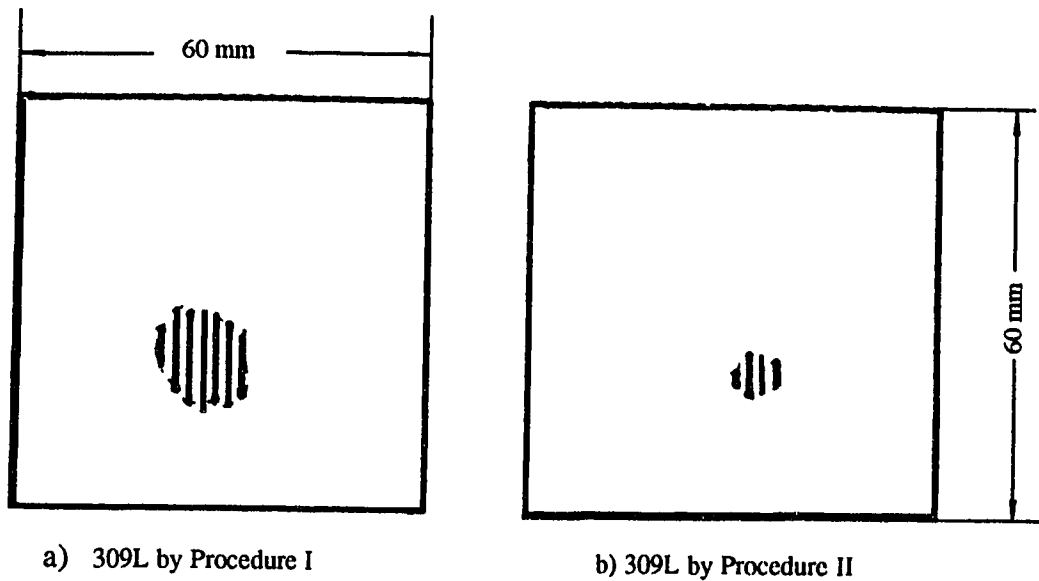


Fig. 42 C-Scan plot revealing disbonding in Overlay 309L after autoclave test.

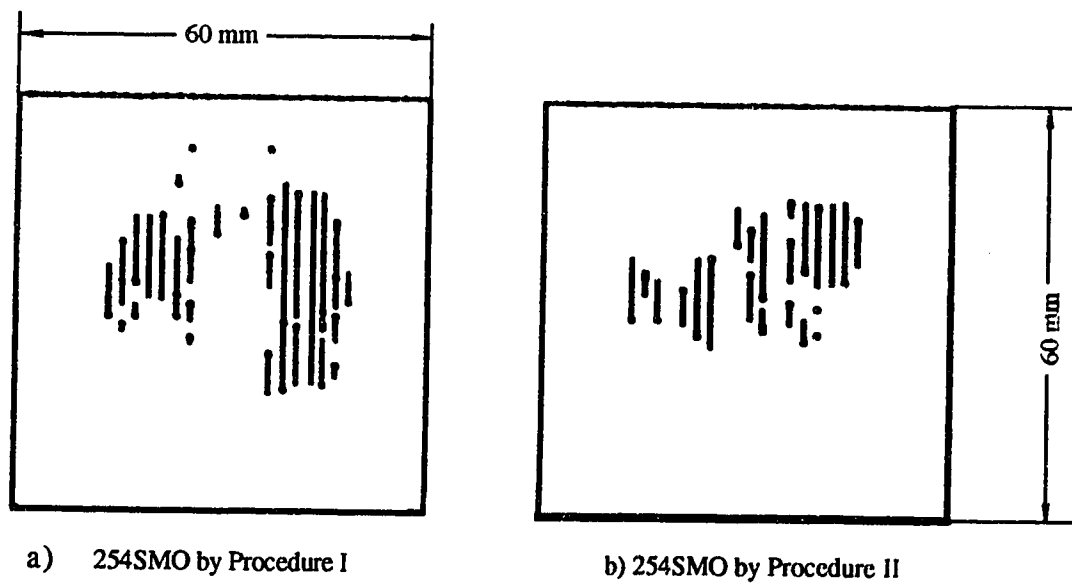


Fig. 43 C-Scan plot revealing disbonding in Overlay 254SMO after autoclave test.



Fig. 44 Optical microstructure of Specimen 2205 by Procedure I, as-welded.



Fig. 45 Optical microstructure of Specimen 2205 by Procedure II, as-welded

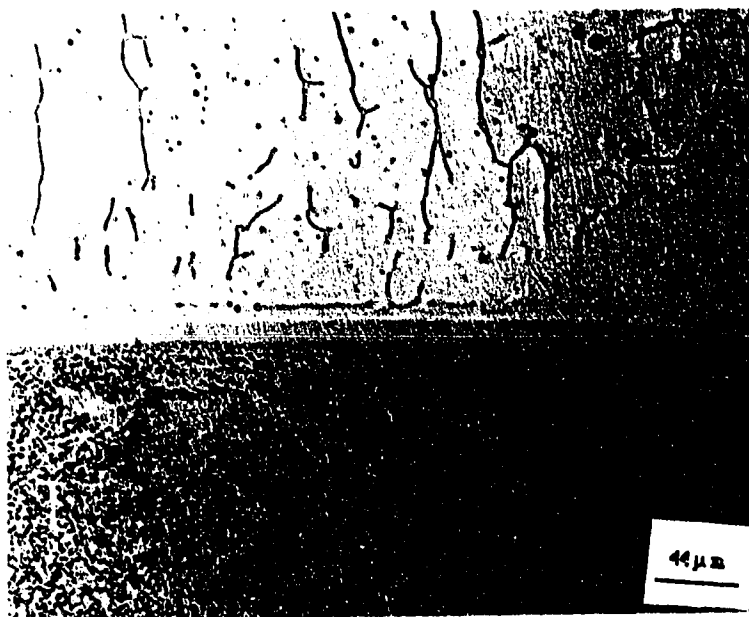


Fig. 46 Optical microstructure of Specimen 309L by Procedure I, as-welded.

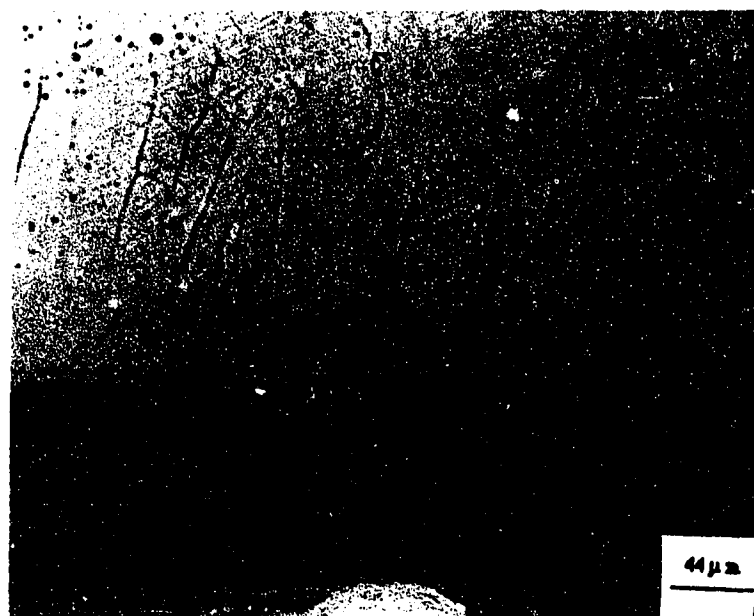


Fig. 47 Optical microstructure of Specimen 309L by Procedure II, as-welded.

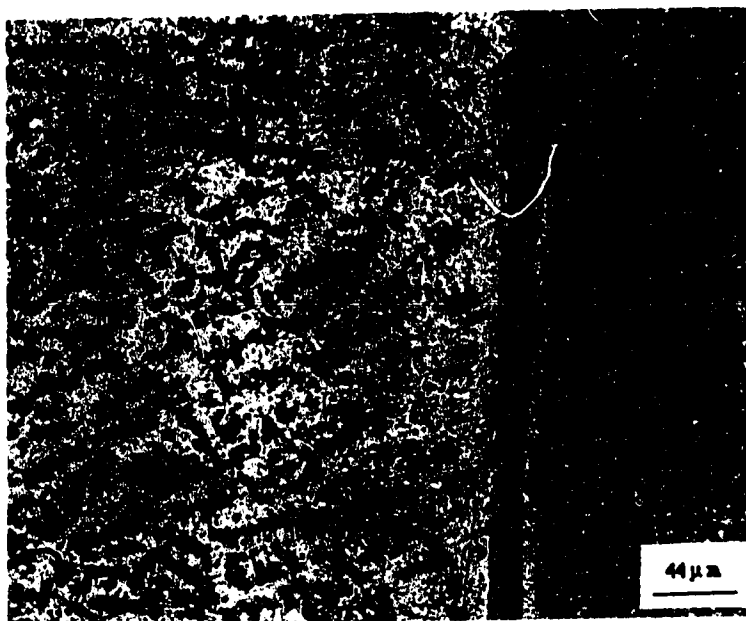


Fig. 48 Optical microstructure of Specimen 309LMo by Procedure I, as-welded

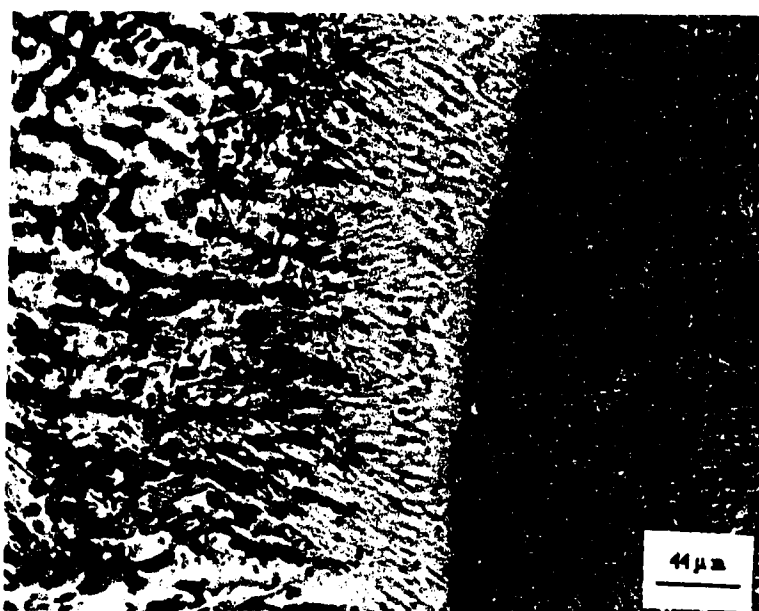


Fig. 49 Optical microstructure of Specimen 309LMo by Procedure II, as-welded.

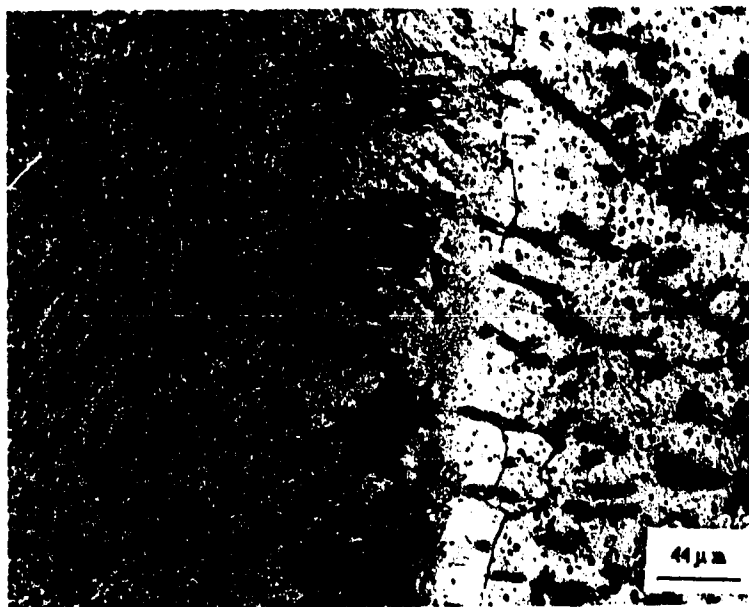


Fig. 50 Optical microstructure of Specimen 309LNb by Procedure I, as-welded.



Fig. 51 Optical microstructure of Specimen 309LNb by Procedure II, as-welded.

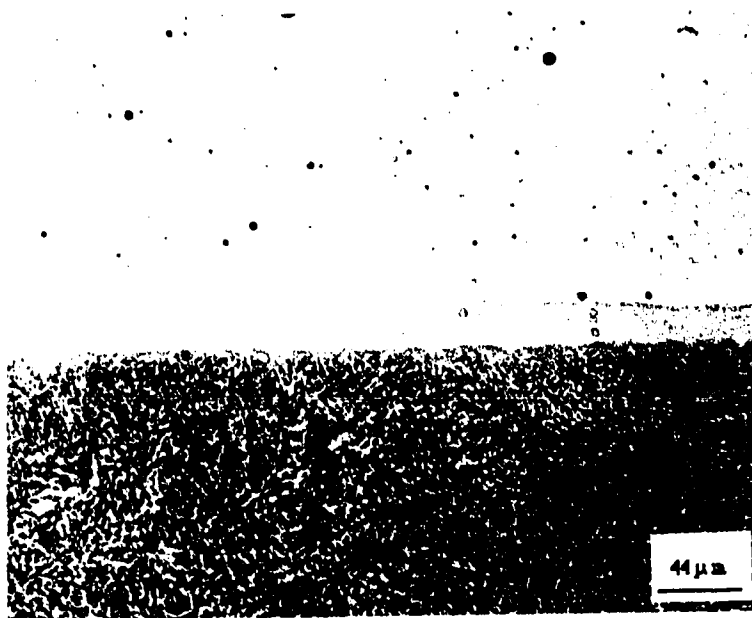


Fig. 52 Optical microstructure of Specimen 254SMO by Procedure I, as-welded.



Fig. 53 Optical microstructure of Specimen 254SMO by Procedure II, as-welded.

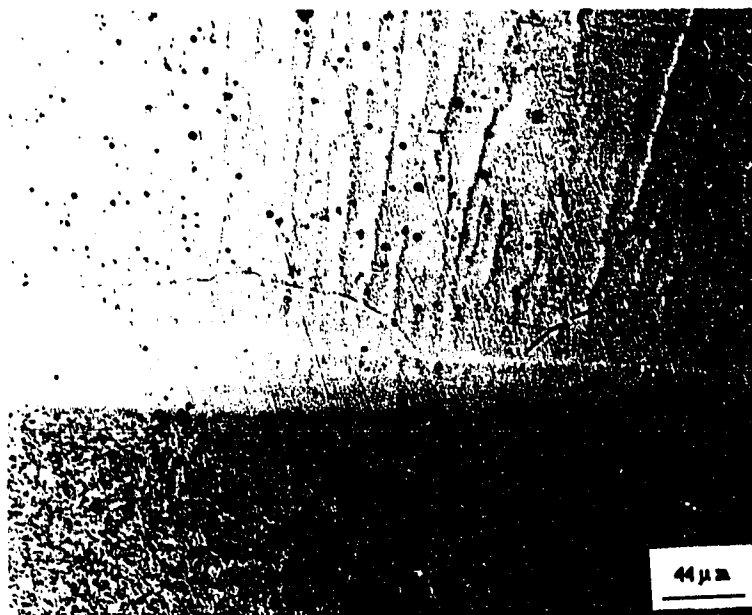


Fig. 54 Optical microstructure of Specimen 904L by Procedure I, as-welded.

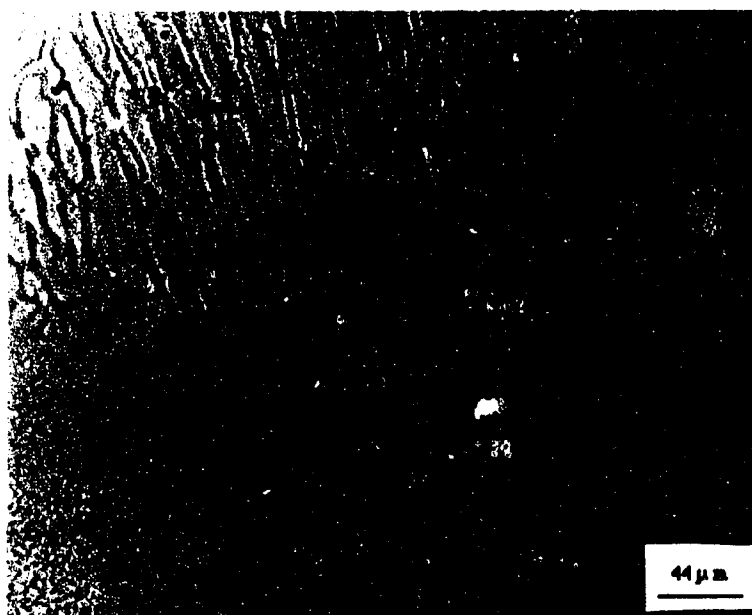


Fig. 55 Optical microstructure of Specimen 904L by Procedure II, as-welded.

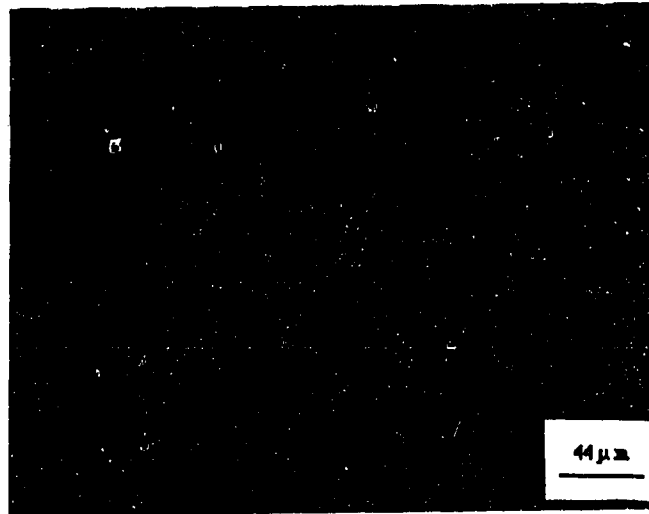


Fig. 56 Optical microstructure of Specimen C-22 by Procedure I, as-welded.

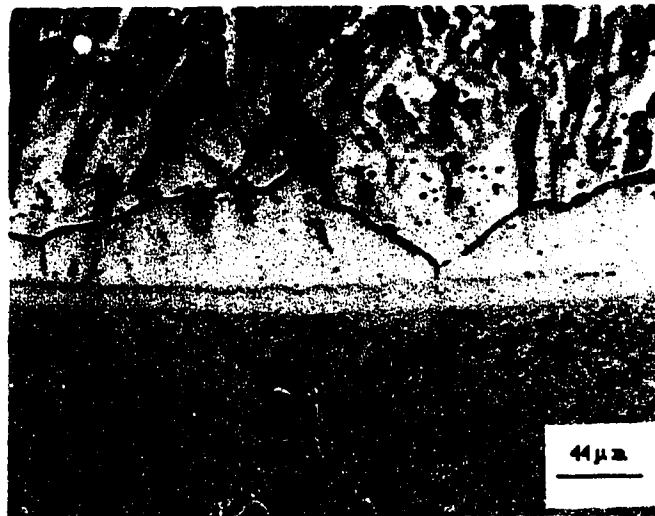


Fig. 57 Optical microstructure of Specimen C-22 by Procedure II, as-welded.

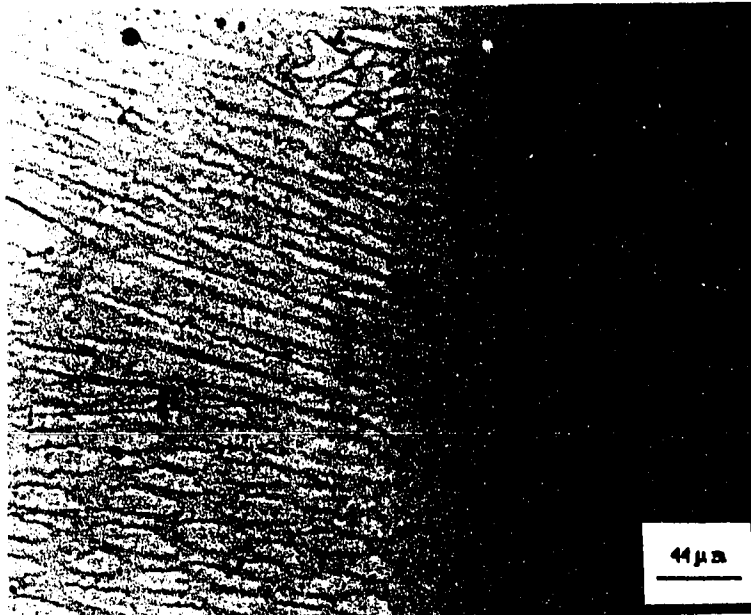


Fig. 58 Optical microstructure of Specimen 5923 by Procedure I, as-welded.

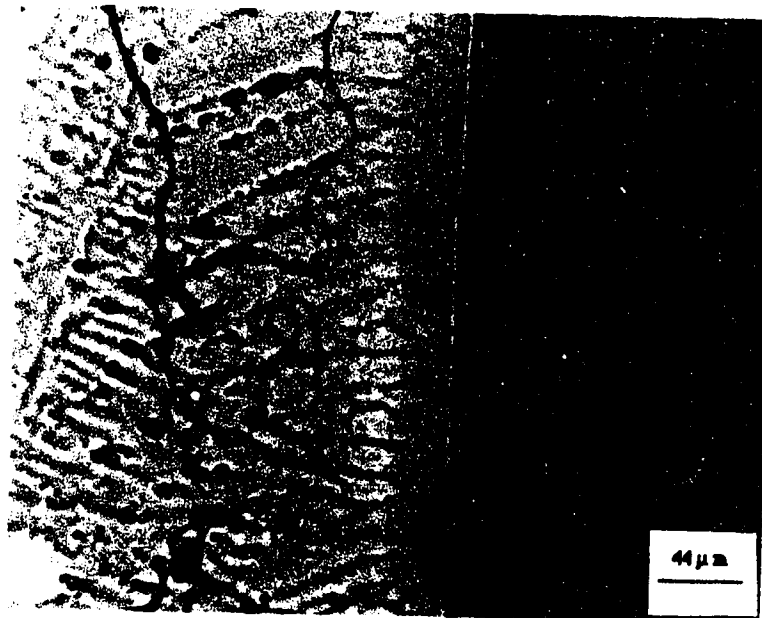


Fig. 59 Optical microstructure of Specimen 5923 by Procedure II, as-welded.

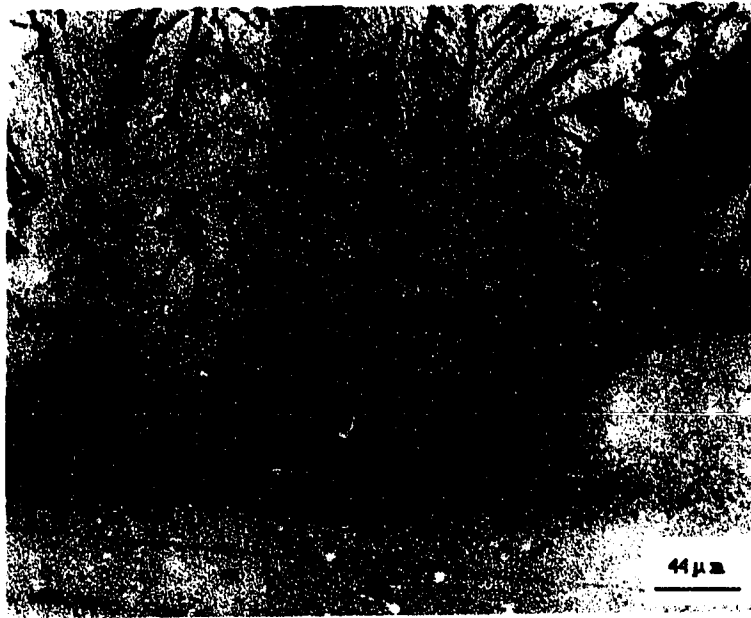


Fig. 60 Optical microstructure of Specimen 2205 by Procedure I, after PWHT.

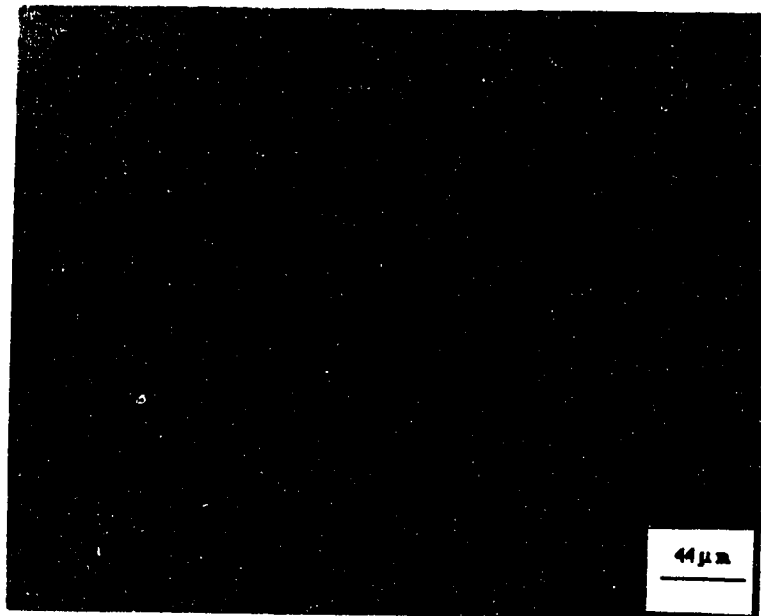


Fig. 61 Optical microstructure of Specimen 2205 by Procedure II, after PWHT.

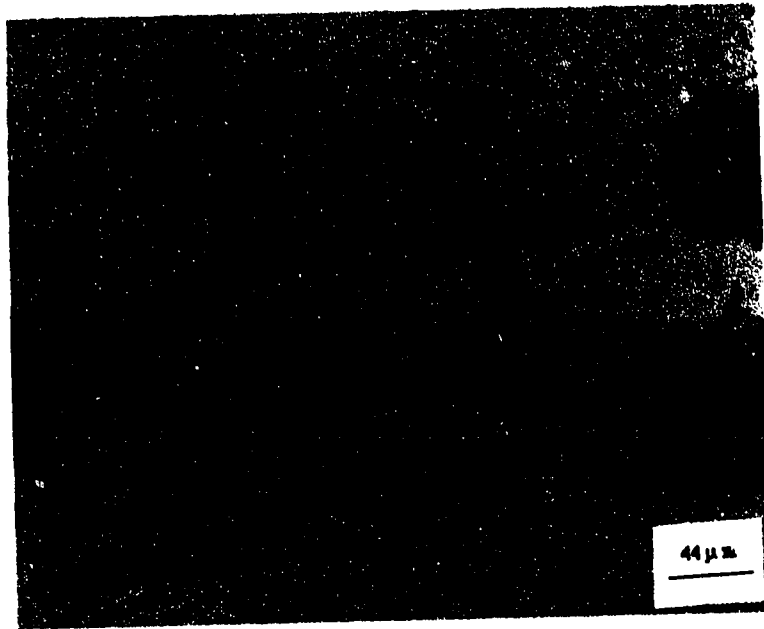


Fig. 62 Optical microstructure of Specimen 309L by Procedure I, after PWHT.

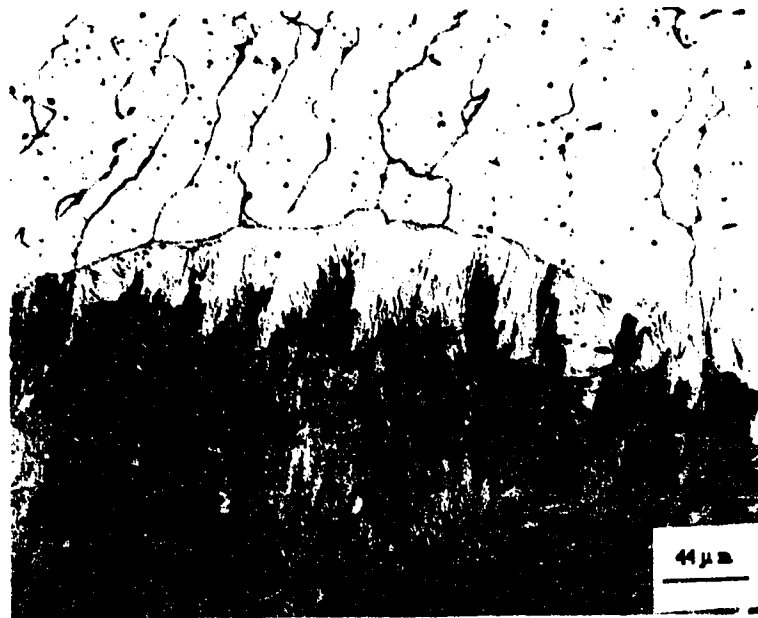


Fig. 63 Optical microstructure of Specimen 309L by Procedure II, after PWHT.

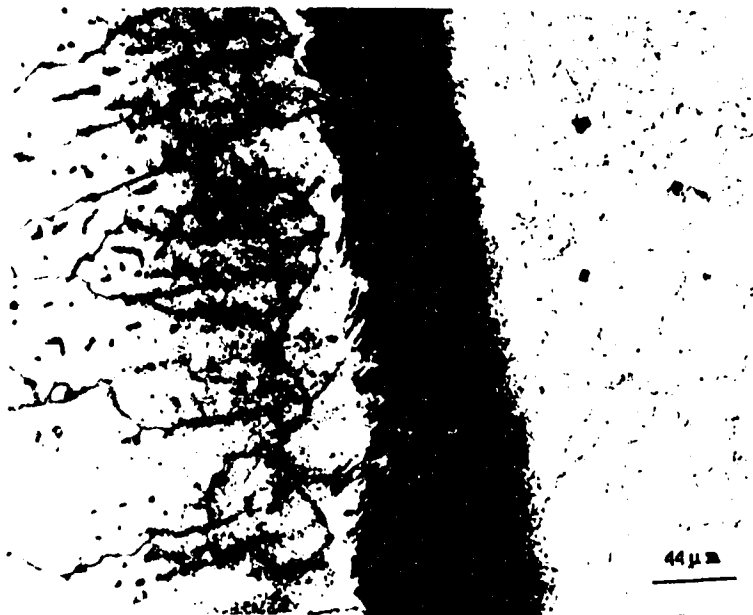


Fig. 64 Optical microstructure of Specimen 309LMo by Procedure I, after PWHT.

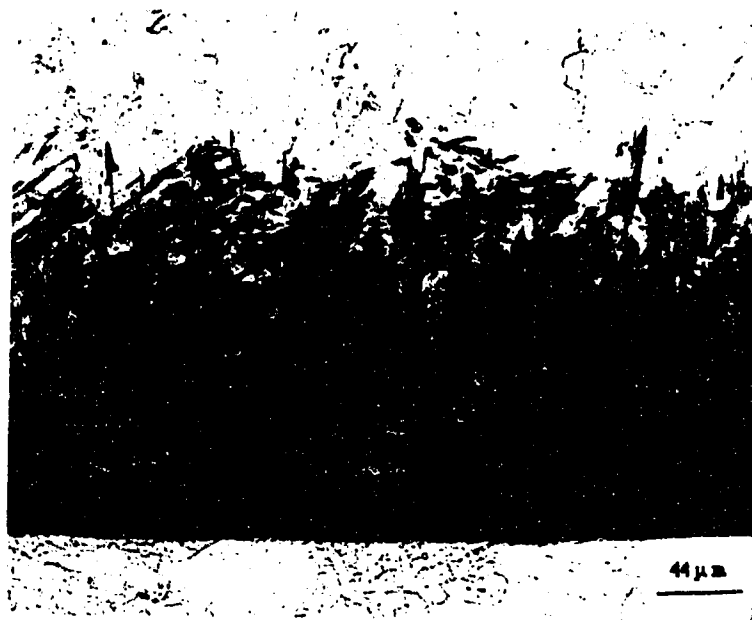


Fig. 65 Optical microstructure of Specimen 309LMo by Procedure II, after PWHT.

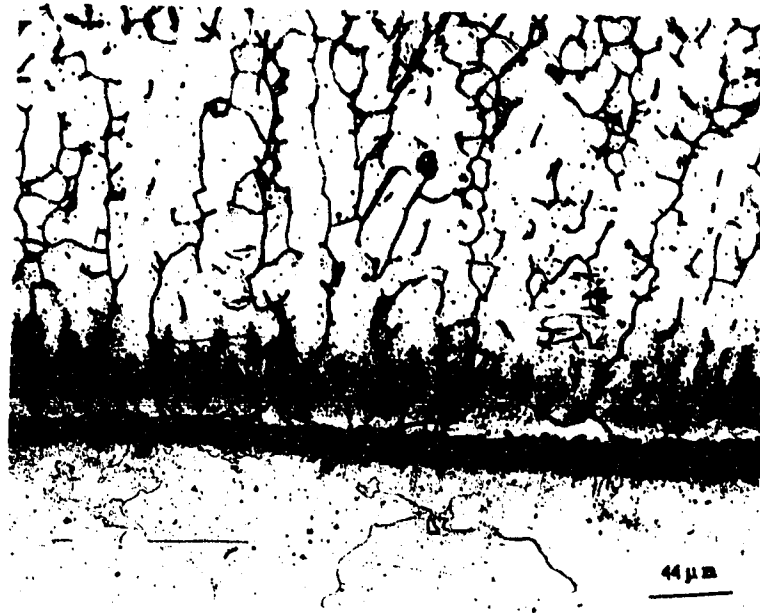


Fig. 66 Optical microstructure of Specimen 309LNb by Procedure I, after PWHT.



Fig. 67 Optical microstructure of Specimen 309LNb by Procedure II, after PWHT.

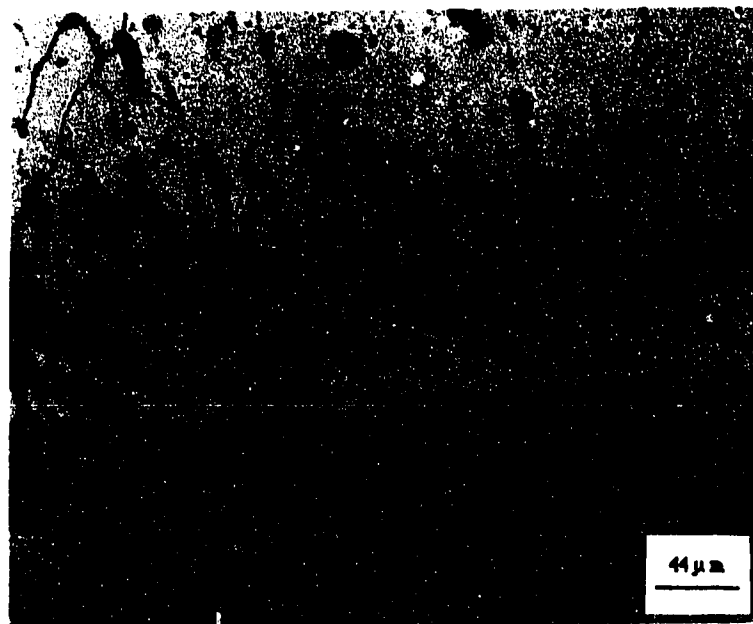


Fig. 68 Optical microstructure of Specimen 254SMO by Procedure I, after PWHT.

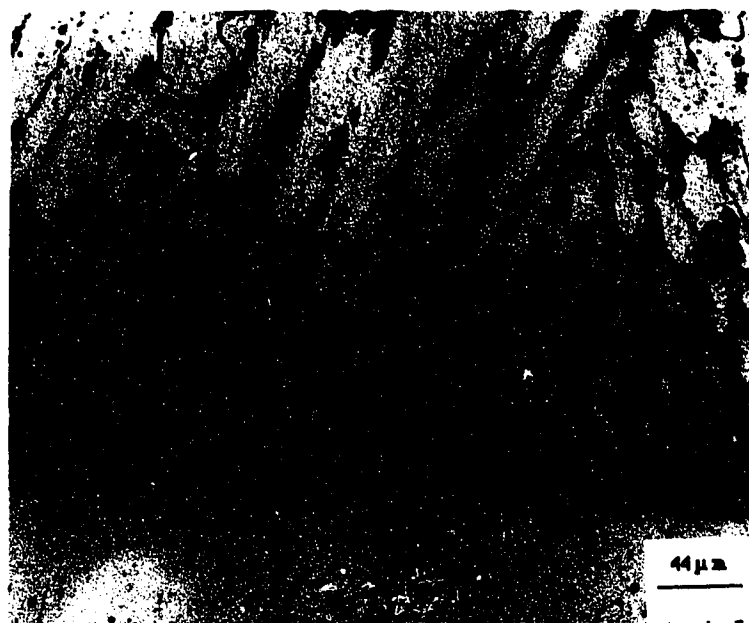


Fig. 69 Optical microstructure of Specimen 254SMO by Procedure II, after PWHT.



Fig. 70 Optical microstructure of Specimen 904L by Procedure I, after PWHT.

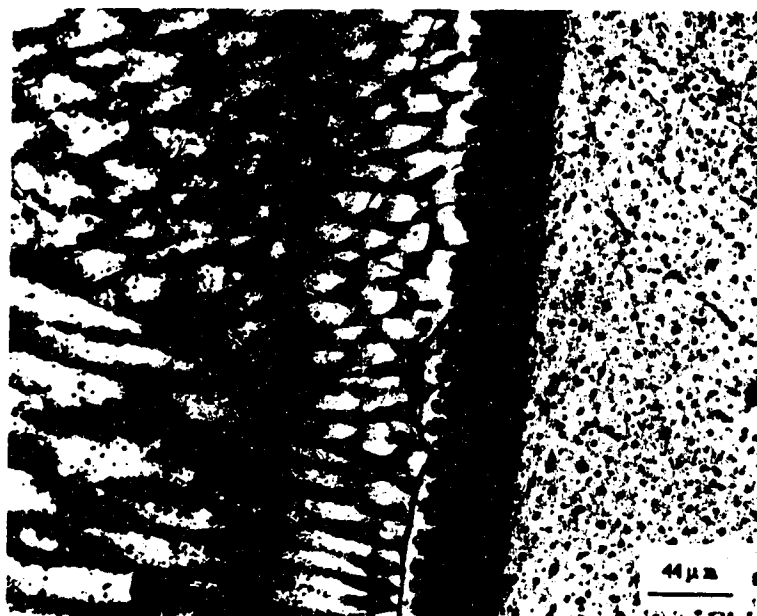


Fig. 71 Optical microstructure of Specimen 904L by Procedure II, after PWHT.



Fig. 72 Optical microstructure of Specimen C-22 by Procedure I, after PWHT.



Fig. 73 Optical microstructure of Specimen C-22 by Procedure II, after PWHT.

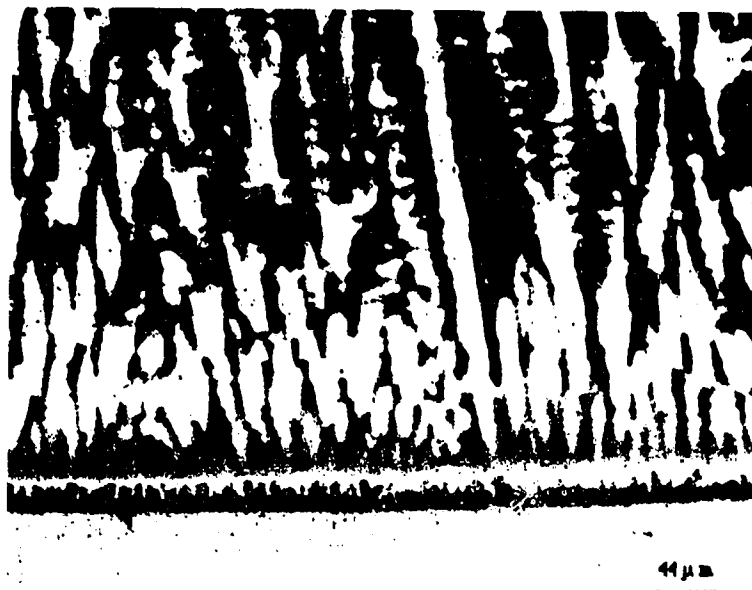


Fig. 74 Optical microstructure of Specimen 5923 by Procedure I, after PWHT.



Fig. 75 Optical microstructure of Specimen 5923 by Procedure II, after PWHT.

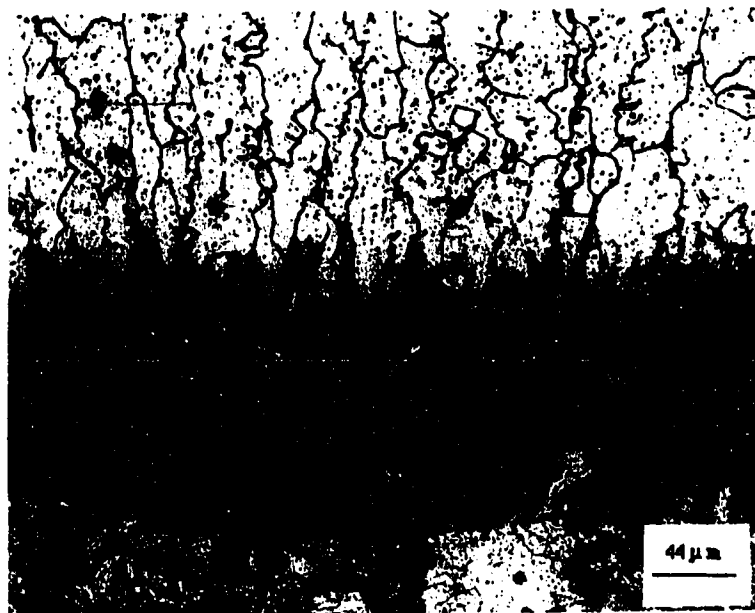


Fig. 76 Disbonding along Type II grain boundary in Overlay 309LMO.

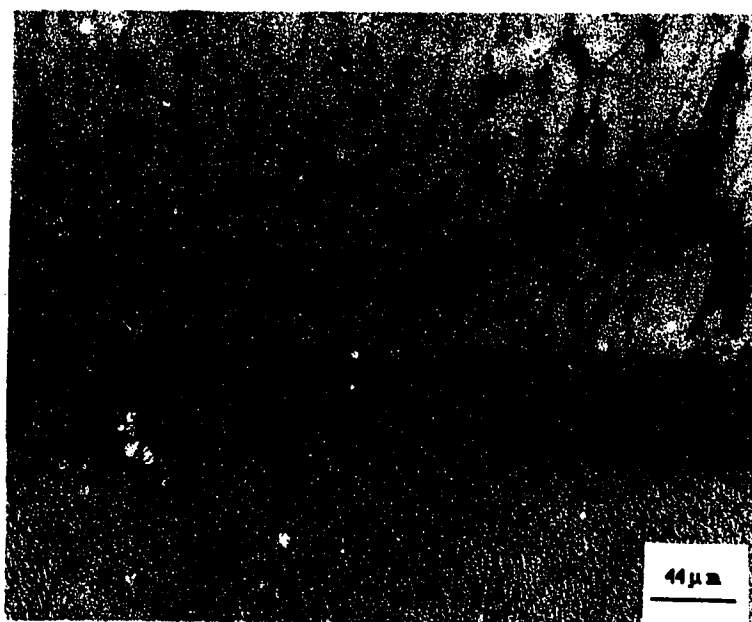


Fig. 77 Disbonding along Type II grain boundary in Overlay 254SMO.

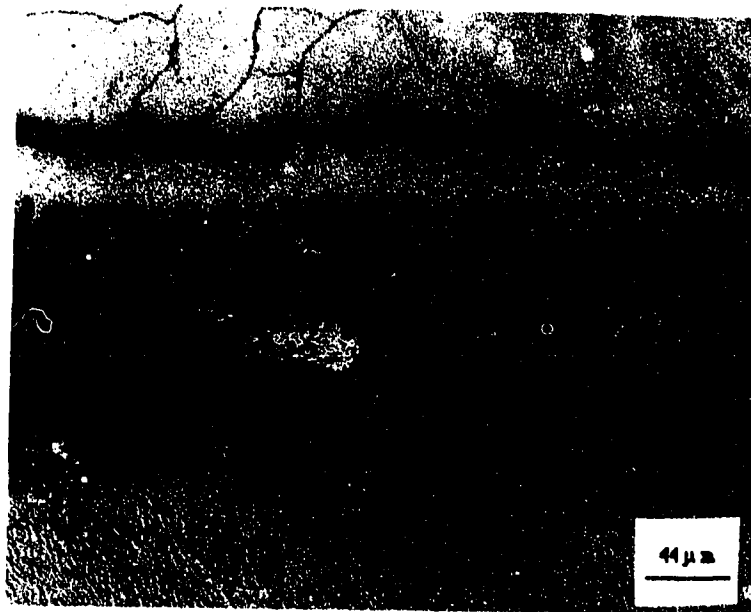


Fig. 78 Disbonding occurs parallel to the interface in Overlay 254SMO.

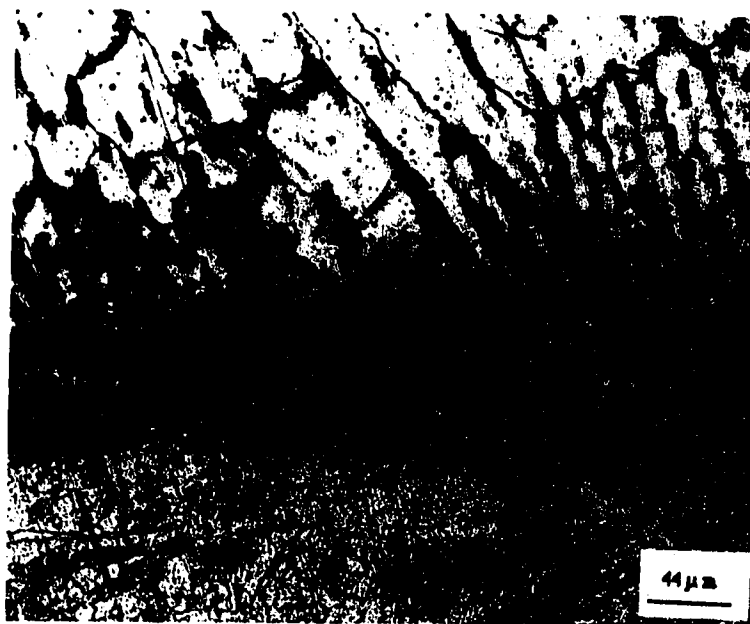


Fig. 79 Disbonding extending from Type II grain boundary to the bainite region.

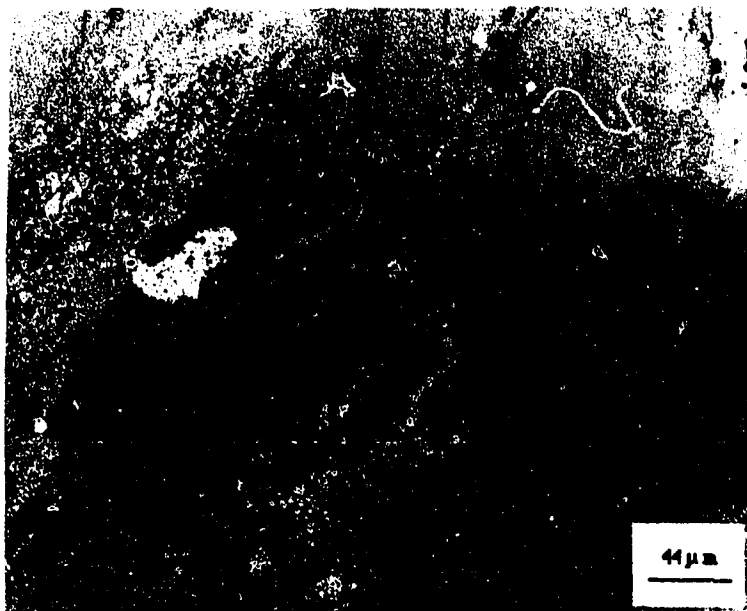


Fig. 80 Disbonding running along Type II grain and though bainite region in Overlay 254SMO.

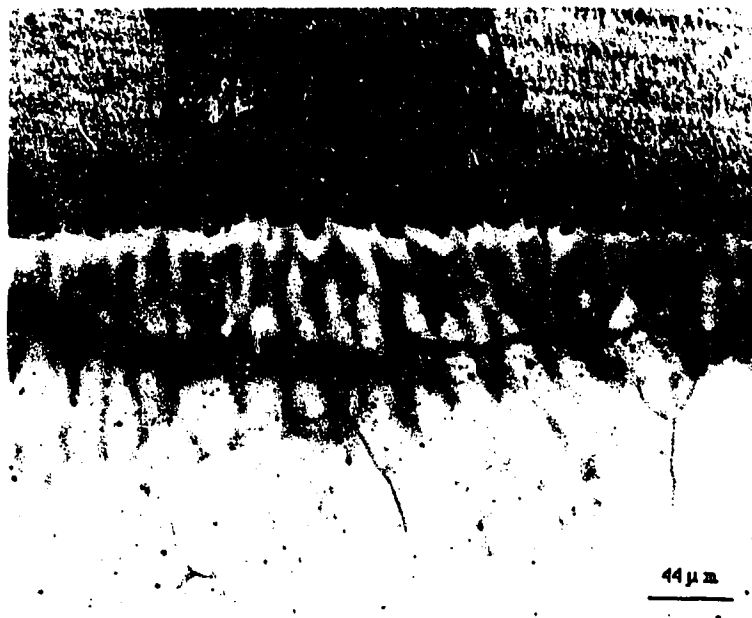


Fig. 81 Disbonding along Type II grain boundary in Overlay 904L.



Fig. 82 Cracking stops at the turning point of planar grain boundaries.

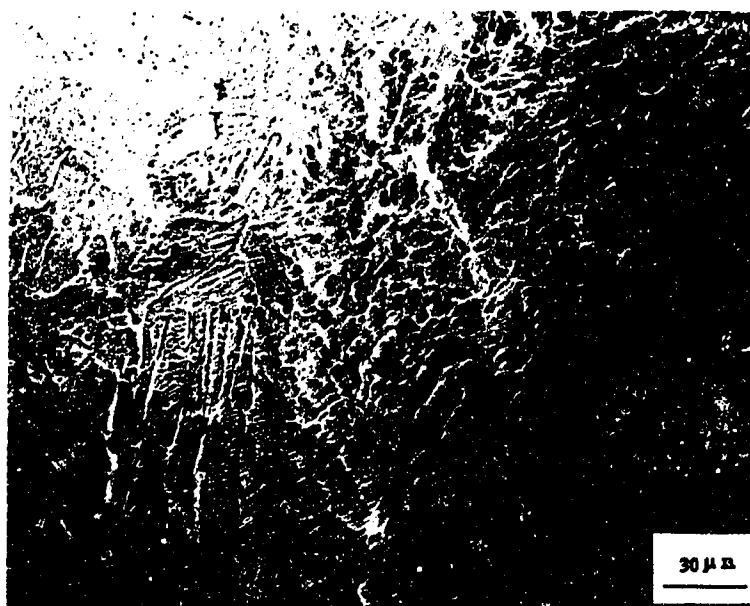
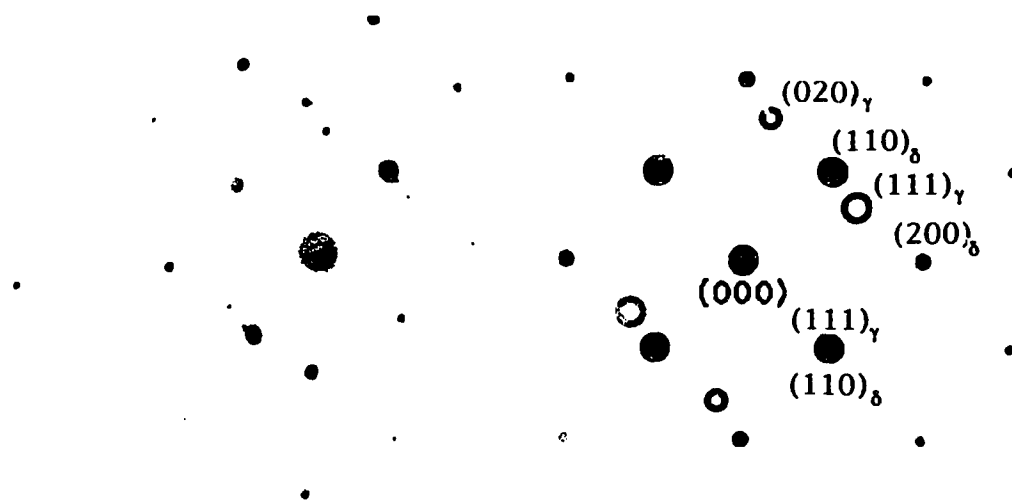


Fig. 83 Microstructure along fusion line in Overlay 2205.



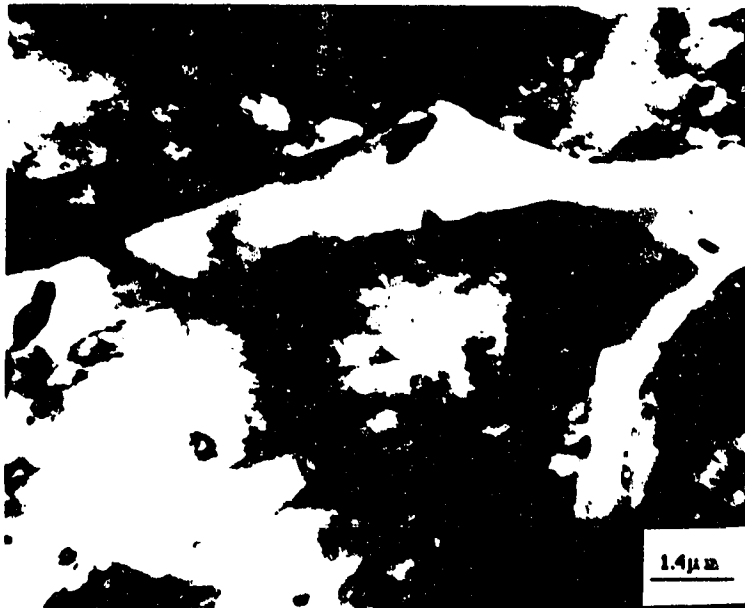
(a) Skeletal ferritic network and enveloped martensite and austenite



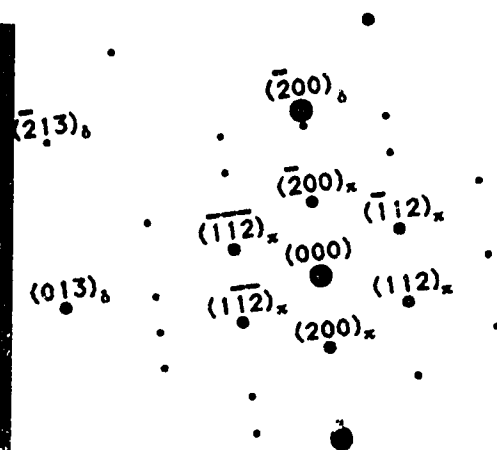
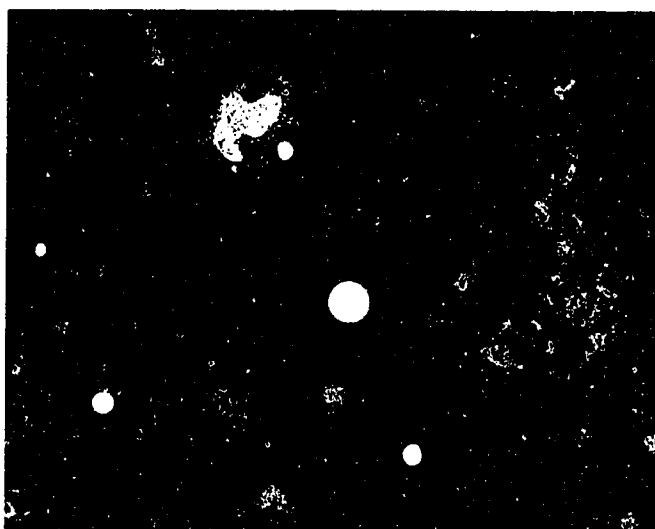
$$ZA_{\gamma} = [101], \quad ZA_{\delta} = [001]$$

(b) Diffraction pattern of the observed area. (c) Indexing of the diffraction pattern, showing the K - S relation between δ - ferrite and γ - austenite:
 $(111)\gamma // (110)\delta, [101]\gamma // [001]\delta.$

Fig. 84 Skeletal ferrite and enveloped martensite, austenite in the transition zone of Overlay 2205 as-welded.



(a) Precipitation in the skeletal ferrite and in the tempered martensite.



$$ZA_{\delta} = [031], \quad ZA_{\pi} = [021]$$

(b) Diffraction pattern of observed area. (c) Indexing of the diffraction pattern.

Fig. 85 Precipitation in skeletal ferrite and tempered martensite in Overlay 2205 after PWHT.

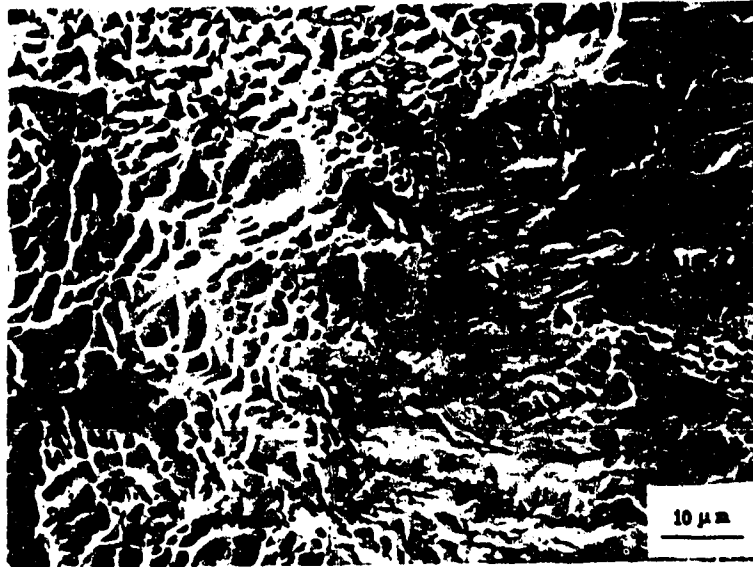


Fig. 86 Microstructure along fusion line between the base steel and the Overlay 254SMO.

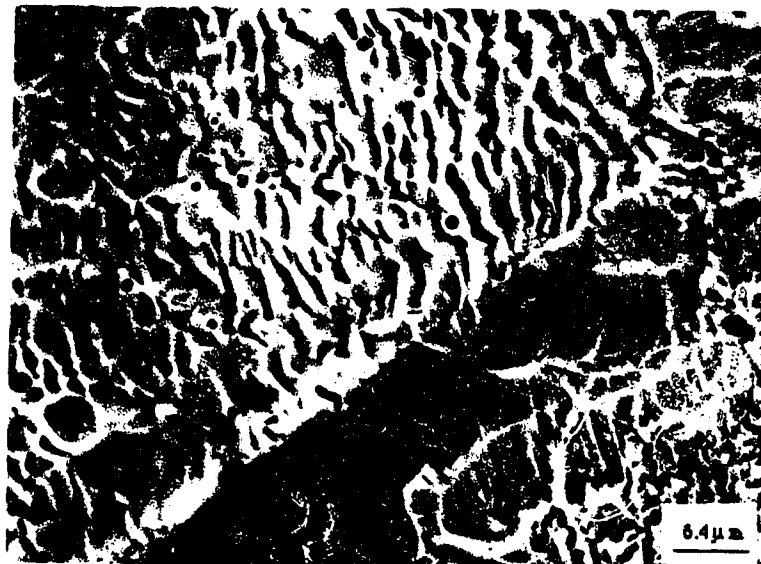


Fig. 87 Type II grain boundary in Overlay 254SMO observed on SEM.



Fig. 88 Fine martensite right on the interface between the base steel and Overlay 254SMO as-welded.



(a) Coarse bainitic structure in the transition zone from the base steel to Overlay 254SMO.



(b) Coarse bainitic structure intruding into the austenite at the end of the transition zone in Overlay 254SMO.

Fig. 89 Coarse bainitic structure in the transition zone from the base steel to Overlay 254SMO as-welded.

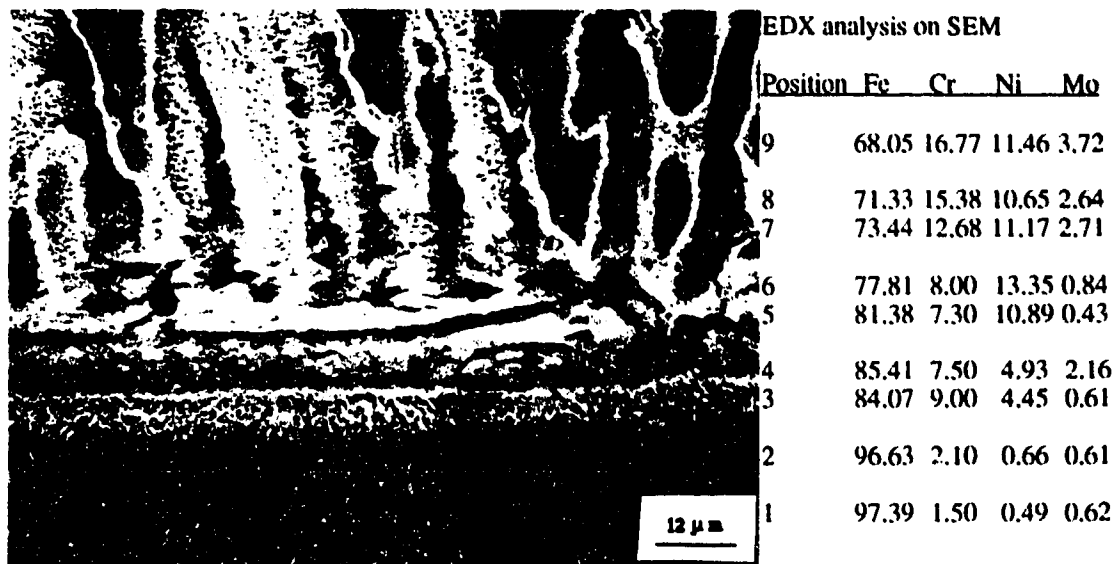


Fig. 90 Microstructure and EDX analysis around Type II grain boundary in Overlay 254SMO after PWHT on SEM.

Position	1	2	3	4
Fe	94.18	93.62	84.56	69.82
Cr	3.31	4.01	7.29	18.09
Ni	2.51	2.39	7.50	8.14
Mo		1.00	3.95	2.83



Fig. 91 Lathes of tempered martensite and precipitates at the root of the interface between the base steel and Overlay 309LMo after PWHT.

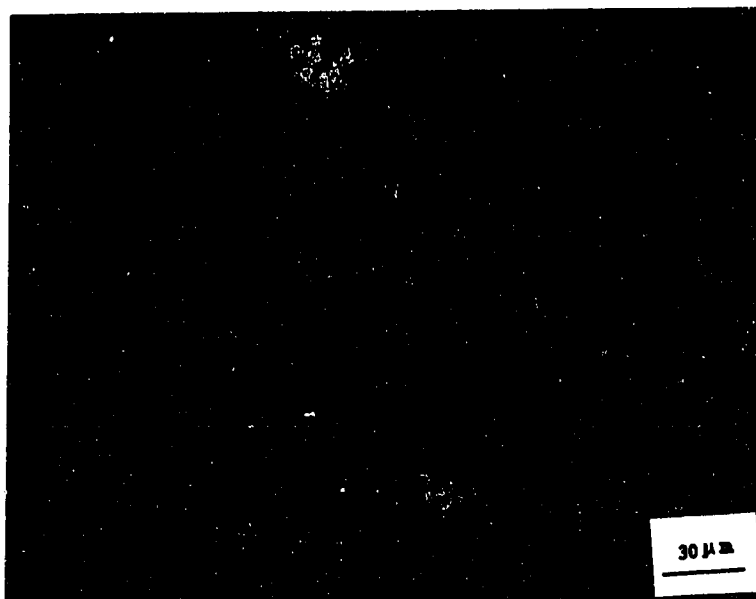


Fig. 92 A narrow planar grain boundary in Overlay C-22 as-welded.

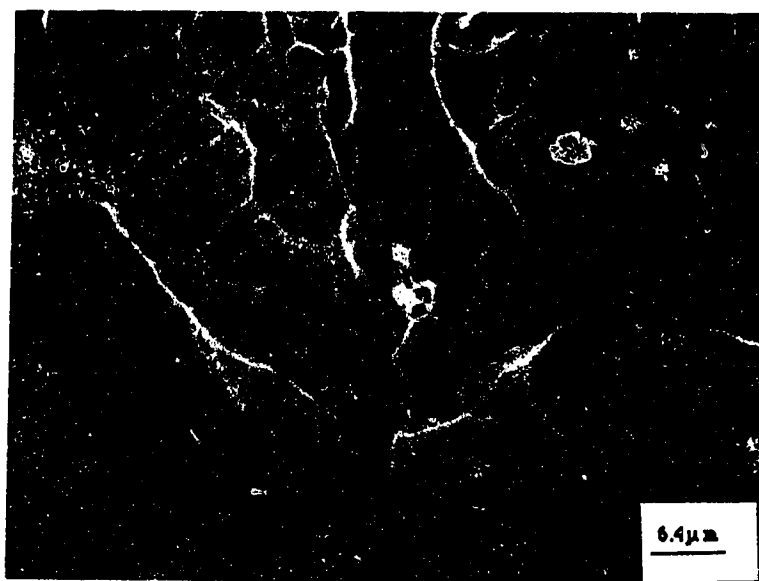


Fig. 93 A close look at the planar grain boundary in Overlay C-22, showing the trace of segregation on the boundary in as-welded condition.

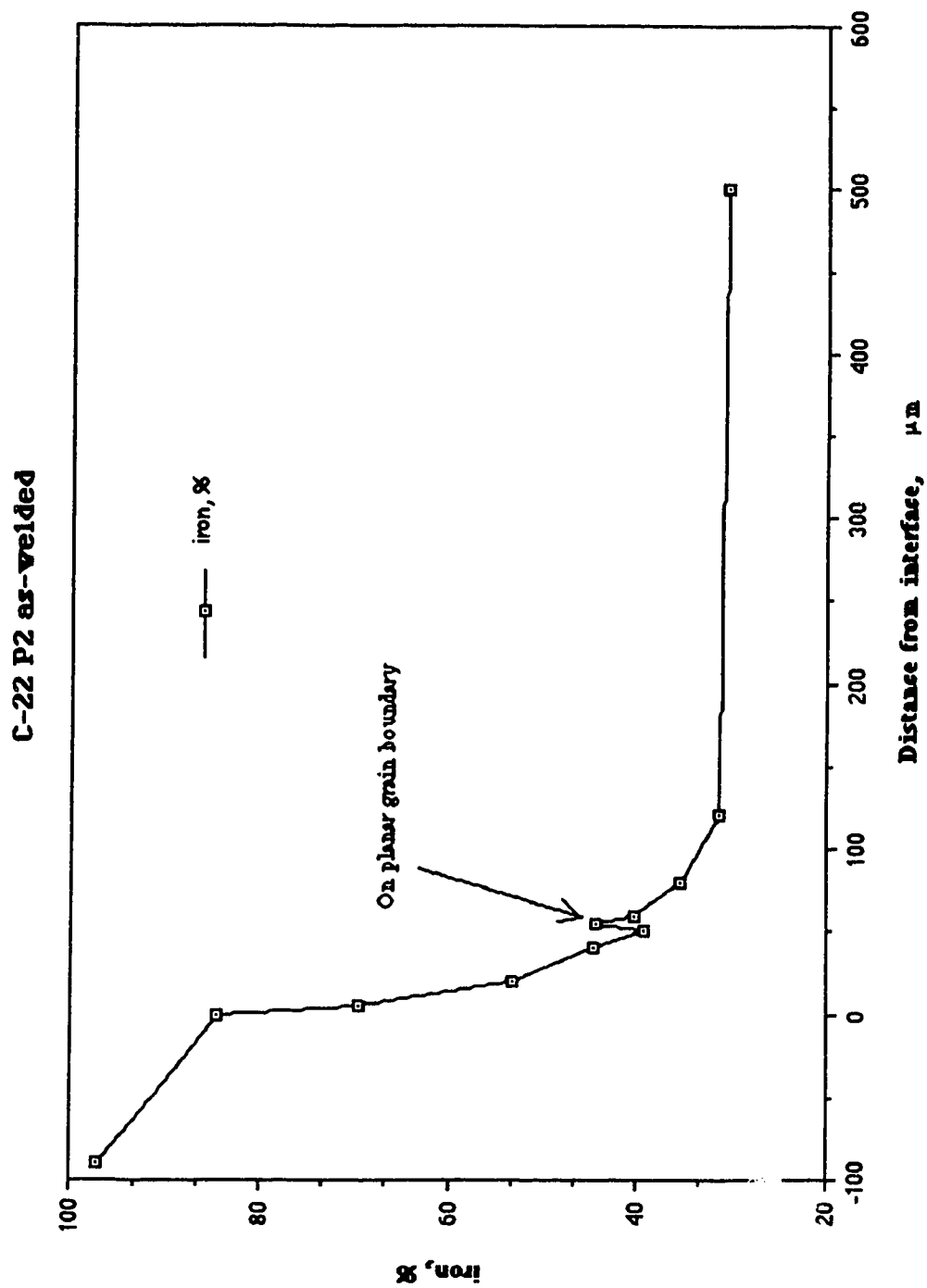
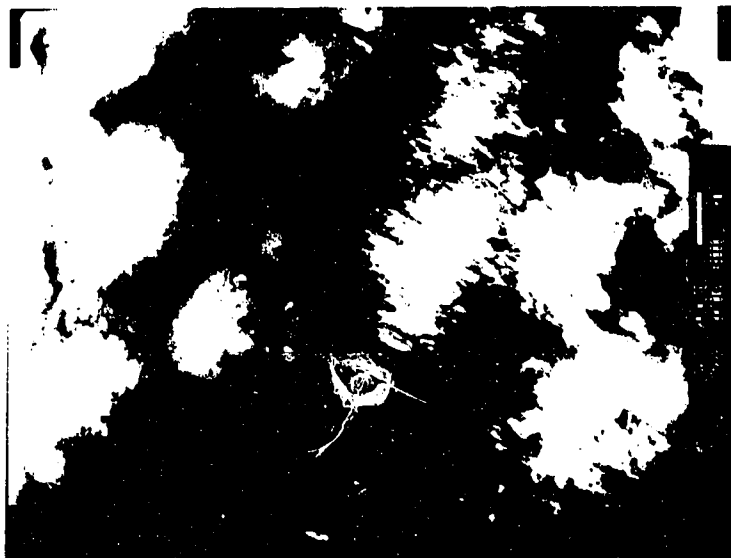
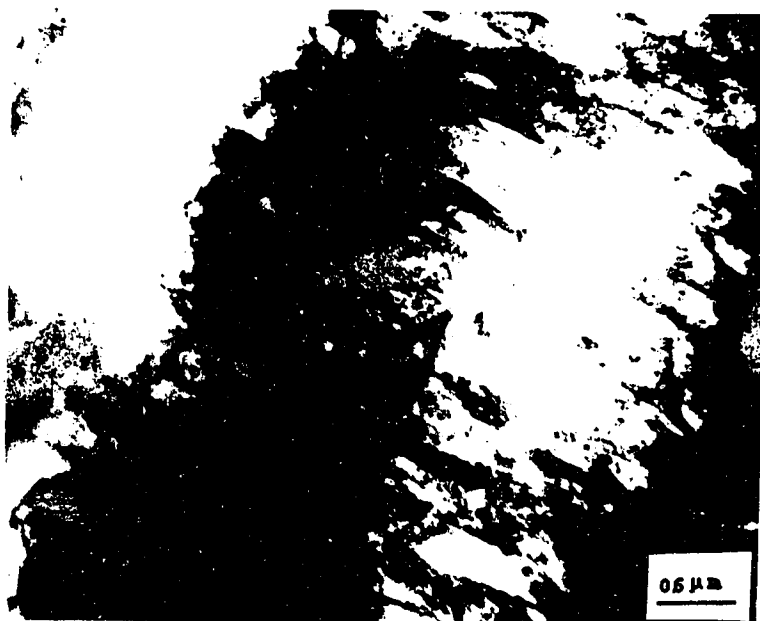


Fig. 94 EDX analysis of iron profile across the transition zone in Overlay C-22 as-welded by high current welding.



(a) A narrow band of martensite along the interface between the base steel and Overlay C-22 to adjust the transition of crystal structures aside the interface.

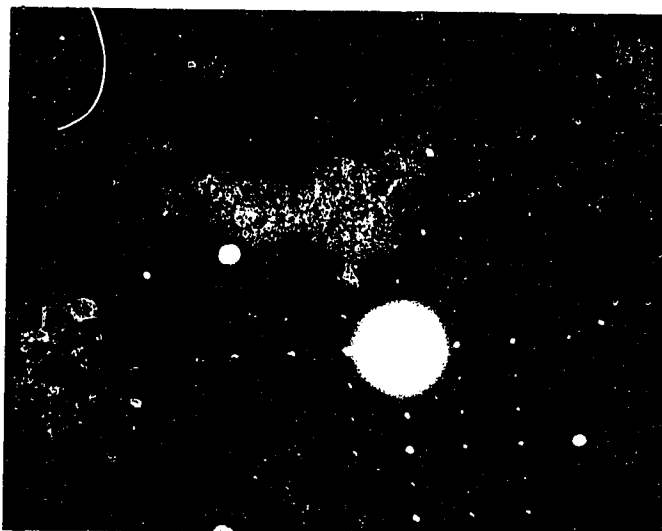


(b) A close look at the above area, showing dense dislocations at the ends of martensite.

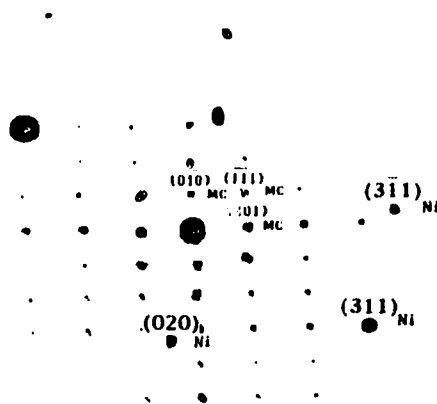
Fig. 95 A narrow band of martensite appears along the interface between the base steel and Overlay C-22 as-welded.



(a) Segregation on the planar grain boundary in Overlay C-22.



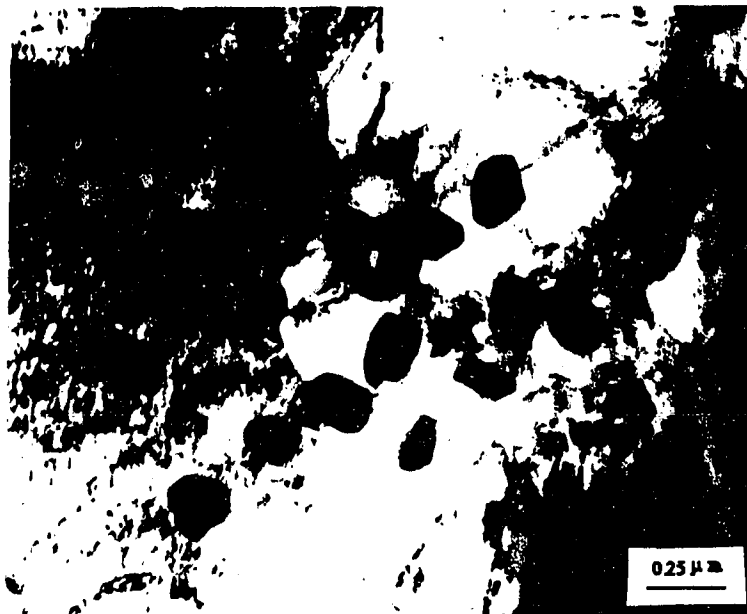
(b) Diffraction pattern of the segregate.



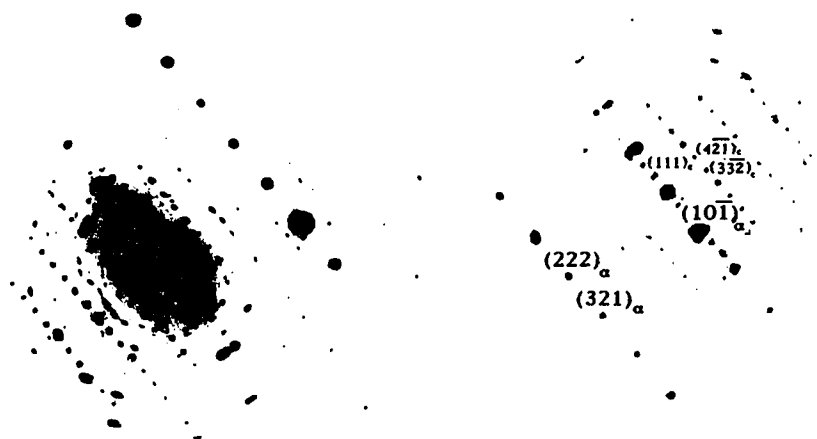
$$Z_{Ni} = [103], Z_{MC} = [101]$$

(c) Indexing of the diffraction pattern.

Fig. 96 Segregation on the planar grain boundary in Overlay C-22 as-welded.



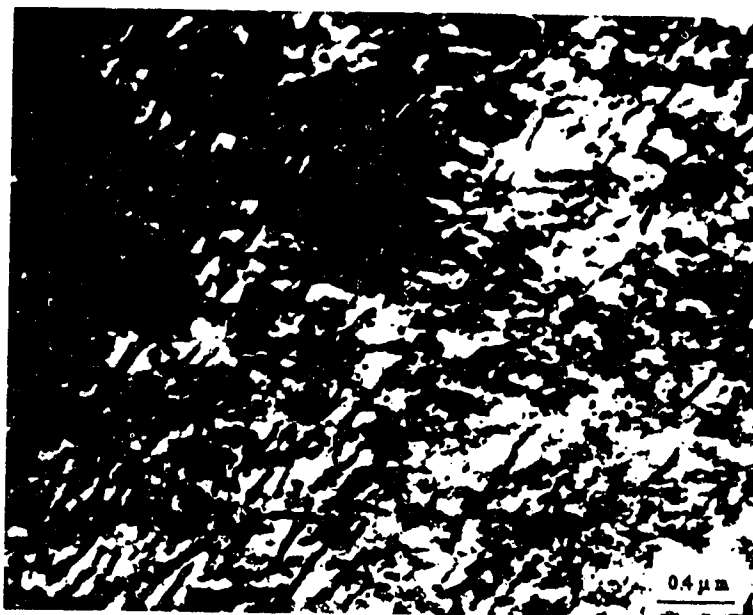
(a1) Coarse carbides precipitated in the base steel side under the interface between the base steel and Overlay C-22.



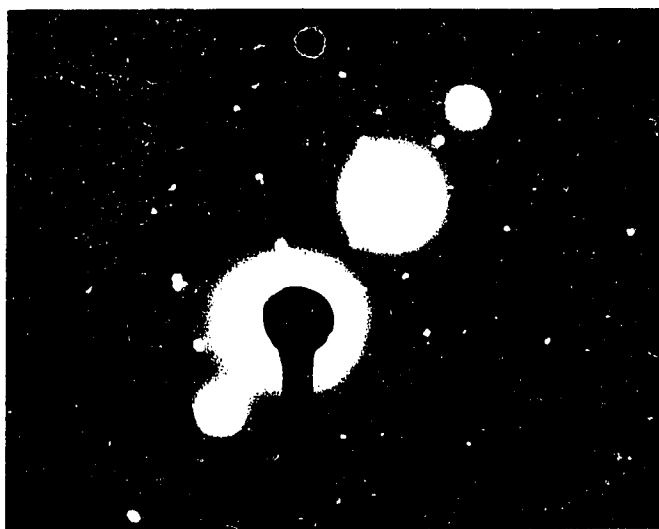
$$ZA_{\alpha} = [121], \quad ZA_{(FeMo)_3C} = [156]$$

(a2) Diffraction pattern of the observed area. (a3) Indexing of diffraction pattern, showing the precipitation of M_3C type carbide.

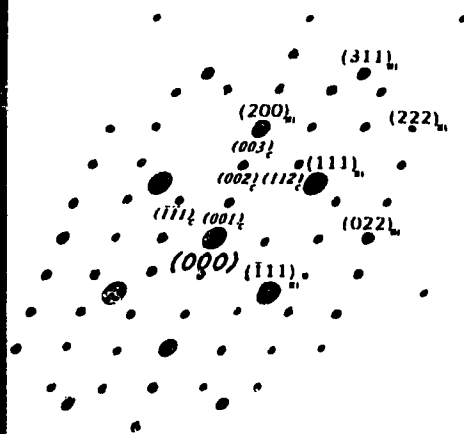
Fig. 97 (a) Precipitation in the base steel side under the interface between the base steel and Overlay C-22, after PWHT. (Continuing to the next page)



(b1) M2C type carbides precipitating in the transition zone in Overlay C-22.



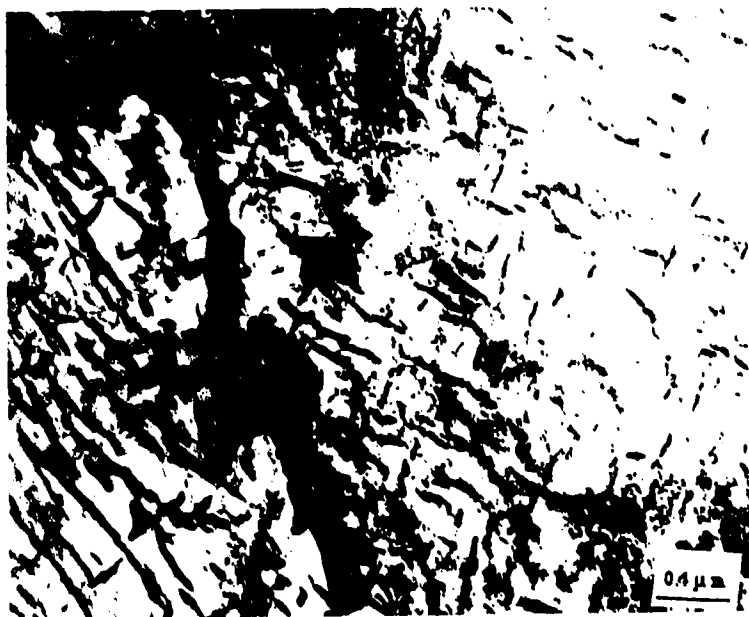
(b2) Diffraction pattern of observed area.



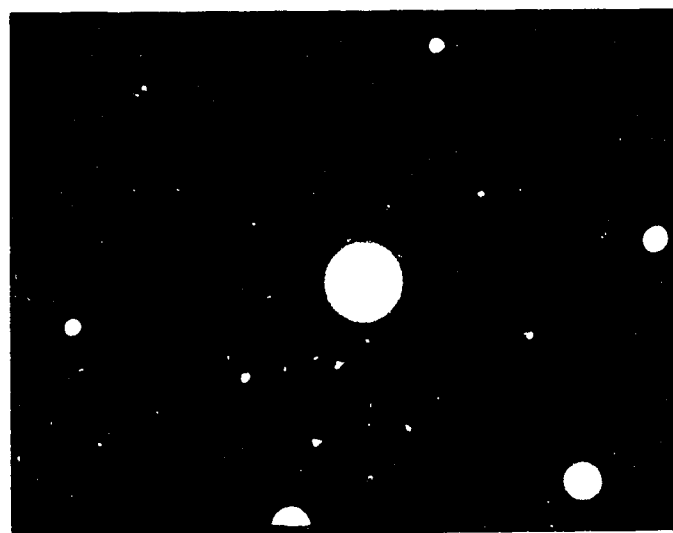
$$Z_{\text{Ni}} = [011], Z_{\text{M}_2\text{C}} = [110]$$

(b3) Indexing of diffraction pattern, the needle-like carbide showing M2C type carbide.

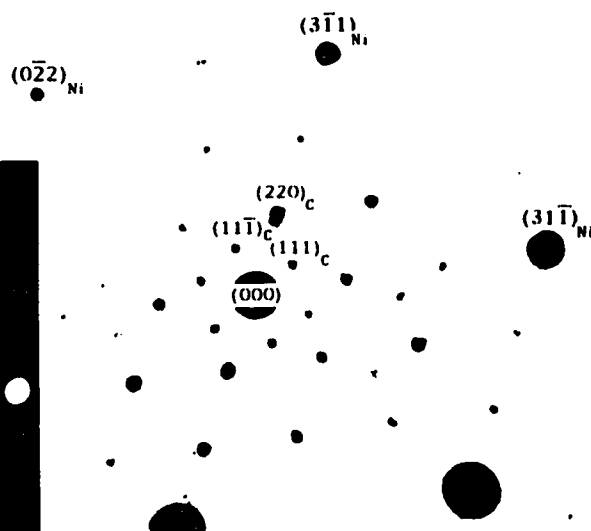
Fig. 97 (b) Precipitation in the transition zone between the base steel and Overlay C-22, after PWHT. (continuing to the next page)



(c1) Precipitation of carbides on the planar grain boundary in Overlay C-22 after PWHT.



(c2) Diffraction pattern of observed area.



$$Z_{Ni} = [011], \quad Z_{M_{23}C_6} = [110]$$

(c3) Indexing of diffraction pattern, showing the carbides being $M_{23}C_6$ type.

Fig. 97 (c) Precipitation of carbides on the planar grain boundary in Overlay C-22 after PWHT.



Fig. 98 Less precipitation occurs in Overlay C-22 by low current welding procedure, after PWHT.

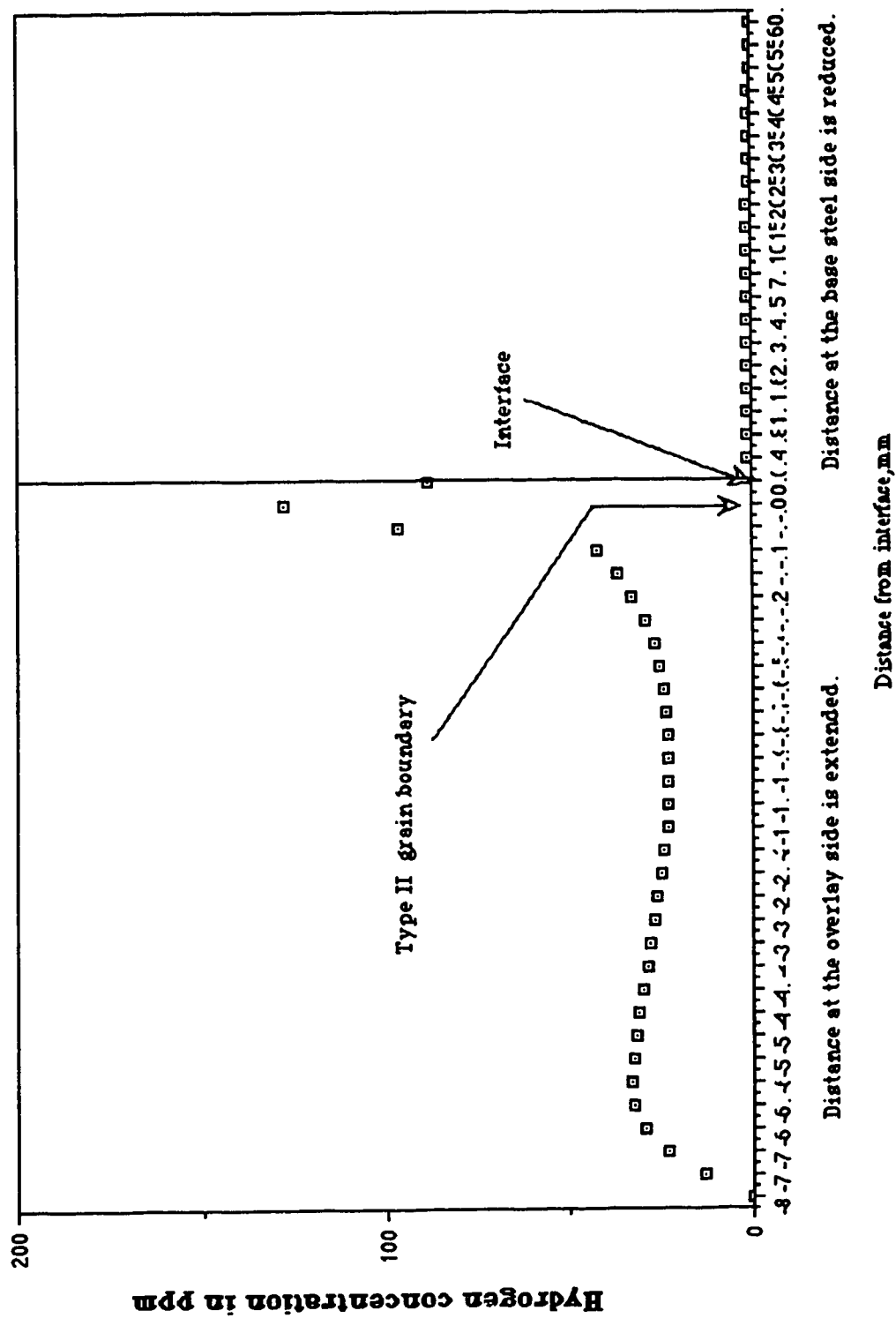


Fig. 9: A simulation of hydrogen accumulation in Type II grain boundary after autoclave testing.

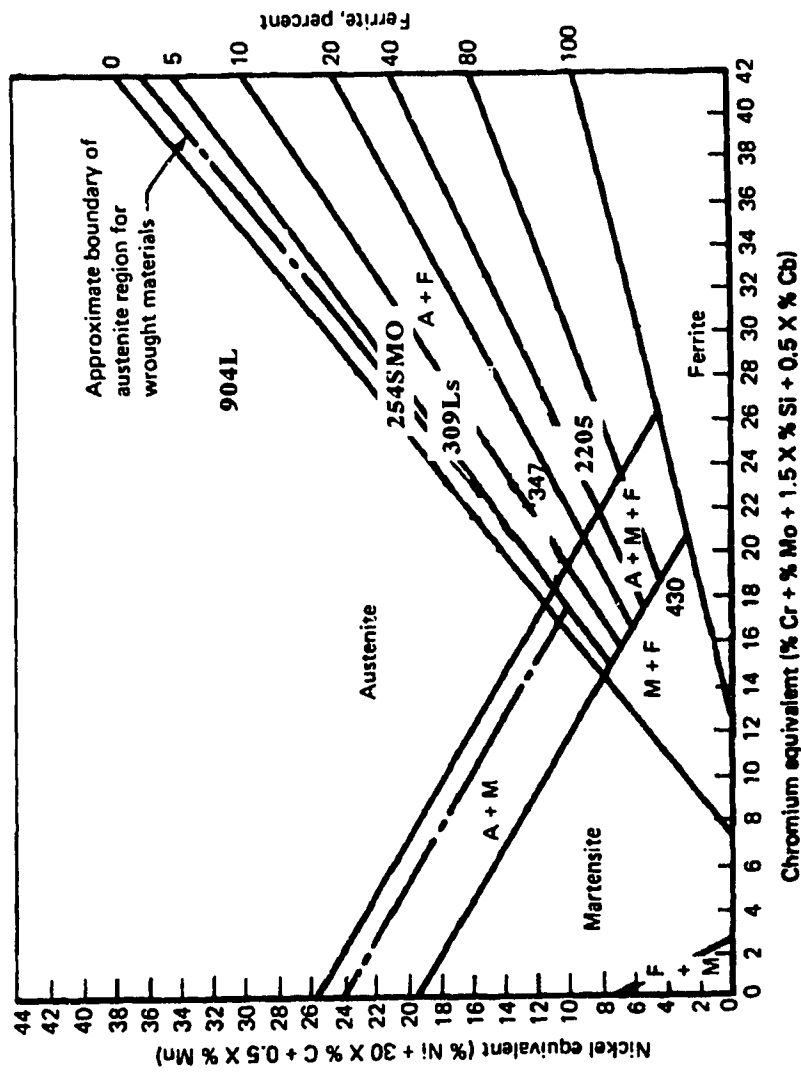


Fig. 101 Schematic of Schaeffler diagram showing possible structures in overlays (Ref. 97)

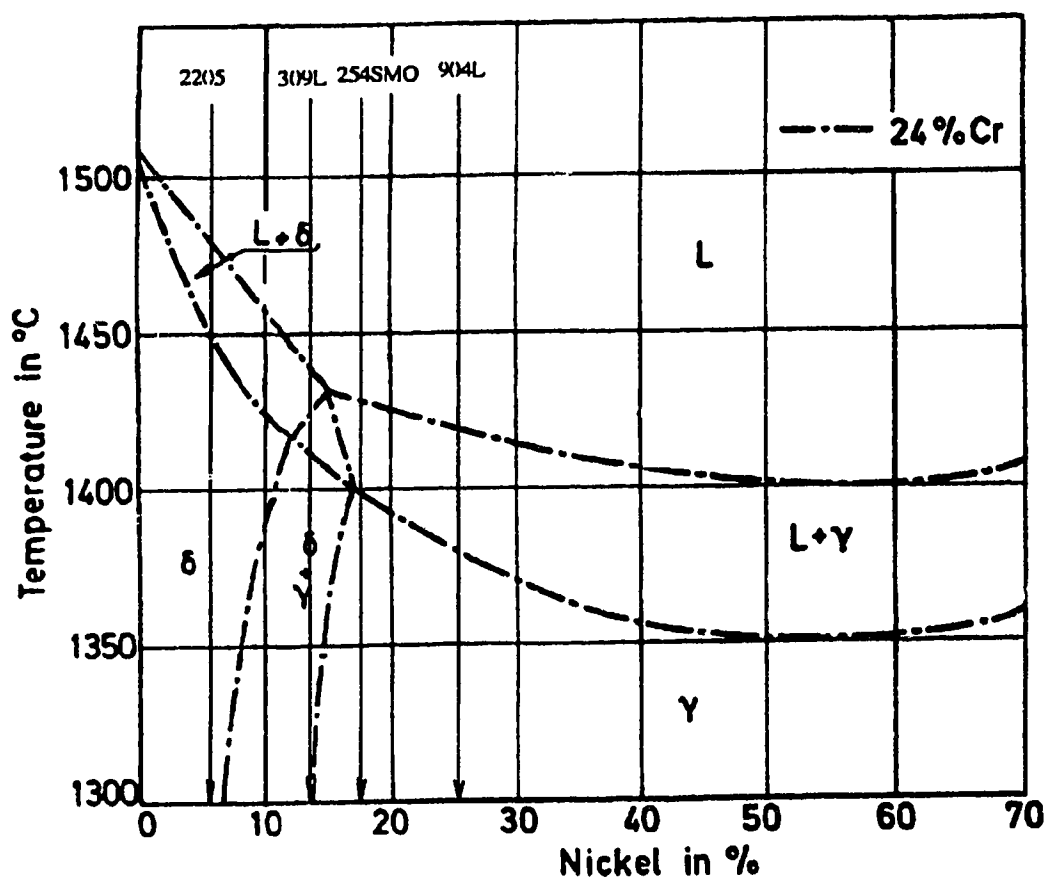


Fig. 102 Concentration profile in the ternary Fe-Cr-Ni constitutional diagram at 24%Cr (Ref. 96), showing the possible solidification processes of alloys used in this experiment.

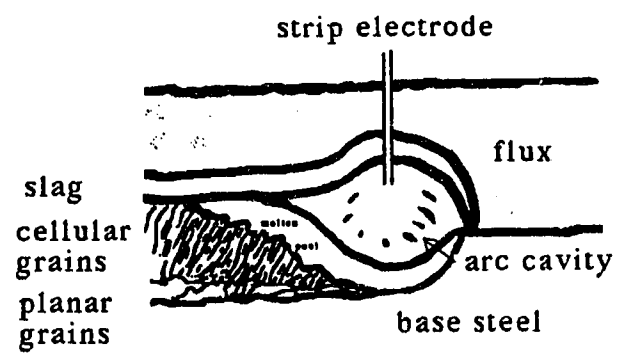


Fig. 103 Schematic illustration of the formation of planar grain boundary in the cladding by submerged arc welding.

REFERENCES

1. R. David, Thomas, Jr., "Corrosion-Resistant Weld Overlay by the Dual Strip Process", British Welding J., V.13, 5, (1966), 307

2. P. G. Cappelli, G. Frigerio, "Strip Cladding with Inconel", Metal Construction and British Welding J., V.16, 12, (1969), 555

3. A. B. Marshall, et al, "Stainless Steel Strip Cladding", Welding and Metal Fabrication, 8, (1973), 292

4. B.F. Kuvin, "Laser Beam Clad Alloys", Welding Design and Fabrication, V.60, 5, (1987), 35

5. J.M. Stone, "The Properties and Application of Explosive Bonded Clads", Explosive Welding , Proceedings of the Institute of Welding, Hove, Sept. 1968, 55

6. F. Matsuda, et al, "Disbonding between 2 1/4 Cr - 1 Mo steel and Overlay Austenitic Stainless Steel by Means of Electrolytic Hydrogen Charging Technique", Trans. Jpn. Weld. Res. Inst., V.13, 2, (1984), 91

7. A. Fuji, E. Kuto, T. Takahashi, and K. Mano, "Mechanical Properties of Stainless Steel Overlay Weld with Resistance to Hydrogen-Induced Disbonding", Trans. Jpn. Weld. Soc., V.17, 1, (1986), 27

8. Y.C. Zhang, H.Nakagama, et al, "Proposal of TZT diagram for Microstructural Analysis of Transition Zone in Welding Dissimilar Metals", Q.J. Jpn. Weld. Soc., V.5, 4, (1987), 74

9. J. Shimomura, et al, "Disbonding of Overlay weldment in Vanadium-Modified 2 1/4 Cr - 1 Mo Steels", J. Iron Steel Inst. Jpn., V.75, 5, (1989), 798

10. M. Godden and L. Seto, "Disbonding of Stainless Steel Weld Overlay Following Simulated Pressure Vessel Service Exposure", Report ERP/PMRL 83 - 69 (TR), CANMET

11. K. Ohnishi, A. Fuji, R. Chiba, T. Adachi, K. Naitoh and H. Okada, "Effect of Strip Overlay Welding Conditions on Resistance to Hydrogen-induced Disbonding", Trans. Jpn. Weld. Soc. V.15, 2, Oct. (1984), 129

12. R.B. Lazor and K.G. Leewis, "Weld Overlay Disbonding", Report RC262/4/88, Welding Institute of Canada

13. Fukuhisa Matsuda and Hiroji Nakagawa, "Simulation Test of Disbonding between 21/4 Cr - 1 Mo Steel and Overlaid Austenitic Stainless Steel by Electrolytic Hydrogen Charging Technique", Trans. JWRI, V.13, 1, (1984), 159

14. J.T. McGrath, R.S. Chandel, R.F. Orr, D.K. Mak, I. Sommervilli and J. Ng-Yelim, Unpublished Manuscript.

15. K. Kohira, et al, "A Numerical Analysis of the Diffusion and Trapping of Hydrogen in Steels and Steel Weldments", J. Jpn. Weld. Soc., V.43, 9, (1974), 921

16. N. Yurioka, et al, "An Analysis of Effects of Microstructure, Strain and Stress on the Hydrogen Accumulation in the Weld Heat-Affected Zone", IIW Doc., IX - 1161 - 80

17. A.P. Chakravarti, L. Malik, unpublished manuscript.

18. Keizo Ohnishi, Ryuichi Chiba, Juro Watanabe, Katsuyuki Naito, Hachiro Okada, "Hydrogen-induced Disbonding of Stainless Steel Overlay Weld", Paper presented at the Pressure Vessel Research Committee Meeting in New York, Sept. 1980, The Japan Steel Works Ltd.

19. Sakai Tadamichi, Asami Kiyoshi, Katsumata Masaaki, Takada Hisashi and Takana Osamu, "Hydrogen Induced Disbonding of Weld Overlay in Pressure Vessels and Its Prevention", Proc. of 1st Int. Conf. on Current Solutions to Hydrogen Problems in Steels. Eds. C.G. Interrante and G.M. Pressouyre. Published by ASM, Washington, Nov. 1982, 340 - 348

20. N. Morishige, et al, "Influence of Low Temperature Hydrogen Degassing on Hydrogen Induced Disbonding of Cladding", Trans. Jpn. Weld. Soc., V.16, 1, (1985), 12

21. M.M. Madrid, S.L.I. Chan, and J.A. Charles, "Hydrogen Occlusivity and Embrittlement in iron. - Effect of Grain Structure and Cold Work", Materials Science and Technology, No.6, 1985, 454 - 460

22. Kazumaru Kohira, Takashi Yatake, and Nobutaka Yurioka, "A Numerical Analysis of the Diffusion and Trapping of Hydrogen in Steels and Steel Weldments", Journal Jpn. Weld. Soc. V.43, No.9, 1974, 921 - 930

23. Nobutaka Yurioka, Shigeru Ohshita, Harumasa Nakamura and Kohichi Asano, "An Analysis of Effects of Microstructure, Strain and Stress on the Hydrogen Accumulation in the Weld Heat-Affected Zone", Report of Nippon Steel Corporation, Sagamihara, Kanagawa, Japan, IIW Doc. 1X - 1161 - 80

24. S.A. David, "Ferrite Morphology and Variations in Ferrite Content in Austenitic Stainless Steel Welds", Welding Journal, V.60, 4, 1981, 63s - 71s

25. R.Kume, et al, "Internal Stresses in Thick Plates Weld-Overlaid with Austenitic Stainless Steel", Trans. Jpn. Weld. Soc., V.5, 1, 1974, 32

26. J. Watanabe, et al, "Hydrogen-Induced Disbonding of Stainless Steel Overlay Found in Desulfurizing Reactor", Conf. Performance of Pressure Vessel with Clad and Overlaid Stainless Steel Linings, Denver, June., 1981, ASME publishing, MPC-116

27. A. Fuji, E. Kudo, and T. Takahashi, "Metallographic Characteristics of Stainless Steel Overlay Weld with Resistance to Hydrogen-Induced Disbonding", Trans. Jpn. Weld. Soc., V.17, 2, Oct. 1986, 145

28. A. Fuji, E. Kudo, and T. Takahashi, "Tensile Characteristics of Bond of Stainless Steel Overlay Weld after Absorption of Hydrogen", Trans. Jpn. Weld. Soc., V.18, 1, April 1987, 19

29. M. Nakanishi, S. Watanabe, and J. Furusawa, "On the Improvement of ductility and Toughness in Weld Joints of Al - B Treated Thick Plates for Pressure Vessels", Report of the Central Research Laboratories, Sumitomo Metal Industries Limited, Nishinagasu-hondori, Japan, 1984

30. I. Masumoto, S. Wignarajah, and H. Tsujimura, "Microstructure of a 1Cr 1Mo1/4V Steel after Long Service", Trans. Jpn. Weld. Soc., V.16, 1, April 1985, 89 - 94

31. J.F. Lancaster, *Metallurgy of Welding*, 4th Edition, Allen & Unwin, London, 1987, 260 - 340

32. H.C. Campbell, "Strip Electrodes for Overlay Welding", Metals Engineering Quarterly, Vol.9, 4, 1969, 48-51

33. A. Fuji, E. Kudo, et al, "A Stainless Steel Overlay Welding Process for Superior resistance to disbonding", Quarterly J. Jpn. Welding Soc., V.4, 4, 1986, 766

34. W.F. Savage, "Solidification, Segregation and Weld Imperfections", Welding in the World, 18, 5/6, 1980, 89

35. A.K. Bhaduri, V. Seetharaman, and S. Venkadesan, "Effect of Ageing on the Interfacial Microstructure and Mechanical Properties of a Alloy 800/2.25 Cr - 1 Mo Steel Joint", Z. Metallkde, 80, 1989, 630 - 634

36. A.K. Bhaduri, S. Venkadesan, P. Rodriguez, and P.G. Mukunda, "Combined Effect of Post-Weld Heat Treatment and Aging on Alloy 800/2.25 Cr - 1 Mo Steel Joint", Materials Science and Technology, V.7, 11, 1991, 1051 - 1056

37. J. Pavlovsky, B. Million, K. Ciha and K. Stransky, "Carbon Redistribution between an Austenitic Cladding and a Ferritic Steel for Pressure Vessels of a Nuclear Reactor", Materials Science and Engineering, A149, 1991, 105 - 110

38. M.F. Gittos and T.G. Gooch, "The Interface below Stainless Steel and Nickel - Alloy Claddings", Welding Journal, Vol.71, 12, 1992, 461s - 472s

39. R.J. Christoffel and R.M. Curran, "Carbon Migration in Weld Joints at Elevated Temperatures", Welding Journal, V.35, 9, 1956, 457s

40. I. Masumoto, S. Wignarajah and H. Tsujimura, "Microstructure of a 1 Cr 1 Mo 1/4 V Steel after Long service", Trans. Jpn. Weld. Soc., V.16, No.1, 1985, 88 - 94

41. T.Fuji, et al, "A Safety Analysis on Overlay Disbonding of Pressure Vessels for Hydrogen service", *Current Solutions to Hydrogen Problem in Steels*, Proc. 1st Intern. Conf. ASM, Washington, D.C., 1981, 361

42. K. Kinoshita, et al, "Characteristics for Hydrogen Diffusion of Transition Zone Metals between Stainless Steel Weld Overlay and Cr - Mo Steel Base Metal", *Current Solutions to Hydrogen Problem in Steels*, Proc. 1st Intern. Conf. ASM, Washington, D.C., 1981, 369

43. T. Hattori, et al, "Hydrogen Induced Disbonding of Stainless Steel Overlay Weld and Its Preventive Measures", Nippon Kokan Technical Report, N0.47, 1986

-
44. A.M. Horsfield, et al. "Strip Cladding of Steel with Stainless Steel and Nickel Base Alloys", British Welding Journal, V.13, May, 1966, 315
45. B.M. Patchett, G.A. Demos, and R.L. Apps, "The influence of flux composition and welding parameters on heat distribution in submerged arc welding", Welding Research International, V.4, No.2, 1974, 81 - 94
46. B.G. Renwick and B.M. Patchett, "Operating Characteristics of the Submerged Arc Process", Welding Journal, V.23, 3, 1976, 69-s -76-s
47. G. Almqvist and N. Egeman, "Stainless Steel Cladding with Strip Electrodes", Welding and Metal Fabrication, V.31, July, 1963, 294
48. C. Zapffe and C. Sims, "Hydrogen Embrittlement Internal Stress and Defects in Steel", Trans. AIME, V.145, 1941, 225
49. Robert D. Merrick, "An Overview of Hydrogen Damage to Steels at Low Temperatures", Materials Performance, Feb., 1989, 53-55
50. A.R. Troiano, "The Role of Hydrogen and Other Interstitials in the Mechanical Behavior of Metals", Trans. ASM, V.52, 1960, 54
51. J. P. Hirth, "Environment Sensitive Fracture of Metals and Alloys, Proc. Office of Naval Research Workshop, Washington, D.C., June 3-4 , 1985, Office of Naval Research, Arlington, VA, 1987, 79
52. N.R. Moody, M.W. Perra, and S.L. Robinson, "Hydrogen-induced cracking in an iron-based superalloy", *Hydrogen Effects on Material Behavior*, Edited by Neville R. Moody and Anthony W. Thompson, The Minerals, Metals & Materials Society, 1990, 625 - 635

53. P.D. Hicks and C.J. Altstetter, "Hydrogen Embrittlement of Superalloys", *Hydrogen Effects on Material Behavior*, Edited by Neville R. Moody and Anthony W. Thompson, The Minerals, Metals & Materials Society, 1990, 613 - 623

54. C.D. Beachem, "A New Model for Hydrogen-Assisted Cracking (Hydrogen "Embrittlement")", Metall. Trans., V.3, Feb., 1972, 437-451

55. D.A. Jones, *Environment-Induced Cracking of Metals*, R.P. Gangloff and M.B. Ives, eds., NACE, Houston, 1990, 265

56. C.V. Owen and T.E. Scott, "Relation between Hydrogen Embrittlement and the Formation of Hydride in Group V Transition Metals", Metall. Trans. V.3, 1972, 1715-1726

57. D.G. Westlake, " A Generalized Model for Hydrogen Embrittlement", Trans. ASM, V.62, 1969, 1000

58. S. Gahr and H.K. Birnbaum, "On the Isotope Effect in Hydrogen Embrittlement of Niobium", Scripta Metall., V.10, 1976, 635

59. K. Masubuchi, *Analysis of Welded Structures*, Pergamon Press, 1986

60. S.P. Timoshenko, "Analysis of Bi-Metal Thermostats", Journal of the Optical Society of America, V.11, 1925, 233 - 255

61. R.Gunnert, "Penetration and Travel Speed in Metal Arc Welding", Welding Journal, V.27, 1948, 542

62. C.R. Heiple and J.R. Roper, "The Geometry of Gas Tungsten Arc, Gas Metal Arc, and

Submerged Arc Weld Beads". *Welding Theory and Practice, Materials Processing Theories and Practices*, Vol. 8, Edited by D.L. Olson, R. Dixon and A.L. Liby, North-holland, Elsevier Science Publishers B.V. 1990, 1 - 34

63. R.L. Apps, L.M. Gourd and K.A. Nelson, "Effect of Welding Variables upon Bead Shape and Size in Submerged-Arc Welding". Welding and Metals Fabrication, V.31, 1963,453

64. W.F. Savage, E.F. Nippes and J.S. Erickson, "Solidification Mechanisms in Fusion welds". Welding Journal, V.55, 8, 1976, 213-s

65. M.C. Flemings, *Solidification Processing*, McGraw-Hill Book Co. 1974

66. W.F. Savage, "Solidification, Segregation and Weld Defects", in: *Weldments: Physical Metallurgy and failure Phenomena*, 5th Bolton landing Conf., August 1978, Eds. R.J. Christoffel, E.F. Nippes and H.D. Solomon, General Electric Co., Schenectady, New York, p.1ff

67. K.E. Easterling, "Solidification Microstructure of Fusion Welds". Materials Science and Engineering, V.65, 1984, 191

68. J.A. Brook and K.W. Mahin, "Solidification and Structure of Welds". *Welding Theory and Practice*, Materials Processing Theory and Practice, Vol.8, Edited by D.L.Olson, R. Dixon and A.L. Liby, Nortyh-Holland, Elsevier Science Publishers B.V., 1990, 35 - 78

69. R.Trivedi, "Interdendritic Spacing: Part II. A comparison of Theory and Experiment". Metallurgical Transactions, A15, 6, 1984, 977

70. C.R. Loper, and J.T. Gregory, *Solidification and Casting of Metals*, Conf. Proc. on Solidification, Sheffield, UK, July 1977, Metals Society, London, UK, 1979, 433

71. S.Yatsuya, and T.B. Massalski, "Laser Beam Interaction with the Pd-Si-Cu Eutectic", Materials Science and Engineering, V.54, 1982, 101

72. B.L. Baikie, and D. Yapp, *Solidification and Casting of Metals*, Conf. Proc. on Solidification, Sheffield, UK, July 1977, Metals Society, London, UK, 1979, 438

73. E. Scheil, "Bemerkungen zur Schichtkristallbildung", Z. Metallkd., 34, 3, 1942, 70

74. W.A. Tiller, K.A. Jackson, J.W. Rutter and B. Chalmers, "The Redistribution of Solute Atoms during the Solidification of Metals", Acta Metall. V.1, 4, 1953, 428

75. J.A. Burton, R.C. Primm and W.P. Slichter, "The Distribution of Solute in Crystals Grown from the Melt. Part I. Theoretical", J. Chem. Phys. 21, 1953, 1987

76. J.A. Brooks and M.I. Baskes, Conf. Proc. on *Advances in Welding Science and Technology*, Gatlinburg, TN, May 1986, ed. S.A. David, 1986, 93-100

77. J.A. Brooks, M.I. Baskes and F.A. Greulich, "Solidification and Solid-State Transformations in High Energy Density Stainless Steel welds," Metall. Trans., V18A, 1987, 1034

78. B.M. Patchett, E.A. Dancy, D.D. Schwemmer, D.L. Olson, and Williamson, "Discussion on 'The Relationship of Weld Penetration to the Welding Flux'", Welding Journal, V.59, 1980, 31-s

79. T.H. Hazlett, "Coating Ingredients' Influence on Surface Tension, Arc Stability and Bead Shape", Welding Journal, V.36, 1957, 18-s

80. D.D. Schwemmer, D.L. Olson and D.L. Williamson, "The Relationship of Weld Penetration to the Weld Flux", Welding Journal, V.58, 1979, 153-s

81. Stephen Liu and J.E. Indacochea, "Control of Chemical Composition and Microstructure in Low-Carbon Microalloyed Steel Weldments", *Welding Theory and Practice, Materials Processing Theory and Practices*, Vol.8, Edited by D.L. Olson, R. Dixon and A.L. Liby, North-Holland, 1990

82. N. Christensen, V. de L. Davis and K. Gjermundsen, "Distribution of Temperatures in Arc Welding", *British Welding Journal*, V.12, 2, 1965, 54 - 75

83. A.P. Chakravarti, L. Malik, "Modelling hydrogen distribution in weld overlay system", Report of Welding Institute of Canada, 7 - 186 - 063/F

84. K.-E Thelning, *Steel and Its Heat Treatment*, 2nd Edition, Butterworths, 1984

85. Zhao, Deshan et al, *Welding Processes*, Chemical Engineering Construction Press, 1983, 618 (in Chinese)

86. Z. Wang, B.Xu, and C. Ye, "Study on the Martensite Structures at Weld Bond and Fracture Toughness of Dissimilar-Metal Joints", Abstracts of Paper, presented at 1992 AWS Convention, Chicago, 73rd American Welding Society Annual Meeting, March 22-27, 1992, 38

87. J.-O. Nilsson, P. Liu, "Aging at 400o - 600oC of Submerged Arc Welds of 22Cr - 3Mo - 8Ni Duplex Stainless Steel and Its Effects on Toughness and Microstructure", Materials Science and Technology, V.7, Sept. 1991, 245

88. John J. Hren, Joseph I. Golstein and David C. Joy, *Introduction to Analytical Electron Microscopy*, Plenum Press, New York & London, 1979, 121-168

89. R.B. Benson, R.K. Dann, and L.W. Roberts, "Hydrogen Embrittlement of Stainless Steel", Trans. AIME, V242, Oct., 1968, 2199

90. W.Y. Choo, Jai Young Lee, "Thermal Analysis of Trapped Hydrogen in Pure Iron", Metall. Trans. A., 13A, Jan., 1982, 135

91. G. Lange and W. Hoffmann, "Relation between Hydrogen Up-take and Porosity in Iron", Arch. Eisenhüttenwes., V.37, 5, 1966, 391 - 397

92. E.W. Johnson and M.L. Hill, "The Diffusivity of Hydrogen in Alpha Iron", Trans. AIME., V.218, 12, 1960, 1104 - 1112

93. A.L. Schaeffler, "Selection of austenitic electrodes for welding dissimilar metals", Welding Journal, V.26, 10, 1947, 601-s - 620-s

94. A. Janko and J. Pielaszek, "Change in the real structure of nickel due to the Ni- β NiH phase transformation", *Corrosion of Metals and Hydrogen-Related Phenomena*, Eds. J. Flis, Elsevier, Warszawa, 1991, 322 - 337

95. S.A. David, J.M. Vitek, "Correlation between Solidification Parameters and Weld Microstructures", Int. Materials Reviews, V.34, 5, 1989, 213 - 245

96. Erich Folkhard, *Welding Metallurgy of Stainless Steels*, Springer-Verlag Wien, New York, 1988

97. Welding Handbook, Vol.4: *Metals and Their Weldability*, 6, Aufl, S.65.9. Miami, Florida; American Welding Society 1972

98. J.C. Lippold and W.F. Savage, "Solidification of Austenitic Stainless Steel Weldments: Part 2 - The Effect of Alloy Composition on the Ferrite Morphology", Welding Journal, V.61, 2, 1980, 48-s - 58-2

99. C.F. Hull, "Effects of alloying additions on hot cracking of austenitic chromium - nickel stainless

steels", Proc. American Soc. Test. Matc. 60, 1960, 667 - 690

100. J.C. Borland, R.N. Younger, "Some Aspects of Cracking in Welded Cr - Ni - Austenitic Steels", British Welding Journal, 7, 1960, 22 - 59

101. H.J. Eckstein, "Warmebehandlung von Stahl. Metallkundliche Grundlagen", S. 92, 130, Leipzig: VEB Deutscher Verlag für Grundstoffindustrie 1969

102. J. Friberg, L.E. Torndahl, and M. Hillert, "Diffusion in Iron", Jernkontor. Ann. 153, 1969, 263 - 276

103. K. Fisher, *Fundamentals of Solidification*, 3rd Ed., Trans Tech Publications, 1989,

104. L. Karlsson, "Thermal Stresses in Welding", *Thermal Stresses I*, Edited by R.B. Hetnarski, North-Holland, 1986, 297 - 389

105. G.M. Pressouyre and F.M. Faure, "Quantitative analysis of critical concentrations for hydrogen-induced cracking", *Hydrogen Embrittlement: Prevention and Control*, Edited by L. Raymond, ASTM, STP 962, 1988

106. Sandvik, SAF 2205, Duplex Stainless Steel, UNS S31803, S-1,874-ENG, November 1987

APPENDICES

Appendix A

Coefficients of Compliance for the Plate Components

The following formula for the displacement at the edge $y = 0$ can be obtained by employing the Ribiere solution for a long and narrow strip:

$$u_o(x) = \frac{1}{4G} \sum_{k=1,3,5,\dots} \gamma_k [(3 - \nu - (1 + \nu)u_k \coth u_k) \coth u_k + (1 + \nu)u_k] \sin \alpha_k x, \quad (A1)$$

where $G = \frac{E}{2(1 + \nu)}$, $u_k = \alpha_k h = \frac{k\pi h}{2L}$, and $\gamma_k = \frac{2}{\alpha_k L} \int_0^1 \tau_o(x) \sin \alpha_k x dx$.

In order to obtain a formula for the compliance coefficient the equation (25) in the main text is used:

$$u_o = -\frac{1 - \nu^2}{EhB} \int_0^1 Q(\zeta) d\zeta + \kappa q(x),$$

where the effects of the unrestricted thermal expansion and bending are not taken into account. Utilizing the expansion

$$q(x) = B\tau_o(x) = B \sum_k \alpha_k \gamma_k \sin \alpha_k x,$$

it yields

$$u_o = \frac{1 - \nu^2}{E} \sum_k \frac{\gamma_k}{u_k} \sin \alpha_k x + \kappa B \sum_k \alpha_k \gamma_k \sin \alpha_k x.$$

Comparing this formula with the formula (A1), it is found that

$$\kappa = \frac{\sum_k \gamma_k K(u_k) \sin \alpha_k x}{EB \sum_k \alpha_k \gamma_k \sin \alpha_k x}, \quad (A2)$$

where

$$K(u_k) = \frac{1+\nu}{2} \left[(3-\nu-(1+\nu)u_k \coth u_k) \coth u_k + (1+\nu)u_k - \frac{2(1-\nu)}{u_k} \right].$$

For sufficient small h/L ratios (say, less than 1), the hyperbolic function can be as:

$$\coth u_k \approx \frac{1}{u_k} + \frac{u_k}{3},$$

and
$$K(u_k) = \frac{2}{3}(1+\nu)u_k = \frac{2}{3}(1+\nu)\alpha_k h.$$

Then the expression (A2) reduces to the following simple formula for the compliance coefficient:

$$\kappa = \frac{2(1+\nu)}{3E} \frac{h}{B} = \frac{h}{3GB}.$$

Appendix B

Analysis of Stress Field of Bonded Dissimilar Materials

The first terms in Eqs. (4 - 25) and (4 - 26) are the unrestricted thermal expansions of the strips. The second terms due to the force $Q(x)$ and are calculated under assumption that these forces are uniformly distributed over the strip thickness and that there are no significant displacements in the direction of the plate width. The third terms account for the actual nonuniform distribution of the force $Q(x)$ and reflect an assumption that the corresponding corrections are directly proportional to the shearing force in the given cross section and are not affected by the shearing forces in other cross sections. The last terms are due to bending. On the interface the condition $u_1(x) = u_2(x)$ of the displacement compatibility yields

$$\kappa q(x) - \left(\frac{1 - \nu_1^2}{E_1 h_1} + \frac{1 - \nu_2^2}{E_2 h_2} \right) \int_0^x Q(\zeta) d\zeta + \frac{Bh}{2} \int_0^x \frac{d\zeta}{\rho(\zeta)} = B\Delta\alpha\Delta T x \quad (B1)$$

where $h = h_1 + h_2$, $\Delta\alpha = \alpha_2 - \alpha_1$, and

$$\kappa = B(\kappa_1 + \kappa_2) \quad (B2)$$

The equation of equilibrium for a portion of the plate is as follows (refer to Figure 17):

$$M_1(x) + M_2(x) - \frac{h}{2} q(x) = 0 \quad (B3)$$

$$\text{where } M_1(x) = \frac{BD_1}{\rho(x)}, M_2(x) = \frac{BD_2}{\rho(x)} \quad (B4)$$

are bending moments for the strips, and

$$D_1 = \frac{E_1 h_1^3}{12(1 - \nu_1^2)}, D_2 = \frac{E_2 h_2^3}{12(1 - \nu_2^2)} \quad (B5)$$

are flexural rigidities. From the equations (B3) and (B4), it gives

$$\frac{1}{\rho(x)} = \frac{h}{2BD} Q(x), D = D_1 + D_2. \quad (B6)$$

By substituting this formula in Eq. (B1) the following integral equation is obtained for the unknown shearing force function $q(x)$:

$$q(x) - k^2 \int_0^x Q(\zeta) d\zeta = B \frac{\Delta\alpha\Delta T}{\kappa} x, \quad (B7)$$

where $k^2 = \frac{\lambda}{\kappa}, \lambda = \frac{1}{12} \left(\frac{h_1^2}{D_1} + \frac{h_2^2}{D_2} + \frac{3h^2}{D} \right).$ (B8)

Equation (B7) has the following solution¹, which satisfies the boundary conditions $q(0) = 0, Q(L) = 0$:

$$q(x) = \frac{B\Delta\alpha\Delta T}{k\kappa \cosh kL} \sinh kx. \quad (B9)$$

And this force causes the following shearing stress:

$$\tau(x) = \frac{q(x)}{B} = \frac{\Delta\alpha\Delta T}{k\kappa \cosh kL} \sinh kx. \quad (B10)$$

The maximum shear stress occurs at the edge of the plate:

$$\tau_{\max} = \tau(L) = \frac{\Delta\alpha\Delta T}{k\kappa} \tanh kL = \frac{\Delta\alpha\Delta T}{\sqrt{\lambda\kappa}} \tanh kL \quad (B11)$$

After substituting (B9) into (4-29) and integrating it yields

$$Q(x) = -\frac{B\Delta\alpha\Delta T}{\lambda} \chi(x), \quad (B12)$$

where the function

$$\chi(x) = 1 - \frac{\cosh kx}{\cosh kL} \quad (B13)$$

characterizes the distribution of the forces $Q(x)$ and the resulting normal stresses along the plate.

Using Eq.(B12) the formula for the plate curvature, Eq.(B6), is rewritten as

$$\frac{1}{\rho(x)} = -\frac{h\Delta\alpha\Delta T}{2\lambda D} \chi(x). \quad (B14)$$

Then Eqs.(B4) for the bending moments yield:

$$M_1(x) = -\frac{Bh\Delta\alpha\Delta T}{2\lambda D} D_1 \chi(x), \quad (B15)$$

and $M_2(x) = -\frac{Bh\Delta\alpha\Delta T}{2\lambda D} D_2 \chi(x). \quad (B16)$

¹. E. Suhir, "Stresses in Bi-metal Thermostats", Journal of App. Mech., V.53, Sept. 1986, 657 - 660

The normal stresses due to the combined action of the forces $Q(x)$ and moments are maximum on the interface, where they are as follows:

$$\sigma_o(x) = \frac{\Delta\alpha\Delta T}{\lambda h_1} \left[1 + \frac{3hD_1}{h_1D} \right] \chi(x) \quad (B17)$$

and

$$\sigma_b(x) = -\frac{\Delta\alpha\Delta T}{\lambda h_2} \left[1 + \frac{3hD_2}{h_2D} \right] \chi(x) \quad (B18)$$

The transverse normal, or "peeling", stresses $p(x)$ acting on the interface can be found on the basis of the equilibrium equations written down for the portion of the plate as shown in Figure 17(c):

$$(x+L)N_o - B \int_{-L}^x \int_{-L}^{\zeta} p(\zeta') d\zeta' d\zeta = M_1(x) - \frac{h_1}{2} Q(x) = -M_2(x) + \frac{h_2}{2} Q(x) = \omega Q(x), \quad (B19)$$

$$\text{where } \omega = \frac{h_2D_1 - h_1D_2}{2D}. \quad (B20)$$

By differentiating Eq.(B19) it gives

$$N(x) = B \int_{-L}^x p(\zeta) d\zeta = N_o - \omega q(x) = N_o - B\omega\tau(x), \quad (B21)$$

$$p(x) = \frac{\omega}{\kappa} \Delta\alpha\Delta T \frac{\cosh kx}{\cosh kL}. \quad (B22)$$

Since the equilibrium requires that $N(L) = 0$, then

$$N_o = B\omega\tau_{\max}. \quad (B23)$$

The "peeling" stresses are maximum at the end of the cross sections:

$$p_{\max} = p(L) = \frac{\omega}{\kappa} \Delta\alpha\Delta T = \omega k \tau_{\max} \coth kL. \quad (B24)$$

APPENDIX C

A Computer Program to Simulate the Hydrogen Accumulation in Type II Grain Boundary

```

C THIS PROGRAM IS TO SOLVE THE DIFFUSION OF HYDROGEN
C IN THE WELD OVERLAY WITH TRAPPING SITES
C
C DXO, DYO ARE DIFFUSION COEFFICIENTS IN OVERLAY.
C DXB, DYB ARE DIFFUSION COEFFICIENTS IN BASE STEEL.
C SLO AND SLB ARE SOLUBILITY COEFFICIENTS.
C CONHO AND CONHB ARE HYDROGEN CONCENTRATION.
C COOLRT IS THE COOLING RATE, C/HOUR.
C
REAL COOLRT,PRESS,FPRES,DELTAT,TEMPI
REAL TEMP,CONHB(50),CONHO(50)
REAL AO(50),BAO(50),X(2)
REAL SK1,BK1,SD,BD,sk,bk,DS,DB,SDO(40),SDB(100)
REAL TRANS(50),TRANSB(50),R1(50),R1B(50),SIZE(50),SIZEB(50)
INTEGER NEO,NONODO,NEB,NONODB,NN(2)
COMMON ICONNO(50,2),ICONNB(50,2),XNODO(100),XNODB(100)
CHARACTER*30 INFILE,OUTFLE
C=====
C OPEN INPUT AND OUTPUT FILES TO RECORD CONDITONS
C=====
WRITE(*,100)
100 FORMAT(' ENTER INPUT FILE NAME (MAX.30 CHARACTERS)')
READ(*,110) INFILE
110 FORMAT(A30)
WRITE(*,120)
120 FORMAT(' ENTER OUTPUT FILE NAME (MAX.30 CHARACTERS)')
READ(*,130) OUTFLE
130 FORMAT(A30)
OPEN(5, FILE = INFILE)
OPEN(6, FILE = OUTFLE)
C=====
C 1. INPUT AND OUTPUT OF THE PROBLEM DATA
C=====
C 1.1 INPUT AND OUTPUT GLOBAL PARAMETERS
C=====
READ(5,*) NONODO,NEO,NONODB,NEB
WRITE(6,200)
200 FORMAT('//10X, ' INPUT AND OUTPUT OF PROBLEM DATA')
WRITE(6,210)
210 FORMAT('///10X, '1.1 GLOBAL PARAMETERS')
WRITE(6,220) NONODO,NEO,NONODB,NEB
220 FORMAT('//10X, 'THE NUMBER OF NODES IN OVERLAY= ',I5,
1 //10X,'THE NUMBER OF ELEMENTS IN OVERLAY= ', I5,
2 //10X,'THE NUMBER OF NODES IN BASE METAL= ',I5,
3 //10X,'THE NUMBER OF ELEMENTS IN BASE METAL= ',I5)
C=====
C 1.2 INPUT AND OUTPUT OF NODAL COORDINATES
C=====

```

```

      WRITE(6,230)
230  FORMAT(///10X,'1.2  NODAL COORDINATES',
1      //10X,'NODE NUMBER IN OVERLAY',8X,'X in cm')
      DO 280 I = 1, NONODO
          READ(5,*) XNODO(I)
          WRITE(6,250) I,XNODO(I)
250      FORMAT(10X,I5,24X,G12.5)
280  CONTINUE
      WRITE(6,290)
290  FORMAT(///10X,'NODE NUMBER  IN BASE METAL',8X,'X in cm')
      DO 295 I = 1, NONODB
          READ(5,*) XNODB(I)
          WRITE(6,292) I,XNODB(I)
292      FORMAT(10X,I5,24X,G12.5)
295  CONTINUE
C=====
C   1.3 INPUT AND OUTPUT OF ELEMENT/ NODE CONNECTIVE DATA
C=====
      WRITE(6,300)
300  FORMAT(///10X,'1.3  ELEMENT/NODE CONNECTIVE DATA',
1      //10X,'1.3.1 ELEMENT IN OVERLAY', 10X,'NODES')
      DO 360 I = 1, NEO
          IELO = I
          DO 320 J = 1,2
              ICONNO(IELO,J) = J + IELO - 1
320          CONTINUE
              WRITE(6,330) IELO,(ICONNO(IELO,J),J=1,2)
330          FORMAT(/10X,I5,20X,2I7)
360  CONTINUE
      WRITE(6,365)
365  FORMAT(///10X,'1.3.2 ELEMENT IN BASE METAL', 10X,'NODES')
      DO 380 I = 1, NEB
          IELB = I
          DO 370 J = 1, 2
              ICONNB(IELB,J) = J + IELB - 1
370          CONTINUE
              WRITE(6,375) IELB,(ICONNB(IELB,J),J=1,2)
375          FORMAT(/10X,I5,20X,2I7)
380  CONTINUE
C=====
C   1.4 PRESCRIBING THE INITIAL CONDITIONS
C      TEMPI = INITIAL TEMPERATURE (STEADY-STATE)
C      COOLRT = COLLING RATE
C      PRESS = INITIAL HYDROGEN PRESSURE KG/CM2
C=====
      WRITE(6,440)
440  FORMAT(///10X,'1.4 INITIAL CONDITIONS OF THE PROBLEM')
      WRITE(6,441)
441  FORMAT(///10X,'INITIAL TEMPERATURE C')
      READ(5,*) TEMPI
      WRITE(6,442) TEMPI
442  FORMAT(/10X,G10.5)
      WRITE(6,443)
443  FORMAT(///10X,'INITIAL PRESSURE IN kg/cm2')

```

```

      READ(5,*) PRESS
      WRITE(6,444) PRESS
444  FORMAT(/10X,G12.5)
      FPRES = PRESS
      WRITE(6,450)
450  FORMAT(/10X,'COOLING RATE, C/H',8X,'TIME INTERVAL,min.')
      READ(5,*) COOLRT,DELTAT
      WRITE(6,460) COOLRT,DELTAT
460  FORMAT(/10X,G12.5,15X,G12.5)
C=====
C    1.5 COEFFICIENT FUNCTIONS
C      KB = SOLUBILITY OF HYDROGEN IN BASE METAL
C      KS = SOLUBILITY OF HYDROGEN IN OVERLAY
C      DB = DIFFUSIVITY OF HYDROGEN IN BASE METAL
C      DS = DIFFUSIVITY OF HYDROGEN IN OVERLAY
C      ALPHA = KS/KB
C      BECAUSE THESE FUNCTIONS DEPEND ON TEMPERATURE,
C      THEY WILL BE PUT IN MATRICES AT THE PROPER TIME.
C=====
C    2. STEADY-STATE DISTRIBUTION OF HYDROGEN
C=====
      TEMP1 = TEMPI + 273.15
      SK1= 7.6*EXP(-630./TEMP1)
      BK1= 23.4*EXP(-3257./TEMP1)
      SD = .04266*EXP(-4555./TEMP1)
      BD = .144*EXP(-2132./TEMP1)
      ALPHA = SK1/BK1
      CONHO(1) = SK1*SQRT(PRESS)
      BTHICK = XNODB(NONODB) - XNODB(1)
      OTHICK = XNODO(NONODO) - XNODO(1)
      CONHB(1) = SD*CONHO(1)*BTHICK/(BD*OTHICK + ALPHA*SD*BTHICK)
      CONHO(NONODO) = ALPHA*CONHB(1)
      WRITE(6,800)
800  FORMAT(/12X,' STEADY-STATE HYDROGEN DISTRIBUTION IN OVERLAY',
1 //10X,'DISTANCE FROM SURFACE,cm',8X,'CON. OF HYDROGEN,ppm')
      DO 820 I = 1,NONODO
      XT = XNODO(I) - XNODO(1)
      CONHO(I)=(CONHO(NONODO)-CONHO(1))*XT/OTHICK+CONHO(1)
      AO(I) = CONHO(I)
      WRITE(6,810) XT,CONHO(I)
810  FORMAT(10X, G12.5,15X,G12.5)
820  CONTINUE
      WRITE(6,840)
840  FORMAT(/12X,' STEADY-STATE HYDROGEN DISTRIBUTION IN BASE METAL',
1 //10X,'DISTANCE FROM INTERFACE,cm',8X,'CON.OF HYDROGEN,ppm')
      DO 880 I = 1,NONODB
      BT = XNODB(I) - XNODB(1)
      CONHB(I) = -CONHB(1)*BT/BTHICK + CONHB(1)
      BAO(I) = CONHB(I)
      WRITE(6,860) BT,CONHB(I)
860  FORMAT(10X,G12.5,15X,G12.5)
880  CONTINUE
C*****
C    3. OUTPUT THE CALCULATION

```

```

C
C   A LONG DO-LOOP TO SETUP THE GLOBAL MATRIX
C   THE END OF THE LOOP AT 3000
C   THE INCREMENT IS THE TIME INTERVAL(DELTAT)
C*****
      TIME = 0.0
C   SET UP THE TOTAL TIME = NUN*DELTAT
C   WHERE NUM IS THE TIMES TO RUN
C+++++
      READ(5,*) NUM
      WRITE(6,500) NUM
500  FORMAT(/2X,'THE CALCULATING TIMES, NUM =',I5)
      DO 3000 NO = 1,NUM
          TIME = TIME + DELTAT/60.
          TEMP = -COOLRT*TIME + TEMPI + 273.15
          IF(TEMP .GT. 423.15 .AND. TEMP .LE. 573.15) GOTO 530
          IF(TEMP .GT. 293.15 .AND. TEMP .LE. 423.15) GOTO 540
          IF(TEMP .LE. 293.15) GOTO 545
          GOTO 550
530  bk = 1.8*EXP(-1789./TEMP)
      sk = 7.6*EXP(-630./TEMP)
      DS = .36*EXP(-5781./TEMP)
      DB = .144*EXP(-2132./TEMP)
      GOTO 560
540  bk = 1.8*EXP(-1789./TEMP)
      sk = 7.6*EXP(-630./TEMP)
      DS = .36*EXP(-5781./TEMP)
      DB = .0258*EXP(-3358./TEMP)
      GOTO 560
545  TEMP = 293.15
      bk = 1.8*EXP(-1789./TEMP)
      sk = 7.6*EXP(-630./TEMP)
      DS = .36*EXP(-5781./TEMP)
      DB = .0258*EXP(-3358./TEMP)
      GOTO 560
550  sk = 7.6*EXP(-630./TEMP)
      bk = 2.4*EXP(-3257./TEMP)
      DS = .04266*EXP(-4555./TEMP)
      DB = .144*EXP(-2132./TEMP)
560  ALPHA = sk/bk
      FPRES = FPRES/10.
      AO(1) = sk*SQRT(FPRES)
      CONHO(1) = AO(1)
      DO 608 I = 1,NEO
608      SDO(I) = DS
      DO 609 I = 1,NEB
609      SDB(I) = DB
C
C   CALCULATING HYDROGEN DISTRIBUTION IN OVERLAY
C
C   RATIO OF ACTIVITY COEFFICIENTS GAMRAT = GAMAA/GAMAG
C   WHICH IS GIVEN BY  $1 + .001228 * V_{pore} * EXP(6733/RT)$ 
C   FOR THE SECONDARY BOUNDARY  $V_{pore} = .5\%$ 
C   SO THE RATIO CAN BE CALCULATED AS

```

```

VPORE = 0.5
RATGAM = 1.+ .001228*VPORE*EXP(6733./(2.*TEMP))
DO 900 I = 1,NEO-1
  IEL = I
  NN(1) = ICONNO(IEI,1)
  NN(2) = ICONNO(IEI,2)
  X(1) = XNODO(NN(1))
  X(2) = XNODO(NN(2))
  SIZE(IEI) = X(2) - X(1)
  IF(IEI .EQ. NEO-1) SDO(IEI) = SDO(IEI)/RATGAM
  TRANS(IEI) = SDO(IEI)*DELTAT
  R1(IEI) = TRANS(IEI)/(SIZE(IEI)*SIZE(IEI))
  IF(NO .EQ. 2) THEN
    write(6,719) IEL,R1(IEI)
719  format(/2x,'the r parameter OF ELEMENT ',2X, I5,5x,G12.5)
  ENDIF
  CHJ = AO(NN(2))
  CHI = AO(NN(1))
  CHK = AO(NN(2)+1)
  AO(NN(2)) = CHJ + R1(IEI)*(CHK + CHI - 2.*CHJ)
C  STORE UP THE RESULT AT THE END OF TIME BEING
  CONHO(NN(2)) = AO(NN(2))
900  CONTINUE
C
C  CALCULATING THE CONC. AT THE BOUNDARY
C
  CALPHA1= 2.*CONHO(NONODO-2)/(1.+ RATGAM)
  CBETA1= 2.*CONHO(NONODO-2)/(1.+1./RATGAM)
  CALPHA2= 2.*CONHO(NONODO-1)/(1.+RATGAM)
  CBETA2= 2.*CONHO(NONODO-1)/(1.+1./RATGAM)
  CONHO(NONODO-2) = CONHO(NONODO-2) +
+    2.*R1(NEO-2)*(CONHO(NONODO-3) - CALPHA1) +
+    2.*R1(NEO-1)*(CONHO(NONODO-1)-CBETA1)
  CONHO(NONODO-1) = CONHO(NONODO-1) +
+    2.*R1(NEO-1)*(CONHO(NONODO-2) -CBETA2) +
+    2.*R1(NEO-2)*(CONHO(NONODO-1) -CALPHA2)
  DELS = XNODO(NONODO) - XNODO(NONODO-1)
  DELB = XNODB(2)-XNODB(1)
  CONH = DS*CONHO(NONODO-1)/DELS + DB*CONHB(2)/DELB
  AO(NONODO) = CONH/(DS/DELS + DB/(ALPHA*DELB))
  CONHO(NONODO) = AO(NONODO)
C
C
C=====
C  CALCULATING HYDROGEN DISTRIBUTION IN BASE METAL
C=====
  CONHB(1) = CONHO(NONODO)/ALPHA
  DO 1900 I = 1,NEB-1
    IEL = I
    NN(1) = ICONNB(IEI,1)
    NN(2) = ICONNB(IEI,2)
    X(1) = XNODB(NN(1))
    X(2) = XNODB(NN(2))
    SIZEB(IEI) = X(2) - X(1)

```



```

        TRANSB(IEL) = SDB(IEL)*DELTAT
        R1B(IEL) = TRANSB(IEL)/(SIZEB(IEL)*SIZEB(IEL))
        IF(NO.EQ. 1) THEN
            write(6,2061) IEL,R1B(IEL)
2061  format(2x,'R parameter of BM ELEMENT',2x, 15,8x,G12.5)
        ENDIF
        CHJ = BAO(NN(2))
        CHI = BAO(NN(1))
        CHK = BAO(NN(2)+1)
        BAO(NN(2))= CHJ + R1B(IEL)*(CHK + CHI - 2.*CHJ)
        CONHB(NN(2)) = BAO(NN(2))
1900  CONTINUE
        BAO(NONODB) = 0.0
        CONHB(NONODB) = BAO(NONODB)
C
C   WRITE OUT THE RESULT
C
        IF(NO.LT. NUM) GO TO 3000
        WRITE(6,2000) TIME
2000  FORMAT(/ 25X,'AT TIME',2X,G8.3,2X,'HOURS',
1      //8X,'DISTANCE FROM SURFACE,cm',5X,
2      'HYDROGEN CONCENTRATION, ppm')
        DO 2050 I = 1,NONODO
            WRITE(6,2030) XNODO(I),CONHO(I)
2030  FORMAT(/10X,G12.5,20X,G12.5)
2050  CONTINUE
            WRITE(6,2060) CALPHA1,CBETA1,CALPHA2,CBETA2
2060  FORMAT(/2X, 'CONCENTRATION AT THE SECONDARY BOUNDARIES',
1      /2X,4G12.5)
            WRITE(6,2100)
2100  FORMAT(/8X,'DISTANCE FROM INTERFACE,cm',5X,
1      'HYDROGEN CONCENTRATION,ppm')
            DO 2600 I = 1,NONODB
                WRITE(6,2550) XNODB(I),CONHB(I)
2550  FORMAT(/10X,G12.5,20X,G12.5)
2600  CONTINUE
3000  CONTINUE
C
        CLOSE(5)
        CLOSE(6)
        STOP
        END

```

Appendix D

Paper read at the 31st Metallurgists Conference of CIM, Edmonton 1992

FORMATION OF CRACK-SUSCEPTIBLE STRUCTURES OF WELD OVERLAY OF CORROSION RESISTANT ALLOYS

Y. Wu & B.M. Patchett

**Department of Mining, Metallurgical and Petroleum Engineering
The University of Alberta
Edmonton, Alberta, Canada T6G 2G6**

INTRODUCTION

For the manufacture of hydrogenation pressure vessels of heavy wall section, cladding with a layer or multilayer of corrosion resistant alloys on the inside of the vessel wall by Submerged Arc Welding of the strip electrode technology became a common practice (1,2,3,4,5,6,7) due to its ability to combine excellent deposit properties and controllable penetration with high deposition rate. However, the occurrence of overlay disbonding from the base steel, usually Cr-Mo low alloy steel, has remained a major problem confronted by this technique. Several investigations (4,5,6,7,8,9,10,11,12) have been carried out to find the solution to this problem. It is believed that there are three major factors attributing to the disbonding. The first is the accumulation of hydrogen at the interface between the overlay and base steel due to the difference in solubility and diffusivity of hydrogen in these two materials. Secondly, the susceptible microstructure along the interface easily loses its bonding strength at the presence of hydrogen. Finally the difference in thermal expansion between the overlay and base steel will give rise to high residual tension stresses at the interface. Because of the working condition of the pressure vessels, little or nothing can be done to significantly alter the distribution of hydrogen across the vessel wall. The microstructure at the interface, which depends on the welding procedure and the composition of overlay materials, draws the attention of investigators. It has been found (7,13) that the so-called Type-II grain boundary, which develops parallel to the fusion line adjacent to the interface in the overlay side, takes the major responsibility for the hydrogen-related disbonding, not the martensite structure as thought before. Up to now the mechanism of the formation of the Type-II grain boundary is not clear. In this paper the formation of the Type-II grain boundary was investigated by cladding eight types of different corrosion resistant alloys on plates of Cr-Mo low alloy steel. The alloys were chosen to vary the final deposit microstructures from duplex ferrite-austenite to fully austenitic (high nickel level) with solidification modes varying from fully ferritic to fully austenitic.

EXPERIMENTAL

Welding Procedures

Eight strip electrodes (0.5 x 60 mm) of the alloys, 2205, 309L, 309LMo, 309LNb, 254SMO, 904L, 5923 and Hastelloy C-22, were submerged arc welded to 65 mm thick plates of 1.25Cr-0.5Mo low alloy steel. The chemical composition of the alloys for the cladding is listed in Table I.

Two welding procedures were employed in the strip cladding with the same nominal heat input of 9kJ/mm:

Procedure	Current,amp	Voltage, volts	Travel speed, mm/min
I	750	28	140
II	1500	28	280

The other welding parameters were: electrical stick out 35 mm, polarity DC with electrode positive, preheat 150°C, electrode angle 90° to the plate of welding, and overlap thickness about 6 mm. The flux, Sandvik 34SF, was baked for 2 hours at 260 °C, and then placed in the holding oven at 150°C before welding. The flux was considered to form acid slags since its Basicity Index of IIW was 0.81 (< 1.0).

Table I - Chemical Compositions of Alloys Used for Cladding, wt. %

	2205	309L	254SMO	904L	C-22	309LMo	309LNb	5923	Base
C	0.015	0.009	0.014	0.016	0.006	0.012	0.017	0.007	0.125
Si	0.350	0.510	0.390	0.480	<0.020	0.200	0.340	0.040	0.547
Mn	1.610	1.790	0.480	1.750	0.310	1.690	1.930	0.150	0.510
P	0.029	0.015	0.026	0.018	0.010	0.013	0.012	0.002	0.005
S	0.003	0.003	0.001	0.003	<0.003	0.001	0.001	0.003	0.014
Cr	21.77	23.75	20.100	19.92	21.220	20.330	23.740	22.500	1.279
Ni	5.700	12.88	17.900	24.95	56.970	13.520	12.370	60.900	0.206
Mo	2.990	0.060	6.130	4.430	13.430	2.860	0.030	15.500	0.490
Co		0.035			0.840	0.038	0.020	0.020	
Cu		0.037	0.74	1.460		0.070	0.067		0.171
Al									
N	0.160	0.045	0.192			0.029	0.031		
Nb							0.700		
W					3.290				
V					0.140			0.005	
Ti					0.030			0.001	
Fe	bal.	bal.	bal.	bal.	3.170	bal.	bal.	0.340	bal.

Postweld Heat Treatment

Specimens for autoclave testing (54 x 54 x 65) were cut from the center of the weld bead of the clad plates. Postweld heat treatment to standard industrial practice was done to stabilize the structure in the welds and to reduce the residual welding stresses in the specimens. To minimize the risk of developing transient thermal tensile stress in the specimens, the specimens were heated uniformly at a rate of 50 °C per hour to 690 °C in a furnace. The specimens were kept at 690°C for 24 hours then cooled down to room temperature at 50°C per hour.

Autoclave Test to Promote Disbonding

The specimens after PWHT were put into an autoclave and hydrogen was then introduced into the chamber at a pressure of 10 MPa. The autoclave was heated at a rate of 100 °C per hour up to 450 °C, at which the hydrogen pressure increased to 15 MPa. After being held at the temperature of 450 °C and at the hydrogen pressure of 15 MPa for 48 hours, the specimens were cooled down to room temperature at a high cooling rate of 222 °C per hour in order to promote disbonding. The use of the fast cooling rate was to simulate the practical shut-down process of pressure vessels in an emergency situation. It had been found the faster the cooling rate the more severe the disbonding(14). Nitrogen gas was allowed to flow through the chamber to control the cooling rate.

Ultrasonic Examination

The 54 x 54 mm specimens were examined by C-scan U.T.S. in the as-welded and after-autoclave test conditions to locate the disbonding. The probe was placed at the base metal side. The test was carried out with a Sonatest U.T.S. machine and a TSI Ultrasonic Immersion Programmable Scanner. Specimens were immersed in water, the probe was set about 40 mm above the surface of the specimen and full width scanning was carried out with a step interval of 2.5 mm. The frequency used was in the range of 2.5 to 5.0 MHz.

Metallographic Observation

The microstructures of the clad specimens were observed on an optical metallographic microscope in the as-welded and after-autoclave test conditions respectively.

Dilution Effect of Procedures

To evaluate the amount of dilution between the cladding material and the base metal in the overlay, the area of the cross-section of the weld overlay was measured on an image analyzing system. The total area of the cross-section of the weld metal was assigned as $F1 + F2$, where $F1$ was the area of the weld overlay above the original level of the base metal surface, and $F2$ was the area of the overlay in the base metal side. Also the height of the weld bead was measured as the height of crown, C , and the depth of the weld bead as penetration, P .

EXPERIMENTAL RESULTS

Dilution Effect of Welding Procedures

Generally a high current welding procedure will produce a larger weld pool, hence higher dilution. There is no exception for this test as seen in Table II. But the composition of electrode also affects the arc stability, the penetration and the transition of overlay materials to the pool. A significant difference in dilution between the two nickel-based alloys, C-22 and 5923, was noted.

Table II - Dilution Effect of Procedures

		F ₂ , mm ²	F ₁ + F ₂ , mm ²	D, %	W, mm	P, mm	C, mm
Procedure I	2205	53.6	236.3	22.7	57.7	2.04	3.27
	309L	53.9	242.6	22.2	59.0	1.65	3.50
	309LMo	99.8	319.3	31.3	65.1	2.66	4.39
	309LNb	86.1	289.3	29.8	63.7	1.92	3.32
	254SMO	81.2	289.7	28.0	60.9	2.30	3.75
	904L	63.7	274.6	23.2	59.0	1.65	3.50
	C-22	52.9	249.9	21.2	61.5	1.60	3.62
	5923	142.1	419.0	33.9	65.6	3.10	5.20
Procedure II	2205	86.3	267.9	32.0	61.0	1.90	4.6
	309L	147.6	340.9	43.3	60.3	3.20	3.7
	309LMo	145.3	376.2	38.6	64.6	3.62	4.2
	309LNb	131.5	358.8	36.6	65.7	3.34	4.3
	254SMO	119.2	337.8	35.0	64.9	3.45	4.1
	904L	84.5	274.2	31.0	58.9	3.04	3.5
	C-22	93.4	320.2	29.0	60.0	2.26	4.2
	5923	165.7	423.8	39.1	73.3	2.48	5.2

D: the dilution effect; W: the width of weld beads.

Ultrasonic C-scan Test

No disbonding was found immediately after welding and PWHT. Disbonding was discovered in most of the specimens (except in deposits of 2205) after the hydrogen-charged autoclave test, as shown in Table III. The result is presented in terms of the disbonding area percent of the total clad area of the specimen. The degree of disbonding was relatively severe in 254SMO and 904L specimens. However, the extent of disbonding showed a significant statistical difference in the specimens of 309L series and 254SMO when the two welding procedures were compared. Disbonding took place to a certain degree in 904L and 5923 specimens, but there is no significant difference for the two welding procedures. Less disbonding was detected in C-22 specimen.

Microstructures along the Interface and Disbonding Phenomenon

In the as-welded condition, the microstructures adjacent to the fusion line in the overlay showed a notable difference among the specimens, despite the structure in the base steel side being similar to each other in the typical appearance of the heat affected zone in a weld. No obvious border was seen between the overlay and the base steel in the specimen of 2205 (Fig. 1), a duplex stainless steel.

Table III - Disbonding Analysis by Ultrasonic C-scan, %

Specimen No.	1	2	3	mean	1	2	3	mean
Procedure I					Procedure II			
2205	0.0	0.0	0.0	0.0	0.0	0.0	0.0	0.0
309L	7.5	7.6	3.9	6.3	0.0	0.7	3.5	1.4
309LMo	3.1	2.4	4.2	3.2	2.0	1.8	1.1	1.6
309LNb	10.3	8.2	3.2	7.3	7.3	1.3	2.1	3.6
254SMO	28.5	17.8	14.2	20.2	11.4	17.8	10.7	13.3
904L	0.1	23.1	2.8	8.6	19.6	2.1	8.2	10.0
C-22	0.0	0.1	0.0	0.03	0.1	0.0	0.1	0.06
5923	4.2	3.8	1.3	5.8	6.1	9.5	4.8	4.1

A layer of martensitic structure, the thickness of which depended on the dilution effect of welding, formed as the transition zone from the base steel to the overlay. In the specimens of 309L series, cellular grains of the overlay were able to develop directly from the stagnant layer between the overlay and the base steel in some region along the fusion line. But in other regions, planar grains grew first, and then the cellular grains formed on them. So the Type II grain boundary appeared as the result of the growth mode change from the planar to the cellular (Fig.2). The high current and high speed welding procedure increased the thickness of the stagnant layer between the overlay and the base steel, in which more martensite formed and cellular grains were able to directly stretch out from this layer toward the overlay surface without the formation of the Type II grain boundary (Fig.3). As the nickel-equivalent increased in the specimens of 254SMO and 904L, more Type II grain boundaries were observed (Figs. 4 and 5). Different welding procedures did not produce a remarkable change in this kind of microstructure. For the nickel-based alloys, C-22 and 5923, there was a sharp border between the overlay and the base steel (Fig.6), reflecting the distinct change of the crystal growth (even at the initial nucleation stage during the solidification) and the strong resistance of nickel to the carbon diffusion from the base steel to the overlay. The content of nickel was so high that no visible martensite was found in the overlay adjacent to the fusion line. High current welding might dilute more base steel into the weld pool. The precipitation of inclusions near the interface may disturb the growth of the cellular grains, as seen in Figure 7.

After the autoclave test, disbonding was observed in specimens of 309L series, 254SMO and 904L. The typical cracking path was along the Type II grain boundary as seen in Figure 8. In the region where there was no Type II grain boundary, no cracking was detected, even if there was a lot of martensitic structure (Fig.9). This result agrees with the observation of other researchers [4,11,15]. It is obvious that the microstructure susceptible to the hydrogen-related disbonding is the Type II grain boundary. The martensitic structure may only play a minor role.

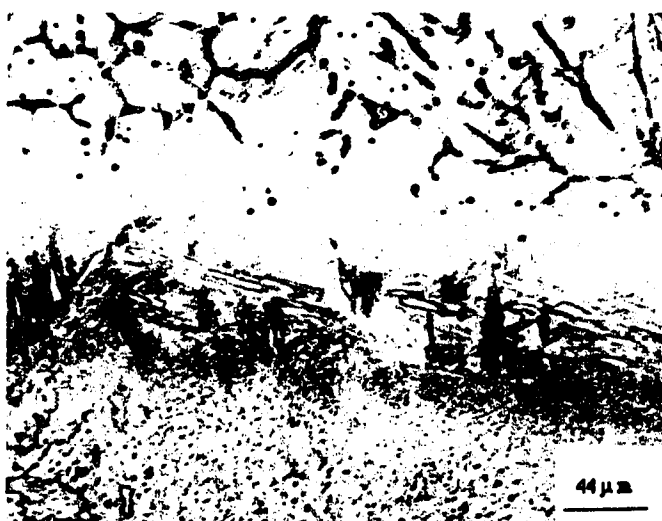


Figure 1 - Microstructure of 2205 along interface, showing no obvious border.



Figure 2 - Microstructure of 309L along interface, showing cellular grains growing from interface and from Type II grain boundary.



Figure 3 - Microstructure of 309LMo along interface, a relative thicker martensite layer without Type II boundary.



Figure 4 - Microstructure of 254SMO along interface, showing Type II grain boundary.

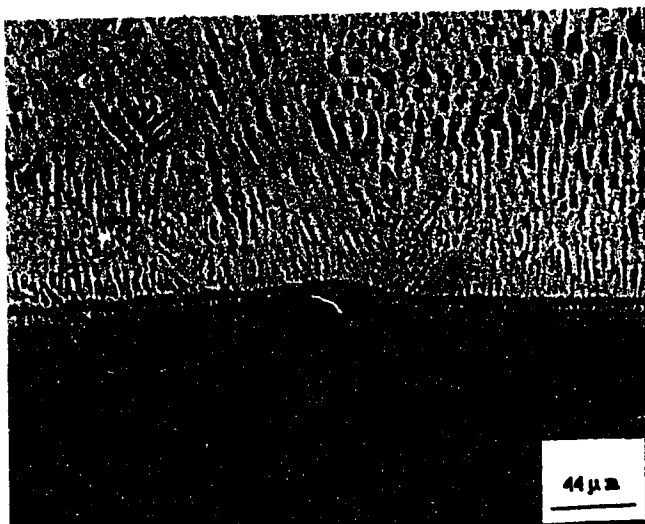


Figure 5 - Microstructure of 904L along interface, showing Type II grain boundary.

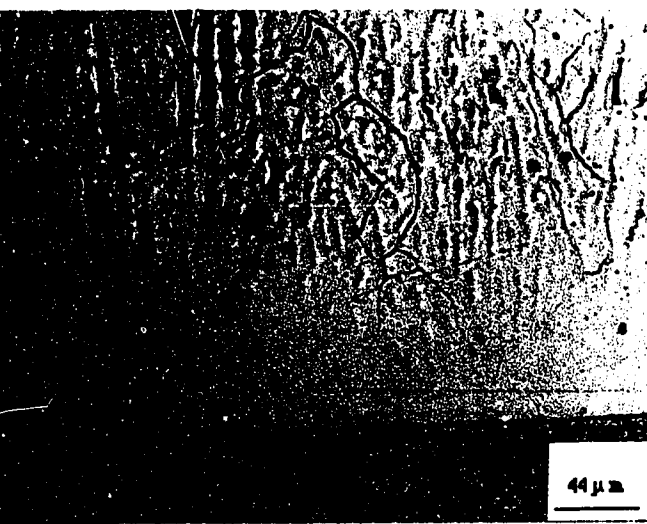


Figure 6 - Microstructure of C-22 along interface, showing sharp border and cellular grains.

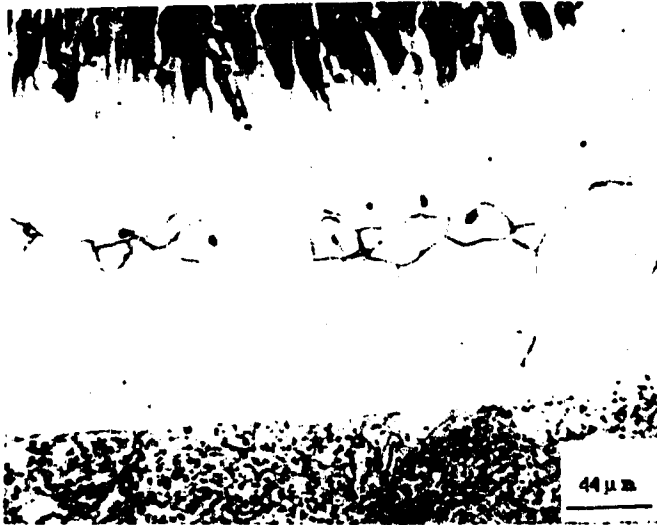


Figure 7 - Higher dilution effect of welding disturbs the cellular grain growth in 5923.



Figure 8 - Disbonding in the specimen of 254SMO, showing the typical cracking path was along the Type II grain boundary.

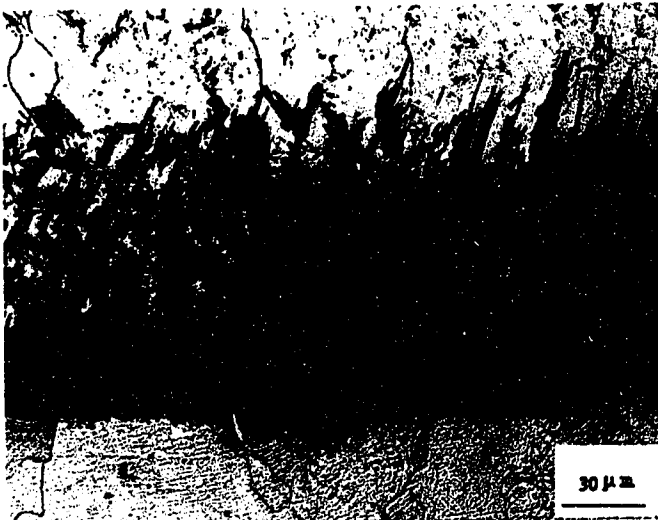


Figure 9 - Martensitic structure in 309L by Procedure II after autoclave test, no cracking in the thick martensite layer.

DISCUSSION

The Formation of the Type II Grain Boundary

As is seen, disbonding in most cases takes place along the Type II grain boundary adjacent to and along the fusion line in the overlay. Therefore, it is important to seek out the factors which affect the formation of the Type II grain boundary. Since the Type II grain boundary is located on the overlay side, it is probable that this structure is related to the solidification processes, i.e. the nucleation and growth of the weld metal, during welding.

Generally, the microstructure of the weld metal can be understood by considering the general theories of nucleation and growth behavior of crystals in the Fe-Cr-Ni system in the special welding condition of the Cr-Mo low alloy steel as the substrate. The development of the weld metals is determined by the welding procedure and the chemical composition of the overlay and base materials.

Effect of Overlay Chemistry

The nucleation of the weld metal at solidification can be realized either by epitaxial growth from the base steel or by heterogeneous nucleation on the pre-existing interface between the weld metal and the base metal. It has been shown that (16) the chemical affinity between the base metal and the solidifying phases and also the lattice discrepancy are important factors affecting the nucleation efficiency during welding. In consideration of the chemical affinity, nickel and chromium, which are the main composition of the overlay materials, have good chemical affinity with iron, the main portion of the base metal. It is therefore unlikely that cracking occurs just after welding. The Cr-Mo steel possesses a BCC structure (δ ferrite) at temperatures close to the fusion temperature, since the carbon level is only 0.125% and Cr and Mo are both ferrite stabilizers. Therefore, a weld metal with a BCC lattice structure as the primary solid phase during solidification would grow epitaxially from or nucleate on the base metal quite easily. If a weld metal solidifies with a partially or wholly different crystal structure from the base steel as the primary solid phase, it might be difficult for grains to grow epitaxially from the base metal. There is then the possibility of a distinctive interface between the base metal and the overlay at some stage, caused by the change in crystal structure.

Referring to the Fe-Cr-Ni ternary phase diagram (17), it is seen (Figure 10) that the compositions of the materials chosen in this test for the overlay locate around the 20%Cr line in the diagram. With the increase of nickel, the primary solid phases during solidification change from δ to $\delta + \gamma$ and then to γ . Accordingly, the possible first solid phase or phases of the solidification of the overlay alloys during welding in this test is: δ - ferrite in 2205; $\delta + \gamma$ in 309L, 309LMo, 309LNb and 254SMO; and γ in 904L, C-22 and 5923. Consequently, the nucleation of weld metal of 2205 would be epitaxial without a distinct interface between the base metal and the overlay, while the interface would be sharp in the specimen of C-22 and 5923 because the crystals nucleated on the surface of a different structure of the base steel. The nucleation of weld metals of 309L, 309LMo, 309LNb and 254SMO might be partly epitaxial as δ -ferrite and partly nucleated as γ -austenite.

The type of the lattice structure of the primary solid phase is crucial for the formation of the Type II grain boundary, as there would be a phase change of the solidifying phase at the solidifying front during solidification. For the overlay of 2205, its content of chromium is so high that the whole solidification process would form δ -phase only. γ can only be obtained in the following solid state transformation, showing a vermicular duplex structure

(18). For the overlays obtained from 309L, 309LMo and 309LNb, the primary solid phase may be δ in some sites on the interface and may be γ in some other sites, depending on the extent of the mixing of the overlay and base metal during the welding. In consideration of the composition of 904L (which lies close to the $L+\gamma+\delta$ eutectic zone), the overlay of 904L may nucleate as δ in some positions along the interface due to the dilution effect, although it mostly forms γ as the primary solid phase. The primary solid phase would be γ in specimens of C-22 and 5923 according to the phase diagram (17).

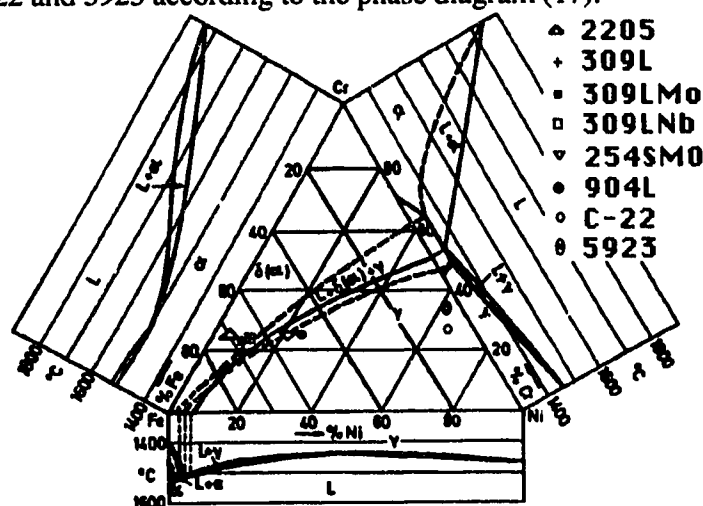


Figure 10- Chemical compositions of overlay alloys in Fe-Cr-Ni ternary system.

The growth mode of the solidifying phase directly affects the formation of the Type II grain boundary. Here two possibilities are proposed to explain the phenomenon of the Type II grain boundary.

For alloys, as is known, the growth of the solidifying phase mainly depends on the composition of the overlay, the cooling rate and the thermal gradient field. In the welding of dissimilar metals, one possible mechanism of the formation of the Type II grain boundary is the solidifying phase changing from δ to γ during solidification in welding, as was reported by (18). Due to the dilution and the sharp variation in chemical compositions, the growing solid phase, which might assume the lattice pattern of the base metal at the beginning of solidification, may be thermodynamically forced to change to another solidifying phase with a different lattice pattern from the base metal. While δ -ferrite grows, the depletion effect of nickel or other elements at the solidifying front and the sharp increase in nickel content as the distance increases away from the stagnant layer may shift the solidifying phase from the δ -ferrite to γ -austenite. The γ phase would then tend to form by newly nucleating, or by peritectic or eutectic reactions. Hence the Type II grain boundary emerged as the result of the mismatch of the BCC and FCC structures during solidification. The followed solid transformation turns the primary δ -ferrite totally or partially to γ -phase as the temperature drops. Some martensite and bainite structures are formed depending on the local composition and the cooling rate. As for 2205, the overlay of 2205 would form δ -ferrite first and then transform partially to γ later. The γ phase formed in the solid transformation would envelop the former δ ferrite. Properly choosing the etchant for the ferritic structure, a less affected band was revealed just above the transition layer from the base metal to the overlay and below the dendritic grains of the

overlay. This band may contain more nickel since it transformed almost fully to austenite and maintained this status (Fig.11). Since the nucleation of overlays of 309L, 309LMo and 309LNb may either be as δ or as γ , the growth of the overlays appeared differently at different positions along the interface. Researchers (18,19), who studied the solidification process of austenitic stainless steels with different dilution levels, attempted to simulate the composition effect on the solidification process of alloys with compositions near and in the peritectic and eutectic range of Fe-Cr-Ni system. These compositions are similar to the 309L series and 254SMO. The solidification process for these alloys would be postulated as follows:

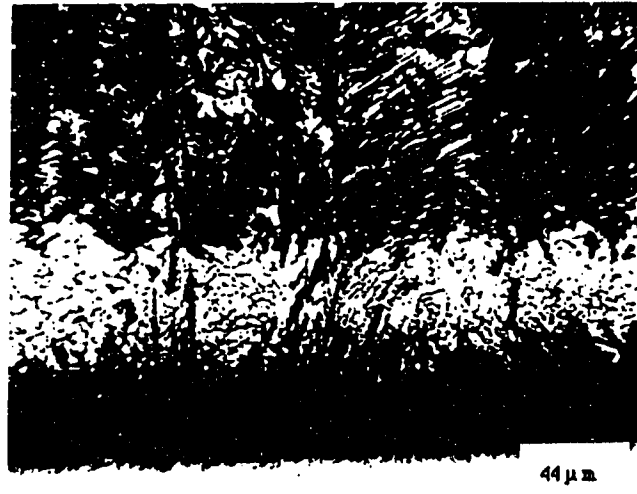


Figure 11 - A band of austenitic structure between transition zone and dendritic grains in 2205.

At positions of the interface where the nuclei are δ -phase, if the thermal gradient and growth orientation are favorable for the growth of cellular grains, the cellular grains grow epitaxially from the base metal. These will penetrate the liquid weld metal relatively fast until the enrichment of nickel ahead of the interface reaches the critical level which may cause the transition from δ -ferrite to primary γ phase as growth proceeds. Thus the cellular growth of δ -ferrite will not necessarily result in a flat solidifying front, so there would not be the Type II grain boundary. As the primary solid phase turned to γ -phase, which also assumes the cellular morphology extending toward to the overlay surface, the ferrite formed afterwards by the depletion effect of Cr during the solidification of γ -phase could then form at the intercellular position of γ -phase. The subsequent solid transformation of austenite at the interface between the overlay and base metal produced a morphology of acicular ferrite or martensitic structure depending on the degree of dilution and the cooling rate. There was no Type II grain boundary at these positions. But, if the thermal gradient and the preferred orientation of HAZ grains were not favorable for the cellular growth of ferrite, the lower growing rate of the planar grain would give a chance to form Type II grain boundaries, since there was more time for nickel atoms to move to the solidifying front. The planar solidifying front may result in the second possibility for the formation of the Type II grain boundary, as described below.

The second possibility is the pile-up of minor inclusions due to segregation to the solidifying front of the γ -phase at positions where the primary solid phase was γ -phase. The segregation of impurities might produce a film of secondary phase just ahead of the solidifying front. In the transition region, more impurities were present, due to the dilution of base metal (which usually contained more impurities than the overlay materials). The segregation of iron had been observed at the grain boundary adjacent to the fusion line in the specimen of C-22 (20). However, this film was not continuous over all the solidifying

front, due to the inhomogeneity of composition near the fusion zone. Cracking may not occur just after welding, since only a relatively thin layer was welded on the base metal. However, a segregated zone of the weld was induced, which acted as the trapping site for the accumulation of hydrogen in the autoclave test and promoted the disbonding later. In addition, the initially formed boundary provides sites for the segregation of carbides and other inclusions during PWHT. For overlays of 904L and 254SMO, Type II grain boundaries might form in accordance to the impurity-film mechanism, since there was little or no ferrite formed to reduce the accumulation of impurities at the solidifying front. As for the overlays of C-22, the much lower level of impurities in this alloy made the Type II grain boundary difficult to form. Only quite faint boundaries were observed after PWHT. The higher level of dilution in the specimen of 5923 gave more chance for the impurity-film to form at the solidifying front near the fusion line. Subsequently, more disbonding was found in the specimen.

As well as Cr and Ni, the major alloy elements in the overlays, other elements also played some roles in the formation of Type II grain boundary. Low carbon (and Cr-Mo alloy elements) in the base metal made it possible for the HAZ grains at the interface to keep the BCC structure for a longer time at the beginning of solidification. A relatively high content of phosphorus and sulfur in alloys 254SMO and 904L increased the tendency to Type II boundary formation by increasing impurity segregation. Also the formation of the Type II grain boundary is affected by the constitutional supercooling condition, the extent of which is dependent upon the welding procedure.

Effect of Welding Procedures

Welding procedures influence the formation the Type II grain boundary by affecting the magnitude of dilution, (hence the composition of the weld pool), the dynamic thermal field, and the cooling rate of the weld metal. Therefore the nucleation and growth mode of the weld metal will depend, to a large extent, on the welding procedure.

In the case of high current and high speed welding, more base metal is mixed into the overlay and the width of the quasi-stagnant zone would increase as seen from the metallographs. The chance of the formation of δ -ferrite would increase, since the composition in the stagnant region was close to that of the base metal and new grains of ferrite would be easier to grow from the half-melted zone. This effect was clearly seen in overlays of alloys which solidify with δ and γ as primary solids. Also, high current and high speed welding would cause high heat-up and cool-down rates. Hence, the nucleation rate of the weld metal or the epitaxial growth rate would be increased. Therefore cellular grains obtained by Procedure II appeared finer than those by Procedure I.

The growth behavior of the weld metal during solidification determines the formation of the Type II grain boundary. As is known (16), the possible growing modes of weld metal can be classified as planar growth, cellular growth, columnar dendritic growth and equiaxial dendritic growth. In an alloy system the growth mode of the weld metal is mainly determined by the extent of constitutional supercooling which can be expressed as $G_L/R < \Delta T_0/D_L$, where G_L is the temperature gradient in liquid at the front of the solidifying phase; R is the growth rate of the solidifying front; ΔT_0 is the temperature difference between liquidus and solidus at composition C_0 and D_L the solute diffusion coefficient in liquid. According to the derived thermal model (21), in the weld pool the steep temperature gradient occurs at the base metal surface while the liquid weld metal just drops on it. Consequently the crystals nucleating on the surface of the base metal will grow along the surface of the base metal in the planar mode as shown schematically in Figure 12 because there is a high temperature gradient and low growth rate near the interface region.

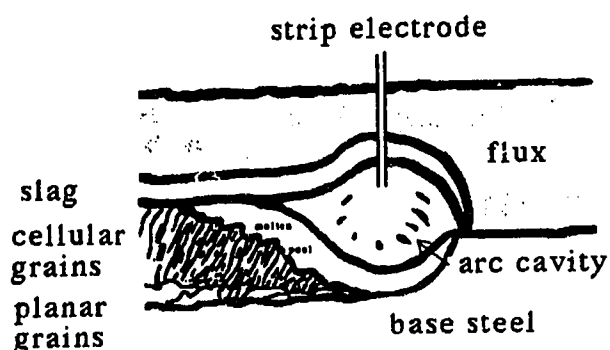


Figure 12 - Schematically showing the solidification of the overlay

The initial crystals of the weld metal are quite like the chill zone in a casting, especially for the nuclei of the γ -phase owing to the lattice disregistry. While the crystals grow towards the top of the overlay and the centreline of the weld pool, the temperature gradient in the liquid ahead of the solidifying front decreases because of the release of the latent heat as a result of the formation of solid phases, and the growing rate will also increase as a consequence of the readjustment of the preferred growth orientation, which usually tends antiparallel to the heat flow direction.

The welding procedures may affect the retaining time for the growth of planar grain as well. The high current and high speed welding would reduce the temperature in a short time due to the faster cooling rate. On the other hand, the low speed and low current of Procedure I would allow the planar grains to develop further and the segregated elements to diffuse to the front of solidifying phase. The tendency of forming Type II grain boundary increased in Procedure I for alloys 309Ls and 254SMO.

For the overlay of 2205, the welding procedure will not alter the solidification process of overlay as mentioned above except for the nucleation and growth rate. For alloys of 309L series, the high current and high speed welding would make δ phase easier to nucleate or to grow from the base metal than that in the low current and low speed welding, as a result of the increase of dilution mentioned above. In the advance of solid transformations during cooling down, γ -phase would envelop the primary δ phase due to the accumulation of nickel at the front of the solidifying phase. As the solidification was not a homogeneous process in consideration of the dilution effect and the temperature distribution, there were still some Type II grain boundaries formed by the high welding speed procedure. But, the tendency is remarkably reduced. The nickel content in 254SMO was high enough that the high current and high speed welding could not produce dilution large enough to change its nucleating and growth mode significantly. Only the cellular or dendritic grains become finer. The disbonding, though reduced, still took place to quite an extent. The nickel content was so high in 904L, C-22 and 5923 that no δ phase would grow as the primary solid phase. Therefore the formation of Type II grain boundary in these high nickel alloys was mainly determined by their compositions. The higher dilution effect, in these cases, may even promote the formation of the Type II grain boundary, due to more impurities from the base metal being involved in the solidification. Other factors such as the dilution effect of carbon and iron might also play some important parts in the formation of the Type II grain boundary.

CONCLUSION

The formation of the Type II grain boundary is determined by the chemical compositions of the cladding alloys and the welding procedure. If the primary solidifying phase of the overlay is δ -ferrite, the chance to form Type II grain boundary would be minimized. If the primary solidifying phases are $\delta + \gamma$, the high current and high speed welding procedure will reduce the tendency to form the Type II grain boundary. For cladding alloys which primary solidifying phase is γ - austenite only, a low level of dilution, corresponding to low current and low speed welding, would produce a better microstructure with less Type II grain boundaries. Without the Type II grain boundary adjacent to the fusion line between the overlay and the base steel, the tendency of disbonding is greatly reduced.

ACKNOWLEDGEMENTS

The authors give their thanks to Mr. C. Bicknell for his help in preparation of specimens for the test and his help in autoclave test .

REFERENCES

1. R.David, Thomas,Jr., "Corrosion -Resistant Weld Overlay by the Dual-Strip Process", British Welding J. Vol.13, 5, (1966), 307
2. P.G.Cappelli , G.Frigerio, "Strip Cladding with Inconel", Metal Construction and British Welding J. Vol.16, 12,(1969), 555
3. A.B.Marshall,et al, "Stainless Steel Strip Cladding" Welding and Metal Fabrication, 8, (1973), 292
4. F.Matsuda, et al, "Disbonding between 2 1/4 Cr -1 Mo steel and Overlay Austenitic Stainless Steel by Means of Electrolytic Hydrogen Charging Technique" Trans. Jpn. Weld. Res. Inst., V.13, 2, (1984), 91
5. A.Fuji,et al, "Mechanical properties Of Stainless Steel Overlay weld with Resistance to Hydrogen- Induced Disbonding", Trans.Jpn.Weld.Soc., V.17, 1, (1986), 27
6. K.Ohnishi, et al, "Hydrogen Induced Disbonding of Stainless Steel Overlay Weld", Report of Jpn. Steel Works.Ltd., Chiyoda Chemical Engr.and Construction Co.Ltd., Sept.1980
7. M.Godden and L.Seto, "Disbonding of Stainless Steel Weld Overlay Following Simulated Pressure Vessel Service Exposure", CANMET report, ERP/PMRL 83-69(TR)
8. J.Shimomura,et al, "Disbonding of Overlay Weldment in Vanadium-modified 2 1/4 Cr-1Mo Steels" J.Iron Steel Inst.Jpn., 75, 5, (1989), 798
9. N.Yurioka, et al, "An Analysis of Effects of Microstructure, Strain and Stress on the Hydrogen Accumulation in the Weld Heat-Affected Zone", IIW Doc., IX-

1161-80

10. N.Morishige, et al, "Influence of Low Temperature Hydrogen Degassing on Hydrogen-Induced Disbonding of Cladding", Trans. Jpn. Weld. Soc. Vol.16,1,(1985), 12
11. K.Ohnishi, A.Fuji,et al, "Effect of Strip Overlay Welding Conditions on Resistance to Hydrogen- Induced Disbonding", Trans. Jpn.Weld.Soc., 5,2, (1984),49
12. J.Watanabe, et al,"Hydrogen-induced disbonding of stainless steel overlay found in desulfurizing reactor", Conf. performance of pressure vessel with clad and overlaid stainless steel linings, Denver, June,1981, ASME publishing , MPC 116
13. J.T.McGrath, et al, unpublished manuscript.
14. A.P. Chakravarti; L.Malik: "Modelling Hydrogen Distribution in Weld Overlay System", The Report of Welding Institute of Canada, 7-186-063/F
15. J.T. McGrath; R.S. Chandel; et al:"Weld Overlay Disbonding", unpublished manuscript, June 1988
16. S.A. David; J.M. Vitek: "Correlation between Solidification Parameters and Weld Microstructures", International Materials Reviews, Vol.34, No.5, 1989, p213 -245
17. Erich Folkhard: Welding Metallurgy of Stainless Steels, Springer-Verlag Wien, New York, 1988
18. J.C. Lippold & W.F.Savage, "Solidification of Austenitic Stainless Steel Weldments: Part 2--The Effect of Alloy Composition on Ferrite Morphology", Welding Journal, Feb.,1980, 48s-58s
19. S.A. David, "Ferrite Morphology and Variations in Ferrite Content in Austenitic Stainless Steel welds", Welding Journal, April 1981, 63s-71s
20. Y. Wu, Experimental Report on Hydrogen Related Disbonding of Weld overlay, Dept. of Min.Met.Pet.Engineering, University of Alberta, Feb. 1992
21. L.Karlsson,"Thermal Stresses in Welding", Thermal Stresses I, Edited by Richard B. Hetnarski, North- Holland, 1986,297-389